Zero Waste Approaches for Cost-Effective Treatment of Industrial Waste

Lead Guest Editor: Erol Yilmaz
Guest Editors: Shuai Cao, Weidong Song, and Ibrahim Cavusoglu

Zero Waste Approaches for Cost-Effective Treatment of Industrial Waste
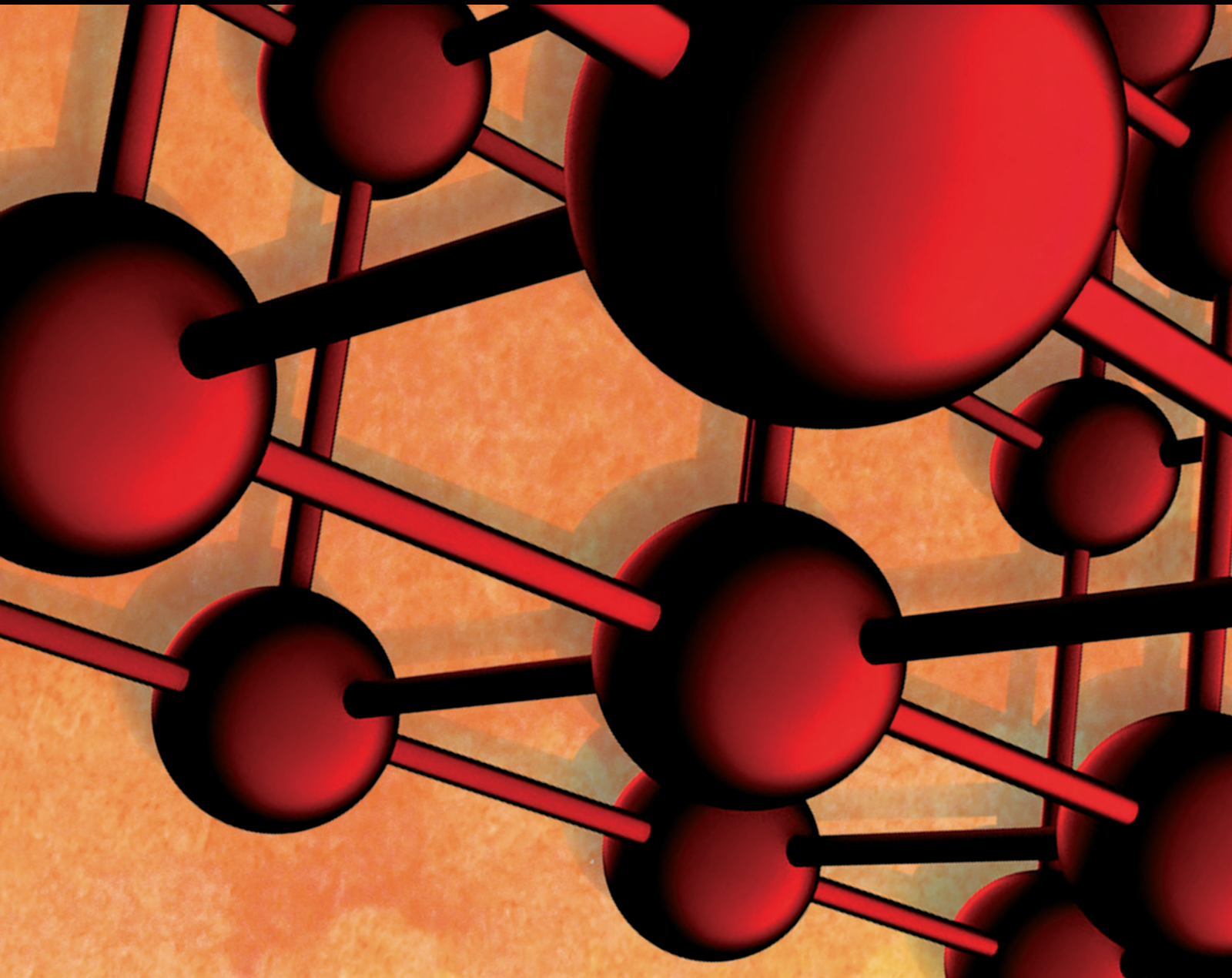
Zero Waste Approaches for Cost-Effective Treatment of Industrial Waste

Lead Guest Editor: Erol Yilmaz
Guest Editors: Shuai Cao, Weidong Song, and
Ibrahim Cavusoglu

Achraf Ghorbal , Tunisia
Georgios I. Giannopoulos , Greece
Ivan Giorgio , Italy
Andrea Grilli , Italy
Vincenzo Guarino , Italy
Daniel Guay, Canada
Jenö Gubicza , Hungary
Xuchun Gui , China
Benoit Guiffard , France
Zhixing Guo, China
Ivan Gutierrez-Urrutia , Japan
Weiwei Han , Republic of Korea
Simo-Pekka Hannula, Finland
A. M. Hassan , Egypt
Akbar Heidarzadeh, Iran
Yi Huang , United Kingdom
Joshua Ighalo, Nigeria
Saliha Ilican , Turkey
Md Mainul Islam , Australia
Ilia Ivanov , USA
Jijo James , India
Hafsa Jamshaid , Pakistan
Hom Kandel , USA
Kenji Kaneko, Japan
Rajesh Kannan A , Democratic People's
Republic of Korea
Mehran Khan , Hong Kong
Akihiko Kimura, Japan
Ling B. Kong , Singapore
Pramod Koshy, Australia
Hongchao Kou , China
Alexander Kromka, Czech Republic
Abhinay Kumar, India
Avvaru Praveen Kumar , Ethiopia
Sachin Kumar, India
Paweł Kłosowski , Poland
Wing-Fu Lai , Hong Kong
Luciano Lamberti, Italy
Fulvio Lavecchia , Italy
Laurent Lebrun , France
Joon-Hyung Lee , Republic of Korea
Cristina Leonelli, Italy
Chenggao Li , China
Rongrong Li , China
Yuanshi Li, Canada

Guang-xing Liang , China
Barbara Liguori , Italy
Jun Liu , China
Yunqi Liu, China
Rong Lu, China
Zhiping Luo , USA
Fernando Lusquiños , Spain
Himadri Majumder , India
Dimitrios E. Manolakos , Greece
Necmettin Maraşlı , Turkey
Alessandro Martucci , Italy
Roshan Mayadunne , Australia
Mamoun Medraj , Canada
Shazim A. Memon , Kazakhstan
Pratima Meshram , India
Mohsen Mhadhbi , Tunisia
Philippe Miele, France
Andrey E. Miroshnichenko, Australia
Ajay Kumar Mishra , South Africa
Hossein Moayedi , Vietnam
Dhanesh G. Mohan , United Kingdom
Sakar Mohan , India
Namdev More, USA
Tahir Muhmood , China
Faisal Mukhtar , Pakistan
Dr. Tauseef Munawar , Pakistan
Roger Narayan , USA
Saleem Nasir , Pakistan
Elango Natarajan, Malaysia
Rufino M. Navarro, Spain
Miguel Navarro-Cia , United Kingdom
Behzad Nematollahi , Australia
Peter Niemz, Switzerland
Hiroshi Noguchi, Japan
Dariusz Oleszak , Poland
Laurent Orgéas , France
Togay Ozbakkaloglu, United Kingdom
Marián Palcut , Slovakia
Davide Palumbo , Italy
Gianfranco Palumbo , Italy
Murlidhar Patel, India
Zbyšek Pavlík , Czech Republic
Alessandro Pegoretti , Italy
Gianluca Percoco , Italy
Andrea Petrella, Italy

Contents

Research Article

Experimental Research on Durability of Fly Ash Pavement Concrete and Mix Proportion Optimization

Hong-xia Zhai,[1] Yu-zhao Tang,[1] Shu-hang Chen,[2] Hui-hua Chen [ID],[3] Bao-quan Cheng [ID],[3] Xi Cai,[3] and Yu-hu Wei[1]

[1]*School of Materials and Chemical Engineering, Anhui Jianzhu University, Hefei 230601, China*
[2]*School of Civil Engineering, Central South University, Changsha, Hunan 410075, China*
[3]*Department of Civil Engineering, Xi'an Jiaotong-Liverpool University, Suzhou, Jiangsu 215123, China*

Correspondence should be addressed to Bao-quan Cheng; curtis_ch@163.com

This paper focused on the optimization of the C40 fly ash concrete pavement, which was considered as a measure to accelerate the consumption of industrial solid wastes such as fly ash, committing to the goal of zero waste. By comparing with three groups of ordinary mix proportion, the performances (e.g., mechanical properties, durability, and brittle property) of the optimized mix proportion were evaluated via multiple mechanical and physical tests. Their air voids' structure was characterized by the BJH method (a method to calculate pore size described by Barrett, Joyner, and Halenda), and the results were combined with the road performances of concrete to analyze the formation mechanism of high durability of optimized fly ash pavement concrete. As for the experimental results for the optimized, its 28 d compressive strength peaked at 50.8 MPa together with corresponding 28 d flexural strength at 8.2 MPa, which indicated a favorable mechanical performance for wide application in pavement construction. Except for the mechanical properties, the better durability indicators obtained after optimization also provided a more compact pore structure for the optimized. The raw materials and construction technology of the two kinds of pavements were compared. Promoting the use of optimized fly ash pavement concrete can break the situation of the asphalt pavement monopolizing heavy-haul highway and greatly reduce the industrial wastes which can be used as raw materials in the production of cement, such as blast furnace slag and fly ash. It was proved that the optimized fly ash concrete pavement can be used to replace the asphalt pavement under the premise of achieving the same working performances.

1. Introduction

Fly ash is the main solid waste discharged from coal-fired power plants. With the development of electric power industry, the emission of fly ash from coal-fired power plants is increasing year by year, which has become one of the industrial waste residues with large emission at present in China. The common method of use is to replace cement as concrete admixture. The concrete pavement is one of the main pavement types in China. Because of the rapid rise of asphalt price and the relative stability of cement price in recent years, using the concrete pavement can save a lot of investment compared with the asphalt pavement. It can also alleviate the oversupply of cement and stimulate local economy [1]. Therefore, promoting the concrete pavement has become the trend of traffic development. However, the concrete pavement was prone to early failure such as cracking and freezing erosion since insufficient attention is paid to the durability [2]. Especially, at present, with the rapid increasing number of vehicles in China, the damage of heavy vehicles to the concrete pavement is quite serious, which causes the real service life of some concrete pavement to fall less than the half of the designed cycle. Maintenance and reconstruction of the damaged concrete pavement cost a large amount of money and materials and meanwhile, generates many construction wastes. As a result, the proportion of the concrete pavement in high-grade highway was less than 10% in China. Several provinces have even banned

the use of concrete pavements in highways. Therefore, how to improve the durability of pavement concrete has become the focus of concrete research [3]. Fly ash referred to the tiny ash particles discharged during coal combustion and will cause serious air and water pollution without treatment. Some of the chemical ingredients will also pose negative impacts on the health of residents and other surrounding lives [4–6].

As an actively pozzolanic material, fly ash was considered for use in cementitious materials to replace part of cement, reducing the consumption of cement clinker and environmental impact. The amount of fly ash in concrete usually varies between 15% and 30% by content of the cementitious binders [7]. Higher replacement levels have also been used for large volume structures to decline the temperature rise in concrete. Studies show that although fly ash will adversely affect the early-age strength development of concrete [8, 9], it can improve the strength and durability of concrete at later ages by consuming $Ca(OH)_2$ to generate secondary hydrates as C-S-H [9]. In addition, fly ash concrete also had a good performance in various types of structural systems. Although previous studies have proved that fly ash can improve the performance efficiently, most of them focused on fly ash concrete in buildings [10–13]. Research studies on the durability of fly ash pavement concrete were still limited. In 2013, Ondova et al. studied the potential use of fly ash as cement replacement in the concrete pavement by measuring mechanical properties, chemical resistance, freezing, and thawing of fly ash concrete, but failed to analyze the relationship between its microstructure and durability [14]. Later, most studies also just try to find the best mix ratio and design of fly ash concrete through experimental tests, but fail to interpret the relationship between durability and their pore structure combined with the road performance of the concrete pavement [15–18]. In addition, there were also many scholars at home and abroad contributing to exploring semiempirical formula for the relationship between strength and total porosity of cement-based materials. The deficiency was considering porosity as the only factor affecting the strength of concrete, without taking other pore structure parameters into account. Taking C40 pavement concrete as the research object, this paper comprehensively analyzed the effects of water-binder ratio and additives on the mechanical properties and durability of pavement concrete through orthogonal experimental data. The nitrogen adsorption method was introduced to characterize the pore structure of fly ash pavement concrete. Combined with the pore structure parameters, the mechanism of the pore structure on the strength, brittle property, and durability of fly ash pavement concrete was analyzed, respectively. The research provided scientific basis for the design method of fly ash pavement concrete mix proportion, which improved the service life of cement pavement concrete.

To address these research limits, this paper tried to improve the durability of concrete through the mix design. Under the premise of meeting the design and construction requirements, the water-binder ratio of concrete was reduced to reduce the porosity. Fly ash was used to replace part of cement to reduce the cement content of single concrete.

Proper amount of water reducer and air-entraining admixtures were applied to improve the impermeability and frost resistance of concrete, which improved the durability of concrete with ordinary strength. The objectives of this article were to overcome the difficulties in the wide application of ordinary concrete by optimizing the proportion of ordinary concrete, such as high brittle property and low durability. In addition, combined with the testing data and road performances, the relationship between pore structure and pavement durability was explained, and then, the mechanism analysis for improving pavement concrete after optimization was derived [19–21], aiming a solution towards zero waste and more ecological and friendly pavement design.

2. Materials and Methods

2.1. Materials. Ordinary Portland cement (P.O42.5R, 50.2 MPa of 28 d compressive strength) was employed to prepare the C40 pavement concrete. Silica fume (SF) and fly ash (FA, Grade II, the main parameters are shown in Table 1) were selected as replacing parts of cement. Water reducer (polycarboxylic acid was the main ingredient, as shown in Table 2) was used to improve the product strength by reducing the water-binder ratio. River sand (the fineness modulus was 2.5) and gravel (particle size ranges from 5 to 31.5 mm) were also used in this research. In addition, with the purpose to get favorable mechanical properties, other additives including air-entraining admixtures and reinforcing agent were applied.

2.2. Orthogonal Design of C40 Pavement Concrete. As specified in China, C40 cement concrete was widely used in concrete pavement construction. In this research, the designed strength grade of concrete was the C40 ordinary fly ash concrete pavement, which has D (serious) for environmental effect grade and 170 mm of the designed slump. In this section, the orthogonal design was carried out with the goal of getting the optimal mix proportion after the determination of the initial mix proportion, as shown in Table 3 (8% silica fume content and 1% compacting agent content). Then, the optimal mix proportion of C40 concrete was determined by analyzing the compressive strength, gas content, compressive strength, and flexural strength when the water-binder ratio (A), water-reducer content (B), fly ash content (C), and amount of air-entraining admixtures (D) were regarded as variables. The orthogonal experiment was designed according to the orthogonal table with four factors and three levels. The specific design and results of orthogonal experiments are shown in Tables 4 and 5, respectively.

2.3. Methods

2.3.1. Preparation of Pavement Concrete. According to GB/T50081-2002, the one-time molding method and vibrating table were selected to mold the 150 mm × 150 mm × 150 mm cube and 150 mm × 150 mm × 550 concrete prismoid for compressive strength and flexural strength testing, respectively. Then, the specimens were put in the standard curing

TABLE 1: The main technical index of fly ash (%).

Alkali content	SO$_3$	f-CaO	CaO	Activity index	Loss of burning	Water demand ratio	Fineness
0.45	0.2	0.03	4.43	84	1.01	94	7.6

TABLE 2: The main technical index of water reducer (%).

Water reduction rate	Solid content	Density	Pressure bleeding rate	Gas content	28 d shrinkage ratio
25.5	18.78	1.056	47	2.2	84

TABLE 3: The initial mix proportion of C40 pavement concrete (kg/m^3).

C	Fy	SF	W	Sand	Stone (5–10 mm)	Stone (10–25 mm)	Stone (25–31.5 mm)	Polycarboxylic acid	Air-entraining admixtures	Compacting agent
345.6	96.0	38.4	168	663	322.8	538	215.2	4.80	0.192	4.8

TABLE 4: The L$_9$ (3^4) orthogonal factor level table.

Factor	Number			
	A (%)	B (%)	C (%)	D (%)
1	0.33	0.6	15	0.08
2	0.35	0.8	20	0.06
3	0.37	1.0	25	0.04

TABLE 5: Orthogonal design for the optimal mix proportion (kg/m^3).

No.	C	FA	SF	W	Sand	Stone (5–10 mm)	Stone (10–25 mm)	Stone (25–31.5 mm)	Water reducer	Air-entraining admixtures	Reinforcing agent
1	301.5	112.5	36.0	167	663	322.8	538	215.2	4.50	0.360	4.5
2	324.0	90.0	36.0	167	663	322.8	538	215.2	3.60	0.270	4.5
3	346.5	67.5	36.0	167	663	322.8	538	215.2	2.70	0.180	4.5
4	345.6	96.0	38.4	168	663	322.8	538	215.2	4.80	0.192	4.8
5	369.6	72.0	38.4	168	663	322.8	538	215.2	3.84	0.384	4.8
6	321.6	120.0	38.4	168	663	322.8	538	215.2	2.88	0.288	4.8
7	385.0	75.0	40.0	165	663	322.8	538	215.2	5.00	0.030	5.0
8	335.0	125.0	40.0	165	663	322.8	538	215.2	4.00	0.020	5.0
9	360.0	100.0	40.0	165	663	322.8	538	215.2	3.00	0.040	5.0

room with humidity greater than 95% and temperature $20 \pm 2°$C to carry out the relevant test at the specified age.

2.3.2. Tests of Concrete Mixture. Referring to the methods specified in GB/T50080-2002 and GB8076-1997, properties of concrete mixtures (including slump and gas content) were tested. A slump cone (Figure 1) was used to measure the slump of concrete mixtures. The GQC-I modified method (Figure 2) was used to test the gas content of fresh concrete to reflect the frost resistance and number of pores in concrete.

2.3.3. Durability Test of Concrete

(1) Permeability. As shown in GB/T 50081-2002, the molding was carried out by the concrete mix proportion designed. After stirring for 3 minutes and vibrating the shaking table,

FIGURE 1: The slump test.

FIGURE 2: The gas content test.

FIGURE 3: The electric flux test.

six cylinder concrete specimens with 175 mm diameter of the top surface, 185 mm diameter of the bottom surface, and 150 mm height were formed as a group to be cured until the age. The water pressure started at 0.1 MPa and raised by 0.1 MPa at 8 h intervals. It was not until three of the six specimens were found to have seeped water on the surface that the test can be stopped to write down the water pressure at that time. The impervious grade of concrete was expressed as the maximum water pressure when four of the six specimens in each group have not been permeable. The formula is shown as follows:

$$P = 10H - 1, \qquad (1)$$

where P is the impervious grade and H is the water pressure in the three of the six specimens.

(2) Electric Flux. Referring to the ASTM C1202-97, the prepared test blocks were drilled core parts, and the end face was smoothed to make a cylinder of $\Phi100$ mm $\times 50$ mm before the specified curing age. Vacuum-saturated water was made for the specimen before the test. During the test, a 60 V DC voltage was added in the axial direction of the specimen. The solution with concentration of 0.3 mol/L of NaOH and 3% of NaCl was placed in the test tank on both sides of the positive and negative electrodes of the specimen, respectively. The total electricity Q value of the passing specimen within 6 hours was the electric flux of the specimen, and six specimens were a group. The test device is shown in Figure 3.

(3) Chloride Diffusion Coefficient. As the RCM method used by the Germany ibac-test, the 150 mm $\times$ 150 mm $\times$ 150 mm test specimen was made. The sample was taken from the standard curing room 4 days before the test. Then, the end face of samples was smoothed and was made into $\Phi95$ mm $\times 50$ mm test specimen (as shown in Figure 4) and put into the standard curing room to the test age. A 15 min ultrasonic bath was prepared for the specimen before the test. While the experiment proceeded, a 30 V DC voltage was applied to both ends of the specimen. The positive and negative electrodes of the specimen were dipped in 0.2 of mol/L KOH

solution and 5% of NaCl solution, respectively. The test device is shown in Figure 5, and the experimental period was determined by the initial current (as shown in Table 6). After electrification, the specimen was taken out and split into half on the hydraulic press machine, and 0.1 mol/L of AgNO$_3$ solution was sprayed on the surface of the split specimen. The chloride diffusion coefficient was tested by measuring the depth of chloride penetration and calculated. The formula for calculating chloride diffusion coefficient is as follows:

$$D_{\text{RCM}} = 2.872 \times 10^{-6} \frac{Th\left(x_d - \alpha\sqrt{x_d}\right)}{t},$$
$$\alpha = 3.338 \times 10^{-3}\sqrt{Th}, \qquad (2)$$

where D_{RCM} is the chloride diffusion coefficient (m^2/s), T is the average of the initial and final temperature of the anode solution (Kessler's temperature), h is the specimen height (m), x_d is chloride diffusion depth (m), t is power-on time (s), and α is auxiliary variable.

(4) Flexural Elastic Modulus. The flexural elastic modulus of concrete was used to reflect the deformation capacity of concrete. As specified in JTG E30-2005, the test started with preloading from 1 kN to 3 kN at speeds of 0.15 to 0.25 kN/s and was held for 30 s, and "0" was noted. Then, "0.5" was noted after continuing to load to $P_{0.5}$, which meant staying for 30 s under 50% of the bending limit. Five compressions were performed, and the fifth continuous load led to the specimen failure. The formula is as follows:

$$Eb = \frac{23L^3\left(P_{0.5} - P_0\right)}{1296J|0.5 - 0|}, \qquad (3)$$

where Eb is the flexural elastic modulus (MPa), $P_{0.5}$ and P_0 represent end load and initial load (kN), 0.5 and 0 are the thousands of meter readings corresponding to $P_{0.5}$ and P_0 (mm), L is the distance between specimen supports (450 mm), J is the moment of inertia of specimen section bh^3/12 (mm^4), and F is the midspan deflection (mm).

2.3.4. Test of Pore-Size Distribution. As specified in GB/T21650.2/ISO 15901-2:2006, the Autosorb-iQ automatic specific surface area and pore-size distribution instrument

(a)

(b)

FIGURE 4: The antichlorine ion permeation test block.

FIGURE 5: The chloride diffusion coefficient test.
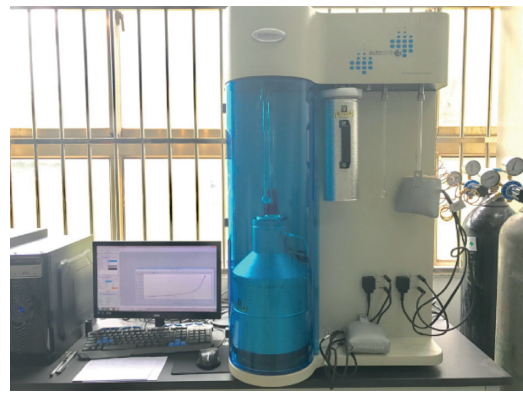
FIGURE 6: The Autosorb-iQ analyzer.

TABLE 6: The relationship between initial current and power-on time.

Initial current I_0 (mA)	Power-on time (h)
$I_0 < 5$	168
$5 \leq I_0 < 10$	96
$10 \leq I_0 < 30$	48
$30 \leq I_0 < 60$	24
$60 \leq I_0 < 120$	8
$120 \leq I_0$	4

made by Quantachrome in America was used, and the working principle was the static capacity method with isothermal physical adsorption.

The sample was vacuumed continuously for 24 h at 100°C in advance to remove volatile substances. The sample mass was about 0.5 g. The relative pressure was 0.00001~0.99800 (111 points) and completed the desorption process. The minimum detection range of the gas adsorption isotherm method used in the study was the diameter of the gas molecules used, which can detect the open pores with pore size greater than 0.5 nm. The BJH method, based on the Kelvin equation, was selected to calculate pore-size distribution. The range of its effective characterization is the mesoporousity over 2 nm. Since Autosorb-iQ had two built-in degassing stations, the analysis and preparation of samples can be conducted at the same time, as shown in Figure 6.

3. Results and Discussion

3.1. The Results of the Orthogonal Design. Table 7 indicated that the compressive and flexural strength was generally relatively stable without much fluctuation. The average strength of groups with a water-binder ratio of 0.35 was just a little higher than other groups. On the contrary, the gas content of different groups varied a lot from 4.9% to 6.9%. The range analysis of the orthogonal test was performed and is shown in Table 8 statistically. *K1* denoted average gas content for a certain variable at level 1. By comparing and evaluating the index values at *K1*, the optimal level of variables can be confirmed. The parameter ΔR, as shown in Table 8, indicated the effect of variables on gas content. A high ΔR value corresponding to a certain variable meant that this variable had a great effect on gas content.

The significance of each independent variable on the gas content was tested using ANOVA, as shown in Table 9. There were three threshold F values corresponding to the three different levels of significance. The three different threshold values defined the significance of each independent variable in one of the four different categories (most significant: if the F value is higher than 6.94; significant: if the F value is between 4.32 and 6.93; less significant: if the F value is between 4.32 and 6.93; least significant: if the F value is lower than 2.00). It can be seen from Table 9 that air-entraining admixtures had the highest impact on the gas

TABLE 7: The results of orthogonal experiments.

No.	Orthogonal combination	Assessment indicators			Power coefficient			Total power coefficient $d = \sqrt[3]{d_1 d_2 d_3}$
		Gas content (%)	3 d CS (MPa)	3 d FS (MPa)	d_1	d_2	d_3	
1	A1B1C1D1	6.9	28.9	1.92	0.710	0.963	0.861	0.847
2	A1B2C2D2	6.7	28.4	1.94	0.731	0.947	0.870	0.844
3	A1B3C3D3	5.4	28.7	1.97	0.907	0.957	0.883	0.915
4	A2B1C2D3	5.0	29.6	2.23	0.980	0.987	1.000	0.989
5	A2B2C3D1	6.3	29.8	2.13	0.778	0.993	0.955	0.904
6	A2B3C1D2	6.4	29.3	1.97	0.776	0.977	0.883	0.871
7	A3B1C3D2	6.0	29.1	1.98	0.870	0.970	0.889	0.890
8	A3B2C1D3	4.9	29.1	2.09	1.000	0.970	0.937	0.968
9	A3B3C2D1	6.1	30.0	1.95	0.803	1.000	0.874	0.889

*CS: compressive strength; FS: flexural strength; d_1: efficiency coefficient of gas content; d_2: 3 d efficiency coefficient of compressive strength; d_3: 3 d efficiency coefficient of flexural strength.

TABLE 8: The results of the extremum difference.

No.	Water-binder ratio	Water reducer (%)	Fly ash (%)	Air-entraining admixtures (%)
K1	6.33	5.97	6.07	6.43
K2	5.9	5.97	5.93	6.37
K3	5.67	5.97	5.9	5.1
ΔR	0.67	0	0.17	1.33
Optimal	A2	B1	C2	D3

TABLE 9: ANOVA for gas content.

Independent variable	Sum of squares	Degrees of freedom	F value	P value	F value at defined level of significance	Evaluation of significance
Water-binder ratio	0.67	2	3.58	0.13	6.94	Less significant
Water reducer (%)	$1.776*10^{-15}$	2	$9.537*10^{-15}$	1.00	4.32	Least significant
Fly ash (%)	0.042	2	0.22	0.67	2.00	Least significant
Air-entraining admixtures (%)	2.67	2	14.32	0.02		Most significant
Residual	0.74	2				
Total	4.12	8				

content of pavement concrete, followed by water-binder ratio, fly ash percentage, and water-reducer content. To make a sum, the optimum mix proportion of C40 fly ash pavement concrete is shown in Table 10 [22, 23].

3.2. Performance of the Optimized Cement Pavement Concrete. In order to further explore the working performance of the optimized C40 fly ash pavement concrete, the contrast experiments were carried out. The experimental design is shown in Table 11. The contrast experiments designed that the optimal mix proportion obtained by orthogonal experiments was compared to three groups of ordinary mix ratio under the conditions of equal strength and slump of design requirements. In this experiment, the 3 d, 7 d, and 28 d compressive and flexural strength and other durability indicators were tested. Besides, the internal pore-size distribution of the optimal mix proportion concrete and ordinary one was characterized and summarized, so as to further account for the relationship between pore structure and mechanical properties and durability of the concrete.

3.2.1. Mechanical Properties. The flexural strength is a direct indicator to characterize the ability to resist bending of road. For pavement concrete, the national standard requires a flexural strength no less than 5 MPa (specified in JTG D40-2011). However, even after meeting this minimum requirement, the application of the concrete pavement was still practically limited to certain locations. Moreover, although the durability of ordinary pavement concrete can conform to design requirements, its whole working performance could be still inefficient due to its irregular pore-size distribution. The mechanical properties are shown in Figure 7, and durability indicators' testing results can be seen in Table 12. In contrast, the compressive and flexural strength of the optimal group were a little higher than that of other three groups. The impermeability grade of another three ordinary groups varied from P8 to P10, but the optimized C40 concrete reached at P10. Besides, it also possessed a lower chloride diffusion coefficient of $6.9*10^{-12}$ m^2/s and a better electric flux of 1828 C. These results could be attributed to the favorable pore structure of the optimized concrete. The following experimental results can prove it.

TABLE 10: The optimal mix ratio of C40 pavement concrete (kg/m^3).

C	Fly	SF	W	Sand	Stone (5–10 mm)	Stone (10–25 mm)	Stone (25–31.5 mm)	Polycarboxylic acid	Air-entraining admixtures	Reinforcing agent
345.6	96.0	38.4	168	663	322.8	538	215.2	4.80	0.192	4.8

TABLE 11: The contrast mix proportion of C40 pavement concrete.

Group	Water-binder ratio	Fly ash (%)	Water reducer (%)	Air-entraining admixtures (%)
1	0.37	15	0.5	0.06
2	0.38	25	0.4	0.08
3	0.41	20	0.7	0.09
Optimal	0.35	20	1.0	0.04

(a)

(b)
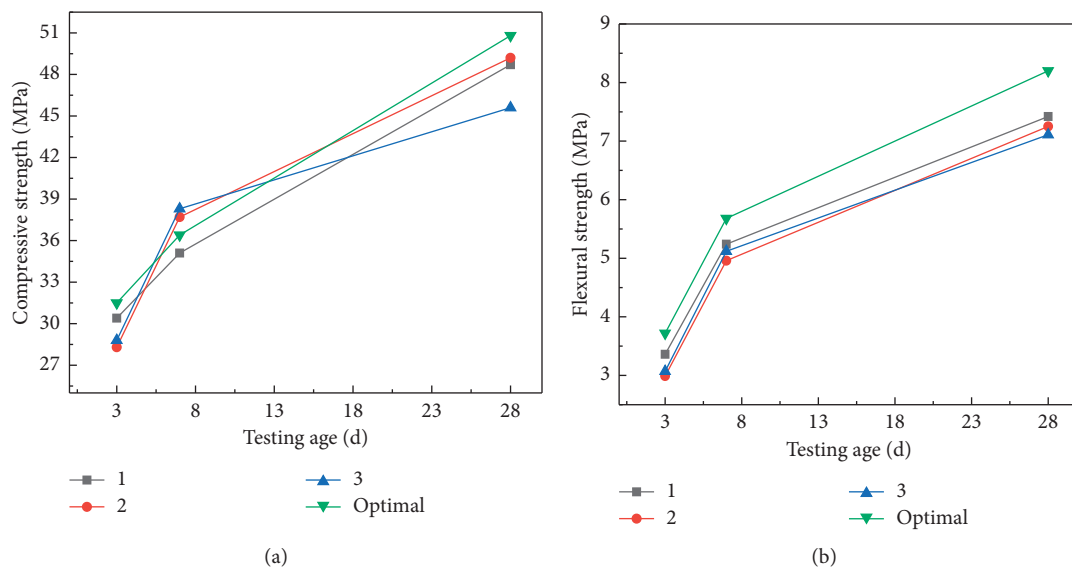
FIGURE 7: Mechanical properties of the contrast groups.

TABLE 12: The durability of contrast groups.

Group	Impermeability grade	D_{RCM} ($*10^{-12}$ m^2/s)	Electric flux (c)
		Durability	
1	P10	8.0	2218
2	P8	8.4	2399
3	P10	8.9	2436
Optimal	P12	6.9	1828

FIGURE 8: The section of optimal proportion.

In the section of the concretes, as shown in Figures 8 and 9, the bubbles forming in the concrete with ordinary mix proportion were larger and relatively concentrated, which directly led to the reduction of the compactness of the concrete. By analyzing the data in Table 11 and Figure 7, we can find that the content of air-entraining admixtures in the ordinary mix proportion was higher than that of the optimal group, resulting in higher gas content. Due to the introduction of too many bubbles, some internal bubbles connected with each other, contributing to the loss of mechanical properties. Combined with the results of the extremum difference from the orthogonal experiments above, when reducing the content of air-entraining admixtures, the ordinary pavement concrete can get optimized by reasonably controlling the content of other additives to possess a homogeneous pore structure of concrete.

FIGURE 9: The section of ordinary proportion.

3.2.2. Durability. Concrete was a typical porous material with complex pore-size distribution. The span of pore size crossed between microscale and macroscale, which had great influence on the mechanical properties and durability of concrete. The permeability and carbonation resistance of concrete seriously affected the durability of the structure. The pores and capillary channels connected inside the concrete were the main reasons for the decrease of impermeability, and the pore-size distribution also had a great influence on the antipermeability. Mehta [24] divided the pores into four grades according to pore size (d): $d < 20$ nm as harmless pores; $d = 20$–50 nm as less harmful pores; $d = 50$–100 nm as harmful pores; $d > 100$ nm as multihazard pores. Obviously, the cementitious pores belonged to the category of harmless pores and have no effect on the durability, impermeability, and strength of concrete. The pore size changed greatly because of the difference of the water-cement ratio and hydration degree, which can be divided into less harmful pores, harmful pores, and multihazard pores, which will seriously harm the permeability and durability of concrete. As for the effect of pores in concrete on durability, the literature introduced a comprehensive damage model under external (environmental) and internal factors, which described the process that pores developed and eventually led to the cracking and collapse of concrete [25–29].

The test results of pore structure are shown in Figures 10 and 11. Based on the pore-size distribution, nearly 80% of the pores in the optimized pavement concrete were smaller than 20 nm, which provided a more compact pore structure for it. In contrast, the pores with radius more than 20 nm in the ordinary group were over twice as much as that in the optimized group. This result caused the increase of pore connectivity and permeability of the ordinary pavement concrete due to climate and load effects, which led to the ability of pore structure to resist the penetration of external forces decreasing, thus making the overall working performance decline [30–35].

3.2.3. Analysis on Brittle Property of the Optimized Pavement Concrete. Compared with other concretes, the failure of pavement concrete was caused by flexible-tensile stress, and the flexural strength of concrete was much lower than compressive strength. When the tensile stress of concrete cannot withstand the vertical stress of load, horizontal impact, and the tensile stress caused by chemical shrinkage and temperature deformation, the concrete appeared to have cracks. Therefore, low brittle property was greatly beneficial to pavement concrete.

Due to the limitation of raw materials, construction technology, and so on, there are a large number of microcracks and inhomogeneous pores in the concrete. The internal structure showed extreme complexity, and it was relatively difficult to improve the brittle property of pavement concrete. Scholars at home and abroad had carried out a lot of research studies on the brittleness of concrete. In essence, effective methods can be found to improve the brittle property of concrete, such as improving its pore structure, reducing internal microcracks, and controlling the cracking and expansion of microcracks during failure. Macroscopically, the brittle property of concrete can be improved by raw materials, mix ratio, construction technology, and so on.

At present, there was no uniform standard for measuring the brittle property of concrete. The compression-flexure ratio and flexural elastic modulus of pavement concrete were regarded as the commonly used indexes in engineering circles. The brittleness coefficient of concrete represented by the compression-flexure ratio reflected the antideformation performance of concrete. The smaller the brittleness coefficient was, the better the antideformation ability was. The above two indexes were tested and calculated in this research, and the results are shown in Figure 12 [36, 37].

It can be seen from the testing results that the compression-flexure ratio decreased with the increase of trial age, and the rate of increase of flexural strength was higher than that of compressive strength. The concrete with the optimum ratio possessed a smaller compression-flexure ratio, which contributed to its higher strength and flexibility than ordinary concrete. On the contrary, the optimum proportion of pavement concrete had higher flexural modulus than ordinary concrete, which achieved lower brittle property and improved the durability of pavement concrete to a degree.

3.2.4. Formation Mechanism of High Durability of Optimized Pavement Concrete. The durability of concrete was a kind of ability that makes it resist climate change, chemical erosion, abrasion, or any other destruction process. For pavement concrete, because of the uncovered exposure to the atmosphere and long-term erosion by the external environment, the pavement structure would suffer damage. Excellent durability not only was an important guarantee for design service life of the concrete pavement but also can reduce the difficult maintenance of the cement concrete pavement and avoid investing a large amount of reconstruction or overlay cost, which was also of great significance to realize the sustainable development of national economy. The formation mechanism of the optimized pavement concrete of high durability was analyzed from the following three aspects:

(a)

(b)
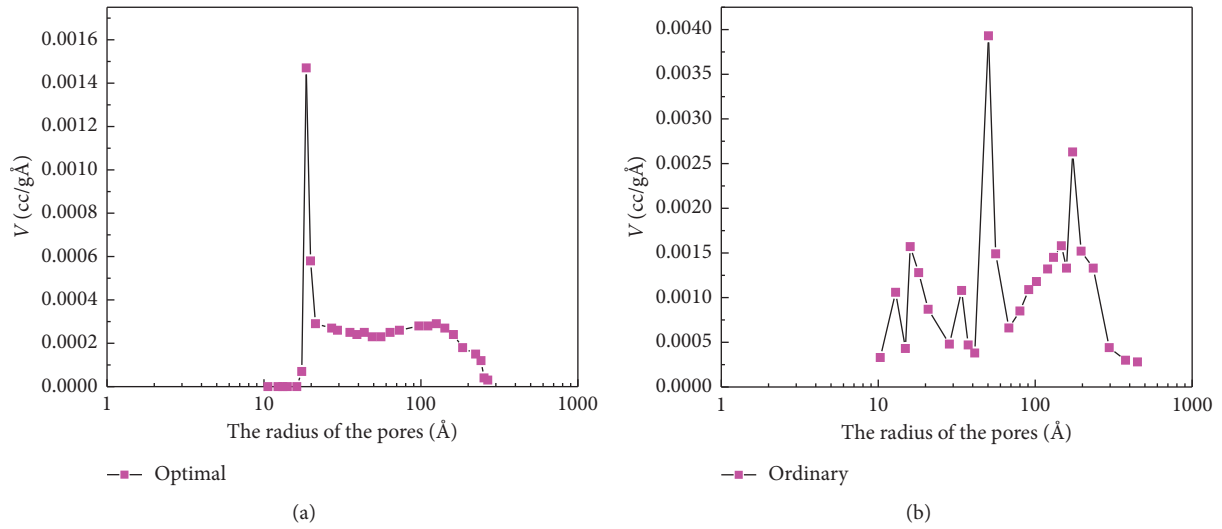
Figure 10: Desorption pore-volume distribution by the BJH method.
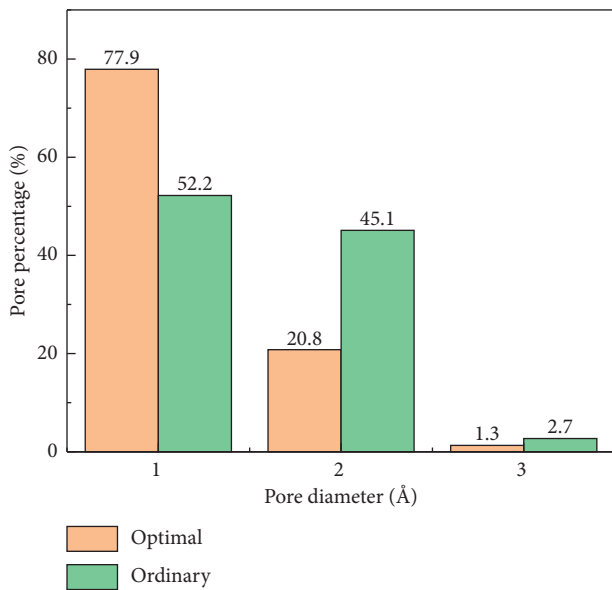
Figure 11: The results of pore-size distribution.

Figure 12: The brittle property of optimized pavement concrete.

(1) The Optimization of Pore Structure Features. Concrete is composed of cement stone, aggregate, and interface, all of which had pores that were the channel of ion permeation. The pore characteristics of concrete determine that the erosion ions generally permeated from the interface into the cement stone. The products of the concrete additive involved in the hydration reaction, and its unreacted fine particles can fill the capillary pores of the cement stone, which makes concrete more compact. With the development of hydration age, the harmful macropores in the optimized concrete decreased and the harmless or less harmful pores or micropores increased, which meant that pore structure and frost resistance of the optimized pavement concrete were improved.

(2) The Enhancement of Interface Transition Zone. With the addition of water reducer, the optimized concrete can obtain lower water-to-glue ratio, which enhanced the strength and elastic modulus of cement stone. Given this, the gap between cement stone and elastic modulus of aggregate was cut down, which made the thickness of the water film layer at the interface decrease, and the free space for crystal growth reduced. Additionally, silica fume and other mineral additives reacted in the interface area, leading to more C-S-H and AFt and less CH in the interface. The crystallization of the hydrates was also interfered, which resulted in the size of the crystalline particles of the hydrates getting smaller and the degree of enrichment and orientation going down. Finally, the interfacial transition zone achieved improvement, thus cutting off the channel of erosive permeation along the interface [38].

(3) The Hard Corrosion of Steel Bar. The corrosion condition of reinforcement in concrete was that the pH value of pore solution was less than 11.5 or the Cl^-/OH^- ratio was greater than 0.63. (1) The fly ash had little effect on the liquid alkalinity of concrete and mainly absorbed the K^+ and Na^+ in the pore solution. Its OH^- concentration suffered very little effect, so its pH value remained over 12.0; (2) the chloride diffusion coefficient of the optimized concrete was small ($D_{RCM} = 6.9 \times 10^{-12}\ m^2/s$), and most of the Cl^- were united during diffusion. Therefore, the free Cl^- at the steel bar interface was very few, which was not enough to destroy the passivation film [39–41].

4. Conclusions

In this paper, the optimized mix proportion was obtained from the orthogonal tests, which was compared to the ordinary concrete by evaluating the mechanical properties, durability, brittle property, and pore structure. Then, based on the results of contrast tests, the relationship between the concrete durability and pore structure was discussed, and the formation mechanism of high durability of optimized pavement concrete was further explained. The main conclusions about optimized C40 concrete performance were drawn as follows:

(i) The optimized product based on the optimal mix ratio obtained from the orthogonal experiments possesses 50.8 MPa of 28 d compressive strength and 8.2 MPa of 28 d flexural strength.

(ii) The durability indexes are summarized as the following: P12 of impermeability grade, 1828 c of 28 d electrical flux, and $6.9 \times 10^{-12}\ m^2/s$ of chloride diffusion coefficient. Results indicated a favorable performance for wide application in pavement engineering.

(iii) The flexural elastic modulus reached 3.6×10^4 MPa, which achieved the goal of low brittleness through the analysis of the compression-flexure ratio.

(iv) The internal pore-size, respectively, showed that the number of less harmful pores ($d = 20$–50 nm) in the ordinary proportion was 24.2% more than that in the optimal group, and the number of harmless pores ($d < 20$ nm) was 25.7% less than that in the optimal group, which proved that the pore structure of the optimized pavement concrete became more compact.

Data Availability

The data used to support the findings of this study are included within the article.

Conflicts of Interest

The author declares that there are no conflicts of interest regarding the publication of this paper.

Authors' Contributions

H. Zhai, B. Cheng, S. Chen, and H. Chen conceptualized the study and developed research design; Y. Tang, B. Cheng,

S. Chen, and H. Chen developed experiment design; Y. Tang, H. Zhai, S. Chen, B. Cheng, and X. Cai carried out experiment test; S. Chen, Y. Tang, and X. Cai analyzed the data; Y. Tang, B. Cheng, H. Zhai, and S. Chen wrote the original article; H. Zhai, Y. Tang, and Y. Wei revised and edited the article; Y. Wei carried out proofing; H. Zhai and H. Chen helped in funding.

Acknowledgments

References

[1] S. Pranav, S. Aggarawal, E. H. Yang et al., "Alternative materials for wearing course of concrete pavements: a critical review," *Construction and Building Materials*, vol. 236, Article ID 117609, 2020.

[2] E. Holt and M. Leivo, "Cracking risks associated with early age shrinkage," *Cement and Concrete Composites*, vol. 26, no. 5, pp. 521–530, 2004.

[3] M. V. Mohod and K. N. Kadam, "A comparative study on rigid and flexible pavement: a review," *IOSR Journal of Mechanical and Civil Engineering*, vol. 13, pp. 84–88, 2016.

[4] C. Belviso, F. Cavalcante, S. Palma, P. Ragone, and S. Fiore, "Mobility of trace elements in fly ash and in zeolitised coal fly ash," *Fuel*, vol. 144, pp. 369–379, 2015.

[5] W. Müllauer, R. E. Beddoe, D. Heinz et al., "Leaching behaviour of major and trace elements from concrete: effect of fly ash and GGBS," *Cement and Concrete Composites*, vol. 58, pp. 129–139, 2015.

[6] H. Wang, Y. Wu, M. Wei, L. Wang, and B. Cheng, "Hysteretic behavior of geopolymer concrete with active confinement subjected to monotonic and cyclic axial compression: an experimental study," *Materials*, vol. 13, no. 18, p. 3997, 2020.

[7] M. Thomas, "Optimizing the use of fly ash in concrete," *Skokie, IL: Portland Cement Association*, vol. 5420, 2007.

[8] A. B. Harwalkar and S. S. Awanti, "Laboratory and field investigations on high-volume fly ash concrete for rigid pavement," *Transportation Research Record: Journal of the Transportation Research Board*, vol. 2441, no. 1, pp. 121–127, 2014.

[9] Y. Kocak and S. Nas, "The effect of using fly ash on the strength and hydration characteristics of blended cements," *Construction and Building Materials*, vol. 73, pp. 25–32, 2014.

[10] S. Altoubat, M. Talha Junaid, M. Leblouba, and D. Badran, "Effectiveness of fly ash on the restrained shrinkage cracking resistance of self-compacting concrete," *Cement and Concrete Composites*, vol. 79, pp. 9–20, 2017.

[11] N. Chousidis, I. Ioannou, E. Rakanta, C. Koutsodontis, and G. Batis, "Effect of fly ash chemical composition on the reinforcement corrosion, thermal diffusion and strength of blended cement concretes," *Construction and Building Materials*, vol. 126, pp. 86–97, 2016.

[12] N. Chousidis, E. Rakanta, I. Ioannou, and G. Batis, "Mechanical properties and durability performance of reinforced concrete containing fly ash," *Construction and Building Materials*, vol. 101, pp. 810–817, 2015.

[13] K. Cox and N. D. Belie, "Durability behavior of high-volume fly ash concrete," in *Proceedings of the 2007 Internationl Conference Sustainable Construction Materials and Technologies*, Coventry, UK, 2007.

[14] M. Ondova, N. Stevulova, L. Meciarova et al., "The potential of higher share of fly ash as cement replacement in the concrete pavement," *Procedia Engineering*, vol. 65, pp. 45–50, 2013.

[15] S.-W. Yoo, G.-S. Ryu, J. F. Choo et al., "Evaluation of the effects of high-volume fly ash on the flexural behavior of reinforced concrete beams," *Construction and Building Materials*, vol. 93, pp. 1132–1144, 2015.

[16] S. A. Kristiawan and M. T. M. Aditya, "Effect of high volume fly ash on shrinkage of self-compacting concrete," *Procedia Engineering*, vol. 125, pp. 705–712, 2015.

[17] X. Wang, Y. B. Wang, L. S. Yang et al., "High-performance, high-volume fly ash concrete," *Bulletin of the Chinese Ceramic Society*, vol. 32, pp. 523–522, 2013.

[18] Z. H. Wang, L. Li, Y. X. Zhang et al., "Bond-slip model considering freeze-thaw damage effect of concrete and its application," *Engineering Structures*, vol. 201, Article ID 109831, 2019.

[19] H. Zhao, X. Qin, J. Liu, L. Zhou, Q. Tian, and P. Wang, "Pore structure characterization of early-age cement pastes blended with high-volume fly ash," *Construction and Building Materials*, vol. 189, pp. 934–946, 2018.

[20] C. Lian, Y. Zhuge, and S. Beecham, "The relationship between porosity and strength for porous concrete," *Construction and Building Materials*, vol. 25, no. 11, pp. 4294–4298, 2011.

[21] X. Chen, S. Wu, and J. Zhou, "Influence of porosity on compressive and tensile strength of cement mortar," *Construction and Building Materials*, vol. 40, pp. 869–874, 2013.

[22] Y. Xu, R. Jin, L. Hu et al., "Studying the mix design and investigating the photocatalytic performance of pervious concrete containing TiO_2-soaked recycled aggregates," *Journal of Cleaner Production*, vol. 248, Article ID 119281, 2020.

[23] H. Chen, H. li, Y. Wang, and B. Cheng, "A comprehensive assessment approach for water-soil environmental risk during railway construction in ecological fragile region based on AHP and MEA," *Sustainability*, vol. 12, no. 19, p. 7910, 2020.

[24] P. K. Mehta, "Durability of concrete—fifty years of progress," in *Proceedings of the 2nd International Conference on Durability of Concrete*, Montreal, Canada, 1991.

[25] H. Y. Moon, H. S. Kim, and D. S. Choi, "Relationship between average pore diameter and chloride diffusivity in various concretes," *Construction and Building Materials*, vol. 20, no. 9, pp. 725–732, 2006.

[26] J. J. Beaudoin and V. S. Ramachandran, "A new perspective on the hydration characteristics of cement phases," *Cement and Concrete Research*, vol. 22, no. 4, pp. 689–694, 1992.

[27] Z.-H. Wang, L. Li, Y.-X. Zhang, and S.-S. Zheng, "Reinforcement model considering slip effect," *Engineering Structures*, vol. 198, Article ID 109493, 2019.

[28] Y. Guo, Z. Chen, X. Qin, A. Shen, S. Zhou, and Z. Lyu, "Evolution mechanism of microscopic pores in pavement concrete under multi-field coupling," *Construction and Building Materials*, vol. 173, pp. 381–393, 2018.

[29] M. A. Vicente, D. C. González, J. Tarifa, G. Ruiz, and R. Hindi, "Influence of the pore morphology of high strength concrete on its fatigue life," *International Journal of Fatigue*, vol. 112, pp. 106–116, 2018.

[30] B. Q. Cheng, H. L. Wang, L. Wang et al., "The study on the whole stress-strain curves of coral fly ash-slag alkali-activated concrete under uniaxial compression," *Materials*, vol. 13, p. 4291, 2020.

[31] D. N. Winslow, M. D. Cohen, D. P. Bentz, K. A. Snyder, and E. J. Garboczi, "Percolation and pore structure in mortars and concrete," *Cement and Concrete Research*, vol. 24, no. 1, pp. 25–37, 1994.

[32] B. B. Das and B. Kondraivendhan, "Implication of pore size distribution parameters on compressive strength, permeability and hydraulic diffusivity of concrete," *Construction and Building Materials*, vol. 28, no. 1, pp. 382–386, 2012.

[33] Y. Yang, T. Zhao, H. Jiao, Y. Wang, and H. Li, "Potential effect of porosity evolution of cemented paste backfill on selective solidification of heavy metal ions," *International Journal of Environmental Research and Public Health*, vol. 17, no. 3, p. 814, 2020.

[34] B. Cheng, J. Li, V. W. Y. Tam, M. Yang, and D. Chen, "A BIM-LCA approach for estimating the greenhouse gas emissions of large-scale public buildings: a case study," *Sustainability*, vol. 12, no. 2, p. 685, 2020.

[35] H. Z. Jiao, S. F. Wang, A. X. Wu et al., "Cementitious property of $NaAlO_2$-activated Ge slag as cement supplement," *International Journal of Minerals, Metallurgy and Materials*, vol. 26, no. 182, pp. 112–121, 2019.

[36] S. B. Zhou, A. Q. Shen, X. Li et al., "A relationship of mesoscopic pore structure and concrete bending strength," *Materials Research Innovations*, vol. 19, 2016.

[37] A. Shen, S. Lin, Y. Guo, T. He, and Z. Lyu, "Relationship between flexural strength and pore structure of pavement concrete under fatigue loads and freeze-thaw interaction in seasonal frozen regions," *Construction and Building Materials*, vol. 174, pp. 684–692, 2018.

[38] S. Yang, X. Zhongzi, X. Ping, and T. Mingshu, "A new method of enhancing cement-aggregate interfaces II. Mechanical properties and sulphate attack resistances of mortars," *Cement and Concrete Research*, vol. 22, no. 5, pp. 769–773, 1992.

[39] M. Ormellese, M. Berra, F. Bolzoni et al., "Corrosion inhibitors for chlorides induced corrosion in reinforced concrete structures," *Cement and Concrete Research*, vol. 36, no. 3, pp. 536–547, 2006.

[40] A. Scott and M. G. Alexander, "Effect of supplementary cementitious materials (binder type) on the pore solution chemistry and the corrosion of steel in alkaline environments," *Cement and Concrete Research*, vol. 89, pp. 45–55, 2016.

[41] H. Zheng, J.-G. Dai, C. S. Poon, and W. Li, "Influence of calcium ion in concrete pore solution on the passivation of galvanized steel bars," *Cement and Concrete Research*, vol. 108, pp. 46–58, 2018.

Research Article

Evaluation of Rheological Parameters of Slag-Based Paste Backfill with Superplasticizer

Zhonghui Zhang,[1,2] Yuanhui Li,[1] Lei Ren,[1] Zhenbang Guo [1] ,[1] Haiqiang Jiang,[1] and Na Liu[3]

[1]*Key Laboratory of Ministry of Education on Safe Mining of Deep Metal Mines, Northeastern University, Shenyang 110819, China*
[2]*Shandong Gold Group Co. Ltd., Jinan 250000, China*
[3]*Shenyang Ecological Environment Monitoring Center of Liaoning Province, Shenyang 110819, China*

Correspondence should be addressed to Zhenbang Guo; wcpp2019@163.com

The use of blast furnace slag-based binders in cemented paste backfill (CPB) has become increasingly popular in China, due to its low cost and superior early-age strength. Increasing the solid content can increase the strength of CPB, but it will lead to a decrease in its fluidity. As a chemical admixture that can improve CPB slurry fluidity, superplasticizer is gaining increased interest in the field of CPB. In this study, the effects of superplasticizer types and dosages, curing time, solid content, and binder content on the rheological properties of fresh CPB made of blast furnace slag-based binder (Slag-CPB) were studied. For Slag-CPB samples, polycarboxylate (PC) has the best water-reducing effect, followed by polymelamine sulfonate (PMS) and polynaphthalene sulfonate (PNS). In the absence of a superplasticizer, the shear yield stress and plastic viscosity of Slag-CPB are lower than those of CPB made of ordinary Portland cement (OPC-CPB). The water-reducing effect of PC on OPC-CPBs samples is stronger than that of Slag-CPB samples. The degradation rate of the water-reducing effect in slag-based samples is higher than that in cement-based samples. The effect of PC is affected by solid content and binder content. These results will contribute to a better understanding of the rheological behavior of Slag-CPB with superplasticizer.

1. Introduction

Mining activities not only obtain mineral resources, but also produce a lot of solid wastes (e.g., tailings) and underground voids [1–5]. The continuous improvement of national environmental protection requirements has prompted mining enterprises to seek scientific and efficient methods for underground voids and tailings management [6]. One of these emerging techniques is cemented paste backfill (CPB) which offers better technical and economic advantages over other filling methods like rock/slurry fills. The cemented paste backfill (CPB) is a composite material prepared by mixing a certain mass ratio of tailing, binders (e.g., cement, fly ash, or slag), and water [7–12]. It offers a range of advantages including efficient disposal of processing tailings, improved

working environment, increased resource recovery, and improved ground controls [13–18].

The CPB should reach certain mechanical stability to resist external dynamic and static loads. Increasing the slurry concentration is one of the most effective ways to improve the mechanical stability of CPB and to reduce the filling cost [19]. However, an increase in slurry concentration will inevitably lead to a decrease in its fluidity. When the slurry concentration exceeds a certain critical value, the shear yield stress and dynamic viscosity can increase exponentially with the concentration, which will easily lead to pipe clogging, which can have significant financial ramifications [20]. Therefore, it is of crucial importance to improve the fluidity of CPB slurry as much as possible without reducing the solid content of slurry. As a chemical admixture that can reduce the water consumption while maintaining the slump of

slurry basically unchanged, the superplasticizer provides a technical solution for the fluidity problem of high concentration CPB slurry [13, 14].

At present, there have been many studies on the effect of the superplasticizer on the fluidity of CPB slurry. For example, Haruna and Fall [21] studied the influence of the superplasticizer on the rheological properties of CPB at different curing temperatures. The results showed that the increase of curing temperature leads to the increase of yield stress and viscosity of fresh CPB slurry incorporating superplasticizer. Panchal et al. [22] evaluated the influence of different superplasticizer contents on the rheological properties of CPB. They indicated that the superplasticizer has an important influence on the rheological properties of CPB, and it can be appropriately used to improve the fluidity of the CPB containing carbonate-rich process tailings. To study the effects of different superplasticizer types on strength and rheological behavior of CPB, Mangane et al. [23] mixed four types of superplasticizers (lignosulfonate, naphthalene, melamine, and polycarboxylate) with CPB slurry containing various binder dosages. They found that polycarboxylate-based superplasticizer showed the best performance; it can reduce the dosage of binder and maintain the strength of CPB at the same time.

However, to our knowledge, most of the previous studies focus on CPB made of ordinary Portland cement (OPC-CPB). There are no studies addressing the effects of the superplasticizer on rheological properties of CPB made of blast furnace slag-based binder (Slag-CPB). As is known to all, the water-binding (or consuming) capacity of cement hydration is weak (a water–cement ratio of 0.2–0.25 is adequate for cement hydration), and a typical water–cement ratio for CPB is 3–8. As a result, CPB made of OPC has a slow hardening rate, leading to a low strength (especially early strength). Moreover, the cost accounts for 75% of the total backfill cost with cement as a sole binder for CPB [24]. In recent years, blast furnace slag-based binders have been rapidly promoted and applied in many mines in China due to their high strength and low price. Therefore, the research on the influence of superplasticizer on the fluidity of slag-based CPB slurry is particularly important for the preparation, transportation, and structural optimization design of slag-based filling materials.

In view of this, this study aims to evaluate the rheological properties of Slag-CPB containing superplasticizer, with a special emphasis on quantifying the effect of superplasticizer type and dosage, curing time, solid content, and binder content on rheological parameters, principally yield stress, and plastic viscosity.

2. Materials and Methods

2.1. Materials

2.1.1. Tailings.
The tailings used in the tests were unclassified tailings of a gold mine in Shandong province, China. The particle size distribution of tailings was determined by Malvern Laser Mastersizer 2000 and the results are shown in Figure 1 and Table 1. The volume proportion of $-20\,\mu m$ particles in the tailings is 42.9%, which can be classified as medium tailings [25]. The coefficient of curvature and coefficient of uniformity are 0.50 and 25.75, respectively. X-ray fluorescence (XRF) results showed that the main chemical components of tailings were SiO_2 (62.5%), Al_2O_3 (16.2%), K_2O (8.11%), Na_2O (3.07%), and CaO (2.98%), and some trace ingredients were also found. X-ray diffraction (XRD) test results showed that the tailing is mainly composed of quartz, albite, and mica (Figure 2).

2.1.2. Binders.
The binder agents used in this study were a commercial OPC (viz., PO 42.5R, used as a reference) and a slag-based binder. The slag-based binder material consists of slag (70%) and compound activator (30%). The main components of the compound activator are a sulphate, a silicate, and an alkali metal salt. The particle size distribution of the slag was determined by Malvern Laser Mastersizer 2000 (Figure 1). Fine particles ($-20\,\mu m$) content in the slag accounted for 70.1%, and the coefficients of curvature and coefficient of uniformity are 1.10 and 3.38, respectively. XRF analysis was used to determine the main chemical components of the slag, and the results showed that the slag mainly contained CaO (40.01 wt.%), SiO_2 (33.8 wt.%), Al_2O_3 (15.71 wt.%), and MgO (6.90 wt.%) and some trace chemical components (Table 1). The XRD analysis of Slag shows a diffuse diffraction pattern typical of an amorphous glassy material, as shown in Figure 3. The basicity coefficient ($K_b = (CaO + MgO)/(SiO_2 + Al_2O_3)$) of slag is 0.95 and hence can be classified to be acid slag. The slag has an activity coefficient ($HM = CaO + MgO + Al_2O_3)/SiO_2$) of 1.85.

2.1.3. Superplasticizer and Water.
Three types of superplasticizers were used in this experiment: a polynaphthalene sulfonate (PNS), a polymelamine sulfonate (PMS), and a polycarboxylate (PC), all in powder form and purchased from BASF (Figure 4). Tap water with a pH of 7.5 was used as mixing water to achieve the desired consistency of the slurry [26]. The water mainly contains Ca (45.33 ppm), Na (4.62 ppm), and Mg (2.74 ppm) [27].

2.2. Mix Proportions.
This experiment is divided into two stages. Stage I: three different types of superplasticizers were tested for water reduction effects under different dosages, and the best type of superplasticizer was selected. Stage II: based on the optimal type of superplasticizer, the effects of curing age, solid content, and binder content on water-reducing effect were studied. The solid content is the ratio of solids (tailing and binder) to total mass. The binder content is the mass ratio between binder and solids. The superplasticizer dosage is the ratio of the mass of the superplasticizer to the total mass of solids. The details of the CPB mixtures are summarized in Table 2.

2.3. Sample Preparation and Rheological Test.
The CPB samples with different superplasticizer types and dosages, curing time, solid content, and binder content were prepared using a double spiral mixer. Before mechanical mixing, the
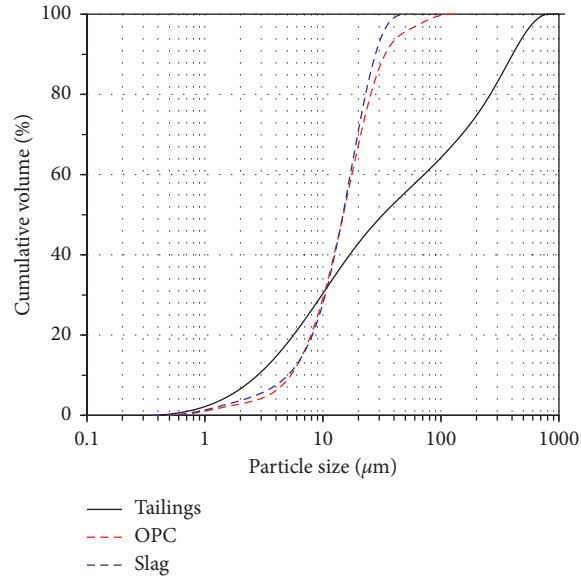
FIGURE 1: Particle size distribution curves for tailings, OPC, and slag.

TABLE 1: Main physical and chemical properties of tailings, OPC, and slag.

Chemical composition (wt.%)	Tailings	OPC	Slag	Physical properties	Tailings	OPC	Slag
CaO	2.98	62.34	40.01	Specific gravity	2.68	3.3	2.90
Fe_2O_3	1.72	5.06	0.38	Specific surface (cm^2/g)	3470	5808	6198
SiO_2	62.5	21.43	33.80	$-20\,\mu m$ content (%)	42.9	66.3	70.1
Al_2O_3	16.2	4.25	15.71	C_u	25.75	3.29	3.38
MgO	0.52	2.61	6.90	C_c	0.50	1.25	1.10
Na_2O	3.07	0.41	0.05	Pozzolanic strength index (%)			
K_2O	8.11	0.73	0.44	7 days	N/A	N/A	69.6
SO_3	0.45	1.48	0.18	28 days	N/A	N/A	90.4
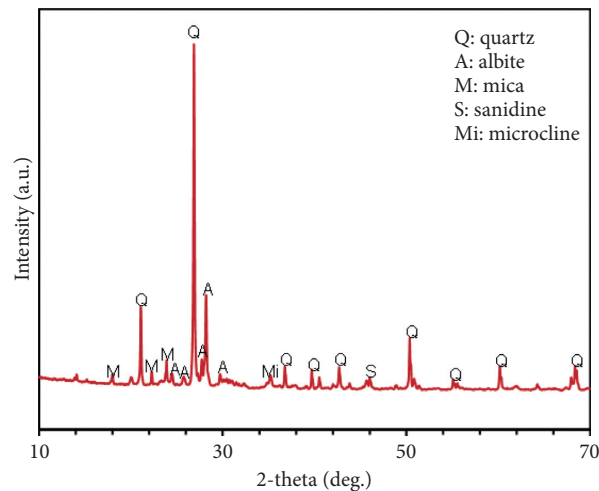
FIGURE 2: XRD pattern of tailings.

preweighed tailings, binder, and superplasticizer were homogenized by hand. Then, the required water was added to the solids, followed by 2 minutes of slow stirring and 2 minutes of fast stirring (see Figures 5 and 6).

The Brookfield RSR-SST rheometer with a four-bladed vane (diameter of 20 mm and length of 40 mm) was used for rheological tests. The rotor was first sheared in 60 s with a shear rate of $100\,s^{-1}$, and then the shear rate was reduced to $0.001\,s^{-1}$ within 60 s. In this study, the upper and lower boundary of the cross plate, the side boundary distance, and the test container boundary distance are both larger than the size requirements specified in ASTM
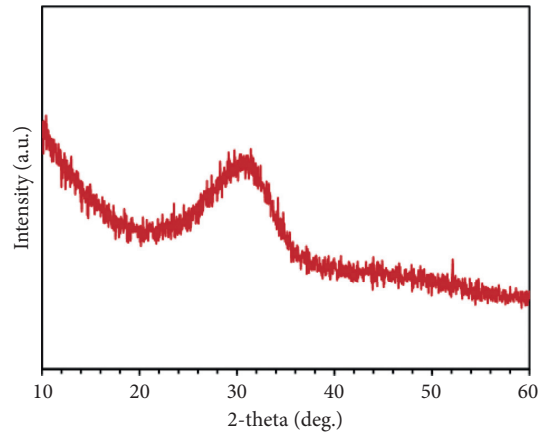
FIGURE 3: XRD pattern of slag material.
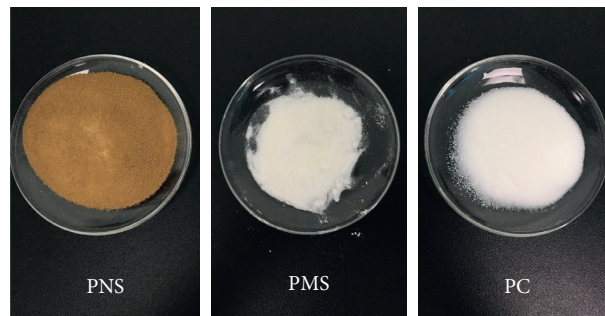
FIGURE 4: Three types of superplasticizers used in the test.

TABLE 2: Mix proportions of fresh CPB.

Stage	Factors	Superplasticizer type	Binder type	Superplasticizer content (‰)	Binder content (%)	Solid content (%)	Curing time (min)
I	Types and dosage of superplasticizer	PNS	Slag-based binder	0, 0.36, 0.73, 1.09, 1.45, 1.81	9.1	76	0
		PMS	Slag-based binder	0, 0.36, 0.73, 1.09, 1.45, 1.81	9.1	76	0
		PC	Slag-based binder	0, 0.36, 0.54, 1.09	9.1	76	0
II	Curing time	PC	Slag-based binder, OPC	0, 0.36, 0.54	9.1	76	0
		PC	Slag-based binder, OPC	0, 0.36, 0.54	9.1	76	30
		PC	Slag-based binder, OPC	0, 0.36, 0.54	9.1	76	60
		PC	Slag-based binder, OPC	0, 0.36, 0.54	9.1	76	120
	Solid content	PC	Slag-based binder	0, 0.36, 0.54	9.1	76	0
		PC	Slag-based binder	0, 0.36, 0.54	9.1	77	0
		PC	Slag-based binder	0, 0.36, 0.54	9.1	78	0
		PC	Slag-based binder	0, 0.36, 0.54	4.8	76	0
	Binder content	PC	Slag-based binder	0, 0.36, 0.54	9.1	76	0
		PC	Slag-based binder	0, 0.36, 0.54	14.3	76	0
		PC	Slag-based binder	0, 0.36, 0.54	20.0	76	0
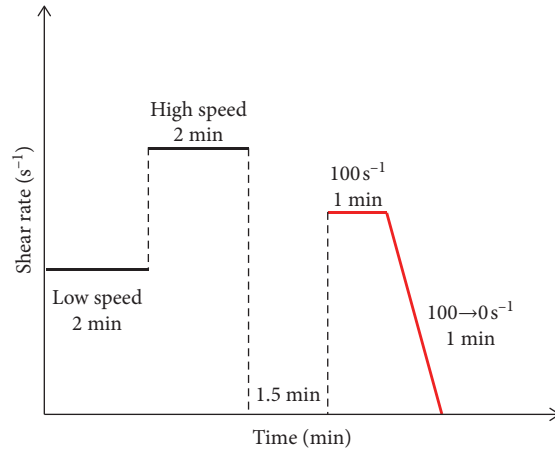
FIGURE 5: Flow chart of the mixing and rheological measurement sequence.

(a)   (b)   (c)

FIGURE 6: The preparation stages of CPB samples: (a) mixing, (b) curing, and (c) testing.

D4648/D4648M-16. Therefore, the boundary effect can be ignored. Each set of experiments were repeated at least 3 times to ensure the repeatability and accuracy of the results.

The Bingham model was used to fit the shear stress-shear rate data of the descending section ($100\,\mathrm{s}^{-1} \longrightarrow 0.0001\,\mathrm{s}^{-1}$), so as to obtain the rheological parameters (yield shear stress and plastic viscosity) of the slurry. It should be noted that the model fitting correlation coefficients R^2 obtained in this experiment were all higher than 0.98:

$$\tau = \tau_0 + \eta \cdot \gamma, \tag{1}$$

where τ is the shear stress (Pa); τ_0 is shear yield stress (Pa); η is the plastic viscosity (Pa·s); and γ is the shear rate (s^{-1}).

3. Results and Discussion

3.1. Effects of Types and Dosages of Superplasticizers. Figure 7 shows the influence of different superplasticizer types and dosages on the rheological parameters of Slag-CPBs at 0 min. It should be noted that the absence of rheological parameters of Slag-CPBs with 1.45‰ and 1.81‰ PC is due to serious bleeding. It can be seen from the figure that the type and dosage of superplasticizer have a significant influence on the rheological parameters of Slag-CPBs. Regardless of the type of superplasticizer, with the increase of superplasticizer dosage, the shear yield stress and plastic viscosity of the Slag-CPBs decreases gradually; that is, the fluidity of slurry is gradually improved. A similar observation has also been obtained by previous studies (e.g., [28, 29]).

The results in Figure 7 also indicate that the type of the superplasticizer has a significant influence on the rheological properties of Slag-CPBs. One can observe that the PC is more efficient in improving the fluidity of Slag-CPBs, compared to the PMS and PNS. A similar observation was also made on CPB made of blended cement (80% slag and 20% Portland cement) by Ouattara et al. [30]. PC significantly reduces both yield stress and plastic viscosity of Slag-CPBs, and this positive effect increases approximately linearly with the PC dosage. At relatively low dosages, PNS shows a good improvement effect on the plastic viscosity of slurry, but when the dosage reaches

(a)

(b)
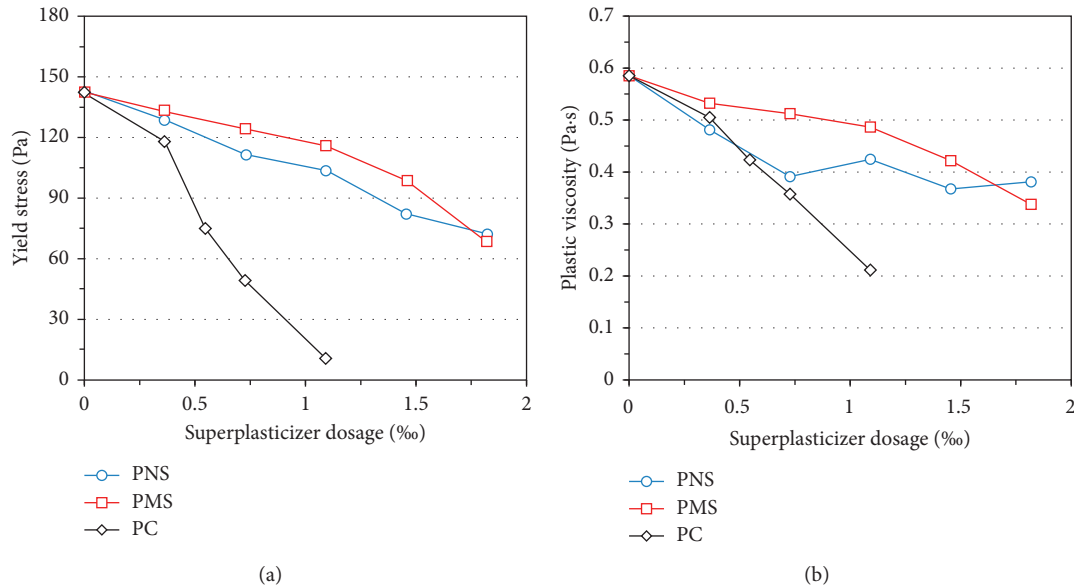
FIGURE 7: Effects of superplasticizer types and dosages on the development of (a) yield stress and (b) plastic viscosity of CPB.

0.72‰, the water-reducing effect tends to be saturated. PMS has the worst water-reducing effect, and its water-reducing effect does not change significantly with the increase of dosage compared with PC and PNS. It can also be seen from Figure 7 that, with the increase of superplasticizer dosage, the difference of water-reducing effect between PC and other superplasticizers gradually increases. The saturated content of PC is much lower than that of PNS and PMS. In addition, by comparing Figures 7(a) and 7(b), it can be seen that the influence degree of superplasticizer on yield stress is higher than that on plastic viscosity.

3.2. Time-Dependent Evolution of Rheological Properties. Figure 8 shows the time-dependent evolution of the rheological properties of OPC and Slag-CPBs with different PC dosages. It is obvious that the yield stress and plastic viscosity of all samples increased with the increase of curing time regardless of PC dosage and binder type. This is mainly because with the increase of curing time, the amount of binder hydration products continues to increase [31, 32]. In absence of the PC, both yield stress and plastic viscosity of OPC-CPB are higher than those of Slag-CPB. This is because the absolute Zeta potential of slag particles is higher than that of cement particles [33, 34]. The binder type significantly affects the effect of PC. The water-reducing effect of the PC on OPC-CPBs is stronger than that of Slag-CPBs. This observation is contrary to the results of the investigations conducted by Ouattara et al. [30], who concluded that the blended binder made of 80% Slag and 20% OPC appeared to be more compatible with the PC compared to the OPC. Moreover, Adjoudj et al. [35] demonstrated that PC superplasticizer becomes more effective when Slag is incorporated. These difference in the effect of PC indicates that the compound activator used in the study

significantly reduces the adsorption of PC to the Slag particles.

The results in Figure 8 also show that, regardless of the binder type, the rheological parameters of the sample containing PC grow at a higher rate over time than those of the sample without PC; that is, the effect of PC degrades over time. This is because with the continuous hydration of the binder, the hydration products generated will cover the absorbent PC on the surface of solid particles, thus resulting in the degradation of the effect of PC. Moreover, the degradation effect of the PC with time is more obvious in Slag-CPBs than that of OPC-CPBs.

3.3. Effect of Solid Content. The influence of PC on the rheological parameters of Slag-CPBs with different solid contents (76%, 77%, and 78%) is shown in Figure 9. The binder content of all samples is 9.1. As can be seen from Figure 9, with the solid content increasing from 76% to 77% and 78%, the shear yield stress of CPB without PC increases from 142 Pa to 201 Pa and 247 Pa, and the corresponding plastic viscosity increases from 0.59 Pa·s to 0.83 Pa·s and 1.17 Pa·s. This indicates that only a slight increase in solid content can result in a significant increase in rheological parameters for high solid content CPB. This observation is consistent with the results of the investigations conducted by Ouattara et al. [36].

Figure 10 shows the percentage decrease of rheological parameters of Slag-CPB with different solid contents and PC dosages. It can be seen from the figure that the degree of improvement in yield stress with different solid contents depends on PC dosages. When the PC dosage is low (0.36‰), the effect of PC on shear yield stress increases with increasing solid content. However, when a high dosage PC (0.54‰) is added, the water-reducing effect tends to weaken with increasing solid content. The results
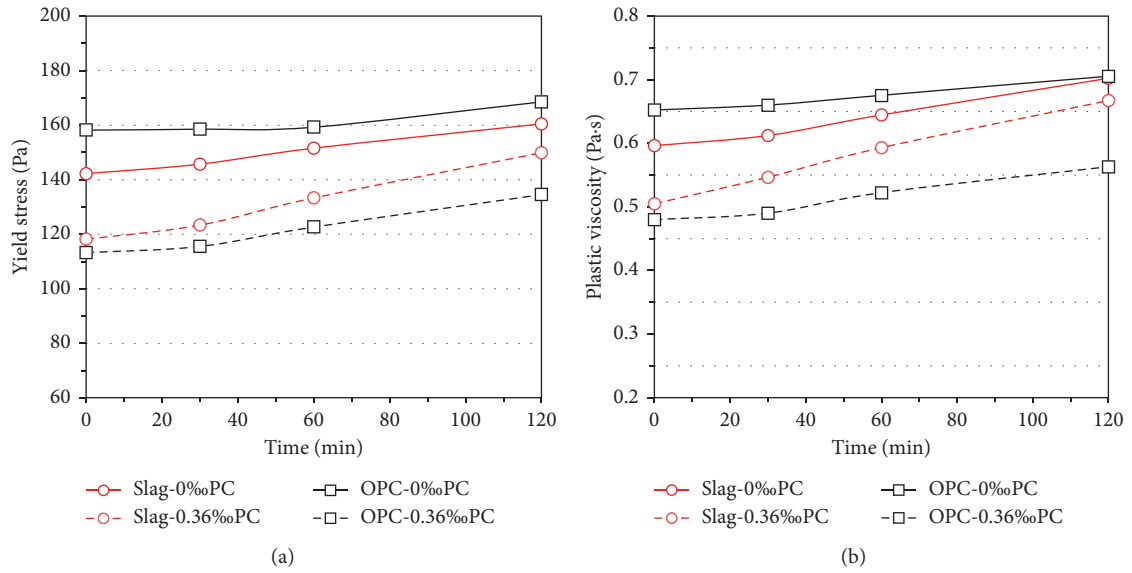
Figure 8: Time-dependent evolution of (a) yield stress and (b) plastic viscosity of CPB containing different binder types and PC dosages.
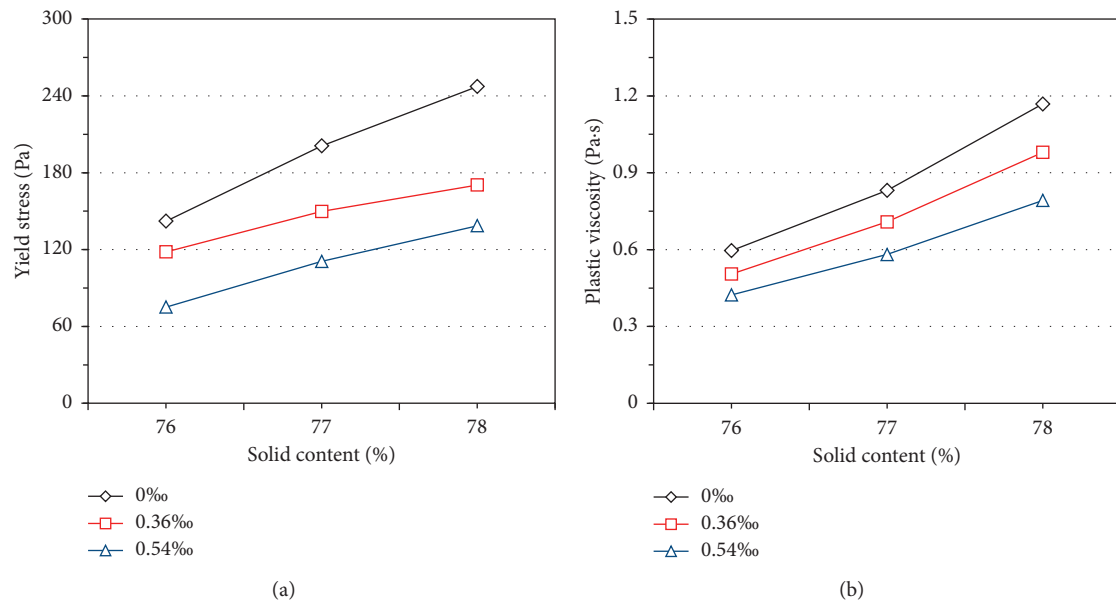
Figure 9: Effects of solid contents and PC dosages on the development of (a) yield stress and (b) plastic viscosity of CPB.

in Figure 10 also show that when the PC dosage is fixed, the degree of improvement in plastic viscosity of PC is positively correlated with the solid content. However, Yang et al. [19] reported that as the solids content increases, the cemented tailings backfill samples with a higher dosage of superplasticizer have a lower rate of decrease in fluidity. This difference in the effect of superplasticizer with increasing solid content can be attributed to the difference in the composition of binder and tailings.

3.4. Effects of Binder Content. The rheological parameters variation of fresh Slag-CPBs with different binder contents and PC dosages is shown in Figure 11. The results presented in Figure 11 show that the shear yield stress and plastic viscosity of the slurry without PC increase gradually with the increase of the binder content. Similar results have been observed by Sandeep et al. [22], Simon and Grabinsky [37], and Phan et al. [38]. However, the rate of the increase in rheological parameters decreases gradually with the PC dosage. Compared with the solid content, the binder content

(a)   (b)
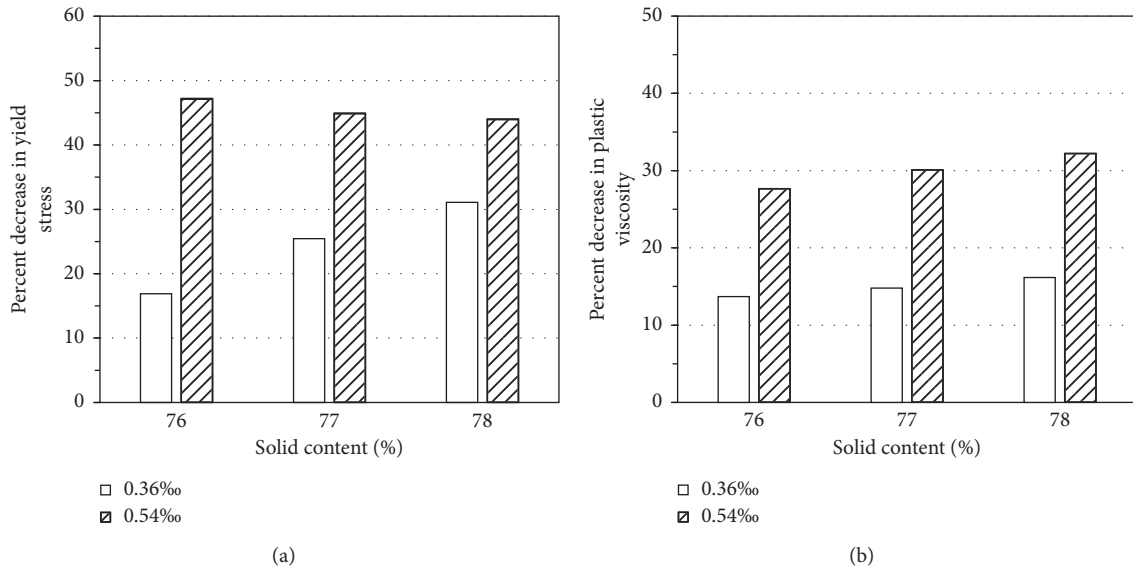
FIGURE 10: Effects of solid contents and PC dosages on the percentage reduction of (a) yield stress and (b) plastic viscosity of CPB.

(a)   (b)
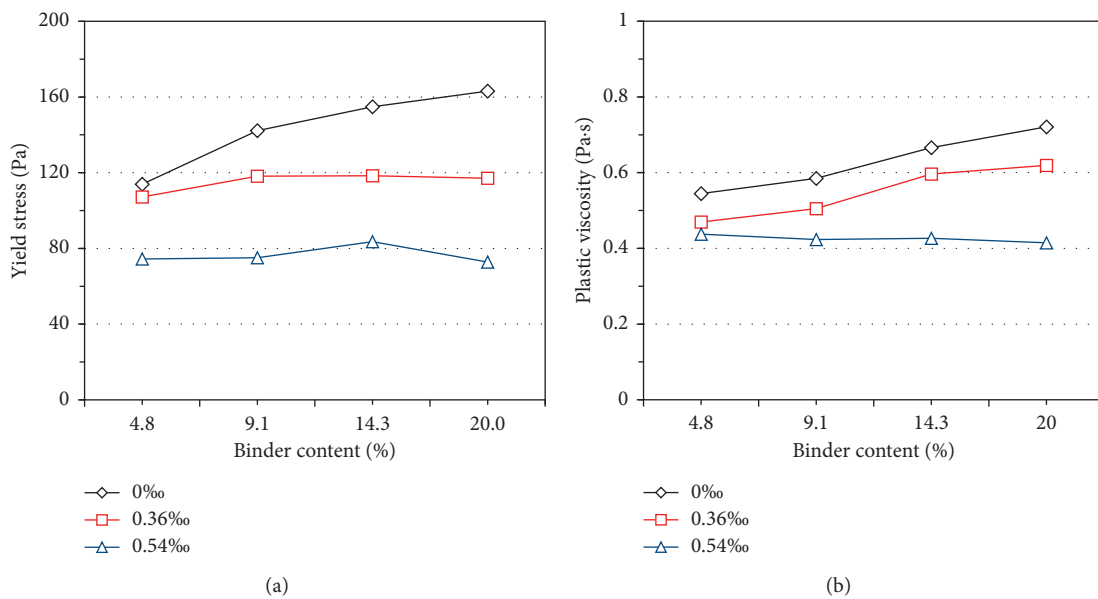
FIGURE 11: Effects of binder content and PC dosages on the development of (a) yield stress and (b) plastic viscosity of CPB.

has less influence on the rheological parameters (see Figures 9 and 11). When the PC dosage is low (0.36‰), the higher the water-to-cement ratio, the higher the yield stress and plastic viscosity of CPB samples. When the PC dosage is high (0.54‰), the yield stress and plastic viscosity of slurry with different solid contents are basically the same.

Figure 12 illustrates the influence of the PC dosages on the percentage reduction of rheological parameters. The results in Figure 12 show that when the PC dosage is low (0.36‰), the positive effect of PC on yield stress increases, while this effect on plastic viscosity decreases as the binder content increases. When the PC content is high (0.54‰), the improvement effect of PC on the yield stress basically does not change with the increase of the binder content, while the corresponding improvement effect of plastic viscosity is more significant.
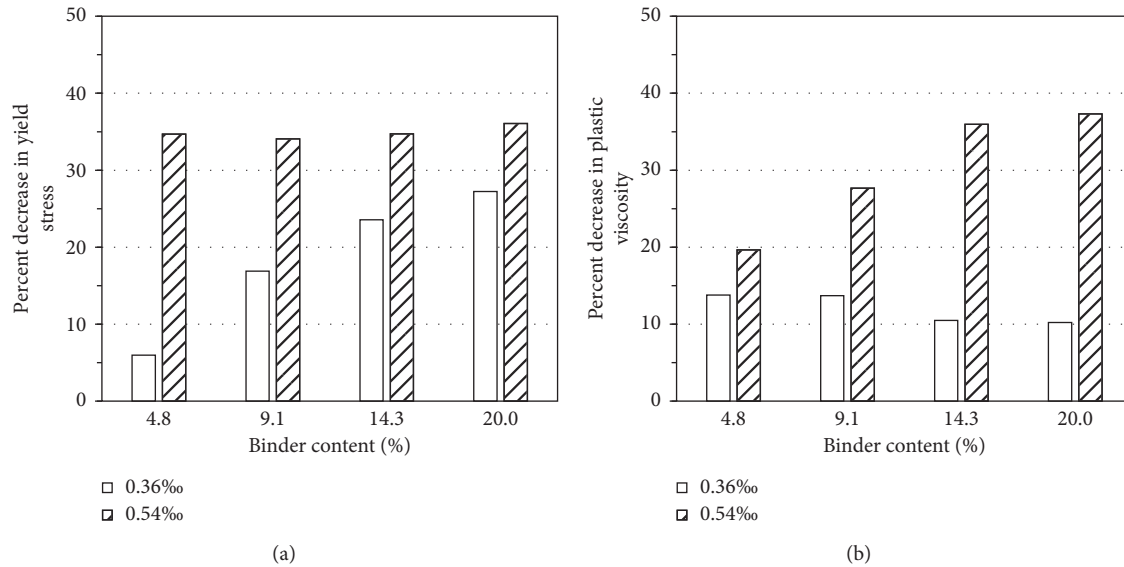
FIGURE 12: Effects of binder content and PC dosages on the percentage reduction of (a) yield stress and (b) plastic viscosity of CPB.

4. Conclusions

In this study, the rheological properties of the Slag-CPBs under different superplasticizer types and dosages were tested, and the influences of solid content and binder content were analysed. The following main conclusions can be drawn:

(1) Both yield stress and plastic viscosity of the Slag-CPBs decrease with increasing superplasticizer dosage; that is, the flow characteristic of slurry increases. Different superplasticizer types have significant differences in water-reducing effects. The PC has the best water-reducing effect, followed by the PMS and PNS.

(2) The yield stress and plastic viscosity of OPC-CPBs are higher than those of Slag-CPBs. The water-reducing effect of PC on OPC-CPBs is stronger than that of Slag-CPBs. The degradation rate of the water-reducing effect in Slag-CPBs is significantly higher than that in OPC-CPBs.

(3) The shear yield stress and plastic viscosity of the Slag-CPB without the addition of PC increase rapidly with the solid content. The degree of improvement of PC to the shear yield stress of slurry with different solid contents depends on PC dosage. When PC dosage is low (0.36‰), the higher the solid content is, the higher the shear yield stress and plastic viscosity are. When PC is added at a higher dosage (0.54‰), the shear yield stress improves more obviously with the increase of solid content, while the plastic viscosity improves less.

(4) The shear yield stress and plastic viscosity of Slag-CPBs without the addition of PC increase with the increase of the binder content. When the PC dosage is low (0.36‰), the improvement effect of PC on yield stress is better and the improvement effect of PC on plastic viscosity is worse as the binder content increases. When the PC dosage is high (0.54‰), the improvement effect of PC on the yield stress basically does not change with the increase of the binder content, while the corresponding improvement effect of plastic viscosity is more significant.

It is noteworthy that the binder in this paper contains only one mineral admixture. Therefore, in future work, we will study the coupling effect of ternary binder made of ordinary Portland cement, fly ash, and granulated blast furnace slag with a superplasticizer.

Data Availability

The data used to support the findings of this study are included within the article.

Conflicts of Interest

The authors declare that there are no conflicts of interest regarding the publication of this paper.

Acknowledgments

References

[1] D. I. Wang, Q.-I. Zhang, Q.-S. Chen, C.-C. Qi, Y. Feng, and C.-C. Xiao, "Temperature variation characteristics in flocculation settlement of tailings and its mechanism," *International Journal of Minerals, Metallurgy and Materials*, vol. 27, pp. 1438–1448, 2020.

[2] M. Fall, J. C. Célestin, M. Pokharel, and M. Touré, "A contribution to understanding the effects of curing temperature

on the mechanical properties of mine cemented tailings backfill," *Engineering Geology*, vol. 114, no. 3-4, pp. 397–413, 2010.

[3] M. Benzaazoua, B. Bussière, I. Demers, M. Aubertin, É. Fried, and A. Blier, "Integrated mine tailings management by combining environmental desulphurization and cemented paste backfill: application to mine Doyon, Quebec, Canada," *Minerals Engineering*, vol. 21, no. 4, pp. 330–340, 2008.

[4] H. Jiang, H. Yi, E. Yilmaz, S. Liu, and J. Qiu, "Ultrasonic evaluation of strength properties of cemented paste backfill: effects of mineral admixture and curing temperature," *Ultrasonics*, vol. 100, Article ID 105983, 2020.

[5] J. Qiu, Z. Guo, L. Yang, H. Jiang, and Y. Zhao, "Effects of packing density and water film thickness on the fluidity behaviour of cemented paste backfill," *Powder Technology*, vol. 359, pp. 27–35, 2020.

[6] A. Tariq and E. K. Yanful, "A review of binders used in cemented paste tailings for underground and surface disposal practices," *Journal of Environmental Management*, vol. 131, pp. 138–149, 2013.

[7] M. Ozkaymak, S. Selimli, D. Kaya, and U. Uzun, "Searching the fertility potential of iron and steel industry blast furnace slag," *World Journal of Engineering*, vol. 13, no. 6, pp. 482–486, 2016.

[8] D. Dutta and S. Ghosh, "The role of delayed water curing in improving the mechanical and microstructural properties of alkali activated fly ash based geopolymer paste blended with slag," *World Journal of Engineering*, vol. 16, no. 1, pp. 103–114, 2019.

[9] S. Raj, A. K. Rai, and V. G. Havanagi, "Suitability of stabilized copper slag and fly ash mix for road construction," *World Journal of Engineering*, vol. 15, no. 3, pp. 336–344, 2018.

[10] M. Fall and M. Benzaazoua, "Modeling the effect of sulphate on strength development of paste backfill and binder mixture optimization," *Cement and Concrete Research*, vol. 35, no. 2, pp. 301–314, 2005.

[11] S. Ben Messaoud and B. Mezghiche, "Experimental analysis of behaviour of light weight high performance concrete with crystallized slag," *World Journal of Engineering*, vol. 13, no. 5, pp. 447–452, 2016.

[12] E. Yilmaz, M. Benzaazoua, T. Belem, and B. Bussière, "Effect of curing under pressure on compressive strength development of cemented paste backfill," *Minerals Engineering*, vol. 22, no. 9-10, pp. 772–785, 2009.

[13] K. Klein and D. Simon, "Effect of specimen composition on the strength development in cemented paste backfill," *Canadian Geotechnical Journal*, vol. 43, no. 3, pp. 310–324, 2006.

[14] A. Kesimal, E. Yilmaz, B. Ercikdi, I. Alp, and H. Deveci, "Effect of properties of tailings and binder on the short-and long-term strength and stability of cemented paste backfill," *Materials Letters*, vol. 59, no. 28, pp. 3703–3709, 2005.

[15] H. Jiang, Z. Qi, E. Yilmaz, J. Han, J. Qiu, and C. Dong, "Effectiveness of alkali-activated slag as alternative binder on workability and early age compressive strength of cemented paste backfills," *Construction and Building Materials*, vol. 218, pp. 689–700, 2019.

[16] B. Ercikdi, G. Külekci, and T. Yılmaz, "Utilization of granulated marble wastes and waste bricks as mineral admixture in cemented paste backfill of sulphide-rich tailings," *Construction and Building Materials*, vol. 93, pp. 573–583, 2015.

[17] S. Zhang, L. Yang, F. Ren, J. Qiu, and H. Ding, "Rheological and mechanical properties of cemented foam backfill: effect of mineral admixture type and dosage," *Cement and Concrete Composites*, vol. 112, Article ID 103689, 2020.

[18] L. Yang, W. Xu, E. Yilmaz, Q. Wang, and J. Qiu, "A combined experimental and numerical study on the triaxial and dynamic compression behavior of cemented tailings backfill," *Engineering Structures*, vol. 219, Article ID 110957, 2020.

[19] L. Yang, E. Yilmaz, J. Li, H. Liu, and H. Jiang, "Effect of superplasticizer type and dosage on fluidity and strength behavior of cemented tailings backfill with different solid contents," *Construction and Building Materials*, vol. 187, pp. 290–298, 2018.

[20] R. J. Jewell and A. B. Fourie, *Paste and Thickened Tailings: A Guide*, Australian Centre for Geomechanics, The University of Western Australia, Perth, Australia, 2006.

[21] S. Haruna and M. Fall, "Time-and temperature-dependent rheological properties of cemented paste backfill that contains superplasticizer," *Powder Technology*, vol. 360, pp. 731–740, 2020.

[22] S. Panchal, D. Deb, and T. Sreenivas, "Variability in rheology of cemented paste backfill with hydration age, binder and superplasticizer dosages," *Advanced Powder Technology*, vol. 29, no. 9, pp. 2211–2220, 2018.

[23] M. B. C. Mangane, R. Argane, R. Trauchessec, A. Lecomte, and M. Benzaazoua, "Influence of superplasticizers on mechanical properties and workability of cemented paste backfill," *Minerals Engineering*, vol. 116, pp. 3–14, 2018.

[24] F. Hassani, S. M. Razavi, and I. Isagon, "A study of physical and mechanical behaviour of gelfill," *CIM Bulletin*, vol. 2, no. 5, pp. 1–7, 2007.

[25] M. Fall, T. Belem, S. Samb, and M. Benzaazoua, "Experimental characterization of the stress-strain behaviour of cemented paste backfill in compression," *Journal of Materials Science*, vol. 42, no. 11, pp. 3914–3922, 2007.

[26] S. Bechar and D. Zerrouki, "Effect of natural pozzolan on the fresh and hardened cement slurry properties for cementing oil well," *World Journal of Engineering*, vol. 15, no. 4, pp. 513–519, 2018.

[27] Z. Guo, J. Qiu, H. Jiang, J. Xing, X. Sun, and Z. Ma, "Flowability of ultrafine-tailings cemented paste backfill incorporating superplasticizer: insight from water film thickness theory," *Powder Technology*, vol. 381, pp. 509–517, 2021.

[28] L. Huynh, D. A. Beattie, D. Fornasiero, and J. Ralston, "Effect of polyphosphate and naphthalene sulfonate formaldehyde condensate on the rheological properties of dewatered tailings and cemented paste backfill," *Minerals Engineering*, vol. 19, no. 1, pp. 28–36, 2006.

[29] B. Ercikdi, F. Cihangir, A. Kesimal, H. Deveci, and İ. Alp, "Utilization of water-reducing admixtures in cemented paste backfill of sulphide-rich mill tailings," *Journal of Hazardous Materials*, vol. 179, no. 1-3, pp. 940–946, 2010.

[30] D. Ouattara, M. Mbonimpa, A. Yahia, and T. Belem, "Assessment of rheological parameters of high density cemented paste backfill mixtures incorporating superplasticizers," *Construction and Building Materials*, vol. 190, pp. 294–307, 2018.

[31] H. Jiang and M. Fall, "Yield stress and strength of saline cemented tailings in sub-zero environments: Portland cement paste backfill," *International Journal of Mineral Processing*, vol. 160, pp. 68–75, 2017.

[32] D. Wu, M. Fall, and S. J. Cai, "Coupling temperature, cement hydration and rheological behaviour of fresh cemented paste backfill," *Minerals Engineering*, vol. 42, pp. 76–87, 2013.

[33] J. Haiqiang, M. Fall, and L. Cui, "Yield stress of cemented paste backfill in sub-zero environments: experimental results," *Minerals Engineering*, vol. 92, pp. 141–150, 2016.

[34] H. Jiang, M. Fall, E. Yilmaz, Y. Li, and L. Yang, "Effect of mineral admixtures on flow properties of fresh cemented paste backfill: assessment of time dependency and thixotropy," *Powder Technology*, vol. 372, pp. 258–266, 2020.

[35] M. h. Adjoudj, K. Ezziane, E. H. Kadri, T.-T. Ngo, and A. Kaci, "Evaluation of rheological parameters of mortar containing various amounts of mineral addition with polycarboxylate superplasticizer," *Construction and Building Materials*, vol. 70, pp. 549–559, 2014.

[36] D. Ouattara, A. Yahia, M. Mbonimpa, and T. Belem, "Effects of superplasticizer on rheological properties of cemented paste backfills," *International Journal of Mineral Processing*, vol. 161, pp. 28–40, 2017.

[37] D. Simon and M. Grabinsky, "Apparent yield stress measurement in cemented paste backfill," *International Journal of Mining, Reclamation and Environment*, vol. 27, no. 4, pp. 231–256, 2013.

[38] T. H. Phan, M. Chaouche, and M. Moranville, "Influence of organic admixtures on the rheological behaviour of cement pastes," *Cement and Concrete Research*, vol. 36, no. 10, pp. 1807–1813, 2006.

Research Article

Strength Investigation of the Silt-Based Cemented Paste Backfill Using Lab Experiments and Deep Neural Network

Chongchun Xiao,[1,2] Xinmin Wang,[1] Qiusong Chen ®**,[1,3] Feng Bin,[2] Yihan Wang,[1,4] and Wei Wei[1,5]**

[1]*School of Resources and Safety Engineering, Central South University, Changsha 410083, China*
[2]*Feny Co. Ltd., Changsha 410083, China*
[3]*Sinosteel Maanshan Institute of Mining Research Company Limited, Maanshan 243000, China*
[4]*Hunan Filling Engineering Technology Co. Ltd., Changsha 410083, China*
[5]*Wanbao Mining Ltd., Beijing 100000, China*

Correspondence should be addressed to Qiusong Chen; qiusong.chen@csu.edu.cn

The cemented paste backfill (CPB) technology has been successfully used for the recycling of mine tailings all around the world. However, its application in coal mines is limited due to the lack of mine tailings that can work as aggregates. In this work, the feasibility of using silts from the Yellow River silts (YRS) as aggregates in CPB was investigated. Cementitious materials were selected to be the ordinary Portland cement (OPC), OPC + coal gangue (CG), and OPC + coal fly ash (CFA). A large number of lab experiments were conducted to investigate the unconfined compressive strength (UCS) of CPB samples. After the discussion of the experimental results, a dataset was prepared after data collection and processing. Deep neural network (DNN) was employed to predict the UCS of CPB from its influencing variables, namely, the proportion of OPC, CG, CFA, and YS, the solids content, and the curing time. The results show the following: (i) The solid content, cement content (cement/sand ratio), and curing time present positive correlation with UCS. The CG can be used as a kind of OPC substitute, while adding CFA increases the UCS of CPB significantly. (ii) The optimum training set size was 80% and the number of runs was 36 to obtain the converged results. (iii) GA was efficient at the DNN architecture tuning with the optimum DNN architecture being found at the 17th iteration. (iv) The optimum DNN had an excellent performance on the UCS prediction of silt-based CPB (correlation coefficient was 0.97 on the training set and 0.99 on the testing set). (v) The curing time, the CFA proportion, and the solids content were the most significant input variables for the silt-based CPB and all of them were positively correlated with the UCS.

1. Introduction

Mining and minerals industries are very likely to cause widespread environmental damage, such as noise pollution, air and water contamination, and solids waste generation [1, 2]. Thus, recycling has been an important issue encountered by mining and minerals industries, especially the solids waste recycling [3–6]. As for the metal mining, solid waste recycling mainly deals with the large amount of mine tailings generated due to the high waste-to-product ratio [7, 8]. It has been shown that the waste-to-product ratio for

the metal mining is often 100 : 1 in volume, which can be as high as 1,000,000 : 1 in some cases [9]. Interested readers could refer to the review paper in [7] for a detailed presentation of the tailings generated for typical ores.

In the era of sustainable development and cleaner production, the recycling of mine tailings has been a hot topic that has undergone extensive investigations. A number of recycling methods have been proposed, among which the cemented paste backfill (CPB) is one of the most popular methods. CPB is advantageous in that it can not only promote the tailings recycling, but also improve working

conditions, stabilise surrounding rock mass, and sometimes work as the platform for the subsequent mining operations. Therefore, CPB has been widely used throughout the world, such as in China [10–13], Australia [14], Canada [15], and Turkey [16, 17], to name a few.

Depending on the intended function of the backfill, a certain amount of mechanical properties, often indicated by unconfined compressive strength (UCS), is needed for CPB. For example, a UCS between 150 kPa and 300 kPa is required to reduce the liquefaction possibility while a UCS larger than 4 MPa is recommended by Grice when CPB is used for roof support [7]. The determination of UCS is essential prior to any engineering application of the CPB technology. Traditionally, lots of lab experiments are conducted for each mine site, which consumes a large amount of time, materials, and human resources. The strength prediction from its influencing variables is attracting increasing attention from both academia and industry. A large number of studies have been performed by Qi and his co-authors [18–20], followed by the most up-to-date papers like [21–23].

Up to now, the advantages of CPB, the importance of UCS, and the significance of strength prediction have been presented mainly for metal mining. The application of CPB in coal mines has also been investigated. For example, Huang et al. [24] proposed a technological framework for the backfill technology that used coal waste and fly ash as the main ingredients. Zhang et al. [25] investigated the surface subsidence in backfill coal mining based on the equivalent mining height theory. In contrast to the CPB technology in metal mining that recycles mine tailings, the application of the CPB technology in coal mining requires the selection of aggregates. In some cases, the lack of suitable aggregates limits the application of CPB, thus hindering the cleaner production in coal mining.

In this work, the strength development of silt-based CPB was investigated using lab experiments and deep neural network (DNN). The main contributions of this work to the literature are as follows:

(i) To facilitate the application of CPB in coal mines, the utilization of Yellow River silts (YRS) as aggregates in CPB was investigated

(ii) The comparison of ordinary Portland cement (OPC), OPC + coal gangue (CG), and OPC + coal fly ash (CFA) as the cementitious materials was conducted

(iii) A DNN model was proposed for the strength prediction of the silt-based CPB

2. Study Site

A coal mine (referred to as 'A-Mine'), located in Shandong Province, China, is a medium-sized coal mine with the production of 900,000 tonnes per year. As an underground coal mine, the earth surface above the mined-out area is covered with town and farmland, and the CPB technology has thus become legally required. To realize the engineering application of CPB, the first work is choosing the backfill aggregate and cementitious materials, which affect the

mechanical properties of CPB. The principals of selecting backfill materials include extensive source, low cost, pollution free, etc. Considering the location of A-Mine that is nearby the Yellow River and a thermal power plant, as shown in Figure 1, the silt from Yellow River (YRS), CG, and CFA were considered as potential materials for CPB.

3. Materials and Methods

3.1. Materials. The YRS has been analyzed as a potential backfill aggregate, which was selected from a silts plant near A-Mine. The main cementitious material was No. 42.5 ordinary Portland cement (OPC, according to Chinese National Standard, GB175-2007) provided by A-Mine. In order to improve the mechanical and pipe transport properties of CPB, other materials, CFA and CG, were also used for modification. The CFA was collected from a thermal power plant, as shown in Figure 1, while the CG was collected from a CG dump belonging to A-Mine. All these materials were collected and sealed and then sent to Central South University for test. The underground water from A-Mine was used for preparing the CPB samples. It should be noted that the YRS needs to be pretreated to remove the impurities, and the CG particles were controlled in 5 mm, as presented in Figure 2.

The particles size distributions of YRS and CG were measured by sieving method and laser particle size analyzer (Malvern Mastersizer 2000), as shown in Figure 3, and Table 1 summarizes the main PSD parameters. The mineral components were tested using x-ray diffraction (XRD; Bruker AXS D8 Advance Diffractometer), as shown in Figure 4. The results show that the median particle size of silts and CG was 145 μm and 380 μm, which can be classified as coarse aggregates [26]. Table 2 presents the chemical properties of YRS and CG. The main mineral components of the YRS are quartz, feldspar, and calcite. Among them, the quartz and feldspar have been proven important for the strength of CPB. The kaolinite, quartz, and calcite gypsum are the main components of CG, which are good for improving the mechanical properties of CPB.

3.2. Lab Experiments

3.2.1. CPB Preparation. The backfill materials, i.e., YRS, CG, CFA, OPC, water, etc., were measured as designed and then mixed using an electric mixer (JJ-5, Hebei, China). After being mixed for 5 min, the uniform CPB slurry was formed and poured into triple plastic moulds (7.07 × 7.07 × 7.07 cm). The moulds should be poured with CPB slurry as much as possible, to avoid the effects of consolidation shrinkage [27], as shown in Figure 5(a). After 24 hours and CPB initial setting, the samples were scraped to form a smooth surface (Figure 5(b)), and the moulds were removed. The cubic CPB samples (Figure 5(c)) were then cured in a curing box (YH–40B, Qingda, Tianjin of China) with the temperature of 25°C and humidity of 90% (Figure 5(d)).

3.2.2. UCS Test. The CPB samples after curing for 1 d, 3 d, and 28 d were taken out for UCS tests using pressure testing machine (WDW-20), as shown in Figure 6. The test sample

FIGURE 1: The location of study site.

FIGURE 2: YRS pretreatment and CG sieving.

was placed in the circular testing plate and tested with a loading speed of 0.5 mm/min [28]. Three samples were tested in each group of experiments, and the average value of the two results with errors less than 5% was taken as UCS.

3.3. Deep Neural Network Prediction. Artificial neural network (ANN) is a computing technique inspired by the biological neural networks in brain. ANN is designed to learn the mapping from inputs to outputs with a large number of
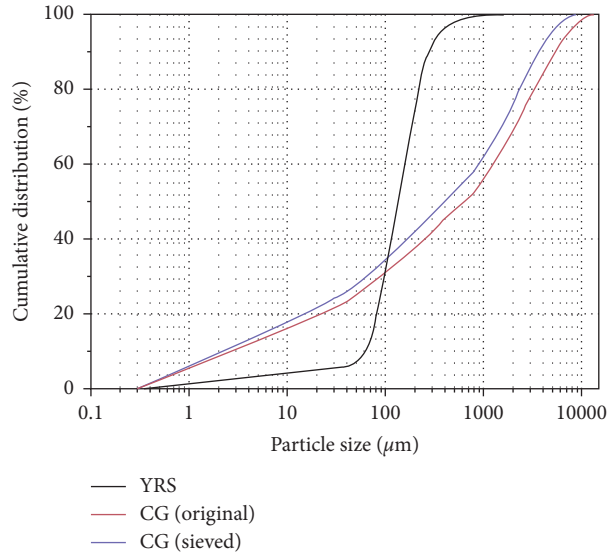
FIGURE 3: Particle size distribution curve of aggregate.

TABLE 1: Main geotechnical properties of aggregate.

Aggregate	Specific gravity (GS) (t/m^3)	d_{60} (μm)	d_{50} (μm)	d_{30} (μm)	d_{10} (μm)	Uniformity coefficient (C_u)	Curvature coefficient (C_c)
YRS	2.57	165	145	100	50	3.3	1.21
CG (sieved)	2.53	890	380	62	2.2	404.5	1.96

1–Quartz 5–Chlorite
2–Feldspar 6–Amphibole
3–Calcite 7–Mica
4–Dolomite

(a)

1–Quartz 4–Chlorite
2–Burning lime 5–Mica
3–Kaolinite 6–Pyrite

(b)
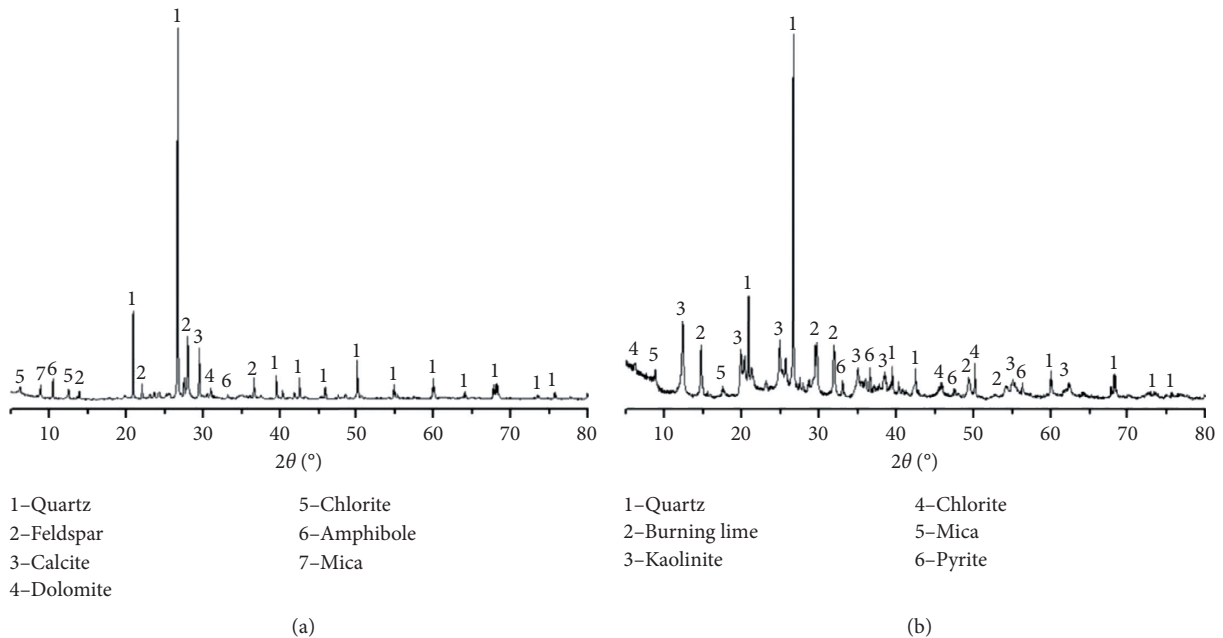
FIGURE 4: XRD mineralogical composition analysis results of aggregate: (a) YRS and (b) CG.

connected neurons, or processing units. Neurons are made up of input units and output units, where input units receive information from the previous layer and, after proper processing, output such information to the next layer. DNN is a type of ANN that has multiple hidden layers, usually larger than 3. Interested readers about ANN could refer to [29] for a detailed explanation of ANN. In this work, DNN with 5 hidden layers was used as the prediction method [30].

TABLE 2: The chemical properties of YS and CG (%).

Composition	Quartz	Feldspar	Calcite	Dolomite	Chlorite	Amphibole	Mica
YRS	32.73	31.29	14.73	3.27	5.82	5.29	6.87
CG	25.01	15.51	10.31	4.56	4.89	5.22	34.50

Except the number of neurons in each hidden layer, which are tuned by genetic algorithm, other DNN parameters were selected to be the default values from Sklearn [31].

The experimental results were collected for the preparation of the dataset. In this work, the proportion of OPC, CG, CFA, and silts, the solids content, and the curing time were selected to be the inputs while the UCS was selected to be the output. A total number of 126 data samples were included in the dataset. Data normalisation was performed to speed up the DNN calculations and improve its performance. The correlation coefficient, which ranged from −1 to 1, was used as the performance indicator.

In supervised learning, the whole dataset needs to be split into the training set (for DNN training) and the testing set (for DNN verification). However, the training set size has a significant influence on the DNN performance and thus needs to be properly determined. A convergence test was conducted in this work where the training set size was increased from 30% to 90%. Note that the default ANN structure from [31] was used during the convergence test for the training set size. Moreover, each training set size was repeated 50 times to obtain the converged results. The training performance was determined by 5-fold cross-validation. As for the testing performance, the whole training set was used to train the ANN model and the trained ANN model was used to make a prediction on the testing set.

Figure 7 illustrates the results of the convergence test. As shown, the training performance increased with the increasing training set size. In contrast, the testing performance increased when the training set size was increased from 30% to 80%. Then, the testing performance decreased when the training set size was further increased to 90%. Therefore, the training set size was determined to be 80% in the following calculations.

As indicated before, 50 runs were repeated for each training set size to obtain the converged results. However, 50 runs might not be necessary. Moreover, it would be too computationally intensive if 50 runs were repeated for each DNN architecture during the tuning of the number of neurons in each hidden layer. Thus, a convergence test was also conducted to determine the number of runs needed for the converged results. Figure 8 shows the influence of the number of runs on the average correlation coefficient and its standard deviation. It was found that the average correlation coefficient and its standard deviation stabilized after 36 runs. Therefore, the number of runs was determined to be 36 in the following calculations.

The employed DNN had one input layer with 6 neurons, one output layer with 1 neuron, and 5 hidden layers. The number of neurons in each hidden layer would affect the DNN performance, as indicated in many previous studies [18, 30]. In this work, the number of neurons was determined for each hidden layer within the range of 1 to 200.

Genetic algorithm (GA) was used for the tuning of the number of neurons in each hidden layer, which was equivalent to the optimization of the DNN architecture. During the GA optimization, each DNN structure would be represented by a chromosome. The average training performance of the DNN architecture was used as the objective function for GA, which would be maximized during GA iterations.

In this study, the number of chromosomes in GA was selected to be 100 and the maximum generation was 50. Tournament selection was utilized to select the chromosomes that will be maintained in the next generation. The crossover probability and the mutation probability were selected to be 0.90 and 0.02, respectively. The authors note that the selection of GA parameters was based on the recommendations from the literature [32]. Interested readers could refer to [30] for a detailed discussion about the optimization of ANN architecture using GA, which was not covered in detail for clarity purpose.

4. Results and Discussion

4.1. Strength Development of CPB. Figure 9 presents the relation of UCS and the solid content of CPB at the cement/sand ratio of 1 : 8. It can be seen that the UCS values increase with the increase of solid content. Take YRS group, for example; the UCS values of CPB samples curing for 28 days at the solid content of 73%, 74%, and 75% are 0.73 MPa, 0.79 MPa, and 0.88 MPa, respectively. As studied before, the hardened CPB is an inhomogeneous body composed of crystals, gels, incompletely hydrated cement particles, free water, and pores. Among them, the crystals and gels play a role in increasing strength, while the free water leads to the decrease of strength [33]. Thus, increasing the solid content leads to the reduction of free water in the CPB mixture, which will increase the strength of the CPB thereby.

Figure 10 presents the relation of UCS and cement/sand ratio at the solid content of 74%. It can be seen that increasing the cement/sand ratio significantly improves the UCS values, especially for the CPB samples curing for 28 days. Take YRS group, for instance; the UCS values of CPB curing for 28 days at the cement/sand ratio of 1 : 15, 1 : 10, 1 : 8, and 1 : 6 are 0.17 MPa, 0.51 MPa, 0.79 MPa, and 1.30 MPa, respectively. It is well known that the hydration of cement provides crystals and gels in the CPB mixture, which is the essential reason for hardening the CPB [4, 28]. Thus, improving the consumption of cement is the direct approach to increase the strength of CPB. However, the cement/sand ratio should be controlled at a balanced value to save the cost of CPB. Similar findings were also obtained in the studies of Ercikdi [34] and Yılmaz and Ercikdi [35]. They remarked that the strength of CPB increased as the cement dosage increased (from 5 to 6 and 7 wt.%) regardless of the tailings

FIGURE 5: CPB specimens preparation and curing process.

FIGURE 6: Laboratory UCS test.

type and curing periods. It was also manifested by the previous authors [35, 36] that the increase in the cement dosage had precious influence on the production of higher cementing bonds which in turn improved the strength gain.

Figure 11 presents the UCS values adding different cementitious materials, such as OPC, OPC + CG, and OPC + CFA, and the OPC is the control group. It can be seen that adding CG slightly improves the mechanical UCS, and the increments of CPB curing for 1 day, 3 days, and 28 days are 0.02 MPa, 0.08 MPa, and 0.08 MPa. Thus, CG is not a suitable OPC substitute, which cannot improve the early strength, while adding CFA increases the UCS of CPB significantly, including the samples curing for 3 days and 28 days. Compared to the OPC group, the UCS increments of OPC + CFA group samples curing for 3 days and 28 days are 0.34 MPa and 4.67 MPa. It can be attributed to pozzolanic reaction occuring between CFA and calcium hydroxide

$(CaOH_2)$ produced by OPC hydration [36, 37]. Furthermore, the previous researcher reported that the CFA has binding property as well as pozzolanic characteristic.

4.2. DNN Architecture Optimization. Figure 12 illustrates the update of the maximum correlation coefficient with GA iteration. It can be seen that the maximum correlation coefficient was 0.977 at the first iteration. The maximum correlation coefficient was increased to 0.979 at the seventh iteration and further increased to 0.989 at the 17th iteration. After that, the maximum correlation coefficient remained the same until the 50th iteration. The above results indicate that GA was efficient in the architecture tuning of DNN.

The optimum DNN architecture was determined after the GA iteration. The number of neurons was 95, 72, 158, 44, and 169 for the first to fifth hidden layer, respectively.
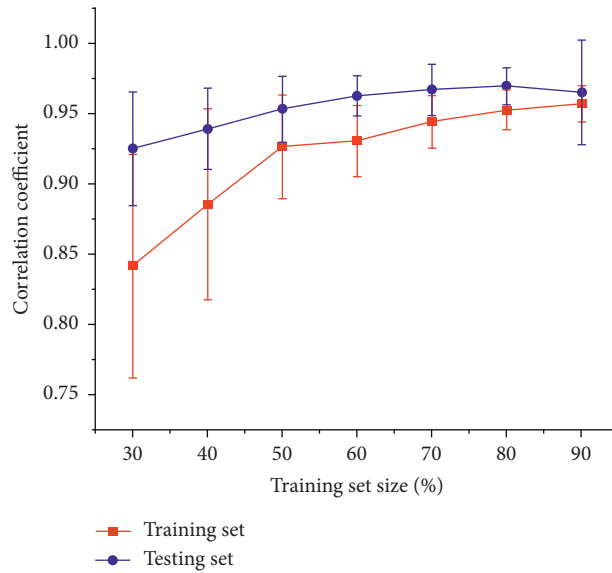
FIGURE 7: Influence of training set size on the performance of ANN modelling.

(a)

(b)
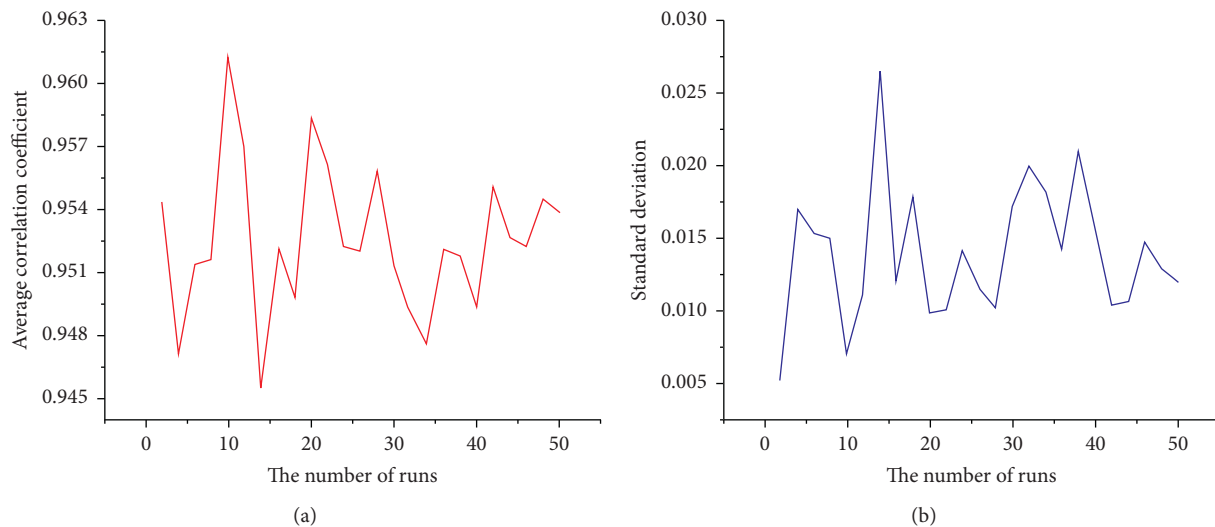
FIGURE 8: Influence of the number of runs on the average correlation coefficient and its standard deviation.

Considering the input layer and the output layer, the whole DNN architecture is illustrated in Figure 13.

4.3. DNN Prediction of UCS. In this section, the performance of the optimum DNN model is analyzed. Figure 14 illustrates the performance of the optimum DNN model on the training set and the testing set. As shown, the optimum DNN model achieved an average correlation coefficient of 0.97 on the training set and an average correlation coefficient of 0.99 on the testing set. The slight performance improvement on the testing set is due to the calculation difference on the training set and the testing set. As indicated before, the training performance was obtained by 5-fold cross-validation and the testing performance was obtained after the training of the DNN using the whole training set.

The better performance on the testing set has been well documented in the literature, such as in [19].

Moreover, the standard deviation of the correlation coefficients was 0.0112 on the training set and 0.0065 on the testing set. Thus, the performance on the testing set was more stable than that on the training set.

Figure 15 presents a visualization of the performance of the optimum DNN model on the whole dataset. It can be seen that the predicted UCS agreed well with the experimental UCS, especially the changing trend. Moreover, the optimum DNN model could achieve good performance on CPB samples with high UCS values, as shown around the right part of Figure 7. The above results further imply the robustness of the DNN model and its feasibility of the DNN prediction.
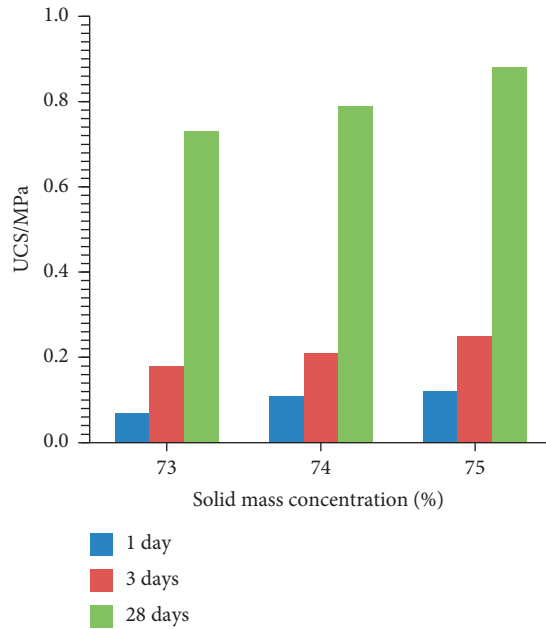
FIGURE 9: The results of UCS of CPB with cement/sand ratio of 1 : 8.
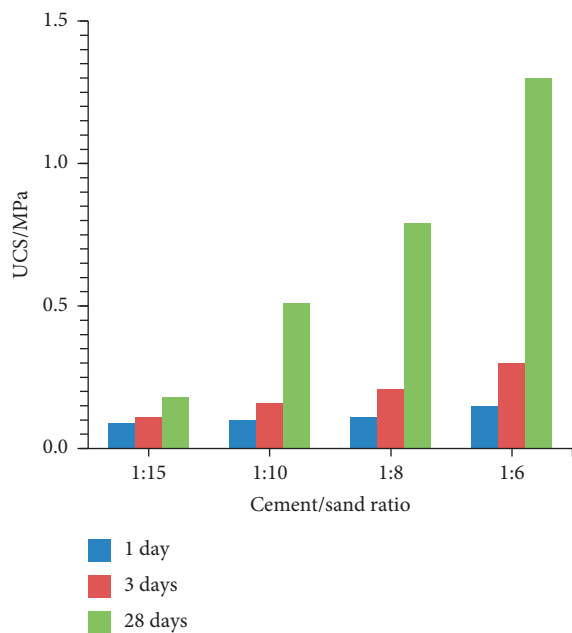
FIGURE 10: The results of UCS of CPB with solid mass concentration of 74%.
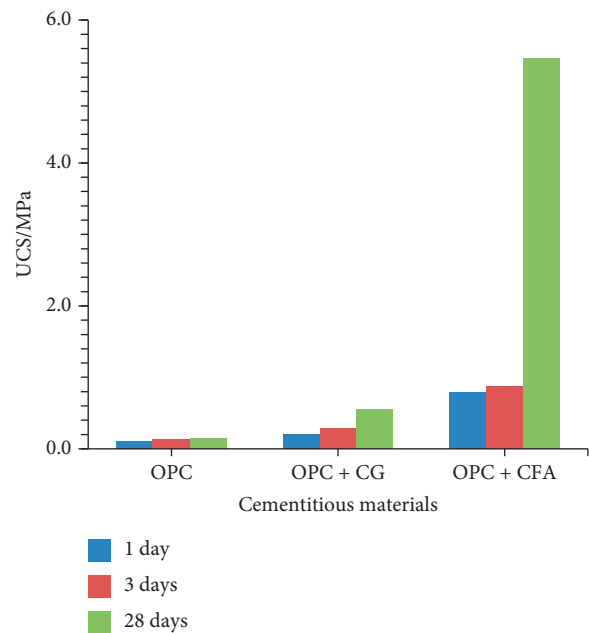
FIGURE 11: The results of UCS of CPB adding different cementitious materials.

4.4. Partial Dependence Plots and Importance Analysis. In this work, the partial dependence plots and importance score (IS) were used to investigate the influence of each input variable to the UCS of CPB. Partial dependence plots and IS are two important methods for the variable analysis and a detailed explanation of these two methods has been provided in [19]. The authors note that the summation of IS values was normalized to one for comparison purpose. Figure 16 illustrates the partial dependence plots and IS for each input variable.

It can be found that the UCS had an overall positive correlation with the OPC proportion, the CFA proportion, the solids content, and the curing time. A negative correlation was observed between the silt proportion and the UCS while the UCS had little correlation with the CG proportion. Based on the partial dependence plots, curing time was the most significant variable for UCS, followed by the CFA proportion. The CG was the least important variable for the CPB UCS.

The significance of each input variable to the UCS could be as easily indicated by the IS values. The IS value of the curing
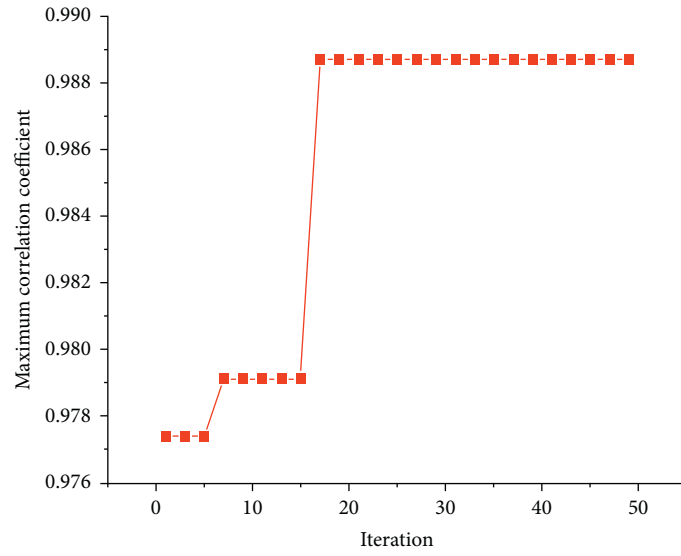
Figure 12: Update of the maximum correlation coefficient with GA iteration.
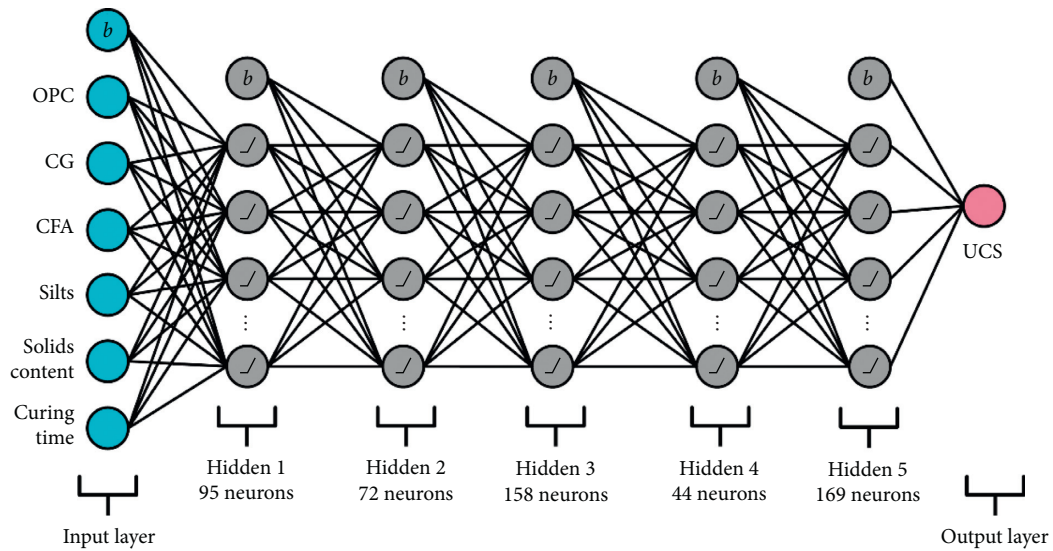
Figure 13: The optimum DNN architecture.
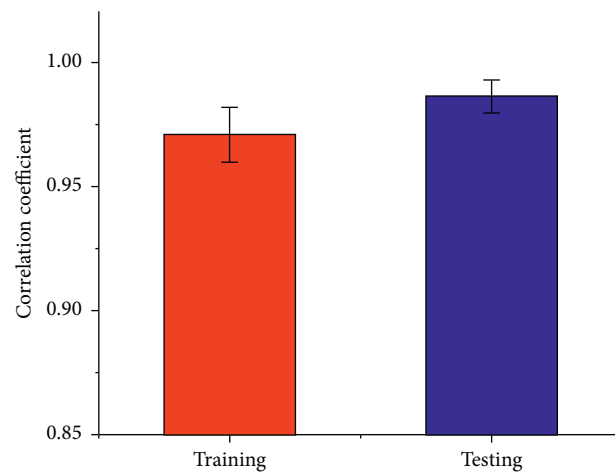
Figure 14: The performance of the optimum DNN model on the training set and the testing set.
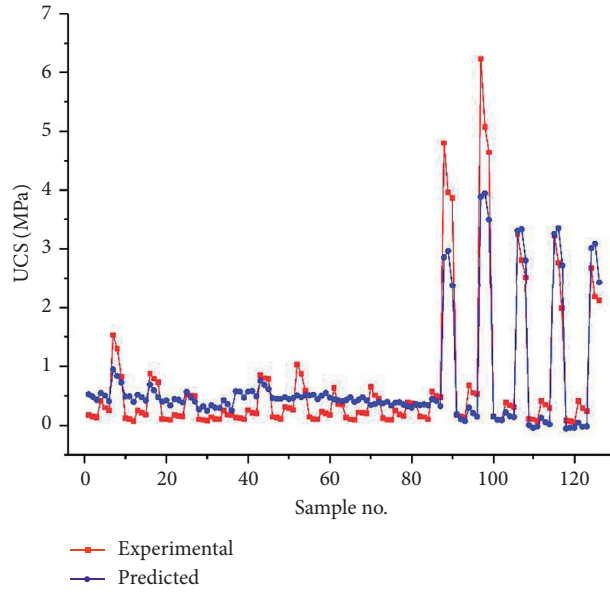
Figure 15: Performance visualization of the optimum DNN model on the whole dataset.

(a)

(b)

(c)

(d)
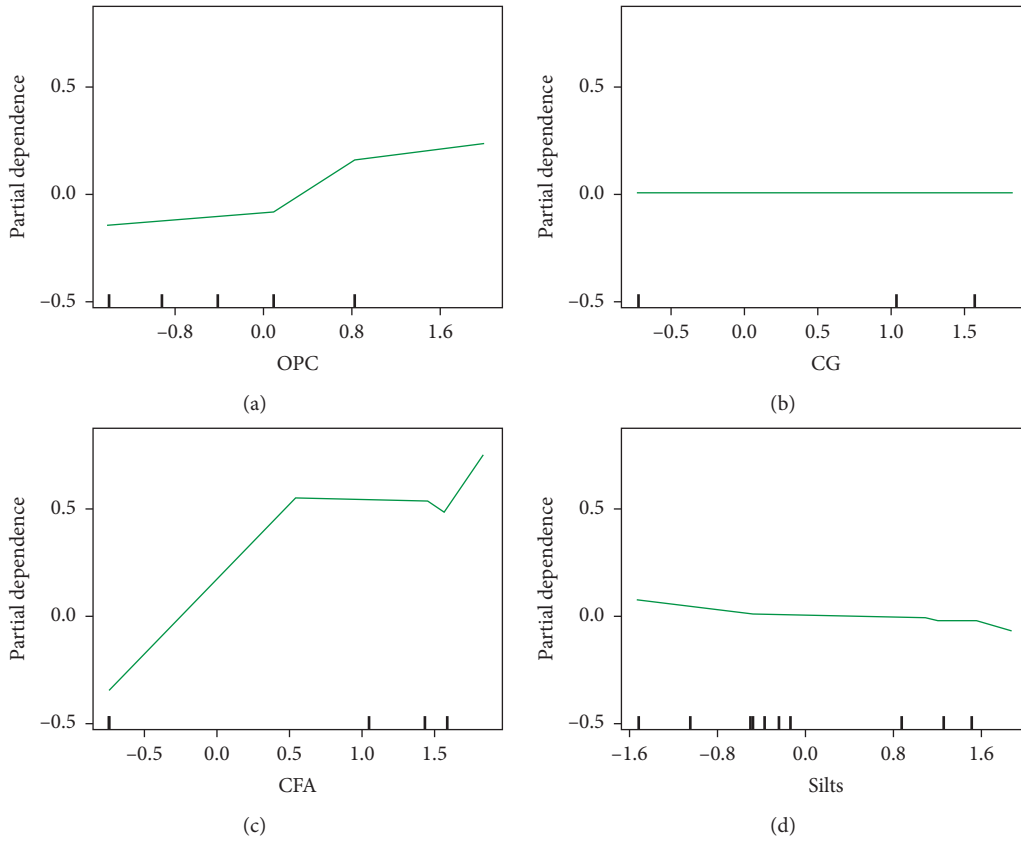
Figure 16: Continued.

(e)

(f)
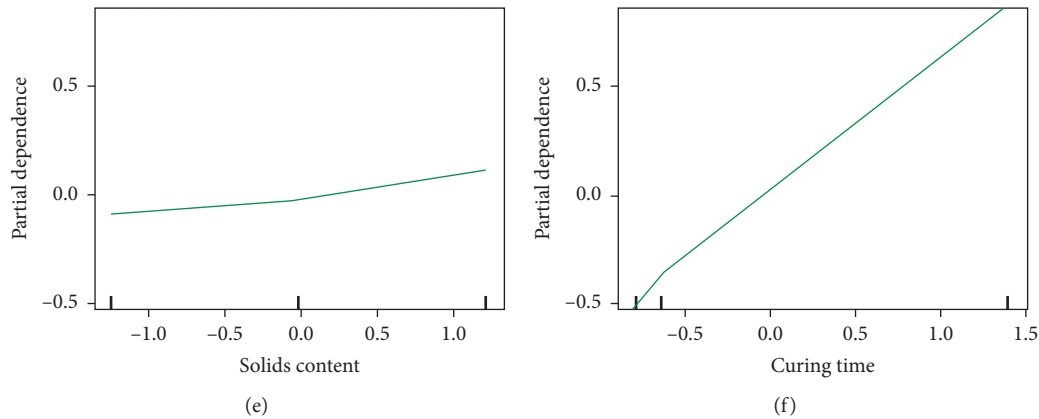
FIGURE 16: Partial dependence plots and IS values for each input variable. (a) IS = 0.085. (b) IS = 0.011. (c) IS = 0.257. (d) IS = 0.045. (e) IS = 0.198. (f) IS = 0.404.

time was found to be 0.404, followed by 0.257 of the CFA proportion and 0.198 of the solids content. The IS values of the remaining three input variables were lower than 0.1, which were 0.085 of the OPC proportion, 0.045 of the silt proportion, and 0.011 of the CG proportion. Generally speaking, the IS results agreed well with the partial dependence plots.

5. Conclusions

To facilitate the application of CPB in coal mines, the strength development of the silt-based CPB with different cementitious materials was investigated by lab experiments and DNN prediction. Based on the above results, the following conclusions can be drawn:

(1) The solid content, cement content (cement/sand ratio), and curing time present positive correlation with UCS. The CG can be used as a kind of OPC substitute, while adding CFA increases the UCS of CPB significantly.

(2) The convergence tests indicate the optimum training set size was 80% and the number of runs needs to be larger than 36 for the converged results.

(3) GA was efficient in the DNN architecture tuning with the maximum correlation coefficient being increased from 0.977 at the first iteration to 0.989 at the 17th iteration. The optimum DNN architecture was characterized by 95, 72, 158, 44, and 169 within the first to fifth hidden layers.

(4) DNN was robust in predicting the UCS of CPB. The average correlation coefficient was 0.97 on the training set and was 0.99 on the testing set.

(5) Partial dependence plots indicate an overall positive correlation between the OPC proportion, the CFA proportion, the solids content, and the curing time with the UCS. In contrast, the silt proportion was negatively correlated with the UCS and CG proportion had little correlation with the UCS.

(6) The curing time was the most significant input variable for the UCS with an IS value of 0.404,

followed by 0.257 of the CFA proportion and 0.198 of the solids content. The CG proportion was the least significant input variable for the UCS with an IS value of 0.011.

Data Availability

The data used to support the findings of this study are included within the article.

Conflicts of Interest

The authors declare that there are no conflicts of interest.

Authors' Contributions

C. X. and Q. C. conceived the project; C. X., Q. C, D. W., and Y. W. carried out experimental tests; X. W., C. X., and W. W. analyzed the experimental data. All authors discussed the results and commented on the manuscript.

Acknowledgments

References

[1] C.-C. Qi, "Big data management in the mining industry," *International Journal of Minerals, Metallurgy and Materials*, vol. 27, no. 2, pp. 131–139, 2020.

[2] G. Hilson, "Pollution prevention and cleaner production in the mining industry: an analysis of current issues," *Journal of Cleaner Production*, vol. 8, no. 2, pp. 119–126, 2000.

[3] W. Zhou, X. Shi, X. Lu, C. Qi, B. Luan, and F. Liu, "The mechanical and microstructural properties of refuse mudstone-GGBS-red mud based geopolymer composites made with sand," *Construction and Building Materials*, vol. 253, Article ID 119193, 2020.

[4] Q. Chen, Q. Zhang, C. Qi, A. Fourie, and C. Xiao, "Recycling phosphogypsum and construction demolition waste for cemented paste backfill and its environmental impact," *Journal of Cleaner Production*, vol. 186, pp. 418–429, 2018.

[5] Q. Chen, Q. Zhang, A. Fourie, and C. Xin, "Utilization of phosphogypsum and phosphate tailings for cemented paste backfill," *Journal of Environmental Management*, vol. 201, pp. 19–27, 2017.

[6] X. Chen, X. Z. Shi, S. Zhang et al., "Fiber-Reinforced cemented paste backfill: the effect of fiber on strength properties and estimation of strength using nonlinear models," *Materials*, vol. 13, 2020.

[7] C. Qi and A. Fourie, "Cemented paste backfill for mineral tailings management: review and future perspectives," *Minerals Engineering*, vol. 144, Article ID 106025, 2019.

[8] Z. Su, Q. S. Chen, Q. L. Zhang, and D. M. Zhang, "Recycling lead-zinc tailings for cemented paste backfill and stabilisation of excessive metal," *Minerals*, vol. 9, no. 11, 2019.

[9] A. W. L. Dudeney, B. K. C. Chan, S. Bouzalakos, and J. L. Huisman, "Management of waste and wastewater from mineral industry processes, especially leaching of sulphide resources: state of the art," *International Journal of Mining, Reclamation and Environment*, vol. 27, no. 1, pp. 2–37, 2013.

[10] S. Cao, W. Song, and E. Yilmaz, "Influence of structural factors on uniaxial compressive strength of cemented tailings backfill," *Construction and Building Materials*, vol. 174, pp. 190–201, 2018.

[11] X. Deng, B. Klein, L. Tong, and B. De Wit, "Experimental study on the rheological behavior of ultra-fine cemented backfill," *Construction and Building Materials*, vol. 158, pp. 985–994, 2018.

[12] H. Lu, C. Qi, C. Li, D. Gan, Y. Du, and S. Li, "A light barricade for tailings recycling as cemented paste backfill," *Journal of Cleaner Production*, vol. 247, Article ID 119388, 2020.

[13] L. Liu, Z. Fang, M. Wang, C. Qi, Y. Zhao, and C. Huan, "Experimental and numerical study on rheological properties of ice-containing cement paste backfill slurry," *Powder Technology*, vol. 370, pp. 206–214, 2020.

[14] C. Qi and A. Fourie, "Numerical investigation of the stress distribution in backfilled stopes considering creep behaviour of rock mass," *Rock Mechanics and Rock Engineering*, vol. 52, no. 9, pp. 3353–3371, 2019.

[15] D. Ouattara, T. Belem, M. Mbonimpa, and A. Yahia, "Effect of superplasticizers on the consistency and unconfined compressive strength of cemented paste backfills," *Construction and Building Materials*, vol. 181, pp. 59–72, 2018.

[16] T. Yılmaz, B. Ercikdi, and H. Deveci, "Utilisation of construction and demolition waste as cemented paste backfill material for underground mine openings," *Journal of Environmental Management*, vol. 222, pp. 250–259, 2018.

[17] F. Cihangir, B. Ercikdi, A. Kesimal, S. Ocak, and Y. Akyol, "Effect of sodium-silicate activated slag at different silicate modulus on the strength and microstructural properties of full and coarse sulphidic tailings paste backfill," *Construction and Building Materials*, vol. 185, pp. 555–566, 2018.

[18] C. Qi, A. Fourie, and Q. Chen, "Neural network and particle swarm optimization for predicting the unconfined compressive strength of cemented paste backfill," *Construction and Building Materials*, vol. 159, pp. 473–478, 2018.

[19] C. Qi, A. Fourie, Q. Chen, and Q. Zhang, "A strength prediction model using artificial intelligence for recycling waste tailings as cemented paste backfill," *Journal of Cleaner Production*, vol. 183, pp. 566–578, 2018.

[20] C. Qi, Q. Chen, A. Fourie, and Q. Zhang, "An intelligent modelling framework for mechanical properties of cemented paste backfill," *Minerals Engineering*, vol. 123, pp. 16–27, 2018.

[21] J. Qiu, Z. Guo, L. Li, S. Zhang, Y. Zhao, and Z. Ma, "A hybrid artificial intelligence model for predicting the strength of foam-cemented paste backfill," *IEEE Access*, vol. 8, pp. 84569–84583, 2020.

[22] E. Li, J. Zhou, X. Shi et al., "Developing a hybrid model of salp swarm algorithm-based support vector machine to predict the strength of fiber-reinforced cemented paste backfill," *Engineering with Computers*, vol. 2020, 2020.

[23] Y. Sun, G. Li, J. Zhang, J. Sun, and J. Xu, "Development of an ensemble intelligent model for assessing the strength of cemented paste backfill," *Advances in Civil Engineering*, vol. 2020, Article ID 1643529, 6 pages, 2020.

[24] Y. Huang, J. Zhang, Q. Zhang, and S. Nie, "Backfilling technology of substituting waste and fly ash for coal underground in China coal mining area," *Environmental Engineering and Management Journal*, vol. 10, no. 6, pp. 769–775, 2011.

[25] J. Zhang, Q. Zhang, Q. Sun, R. Gao, D. Germain, and S. Abro, "Surface subsidence control theory and application to backfill coal mining technology," *Environmental Earth Sciences*, vol. 74, no. 2, pp. 1439–1448, 2015.

[26] D. Wang, Q. Zhang, Q. Chen, C. Qi, Y. Feng, and C. Xiao, "Temperature variation characteristics in flocculation settlement of tailings and its mechanism," *International Journal of Minerals, Metallurgy and Materials*, vol. 21, pp. 1–11, 2020.

[27] Y. He, Q. S. Chen, C. C. Qi, Q. L. Zhang, and C. C. Xiao, "Lithium slag and fly ash-based binder for cemented fine tailings backfill," *Journal of Environmental Management*, vol. 248, Article ID 109282, 2019.

[28] Q.-S. Chen, Q.-L. Zhang, A. Fourie, X. Chen, and C.-C. Qi, "Experimental investigation on the strength characteristics of cement paste backfill in a similar stope model and its mechanism," *Construction and Building Materials*, vol. 154, pp. 34–43, 2017.

[29] M. Kuhn and K. Johnson, *Applied Predictive Modeling*, Springer-Verlag, New York, NY, USA, 2013.

[30] J. Tian, C. Qi, Y. Sun, Z. M. Yaseen, and B. T. Pham, "Permeability prediction of porous media using a combination of computational fluid dynamics and hybrid machine learning methods," *Engineering with Computers*, vol. 2020, 2020.

[31] F. Pedregosa, G. Varoquaux, A. Gramfort et al., "Scikit-learn: machine learning in Python," *Journal of Machine Learning Research*, vol. 12, pp. 2825–2830, 2011.

[32] J. Grefenstette, "Optimization of control parameters for genetic algorithms," *IEEE Transactions on Systems, Man, and Cybernetics*, vol. 16, no. 1, pp. 122–128, 1986.

[33] Y. K. Liu, Q. L. Zhang, Q. S. Chen, C. C. Qi, Z. Su, and Z. D. Huang, "Utilisation of water-washing pre-treated phosphogypsum for cemented paste backfill," *Minerals*, vol. 9, no. 3, 175 pages, 2019.

[34] B. Ercikdi, T. Yılmaz, and G. Külekci, "Strength and ultrasonic properties of cemented paste backfill," *Ultrasonics*, vol. 54, no. 1, pp. 195–204, 2014.

[35] T. Yılmaz and B. Ercikdi, "Predicting the uniaxial compressive strength of cemented paste backfill from ultrasonic pulse velocity test," *Nondestructive Testing and Evaluation*, vol. 31, no. 3, pp. 247–266, 2015.

[36] X. Chen, X. Z. Shi, J. Zhou, Z. Yu, and P. S. Huang, "Determination of mechanical, flowability, and microstructural properties of cemented tailings backfill containing rice straw," *Construction and Building Materials*, vol. 246, Article ID 118520, 2020.

[37] Y. Feng, Q. S. Chen, Y. L. Zhou et al., "Modification of glass structure via CaO addition in granulated copper slag to enhance its pozzolanic activity," *Construction and Building Materials*, vol. 240, Article ID 117970, 2020.

Research Article

Study on Stress Distribution Law of High-Efficiency Paste Backfilling Working Face with Solid Waste in Thick Coal Seam

Meng Zhang [1] **and Dan Fang** [2]

^{1}School of Civil & Architecture Engineering, Xi'an Technological University, Xi'an 710021, China
^{2}School of Art and Media, Xi'an Technological University, Xi'an 710021, China

Correspondence should be addressed to Dan Fang; fangdan992@gmail.com

The high-efficiency paste backfilling mining technology of solid waste in thick coal seam above 6 m is a complex system engineering, which involves mining, backfilling, supporting, subsidence, safety, and other aspects, so it is of great strategic significance to study the technology. In this paper, on the basis of comprehensive research methods such as laboratory experiments, theoretical analysis, computer programming, and other comprehensive research methods, aiming at the problems of low production capacity and high paste backfilling cost, taking the mining of No. 3 Coal Seam under buildings in Lu'an area as the research object, the stress distribution law of high-efficiency paste backfilling working face with solid waste in more than 6-meter-thick coal seam was carried out. The main achievements are as follows: On the basis of the theoretical establishment of the program method for the instability discriminant analysis of roof rock beam failure with the change of backfilling body unit strength with time, a numerical calculation model considering the change process of backfilling body strength is established. The stress distribution analysis of the E1302 working face before and during the mining process plays a guiding role in the actual production of the whole working face and roadway. The research results support the sustainable development of coal mining enterprises from technology, which has great economic, social, and environmental benefits, and can promote the industrialization of green mining high-tech in Shanxi Province and even the whole country and can promote the green mining technology progress of paste backfilling in coal mines in China, which is of great significance to the sustainable development of mining production and environmental construction.

1. Introduction

BP world energy statistical yearbook (2018) [1] points out that, in 2017, the proportion of coal in China's energy structure dropped from 73.6% a decade ago and 62.0% in 2016 to 60.4% in 2017. However, coal is still the main energy source. However, for a long time, China's coal resource mining has ignored the cost of resources and the environment, resulting in a low recovery rate of coal resources, high waste emissions, and serious environmental damage [2–4]. The key to the sustainable development of coal mining is to solve the contradiction between coal mining and environmental protection in the world [5–13]. Solid waste paste backfilling mining is an important part of green coal mining advocated by Academician Qian et al. [14–19], which can effectively solve the serious waste of resources, low

recovery rate, and ecological and environmental damage caused by high-intensity mining [20, 21].

By the end of 2014, Gaohe coal mine had 271 million tons of coal reserves under buildings. The cost of roadway excavation, waste discharge, mine water treatment, and resource tax can be saved by backfilling mining technology, which is about 50 yuan/T. If the increased cost of backfilling is 80 yuan/T, the comprehensive increase of coal cost per ton is only 30 yuan/T. The backfilling output only accounts for 18% of the total output of the mine, resulting in an increase of only 5.4 yuan/T in the cost per ton of coal, but it will extend the service life of the mine by more than 25 years.

At present, some coal mines in China have carried out the industrial practice of high mining height and high-efficiency paste backfilling by canceling isolation class and solidification class, but the numerical simulation research on

the stress distribution law of paste backfilling face has not kept pace with the pace of production practice. For the high-efficiency paste filling of solid waste, it is necessary to study the rock control technology under the condition of two classes and one cycle of "mining filling" and even backfilling while mining, that is, to study the stress distribution law of high-efficiency paste backfilling working face in more than 6 m thick coal seam, so as to meet the needs of backfilling mining in high-yield and high-efficiency mines.

2. Project Overview

2.1. Model Building. In this paper, FLAC3D software [22, 23] is used to establish a three-dimensional numerical simulation model based on the geological conditions of Gaohe mine and the E1302 backfilling working face. The upper boundary of the model is the position of the main key layer calculated by theory, and the lower boundary is 50 m below the coal seam floor. The upper and lower height is 175 m, and the length and width of the model are 700 m ∗ 500 m. Considering that abnormal pressure may occur in the working face when the working face advances to half of its length, 230 m of goaf is reserved in the south of E1302 backfilling working face, the coal pillar between the goaf and the cut hole in E1302 working face is 50 m, the advancing length of the working face is 390 m, and the distance between the stopping line and the boundary is 80 m. Considering the boundary effect and the influence of goaf, the E1302 ventilation roadway is 100 m away from the boundary, and the coal pillar between the E1302 ventilation roadway and E1302 intake roadway is 20 m. The length of the E1302 backfilling working face is 230 m, and the distance between the E1302 auxiliary transport roadway and E1302 transport roadway is 30 m, as shown in Figure 1.

2.2. Mechanical Parameters of Coal (Rock). The physical properties of surrounding rock in the model refer to the histogram of the roof and floor strata and the test report of coal (rock) mechanical properties of E1302 working face in Gaohe coal mine [2], and some mechanical parameters of coal (rock) are shown in Table 1.

Because the measured rock mechanical parameters are measured in a two-dimensional state, and the rock mass is in a three-dimensional state in the actual simulation, the mechanical parameters in the simulation need to be modified by inversion of the measured data and finally used as the simulation parameters.

2.3. Boundary Conditions and Constitutive Model. The displacement boundary conditions are selected for the front, back, left, right, and bottom of the model, and the stress boundary conditions are selected for the top of the model. The horizontal displacements of the left and right and the front and back boundaries are fixed, and the horizontal and vertical displacements of the lower boundary are fixed. In the upper part of the model, the dead weight of overlying strata is applied according to the uniform load. In this simulation, the buried depth of the coal body is 400 m, the stress

boundary conditions are applied to the upper boundary of the unit body, and the original rock stress is applied to the model. In this simulation, the Moore Coulomb plastic model is adopted, and the initial equilibrium of the model is shown in Figure 2.

2.4. Simulation Steps. The actual construction process of the mine is as follows: first excavate E1302 ventilation roadway, E1302 intake roadway, and E1302 auxiliary transport roadway to serve the extraction of E1302 working face (i.e., the gob part of E1302 working face); after it is stable, excavate E1302 transport roadway (roadway name in the current figure) to serve E1303 working face (the current E1303 working face goaf); after it is stable, the cut hole is excavated to serve E1302 backfilling working face; the interval between backfilling and mining is a cycle mode of two mining and one backfilling; the simulation steps are carried out according to the actual construction steps.

3. Numerical Simulation Optimization

3.1. Stress Distribution before Mining in E1302 Paste Backfilling Working Face. Because E1302 backfilling working has been affected by the mining during the previous working face before mining, and the goaf on both sides of the working face is asymmetric, which leads to the different-stress environment in different positions of the roadway before mining. Therefore, it is necessary to analyze and study the stress in different positions of the roadway. This section analyzes and studies the vertical stress of the cut hole, E1302 auxiliary transport roadway, and E1302 intake roadway before mining, and the research results are used to guide the production practice of working face.

3.1.1. Stress Distribution of Cut Hole before Mining in E1302 Paste Backfilling Working Face. Due to the different-stress environment on both sides of the E1302 backfilling and mining working face, the vertical stress distribution of different positions of the cut hole is shown in Figure 3.

The following can be seen from Figure 4:

(1) In the vicinity of the cut hole, the maximum vertical stress in the vertical direction of the auxiliary roadway side is mainly concentrated near the coal pillar side. With the increase of the distance from the cut hole, the maximum vertical stress gradually transfers to the working face side of the roadway, and the vertical stress of the coal body at the working face side is generally greater than that of the coal pillar side (excluding the plastic zone near the cut hole)

(2) It can be seen from the cross section of the auxiliary haulage roadway within the scope of 0 m~20 m that the stress concentration coefficient of the coal body in the working face side of the roadway increases first and then decreases; the maximum stress concentration coefficient near the side of the roadway 5 m away from the cut hole can reach about 2.51, the maximum stress concentration
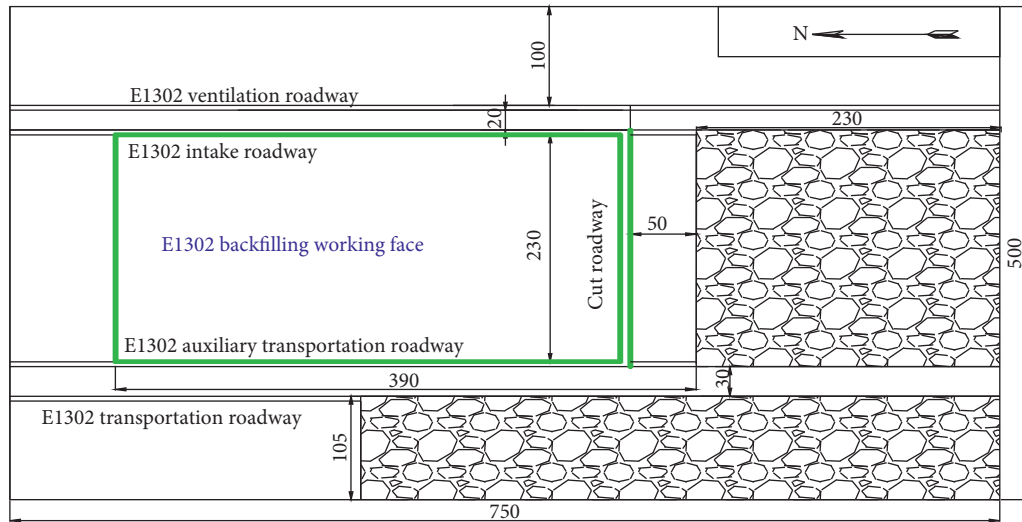
FIGURE 1: E1302 working face mining plane schematic.

TABLE 1: Coal (rock) mechanical parameters.

Layer		Parameters				
		Tensile strength (MPa)	Elastic modulus (GPa)	Poisson's ratio	Cohesion (MPa)	Internal friction angle (°)
Upper strata	Medium grained sandstone	4.32	32.12	0.23	2.72	25
Main roof	Siltstone	3.56	21.16	0.23	2.02	26
Direct roof	Sandy mudstone	2.18	15.73	0.25	1.19	31
Coal seam	Coal	1.35	1.73	0.29	0.53	29
Immediate floor	Sandy mudstone	1.65	13.73	0.24	1.09	30
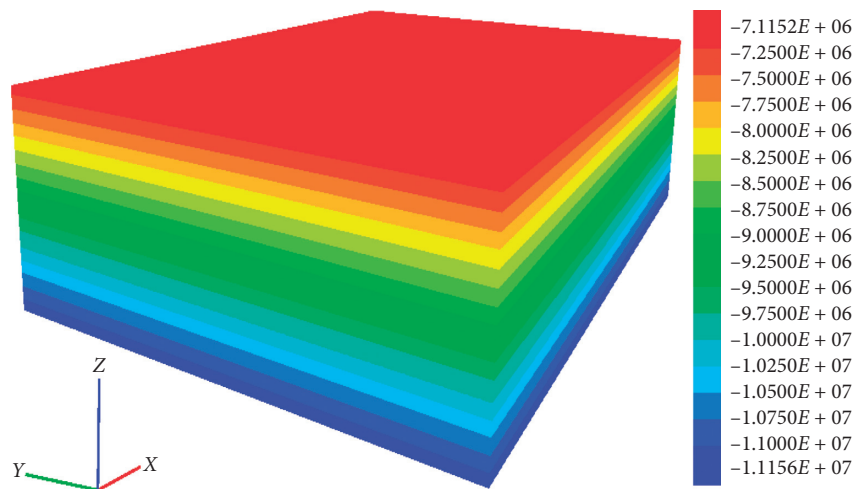
FIGURE 2: Model initial balance diagram.

coefficient near the roadway side 10 m away from the cut hole can reach about 2.53, and the maximum stress concentration coefficient near the roadway side 15 m away from the cut hole can reach about 2.4. It can be seen that the part affected by E1303 and E1302 working face goaf is mainly concentrated in the range of 20 me ahead of the roadway, and the maximum value of stress concentration coefficient near the roadway side will appear between 5 m and 15 m away from the cut hole
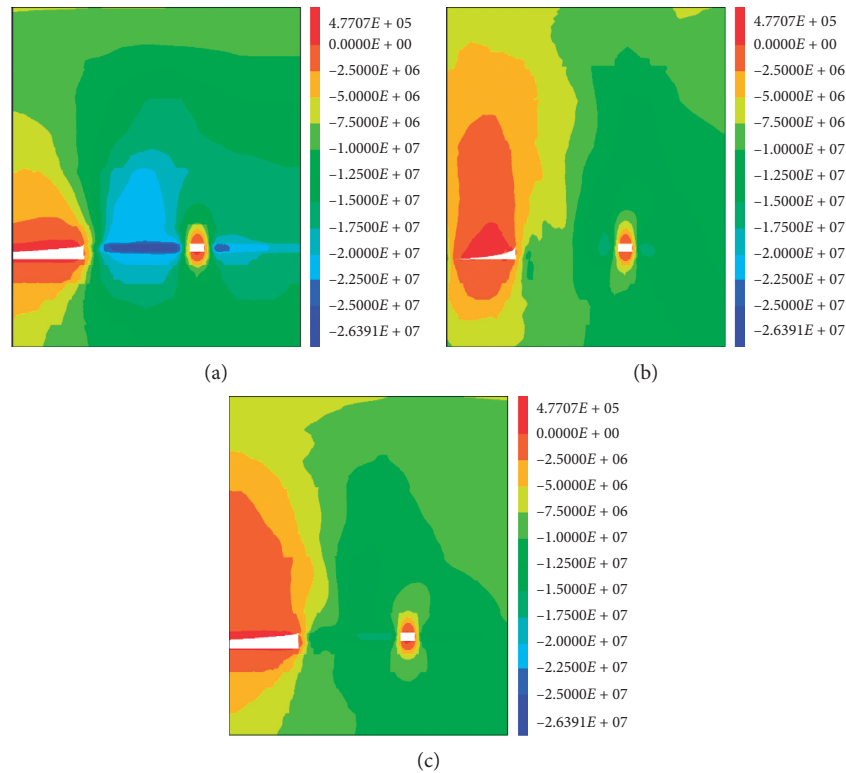
Figure 3: Vertical stress nephogram of cut hole.

(3) Mainly affected by the goaf of E1303 working face, the stress distribution of auxiliary transportation roadway is shown in Figure 5

In Figure 3, the roadway on the right side is the cut hole, and the left side is the E1302 goaf; Figure 3(a) refers to the section of the cut hole at 5 m away from the E1302 auxiliary transport roadway; Figure 3(b) refers to the section of the cut hole at 115 m away from the E1302 auxiliary transport roadway (the middle of the cut hole); Figure 3(c) refers to the section of the cut hole at 5 m away from the E1302 intake roadway.

The following can be seen from Figure 3:

(1) In the part near the goaf side of the E1303 working face, under the roof pressure of overlying strata on the goaf side of the E1303 working face and E1302 working face, the deformation of the cut hole is large. The maximum stress concentration factor is about 2.6, which mainly concentrates on the coal pillar between E1302 backfilling working face and goaf, as well as the upper strata of goaf

(2) With the distance from the goaf farther and farther, the influence of the goaf of E1303 working face goaf is less and less, and it is mainly affected by the goaf of E1302 working face

3.1.2. Stress Distribution of the Auxiliary Transport Roadway before Mining in E1302 Paste Backfilling Working Face. As the eastern section of E1302 auxiliary transport roadway is the goaf of E1303 working face and the south of E1302

working face, considering that it will be affected by the goaf, the E1302 auxiliary transportation roadway is divided into three parts: (1) the part affected by the goaf of E1303 working face and E1302 working face, (2) the part mainly affected by the goaf of E1303 working face, and (3) the part less affected by the goaf of E1303 working face. This section mainly analyzes the first two parts.

(1) Under the comprehensive influence of E1302 and E1303 working face goaf, the stress distribution of auxiliary transportation roadway is shown in Figure 4; the eight pictures in Figure 4 are the profile stress nephogram in the vertical direction of roadway every 5 m within the scope of 0 m~35 m from the cut hole, the right roadway in Figure 4 is E1302 auxiliary transport roadway, and the left is E1303 working face goaf

Figure 5 shows the profile stress nephogram in the vertical direction of the auxiliary haulage roadway at intervals of 10 m from 160 m to 240 m from the cut hole. Among them, before 200 m, the left side of E1302 auxiliary transportation is the goaf of E1303 working face; after 200 m, the left side of E1302 auxiliary transport roadway is E1302 transport roadway, and 200 m is the end of E1303 working face goaf.

The following can be seen from Figure 5:

(1) In the range of 160 m~200 m away from the cut hole, the vertical stress in the coal body side of the transport roadway working face is relatively concentrated compared with the coal pillar side
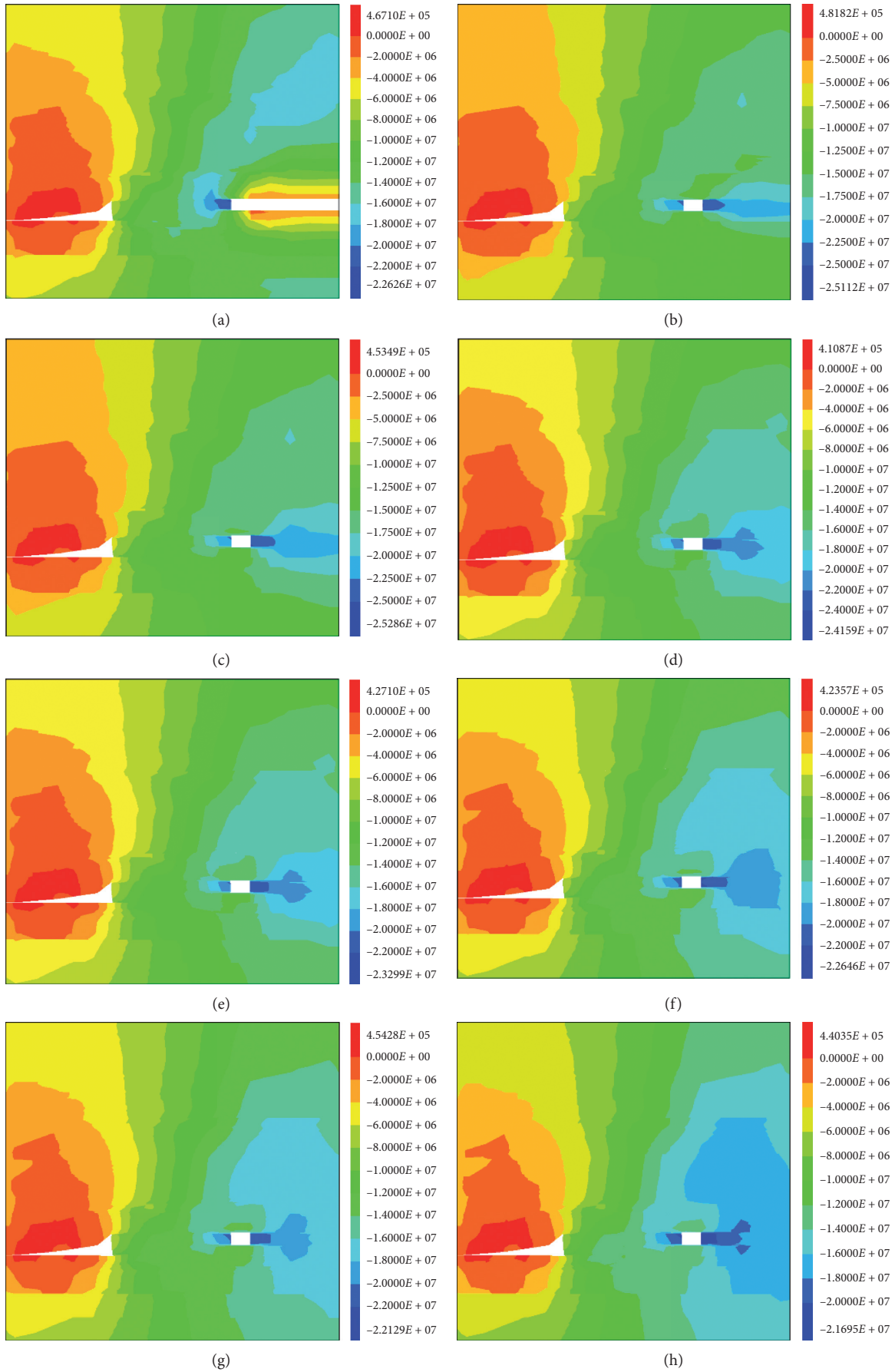
FIGURE 4: Vertical stress nephogram of auxiliary transport roadway: (a) 0 m, (b) 5 m, (c) 10 m, (d) 15 m, (e) 20 m, (f) 25 m, (g) 30 m, and (h) 35 m.
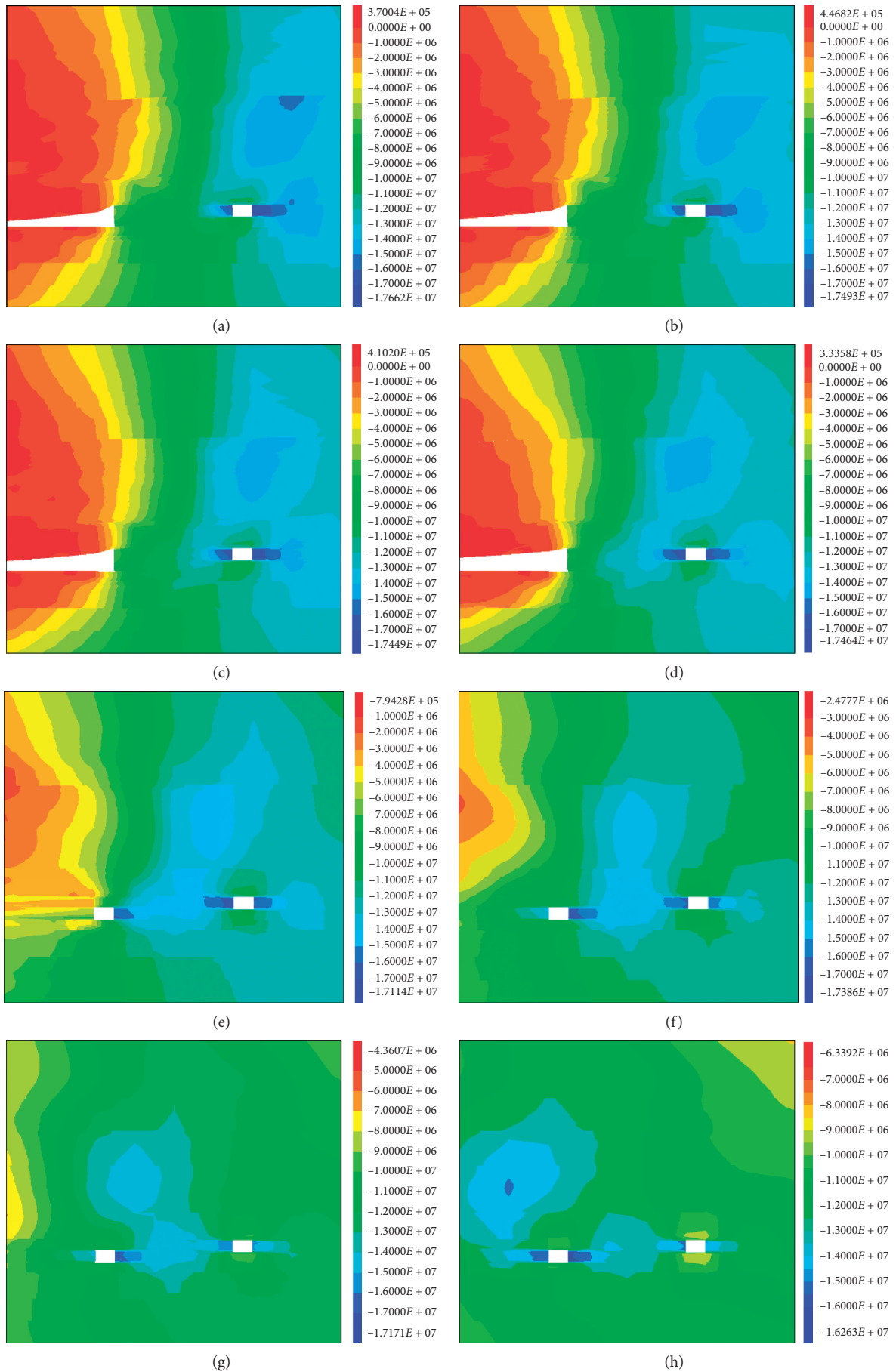
FIGURE 5: Vertical stress nephogram of auxiliary transport roadway: (a) 160 m. (b) 170 m, (c) 180 m, (d) 190 m, (e) 200 m, (f) 210 m, (g) 220 m, and (h) 230 m.

(2) When the distance from the cut hole is more than 200 m, affected by the goaf of E1303 working face, the stress in both sides of the E1302 transport roadway is relatively concentrated. With the distance from the cut hole getting farther and farther, the stress on both sides of the roadway gradually decreases and finally tends to be stable

3.2. Stress Distribution in the Mining Process of E1302 Paste Backfilling Working Face. The previous section mainly analyzes the stress distribution of the E1302 backfilling working face before mining; this section analyzes the stress distribution of working face and overburdens rock during the mining process of the E1302 backfilling working face. This paper mainly analyzes the stress distribution of overburden rock before cutting the first cutting coal, before cutting the second cutting coal, before backfilling and after backfilling, and before cutting the next cutting coal in four stages (0 m from the cut hole, 100 m from the cut hole, 300 m from the cut hole, and after the completion of backfilling and mining).

3.2.1. Stress Distribution of E1302 Working Face in Initial Mining and Backfilling Stage. The initial mining stage of E1302 backfilling working face refers to the fact that after the completion of the excavation, the support equipment should be installed and the working face is about to be ready for mining; in this stage, the vertical stress distribution state of the working face in these four stages is analyzed before the working face advances the first knife, before the working face advances the second knife, before backfilling, and before the next coal cutting after backfilling, as shown in Figure 6 (Figure 6(a) refers to the top-down view, slicing along the roof of the working face, and Figure 6(b) refers to the cross section in the direction of I–I, which is made at 115 m away from E1302 auxiliary transport roadway. The meanings of (a) and (b) in Figures 7–9 are consistent with this).

The following can be seen from Figure 6:

(1) It can be seen from the top view (a) that the main factors affecting the E1302 backfilling working face are the coal pillar behind the working face and the coal pillar between the backfilling working face and E1303 working face. The stress concentration area mainly occurs in the coal pillar near the side of the E1302 auxiliary transport roadway between the goaf of the E1302 working face and the rear of the cut hole. The maximum stress concentration coefficient can reach 2.57 under the joint influence of the two goafs. In the four states of backfilling and mining cycle, the stress concentration in the process of coal mining has a slightly decreasing trend, and the stress concentration has a rising trend in a period of time after mining and in the backfilling process, which is mainly affected by the coal pillar in the initial mining stage

(2) It can be seen from the main view (b) in the figure that the stress in the middle of the working face is

mainly concentrated in front of and behind the working face, and the stress concentration coefficient in the reserved coal pillar behind the working face is slightly greater than that in the front of the working face, which is mainly affected by the goaf of E1302 working face. In the four states in a cycle of backfilling and mining, the stress concentration changes little in the process of coal mining, and the stress tends to increase after mining and backfilling

(3) Comprehensive analysis shows that under the joint influence of E1302 and E1303 working faces and goaf, the stress of the coal pillar in this part is relatively concentrated, and the roadway left in this section needs to be strengthened support (it should be used when mining layered working face)

3.2.2. Stress Distribution of E1302 Backfilling Working Face 100 m away from the Cut Hole. In the initial mining stage, the working face is greatly affected by the goaf of E1302 working face in the south. This section mainly studies the stress distribution of the E1302 working face 100 m away from the cut hole. At this time, the E1302 working face is located in the middle of the E1302 cut hole and the E1303 working face's final mining position. A complete filling mining cycle is taken at 100 points away from the cutting hole. In this stage, the vertical stress distribution state of the working face in these four stages is analyzed before the working face advances the first knife, before the working face advances the second knife, before backfilling, and before the next coal cutting after backfilling, as shown in Figure 7.

The following can be seen from Figure 7:

(1) It can be seen from the top view (a) in the figure that the stress concentration area is still the coal pillar section affected by the goafs on both sides, and it will also be affected by mining. The stress concentration coefficient is about 2 within the range of about 50 m in front of the working face (close to the side of E1303 goaf). The direction stress from E1302 auxiliary transport roadway to E1302 intake roadway gradually decreases, and the stress of backfilling body behind the working face increases gradually from the cutting hole to the working face. In this stage, the vertical stress distribution changes little in a cycle, the stress concentration factor near the working face is about 2, and the maximum stress concentration factor in the stress concentration area affected by multiple stresses can reach 3

(2) From the main view (b), it can be seen that the stress in the coal body in front of the middle of the working face is relatively concentrated, which increases first and then decreases gradually along the advancing direction of the working face. The maximum stress concentration coefficient can reach 1.92 within the range of 10~15 from the working face. The stress in the backfilling body behind the working face is smaller than that in the coal body in front of the working face, and the stress increases gradually from

FIGURE 6: Nephogram of stress distribution in the initial mining stage of E1302 working face under a backfilling mining cycle. (a) Vertical stress distribution before cutting the first coal. (b) Vertical stress distribution before cutting the second coal. (c) Vertical stress distribution before backfilling. (d) Vertical stress distribution before the next coal cutting after backfilling.

(a)

(b)

(c)
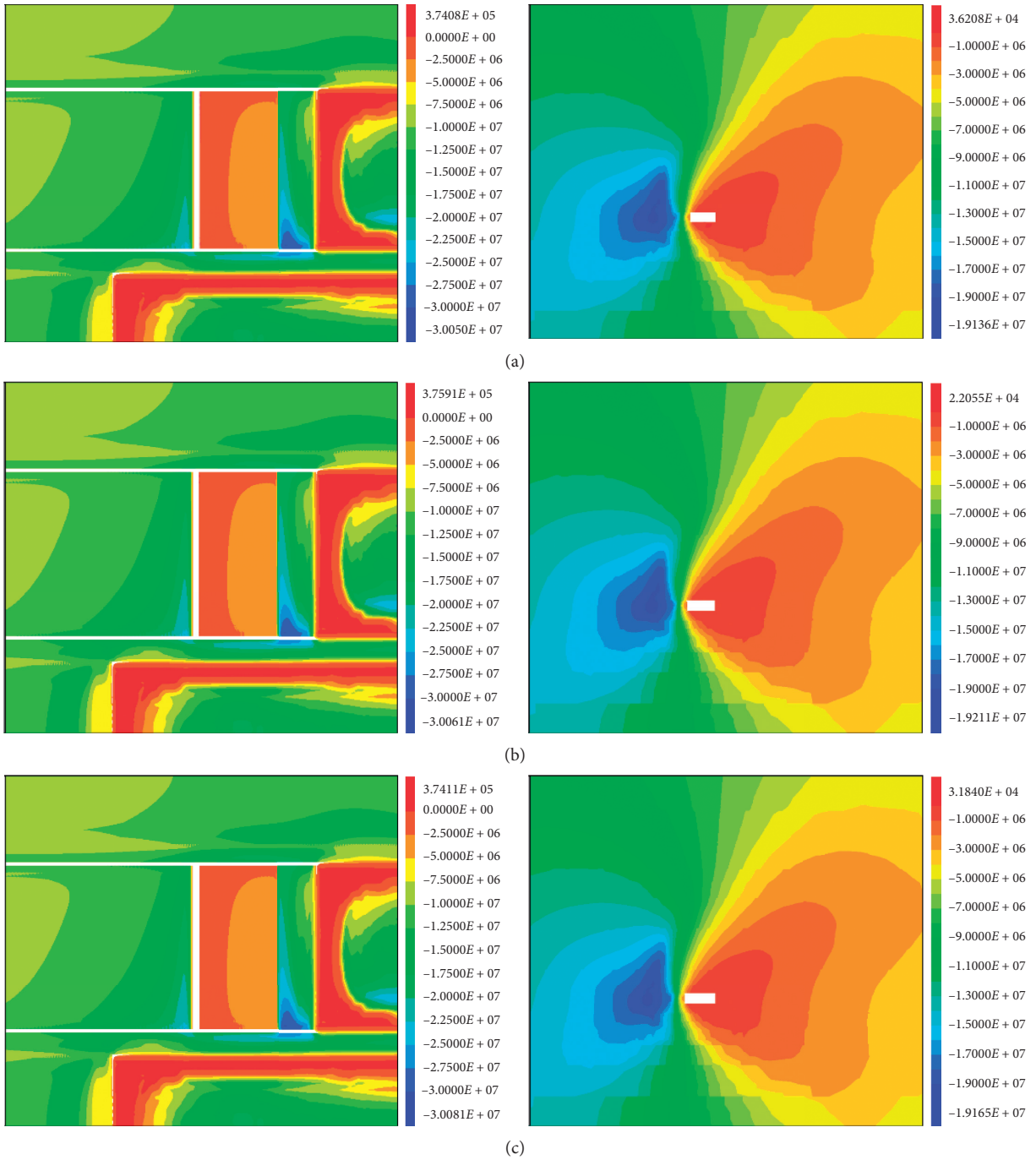
Figure 7: Continued.

(d)
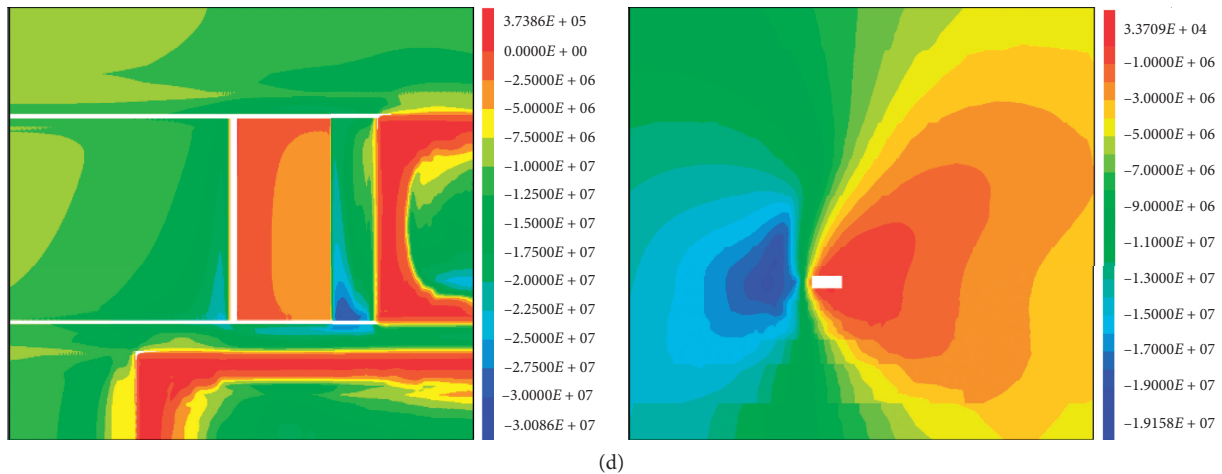
FIGURE 7: Nephogram of stress distribution 100 m away from the cut hole in E1302 working face under a backfilling mining cycle. (a) Vertical stress distribution before cutting the first coal. (b) Vertical stress distribution before cutting the second coal. (c) Vertical stress distribution before backfilling. (d) Vertical stress distribution before the next coal cutting after backfilling.

the working face to the cut hole; the vertical stress distribution changes little in a cycle process

(3) Comprehensive analysis shows that the stress change of the working face is small in a backfilling cycle when the working face is pushed to 100 m away from the cut hole. Therefore, the pressure near the working face is less affected by the mining and backfilling cycle

3.2.3. Stress Distribution of E1302 Backfilling Working Face 100 m away from the Cut Hole.

This section mainly studies the stress distribution of the working face 300 away from the cut hole and takes a full mining and backfilling cycle to study its stress distribution, so as to analyze the stress distribution law of the working face at this stage. At this time, the east, west, and north sides of the working face (in front of the working face) are solid coal, and behind the working face is the backfilling body, as shown in Figure 8.

The following can be seen from Figure 8:

(1) It can be seen from the top view (a) that the stress concentration areas are mainly distributed in the west side of E1302 auxiliary transport roadway (coal pillar side), the east side of E1302 intake roadway, and the coal pillar between E1302 goaf and E1302 cut hole. Among them, the stress near the coal pillar between E1302 goaf and E1302 cut hole is the most concentrated, especially in the side near E1303 goaf, the maximum stress concentration coefficient can reach about 3.1, the second is the coal pillar on the west side of E1302 auxiliary transport roadway, which is affected by mining on both sides at the same time, and E1302 auxiliary transport roadway needs to be preserved to serve the lower layer mining, which makes the stress distribution in the roadway side pillar more concentrated, and the stress concentration coefficient is about 2.25. The

influence of goaf on the coal pillar in the east of the E1302 intake roadway is small, so the stress concentration area is small. According to the stress distribution analysis in the top view, the stress change of the working face is very small in the backfilling and mining cycle. Within the range of 40 m in front of the working face, the stress concentration coefficient is between 1.25 and 2.0. The backfilling body in the west behind the working face is affected by the goaf, and the stress is greater than that of the backfilling body in the east

(2) According to the main view (b) in Figure 8, the coal mass in front of the middle part of the working face is still a stress concentration area, but the stress peak area changes and moves to the top of the working face roof

3.2.4. Stress Distribution of E1302 Working Face after the Backfilling and Mining.

This section mainly analyzes the vertical stress distribution of the backfilling area and surrounding stress after the completion of backfilling and mining, as shown in Figure 9.

The following can be seen from Figure 9:

(1) It can be seen from the top view (a) that after the completion of mining and backfilling, the backfilling body is affected by the goaf, and the stress concentration factor of the two areas is relatively concentrated, especially the coal pillar in the south of E1302 and the north of E1302 goaf, and the maximum stress concentration coefficient can reach 3.14. In the paste backfilling area, the stress increases gradually from the stoppage line side of the working face to the E1302 cut hole. In the area affected by E1303 goaf, the stress in the west area is higher than that in the east area. In the area less affected by E1303 goaf, the stress on both sides of the paste backfilling area is basically symmetrical

(a)
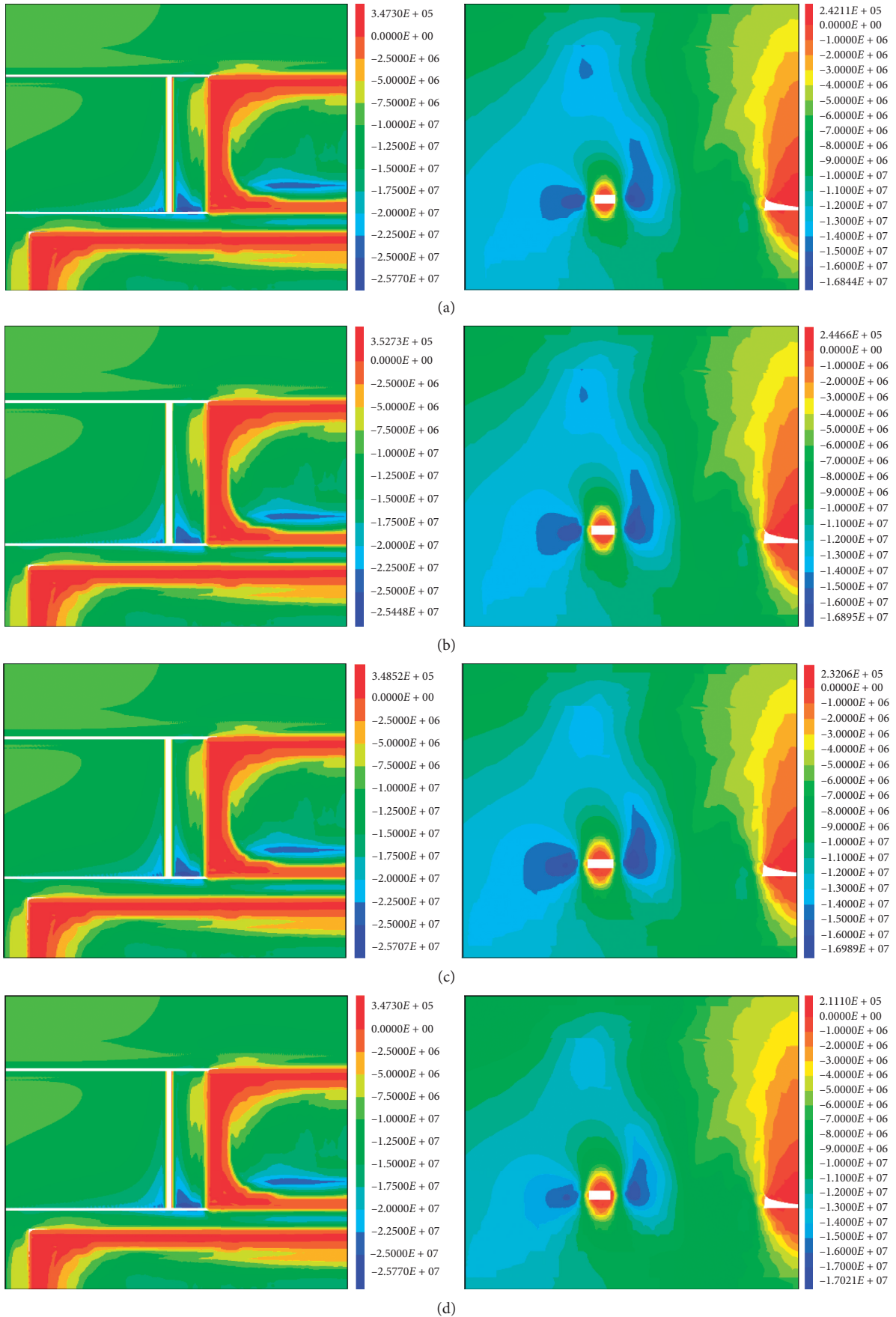

(b)

(c)
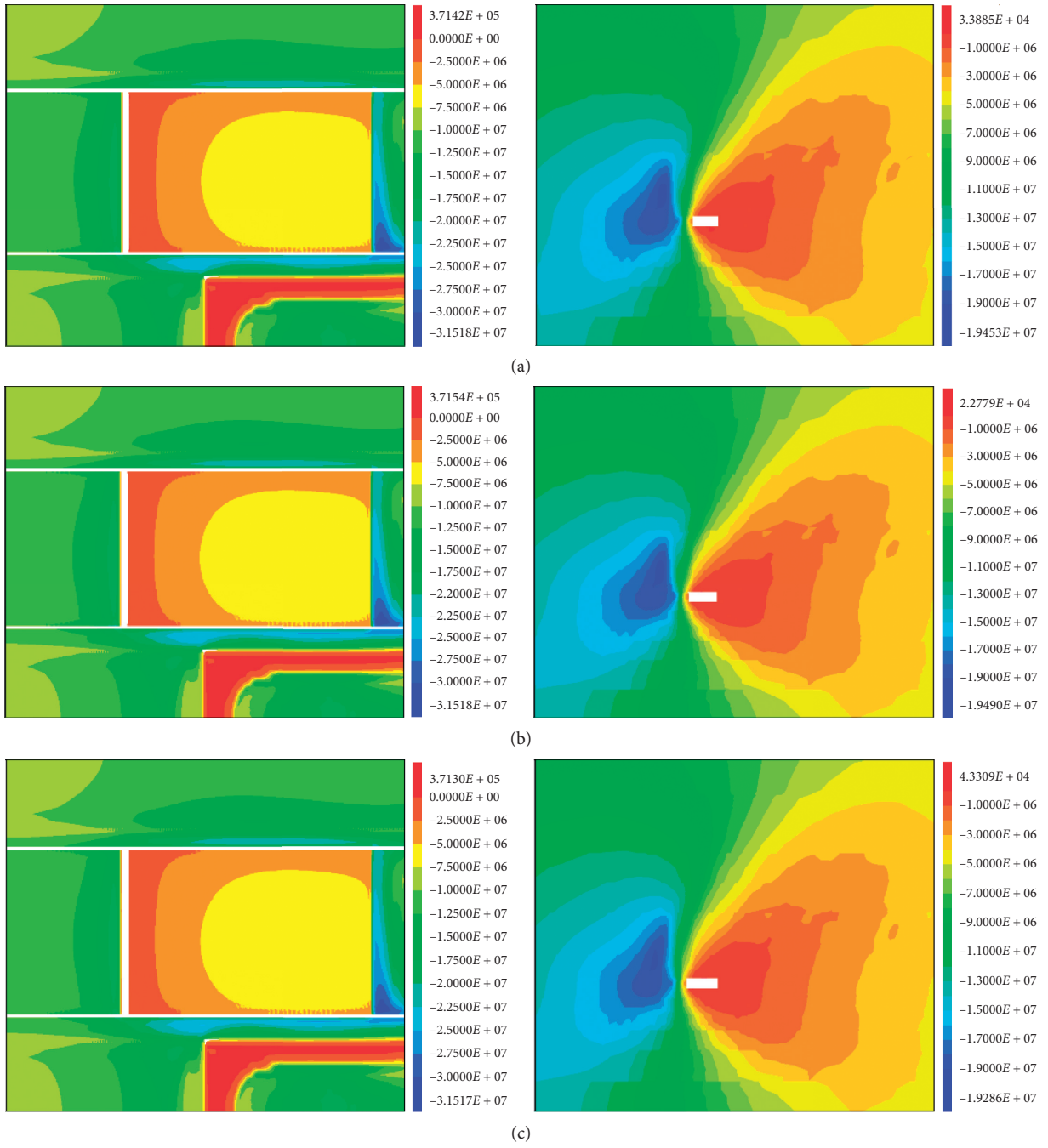
Figure 8: Continued.

(d)
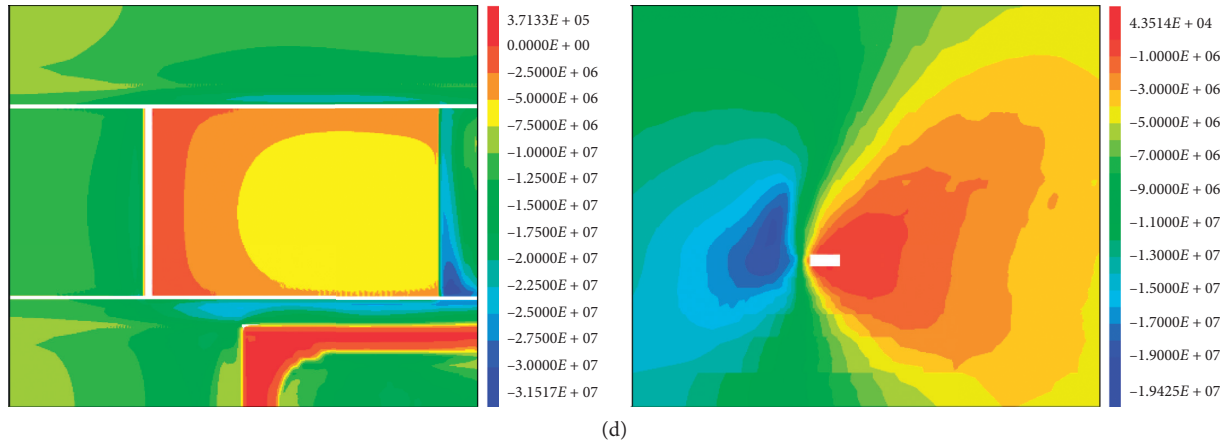
FIGURE 8: Nephogram of stress distribution 300 m away from the cut hole in E1302 working face under a backfilling mining cycle. (a) Vertical stress distribution before cutting the first coal. (b) Vertical stress distribution before cutting the second coal. (c) Vertical stress distribution before backfilling. (d) Vertical stress distribution before the next coal cutting after backfilling.


(a)

(b)
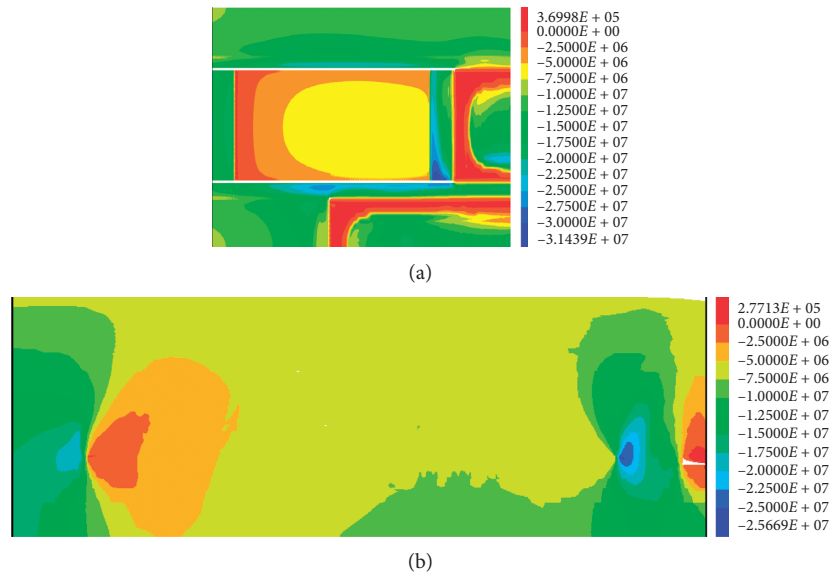
FIGURE 9: Nephogram of stress distribution of E1302 working face after filling and mining.

(2) It can be seen from the main view (b) in Figure 9 that the internal stress in the paste backfilling area is higher than that on both sides before and after the working face, and the stress is generally lower than the original rock stress. The stress concentration area is mainly concentrated in the local scope of the coal pillar in the south of the E1302 cut hole and the stoppage line in the north of the working face

4. Conclusion and Prospect

4.1. Conclusion. Aiming at the problems of low production capacity and high cost of paste backfilling in the coal mine, this paper takes the No. 3 Coal Seam in Lu'an area as the research object and studies the stress distribution law of high-efficiency paste backfilling working face in the thick coal seam above 6 m, so as to solve the problem of solid waste

backfilling mining in thick coal seam represented by Lu'an, so as to improve the recovery rate of mine resources and extend the service life of the mine.

(1) On the basis of the theoretical establishment of the instability criterion of roof rock beam failure with the change of backfilling body unit strength with time, a numerical calculation model considering the change process of backfilling body strength was established. The stress distribution law of E1302 working face before and during mining was analyzed, which played a guiding role in the actual production of the whole working face and roadway

(2) The recovery rate of resources is improved. It is preliminarily estimated that paste backfilling can make the recovery rate of No. 3 coal seam close to 80% and increase the recovery rate by nearly 40%.

More than 210 million tons of coal under buildings can be mined, effectively extending the service life of the mine and increasing employment opportunities

4.2. Research Prospect. On the basis of theory and practice, this paper makes a preliminary study on the stress distribution law of high-efficiency paste backfilling working face in thick coal seam above 6 m from the perspective of numerical simulation. Although some understanding and experience have been obtained, there are still many problems to be further studied, mainly reflected in the following aspects:

(1) It is necessary to refine the model, consider the influence of the stability of the coal side and backfilling side of longwall mining, improve the numerical simulation model, and provide a more solid numerical simulation basis for the wide application of backfilling mining

(2) The current numerical simulation research is only aimed at the conditions of Gaohe mine. The trend and direction of theoretical research and development of backfilling mining should be based on the specific situation of different production practices in the mining area, so as to reduce the difficulty of backfilling and mining technology, reduce the backfilling cost, improve the backfilling rate, control the surface subsidence, and promote the benign development of the mining area

Data Availability

The data used to support the findings of this study are included within the article. And all data are obtained through experiments and tests by our research team in Gaohe mine and laboratory. All the data are true and effective. The right to use data belongs to the authors before the article being published, but after it was published, the data can be referenced.

Conflicts of Interest

The authors declare no conflicts of interest.

References

[1] BP Global, *BP Group Released BP World Energy Statistical Yearbook 2018: Process Industry*, BP Global, London, UK, 2018.

[2] M. Zhang, *Theoretical Study on Overburden Control of High Efficiency Paste Backfilling Working Face*, China University of Mining and Technology, Xuzhou, China, 2019.

[3] X. Huang, "Leading energy industry reform with green development," *People's Forum*, vol. 31, pp. 26-27, 2017.

[4] National Bureau of Statistics, *China Statistical Yearbook 2018*, National Bureau of Statistics, Beijing, China, 2018.

[5] J. Peng and J. Dong, "Research of double layer filter-tube non-sand-mat vacuum preloading in ultra soft seabed silt hydraulic fill site," in *Proceedings of the International Conference on Electric Information and Control Engineering (ICEICE)*, Wuhan, China, 2011.

[6] B. Ercikdi, "Utilization of industrial waste products as pozzolanic material in cemented paste backfill of high sulphide mill tailings," *Journal of Hazardous Materials*, vol. 168, pp. 848–856, 2009.

[7] L. Huynh, "Effect of polyphosphate and naphthalene sulfonate formaldehyde condensate on the theological properties of dewatered tailings and cemented paste backfill," *Minerals Engineering*, vol. 19, pp. 28–36, 2006.

[8] A. Philip, *Engineering Design of Paste Backfill Systems*, Queen's University Kingston, Ontario, Canada, 2003.

[9] C. G. Nicieza, M. I. Álvarez Fernández, A. Menéndez Díaz, and A. E. Álvarez Vigil, "The new three-dimensional subsidence influence function denoted by n-k-g," *International Journal of Rock Mechanics and Mining Sciences*, vol. 42, no. 3, pp. 372–387, 2005.

[10] M. Xie-Xing, Z. Ji-Xiong, and G. Guang-Li, "Study on waste-filling method and technology in fully-mechanized coal mining[J]," *Journal of China Coal Society*, vol. 35, no. 1, pp. 1–6, 2010.

[11] P. Rajeev, P. R. Sumanasekera, and N. Sivakugan, "Lateral variation of the vertical stress in underground mine stopes filled with granular backfills," *Geotechnical and Geological Engineering*, vol. 34, no. 2, pp. 481–492, 2016.

[12] S. Widisinghe and N. Sivakugan, "Vertical stress isobars for trenches and mine stopes containing granular backfills," *International Journal of Geomechanics*, vol. 14, no. 2, pp. 313–318, 2014.

[13] M. Z. Emad, H. Mitri, and C. Kelly, "Effect of blast-induced vibrations on fill failure in vertical block mining with delayed backfill," *Canadian Geotechnical Journal*, vol. 51, no. 9, pp. 975–983, 2014.

[14] M. Qian, G. Xiexin Miao, J. Xu et al., "On scientific mining," *Journal of Mining and Safety Engineering*, vol. 25, no. 1, pp. 1–10, 2008.

[15] M. Qian, "Scientific mining of coal and related issues," *China Coal*, vol. 34, no. 8, pp. 5–10, 2008.

[16] M. Qian and J. Xu, "Concept and technical framework of scientific mining," *Journal of China University of Mining and Technology*, vol. 13, no. 3, pp. 1–7, 2011.

[17] M. Qian, "Scientific mining of coal," *Journal of China Coal Society*, vol. 35, no. 4, pp. 529–534, 2010.

[18] M. Qian, J. Xu, and J. Wang, *Further Discussion on Scientific Mining of Coal*, Journal of China Coal Society, Beijing, China, 2018.

[19] J. Xu, "Strata control and coal scientific mining: academician Qian Minggao's academic thoughts and scientific research achievements," *Journal of Mining and Safety Engineering*, vol. 1, 2019.

[20] T. Liu, *Backfilling Mining Technology and its Application*, Metallurgical Industry Press, Beijing, China, 2001.

[21] A. Zhou, *Cemented Backfilling of Mine Waste*, Metallurgical Industry Press, Beijing, China, 2007.

[22] W. Peng, "FLAC 3D practical course," 2008.

[23] Y. Chen and D. Xu, *FLAC3D Foundation and Engineering Examples*, China Water Conservancy and Hydropower Press, Beijing, China, 2013.

Research Article

Analytical Assessment of Internal Stress in Cemented Paste Backfill

Naifei Liu [1,2] **Liang Cui** [3] **and Yan Wang** [3]

[1]*School of Civil Engineering, Xi'an University of Architecture and Technology, Xi'an 710055, China*
[2]*Shaanxi Key Laboratory of Geotechnical and Underground Space Engineering, XAUAT, Xi'an 710055, China*
[3]*Department of Civil Engineering, Lakehead University, Thunder Bay, Ontario P7B 5E1, Canada*

Correspondence should be addressed to Naifei Liu; liunaifei@xauat.edu.cn and Liang Cui; liang.cui@lakeheadu.ca

To analytically describe the internal stress in a fill mass made of granular man-made material (cemented paste backfill, CPB), a new 3D effective stress model is developed. The developed model integrates Bishop effective stress principle, water retention relationship, and arching effect. All model parameters are determined from measurable experimental data. The uncertainties of the model parameters are examined by sensitivity analysis. A series of model application is conducted to investigate the effects of field conditions on the internal stress in CPB. The obtained results show that the proposed model is able to capture the influence of operation time, stope geometry, and rock/CPB interface properties on the effective stress in CPB. Hence, the developed model can be used as a useful tool for the optimal design of CPB structure.

1. Introduction

As a relatively new backfilling method, cemented paste backfill (CPB, a mixture of dewatered tailings, hydraulic binder, and water) technology has gradually become a standard practice around the world [1, 2]. Due to the rapid strength acquisition [3], CPB can provide reliable ground support to the adjacent stopes and thus enhance mining cycles and productivity. In addition, since the tailings are used as the major ingredient for the CPB preparation and then pumped into mined-out underground space (called stope), CPB technology can be considered as an effective and attractive alternative to the conventional tailings disposal on the surface (i.e., tailings impoundments or dams) [4] and thus enhances the associated mechanical (strength and stability) [5] and microstructural (total porosity and pore size distribution) properties [6] and minimizes the associated environmental issues (e.g., the acid mine drainage, acid/sulphate attack, heavy metal concentration, and so on) [7–9]. Consequently, the CPB technology has been widely adopted in underground mining and started to replace the conventional backfilling methods (i.e., hydraulic fill and cemented rockfill) [10, 11].

However, the binder costs may reach up to 80% of the total backfill operating costs [12,13]. Therefore, optimal design of CPB becomes one of the major tasks for backfill engineers and researchers. The prerequisite for the optimal CPB design is to reliably assess the internal stress in CPB. Previous laboratory and field studies [14] have found that the rock/CPB interface resistance (i.e., the interface friction stress and adhesion) can dramatically reduce vertical stress acting on the stope floor (i.e., the arching effect). Moreover, the water drainage through the barricade (i.e., a retaining structure for fresh CPB constructed near the stope entrance) can cause the dissipation of pore-water pressure (PWP) [15] and thus affect the effective stress in CPB mass. Therefore, to accurately and reliably assess and predict the internal stress in CPB, the hydraulic and mechanical processes under the influence of rock/CPB interface interaction must be fully considered.

To study the variation of internal stress and the associated influencing factors, extensive laboratory experiments and in-situ monitoring programs have been conducted. For example, previous laboratory studies [16–20] have found that curing stress, water drainage, and structural filling

properties (e.g., filling rate and sequences, filling time, filling interval time, and filling surface angle) affect the evolution of material properties (e.g., coefficient of permeability, shear strength parameters, elastic modulus, and so on) and the internal stress in CPB. Moreover, field monitoring programs have been carried out to assess the evolution of PWP [21] and total stress [22] in stopes with various mixture recipes and field conditions. The field measurements provide direct evidence for the arching effect in stopes. In addition, since the analytical models can provide a simple closed-form solution to assess the total stress in CPB, the analytical method has been extensively used in the optimal design of CPB structure. Correspondingly, a series of analytical methods has been proposed through limit equilibrium analysis [23, 24]. However, the skeletal deformation and its strength development are controlled by the effective stress rather than the total stress [25]. Therefore, it is necessary to investigate the changes of effective stress in CPB structure. However, the available analytical methods focus on the evaluation of total stress rather than the effective stress in CPB. Therefore, This study aims to (1) develop a 3D effective stress analytical model to evaluate the internal stress in CPB, which fully considers the effects of hydraulic and mechanical processes in CPB under the influence of rock/CPB interaction and (2) investigate the changes of internal stress of CPB mass with various filling operation time, stope geometry, and rock/CPB interface properties.

2. Formulation of a 3D Effective Stress Analytical Model

To develop a 3D effective stress analytical model for the characterization of internal stress in CPB, the prerequisite is to determine the mechanisms responsible for the stress change. Then, the adopted assumptions for the derivation of the effective stress model should be identified. Afterwards, the limit equilibrium analysis can be carried out to derive the mathematical model. A schematic diagram (see Figure 1) of in-situ CPB mass in underground stope is adopted to elucidate the mechanisms of stress changes in CPB.

As shown in Figure 1, the self-weight load increases with the backfilling operation after placement into stope. Meanwhile, the PWP progressively builds up with the filling process. However, the dissipation of PWP induced by barricade drainage accompanies the filling process. Correspondingly, negative PWP appears in the top area of CPB mass and changes the magnitude and spatial distribution of effective stress in CPB. In addition, the rock/CPB interface interaction can weaken the influence of self-weight stress on the vertical stress in fill mass [26]. Consequently, the resultant vertical stress can be apparently lower than the self-weight stress for a given elevation in CPB. As aforementioned, the backfilling operation, rock/CPB interface interaction, and barricade drainage control the changes of effective stress in fill mass. Considering the realistic underground mining conditions where variable rocks may exist as neighbour rock, the hard rock (igneous or metamorphic rock) is considered in this study.
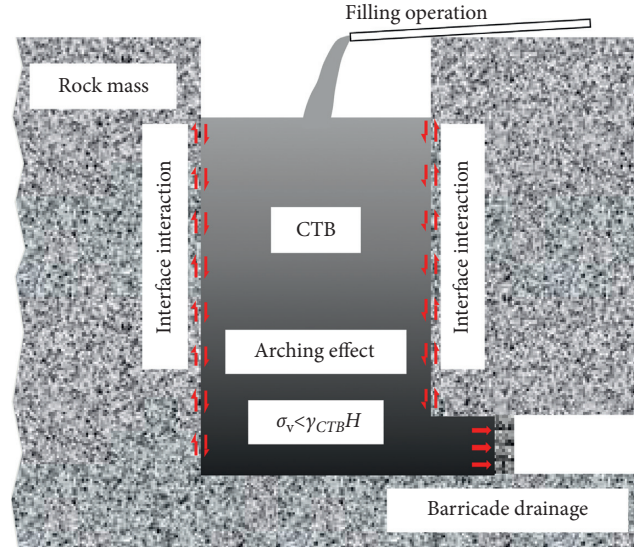
FIGURE 1: Schematic diagram of factors affecting the internal stress in stope (σ_v: total vertical stress, γ_{CPB}: unit weight of CPB, and H: filling height).

2.1. Definition of Effective Stress in CPB.

Due to the barricade drainage, PWP dissipation takes place in CPB and thus causes the change of the saturation state. As a result, an unsaturated zone gradually appears in the top regime of fill mass and is separated from the saturated zone by the local water table. The variation of PWP affects the magnitude and spatial distribution of effective stress in CPB. To analytically describe the change of effective stress, Bishop effective stress σ' [27] is adopted:

$$\sigma' = (\sigma - P_a) + \chi (P_a - P_w), \tag{1}$$

where σ, P_w, and P_a, respectively, represent total stress, PWP, and pore air pressure and χ is the parameter of Bishop effective stress ($\chi = 1$ for saturated CPB and $\chi = 0$ for dry CPB). It has been found that Bishop's parameter χ is strongly dependent on the degree of saturation S (i.e., $\chi = \chi (S)$) [28]. The latter can be determined by matric suction ($P_w - P_a$) via the water retention curve. Therefore, Bishop's parameter χ can be related to matric suction as well. In this study, the empirical model proposed by Khalili and Khabbaz [29] is adopted to characterize the relationship between χ and matric suction ($P_w - P_a$):

$$\chi = \left[\frac{(P_a - P_w)}{P_e} \right]^R, \tag{2}$$

where P_e represents the air entry value and R is a fitting parameter. Based on the experimental studies on 14 soils including glacial till, silts, sandy clay, and clays, $R = -0.55$ is obtained [29]. In terms of particle size, the tailings can range from fine sand down to clay-sized particles, which is very close to the investigated soils in the study conducted by Khalili and Khabbaz [29]. Therefore, $R = -0.55$ is adopted in the present study. Moreover, based on the previous study on the water retention curves (WRCs) of CPB [30], the air entry value $P_e = -200$ kPa is used in this study. In addition, it should be noted that equation (2) is only valid when the matric suction is greater than the air entry value; otherwise,

the value of χ is equal to 1 [31], namely, the CPB remains fully saturated.

The pore air pressure is assumed to be zero-gauge pressure against atmospheric pressure (i.e., $P_a = 0$). Therefore, by substituting equation (2) and $P_a = 0$ into equation (1), the effective stress can be rewritten as follows:

$$\sigma' = \sigma + \frac{(-P_w)^{R+1}}{P_e^R}. \tag{3}$$

To incorporate the effect of hydraulic process into the effective stress, the PWP in CPB (including both saturated and unsaturated zones) should be determined. For this purpose, the location (i.e., H_{wt}) of local water table should be identified first. Then, the positive PWP in the saturated zone can be considered as hydrostatic pressure, and the negative PWP above the local water table can be determined by the spatial distribution of saturation degree and water retention relationship (i.e., the WRC model).

It should be noted that the location of local water table changes with time t due to the water drainage through barricade. Hence, the thickness of the unsaturated zone H_{wt} can be expressed as follows:

$$H_{wt} = \int_0^t v_{wt} dt, \tag{4}$$

where v_{wt} is the movement velocity of local water table, which is related to the outflow rate $\bar{v}_{wb}$ of pore water through barricade. In this study, a linear relationship between v_{wt} and $\bar{v}_{wb}$ is assumed as follows:

$$v_{wt} = v_f \frac{l_a l_b}{L_A L_B} \bar{v}_{wb}, \tag{5}$$

where L_A and L_B, respectively, represent the length and width of the stope, la and lb refer to the barricade dimensions, and v_f is a constant scaling parameter which is related to ratio of coefficient of permeability of CPB and barricade ($v_f = K_{CPB0}/K_B$ with K_{CPB0} and K_B as the initial coefficient of permeability of CPB and barricade, respectively). The detailed information about the determination of K_{CPB0} and K_B will be presented in the Section of Determination of Model Parameters. The average pore-water flow velocity $\bar{v}_{wb}$ through barricade can be calculated by Darcy's law:

$$\bar{v}_{wb} = K_b \frac{H - H_{wt}}{W_b}, \tag{6}$$

where K_b denotes the coefficient of permeability of barricade, W_b is the thickness of barricade, and H refers to the backfilling height and can be determined by filling rate $v_{filling}$ and filling strategy:

$$H = \begin{cases} v_{filling}t, & H \le H_{r1}, \\ H_{r1} + v_{filling}(t - t_{r1}), & H_{r_1} < H \le H_{r_2}, \\ \vdots \\ \sum_{i=1}^{n-1} H_{r_i} + v_{filling}(t - t_{r_{n-1}}), & H_{r_{n-1}} < H \le H_{r_n}, \end{cases} \tag{7}$$

where H_{ri} is the total filling height after i-th filling sequence, t_{ri} is the rest time between i-th filling and $(i+1)$-th filling sequences, and n is the total filling sequences adopted by the backfilling operation. As indicated in equation (7), the filling rate and filling sequences are fully considered in the present study. Substituting equations (5) and (6) into equation (4) and applying the initial condition ($H_{wt} = 0$ when $t = 0$) yield the following:

$$H_{wt} = H\left[1 - \exp\left(-\frac{v_f K_b}{W_b} \frac{l_a l_b}{L_A L_B} t\right)\right]. \tag{8}$$

Then, the effective saturation degree S_e ($S_e = (\theta - \theta_r)/(\theta_s - \theta_r)$ with θ_s as saturated water content, θ as current water content, and θ_r as residual water content) is assumed to be linearly distributed in the unsaturated zone (i.e., $S_e = h/H_{wt}$ with h as the thickness of CPB relative to the top surface). Hence, the negative PWP in the unsaturated zone can be determined by the water retention curve (WRC). Previous studies [30, 32] on CPB have proved that the van Genuchten model [33] is able to accurately predict the water retention capacity of CPB materials.

$$S_e = \frac{1}{\left[1 + (-\alpha P_w)^{1/1-m}\right]^m}, \tag{9}$$

where α and m denote the parameters of the van Genuchten model. The detailed information about the determination of parameters of the WRC model will be provided in the Section of Determination of Model Parameters.

Therefore, the negative PWP can be derived by substituting the effective saturation degree (i.e., $S_e = h/H_{wt}$) into the WRC model (i.e., equation (9)):

$$P_w = -\frac{1}{\alpha}\left[\left(\frac{H_m}{h}\right)^{1/m} - 1\right]^{1-m}. \tag{10}$$

Hence, the spatial distribution of effective stress in CPB mass can be expressed as follows:

$$\begin{cases} \sigma' = \sigma + \frac{\left\{(1/\alpha)\left[(H_{wt}/h)^{(1/m)} - 1\right]^{1-m}\right\}^{R+1}}{P_e^R}, & h \le H_{wt}, \\ \sigma' = \sigma - \gamma_w (h - H_{wt}), & h > H_{wt}, \end{cases} \tag{11}$$

with

$$H_{wt} = H\left[1 - \exp\left(-\frac{v_f K_b}{W_b} \frac{l_a l_b}{L_A L_B} t\right)\right], \tag{12}$$

where γ_w refers to the unit weight of pore water.

As previously discussed, the arching effect causes the discrepancy between vertical stress and the self-weight stress. Therefore, the total stress in equation (3) cannot be represented by the overburden stress. The detailed discussion about the determination of total stress in CPB is presented in the following section.

2.2. Total Stress in CPB under Arching Effect. To evaluate the total stress in CPB under arching effect, the force analysis of CPB structure is first conducted through limit equilibrium analysis. Then, the limit equilibrium analysis is used to derive the analytical model for the total stress in CPB. To perform the force analysis in CPB mass, a representative thin-layer CPB is selected from the fill mass. The relevant forces acting on the thin layer are plotted in Figure 2. It should be noted, since the constant material properties are assumed in this study, the spatial variation of material properties due to the different filling and curing conditions is neglected. Consequently, the selection of representative thin-layer CPB is dependent only on the position of local water table. Therefore, one representative layer is selected above water table to determine the total stress in the partially saturated zone, while the other representative layer is selected below the local water to derive the total stress in the fully saturated zone.

As shown in Figure 2, the forces acting on the representative thin layer can be classified into two categories including body force and surface forces. Specifically, the former refers to the self-weight load (i.e., G_{CPB}) due to the gravitational effect, and the latter consists of interface resistance force (i.e., interface shear force F_s and interface adhesion force F_c) and the vertical forces acting on the top (i.e., F_v) and bottom (i.e., $F_v + dF_v$) surfaces of the CPB layer. In addition, the interface shear force (i.e., F_s) should be considered as a type of reaction force induced by the horizontal force (i.e., F_h) on the rock/CPB interface. Since the representative CPB layer is in equilibrium under the action of body force and surface forces, the equilibrium analysis approach can be utilized to derive the total vertical stress. Then, the horizontal stress can be calculated through reaction coefficient.

2.3. Total Stress in Unsaturated Zone. Based on the force analysis on the thin layer of CPB, the body force G_{CPB} in the unsaturated zone (i.e., $h < H_{\mathrm{wt}}$) can be expressed as follows:

$$G_{\mathrm{CPB}} = \gamma_{\mathrm{CPBu}} L_A L_B \mathrm{d}h, \tag{13}$$

where γ_{CPBu} is the unit weight of unsaturated CPB, L_A and L_B, respectively, denote the length and width of the stope, and $\mathrm{d}h$ is the thickness of the representative thin layer.

In addition, the representative element is also subjected to the surface forces including the vertical stress on the top and bottom surface and the interface resistance force (i.e., the interface shear force and adhesion). The former (i.e., the vertical force F_V) can be calculated through the vertical stress σ_V:

$$F_V = \sigma_{vu} L_A L_B. \tag{14}$$

For the interface resistance force, the interface friction component (i.e., F_{As} and F_{Bs}) can be determined by the horizontal stress (i.e., $\sigma_{h\mathrm{Au}}$ and $\sigma_{h\mathrm{Bu}}$) and interface friction angle ϕ:

$$F_{\mathrm{As}} = \sigma_{h\mathrm{Au}} L_A \tan \phi \mathrm{d}h, \tag{15}$$

$$F_{\mathrm{Bs}} = \sigma_{h\mathrm{Bu}} L_B \tan \phi \mathrm{d}h. \tag{16}$$

The horizontal stress can be calculated by the product of vertical stress and the reaction coefficient K.

$$\sigma_{\mathrm{hu}} = K\sigma_{\mathrm{vu}}. \tag{17}$$

Substituting equation (17) into equations (15) and (16), the interface shear force can be rewritten as follows:

$$F_{\mathrm{As}} = \sigma_{\mathrm{vu}} K L_A \tan \phi \mathrm{d}h, \tag{18}$$

$$F_{\mathrm{Bs}} = \sigma_{\mathrm{vu}} K L_B \tan \phi \mathrm{d}h. \tag{19}$$

The interface adhesion force (i.e., F_{Ac} and F_{Bc}) can be calculated as follows:

$$F_{\mathrm{Ac}} = c L_A \mathrm{d}h, \tag{20}$$

$$F_{\mathrm{Bc}} = c L_B \mathrm{d}h. \tag{21}$$

where c represents the rock/CPB interface adhesion.

To derive the analytical solution for the total vertical stress in the unsaturated zone of CPB mass, the force equilibrium equation in the vertical direction is utilized:

$$G_{\mathrm{CPB}} = \mathrm{d}F_V + 2\left(F_{\mathrm{As}} + F_{\mathrm{Ac}}\right) + 2\left(F_{\mathrm{Bs}} + F_{\mathrm{Bc}}\right). \tag{22}$$

Then, substituting equations (13), (14), (18)–(21) into equation (22), the total vertical stress above the local water table ($h < H_{\mathrm{wt}}$) can be solved by applying the initial condition (i.e., $\sigma_{\mathrm{vu}} = 0$ when $h = 0$):

$$\sigma_{\mathrm{vu}} = \frac{\gamma_{\mathrm{CPBu}} L_A L_B - 2c\left(L_A + L_B\right)}{2K \tan \phi \left(L_A + L_B\right)} \left\{ 1 - \exp\left[-\frac{2\tan \phi K\left(L_A + L_B\right)}{L_A L_B} h \right] \right\}. \tag{23}$$

2.4. Total Stress in Fully Saturated Zone. Below the water table (i.e., $h \geq H_{\mathrm{wt}}$), similar force analysis can be conducted on a representative thin layer of CPB. The body force (i.e., CPB gravity G_{CPB}) in the fully saturated zone can be expressed as follows:

$$G_{\mathrm{CPB}} = \gamma_{\mathrm{CPBs}} L_A L_B \mathrm{d}h, \tag{24}$$

where γ_{CPBs} is the unit weight of CPB in the fully saturated state.

In addition, the surface forces acting on the saturated thin layer can be determined in a similar way adopted in the unsaturated CPB layer. The vertical force F_V can be expressed as follows:

$$F_V = \sigma_{\mathrm{vs}} L_A L_B. \tag{25}$$

with σ_{vs} as the vertical stress acting on the saturated thin-layer surface.

The rock/CPB interface resistance force (i.e., interface friction and adhesion forces) can be defined as follows:
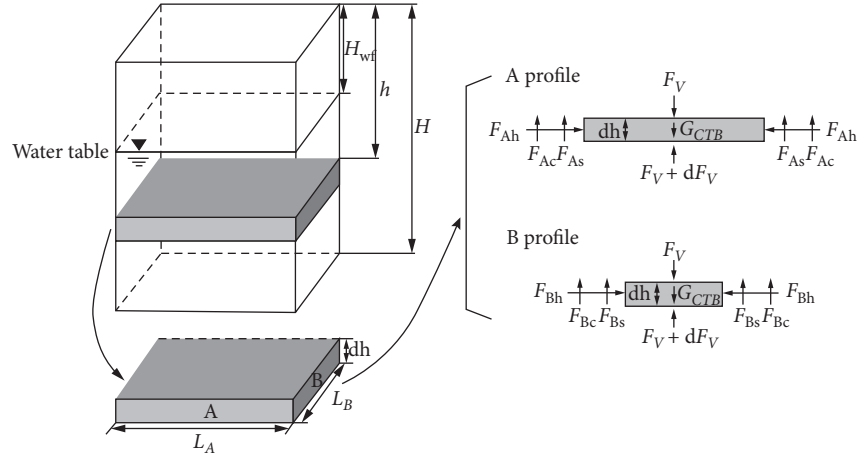
FIGURE 2: Force analysis in the unsaturated zone of CPB mass (H_{wt}: local water table location, h: thickness of CPB relative to top surface, H: filling height, L_A: longitudinal length of CPB mass, L_B: transverse length of CPB mass, dh: thickness of the representative CPB layer, F_h: horizontal force, F_v: vertical force, F_c: interface adhesion, F_s: interface friction force, and G_{CPB}: self-weight load of CPB).

$$F_{As} = \sigma_{vs} K L_A \tan\phi\, dh, \tag{26}$$

$$F_{Bs} = \sigma_{vs} K L_B \tan\phi\, dh, \tag{27}$$

$$F_{Ac} = c L_A dh, \tag{28}$$

$$F_{Bc} = c L_B dh. \tag{29}$$

Below the local water table (i.e., $h \geq H_{wt}$), the force equilibrium equation in the vertical direction can be obtained by substituting equations (24)–(29) into equation (22). To derive the vertical stress in the saturated zone, the boundary condition on the top surface of local water table

(i.e., $h = H_{wt}$) is needed. The corresponding vertical stress can be expressed as follows:

$$\sigma_{v\_wt} = \frac{\gamma_{CPBs} L_A L_B - 2c(L_A + L_B)}{2K \tan\phi (L_A + L_B)}$$
$$\left\{1 - \exp\left[-\frac{2K\tan\phi(L_A + L_B)}{L_A L_B} H_{wt}\right]\right\}. \tag{30}$$

Then, applying the initial condition (i.e., equation (30)), the total vertical stress in the saturated zone (i.e., $h > H_{wt}$) can be derived through integrating equation:

$$\sigma_{vs} = \frac{\gamma_{CPBs} L_A L_B - 2c(L_A + L_B)}{2K\tan\phi(L_A + L_B)}\left\{1 - \exp\left[-\frac{2K\tan\phi(L_A + L_B)}{L_A L_B}(h - H_{wt})\right]\right\} + \frac{\gamma_{CPBu} L_A L_B - 2c(L_A + L_B)}{2K\tan\phi(L_A + L_B)}$$
$$\left\{1 - \exp\left[-\frac{2K\tan\phi(L_A + L_B)}{L_A L_B}H_{wt}\right]\right\}. \tag{31}$$

It should be noted that interface shear strength parameters (adhesion c and friction angle ϕ) adopted in equations (24) and (33) refer to the total stress shear strength parameters which can be measured through direct shear tests on rock/CPB samples. Since the Bishop effective stress (equation (11)) is adopted to define the effective stress in unsaturated (i.e., $\chi < 1$) and fully saturated (i.e., $\chi = 1$) zones,

the effective shear strength parameters are not required in the present study.

2.5. 3D Effective Stress Model of CPB. The effective stress rather than total stress controls the mechanical behaviour of CPB. Therefore, to characterize the variation of internal

effective stress, a 3D effective stress model for CPB materials is needed, which can be derived by substituting equations (23) and (31) to equation (11)) based on the definition of Bishop effective stress.

$$\sigma' = \begin{cases} \dfrac{(\gamma_{CPBu}L_AL_B - 2c(L_A + L_B)/2K\tan\phi(L_A + L_B))\{1 - \exp[-(2K\tan\phi(L_A + L_B)/L_AL_B)h]\}}{P_e^R}, & h \leq H_{wt}, \\[4mm] \dfrac{\gamma_{CPBs}L_AL_B - 2c(L_A + L_B)}{2K\tan\phi(L_A + L_B)}\left\{1 - \exp\left[-\dfrac{2K\tan\phi(L_A + L_B)}{L_AL_B}(h - H_{wt})\right]\right\} \\[4mm] \quad + \dfrac{\gamma_{CPBu}L_AL_B - 2c(L_A + L_B)}{2K\tan\phi(L_A + L_B)}\left\{1 - \exp\left[-\dfrac{2K\tan\phi(L_A + L_B)}{L_AL_B}H_{wt}\right]\right\} - \gamma_w(h - H_{wt}), & h > H_{wt}, \end{cases} \tag{32}$$

with

$$H_{wt} = H\left[1 - \exp\left(-\frac{v_f K_b}{W_b}\frac{l_a l_b}{L_A L_B}t\right)\right]. \tag{33}$$

As indicated in equation (32), there exist a number of model parameters (including reaction coefficient K, WRC parameters α and m, interface friction angle ϕ, adhesion c, and the coefficient of permeability K_b). The detailed discussion about the model parameters is provided in the Section of Determination of Model Parameters.

3. Determination of Model Parameters

To implement the developed 3D effective stress model (i.e., equation (32)), the associated model parameters are required. With respect to the components of the backfilling system, the associated model parameters can be divided into three groups including (1) CPB material properties, (2) rock/CPB interface properties, and (3) properties related to barricade. The relevant discussion about determination of each group of model parameters is provided in the following subsections.

3.1. Rock/CPB Interface Properties. As aforementioned, the vertical stress is mainly affected by the rock/CPB interface shear force and adhesion. Correspondingly, the rock/CPB interface properties including interface friction angle ϕ and adhesion c are required. In this regard, extensive experimental studies have been carried out [14, 34, 35]. The measured rock/CPB interface friction angle is listed in Table 1. The obtained results indicate that the interface properties show no evident variation for each group of experimental data, which proves that the assumption of constant interface properties adopted in this study is reasonable. Hence, the average value of interface friction angle and adhesion from the collected data in Table 1 is used in this study, namely, $\phi = 31.5°$ and $c = 14.2$ kPa.

3.2. CPB Material Properties. Apart from the rock/CPB interface properties, the total horizontal stress σ_h is needed to calculate the interface friction force. The horizontal stress can be defined by the total vertical stress σ_v and reaction coefficient K (i.e., $\sigma_h = K\sigma_v$). Therefore, the reaction coefficient is required to assess the horizontal stress. During and after backfilling operation, the rock wall movement is expected to be small. For this reason, the reaction coefficient at rest K_r (i.e., $K_r = 1 - \sin\varphi$ with φ as the internal friction angle of CPB) is adopted in this study. Moreover, previous studies [14, 34] showed that the internal friction angle of CPB φ is almost equal to the rock/CPB interface friction angle ϕ (i.e., $\varphi = \phi$). As discussed previously, the $\phi = 31.5°$ is adopted. Thus, the internal friction angle of CPB can be obtained, namely, $\varphi = 31.5°$. Compared with the measured data of φ reported in the literature (see Table 2), $\varphi = 31.5°$ is reasonable for CPB materials.

To determine the water retention relationship, the WRC model parameters (i.e., α and m) are required. The parameter α is related to the inverse of air entry value P_e (i.e., $\alpha = -\gamma_w/P_e$ with γ_w as the unit weight of pore water). As aforementioned, the air entry value $P_e = -200$ kPa is adopted in this study. Hence, the parameter $\alpha = 0.049$ m^{-1} can be obtained. Compared with the reported values of α (i.e., 0.002 m^{-1} to 0.065 m^{-1}) in Table 3, $\alpha = 0.049$ m^{-1} is a reasonable value and employed in this study. In addition, the dimensionless parameter m is related to the width of the pore size distribution of solid particles [33]. Based on previous studies on WRCs of CPB (e.g., 30, 39, and 40), the parameter m is in the range from 0.25 to 0.62 (see Table 3). Therefore, the average value $m = 0.44$ is used in this study.

3.3. Material Property of Barricade. The CPB barricade can be constructed by various materials (e.g., porous brick, concrete, timber frame, shotcrete, and so on). However, to avoid excessive PWP acting on the barricade structure, the permeable concrete barricade bricks are commonly adopted to construct the barricade in practice [41, 42]. The measured data of coefficient of permeability of the concrete brick (i.e., K_b) are normally in the range of 0.03 cm/s to 0.31 cm/s (see Table 4). Therefore, the average value of $K_b = 0.17$ cm/s is employed in the present study.

As shown in equation (5), the constant scaling parameter v_f is required for the definition of movement velocity of local water table v_{wt}. In this study, the constant scaling

TABLE 1: Measured data of interface friction angle and adhesion.

Data source	Nasir and Fall [14]	Koupouli et al. [34]	Fall and Nasir [35]
Interface friction angle (°)	20~30	38~40	28~34
Interface adhesion (kPa)	25~30	8~9	3.2~10.2

TABLE 2: Measured data of internal friction angle of CPB.

Data source	Cui and Fall [36]	Koupouli et al. [34]	Ghirian and Fall [37]
Internal friction angle (°)	39~45	27~44	40~55

TABLE 3: Comparison of WRC model parameters collected from the literature.

Data source	α (m^{-1})	m (−)
Abdul-Hussain and Fall [30]	0.008~0.041	0.3~0.47
Cui and Fall [38]	0.002~0.065	0.41~0.45
Benson et al. [39]	0.006~0.057	0.25~0.52
Suazo [40]	0.002~0.013	0.38~0.62

−: dimensionless unit.

TABLE 4: Measured data of coefficient of permeability of concrete brick used for barricade.

Data source	Coefficient of permeability (cm/s)
Sivakugan et al. [41]	0.10~0.31
Berndt et al. [43]	0.03~0.30
Rankine [42]	0.10–0.19

TABLE 5: Measured data of coefficient of permeability of tailings.

Data source	Coefficient of permeability (10^{-4} cm/s)
Aubertin et al. [44]	0.5~4
Xu et al. [45]	3.0~5.6
Banks and Kirkham [46]	2.2~4.7

TABLE 6: Backfilling conditions adopted in the control stope for sensitivity analysis.

Parameters	Control stope
Length of stope L_A (m)	15
Width of stope L_B (m)	7.5
Height of stope H (m)	36
Filling rate (m/d)	12
Filling strategy	Continuous filling
Width of barricade l_a (m)	6
Height of barricade l_b (m)	6
Thickness of barricade W_b (m)	0.3

parameter is defined in terms of the ratio of coefficient of permeability of CPB and barricade (i.e., $v_f = K_{CPB0}/K_b$). In this study, the initial coefficient of permeability is assumed to be equal to the counterpart of tailings. The measured data of coefficient of permeability of tailings are listed in Table 5, and the average value of coefficient of permeability of fresh CPB $K_{CPB0} = 3.4 \times 10^{-4}$ cm/s is obtained. As discussed previously, the average value of $K_b = 0.17$ cm/s is adopted in this study. Therefore, the scaling parameter $v_f = 2 \times 10^{-3}$ is used in this study.

4. Sensitivity Analyses

The material parameters adopted in the developed model may change from mine to mine. Therefore, it is necessary to conduct the sensitivity analysis to analyze the uncertainties induced by the variation of model parameters. In this study, the effect of interface friction angle ϕ (i.e., the rock/CPB interface property) and the coefficient of permeability of barricade K_b (i.e., the property of barricade) were investigated. To clearly demonstrate the effect of investigated parameters on the internal stress in CPB, a control stope is selected as a reference. The dimensions of stope and barricade and filling strategies and rate adopted in the control stope are listed Table 6. The model parameters listed in Table 7 are employed for the control stope. The monitoring point is located at the stope floor.

For the model implementation, the backfilling rate will be used to calculate the present filling height, H, based on equation (7). It should be noted that multiple filling sequences may be adopted in the stopes. Correspondingly, the rest time

(t_{ri}) is considered at the end of each filling sequence, and filling height will be kept constant during each rest time t_{ri}. Hence, the piece-wise function (equation (7)) can be used to capture the backfilling strategy used in practice. After the backfilling height is obtained, the evolution of local water table, H_{wt}, will be quantitatively evaluated by equation (8). As indicated in equation (8), the local water table will change its spatial position as time elapses, which is used to capture the water loss due to the water drainage. When the filling height, H, and local water table position, H_{wt}, are determined, the corresponding total stress, pwp, and effective stress can be calculated by equation (32). Therefore, the proposed model is able to analytically describe the spatiotemporal evolution of internal stresses in CPB. Then, the proposed model was implemented to perform the sensitivity analysis and model application.

4.1. Interface Friction Angle. The interface friction angle ϕ can directly contribute to the development of interface shear stress between CPB mass and surrounding rock and thus affect the internal stress in CPB. In this study, three different interface friction angles including 25°, 31.5°, and 40° were chosen. The development of internal stress in CPB with different interface friction angles is plotted in Figure 3. From this figure, it can be found that the internal stress is sensitive to the change of interface friction angle and thus to the interaction between CPB and rock walls. With the increase in interface friction angle, a decrease in effective stress was observed. This is because larger interface friction angle can

TABLE 7: Model parameters adopted for sensitivity analysis and model application.

Type of model parameters	Model parameters	Value
Interface properties	Interface friction angle ϕ (°)	31.5
	Interface adhesion c (kPa)	14.2
CPB material properties	Internal friction angle φ (°)	31.5
	Reaction coefficient K (−)	0.27
	Parameter of the WRC model α (m^{-1})	0.049
	Parameter of the WRC model m (−)	0.44
	Air entry value of CPB P_e (kPa)	200
	Fitting parameter of effective stress R (−)	−0.55
	Saturated unit weight of CPB γ_{CPBs} (kN/m^3)	18
	Unsaturated unit weight of CPB γ_{CPBu} (kN/m^3)	14
Barricade parameter	Coefficient of permeability K_b (cm/s)	0.17

Symbol "-" indicates dimensionless unit.
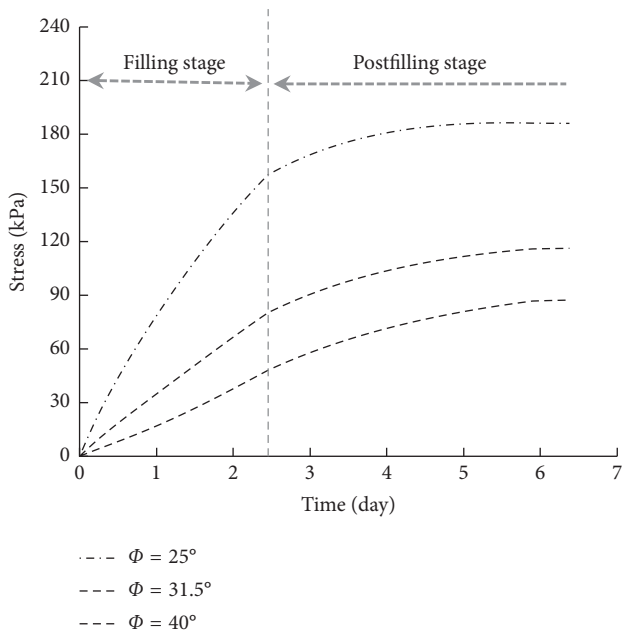
FIGURE 3: Variation of effective stress in CPB with different interface friction angles.

cause higher interface shear stress and thus, to a larger extent, reduce the internal stress in CPB (i.e., strengthen the arching effect).

4.2. Coefficient of Permeability of Barricade. Water drainage through barricade structure causes the variation of PWP and thus affects the effective stress in CPB. Correspondingly, coefficient of permeability K_b plays a crucial role in the process of barricade drainage. Therefore, it is necessary to investigate the effect of K_b on the variation of internal stress in CPB. In this study, a range of coefficient of permeability including 0.2 cm/s, 0.17 cm/s, and 0.14 cm/s were selected. As shown in Figure 4, the effective stress demonstrates an increasing trend with the increase in K_b. This is because higher value of K_b can enhance the barricade drainage and thus reduce the PWP to a larger extent. Consequently, a higher effective stress was observed in CPB with a larger value of K_b.
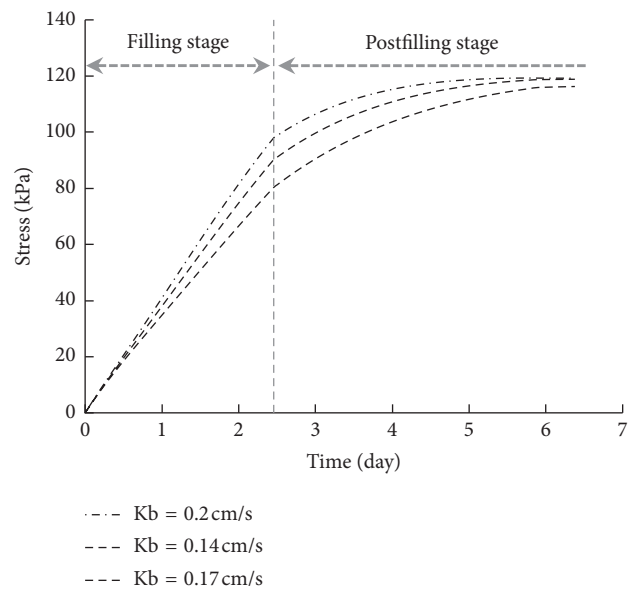
FIGURE 4: Variation of effective stress in CPB with different coefficient of permeability of barricade.

4.3. Model Application. Due to the irregularities of ore bodies, various mining methods, and backfilling strategies, the resultant backfilling conditions may differ from mine to mine [38]. Hence, the developed model was used to address the practical problems including the effects of operation time, stope geometry, and rock/CPB interface properties on the internal stress in CPB. To clearly demonstrate the effects of factors investigated in the following subsections, a control stope is chosen as a reference. All investigations are conducted through some specific adjustments to the control stope. The model parameters listed in Table 7 are employed for the control stope. The dimensions of stope and barricade and filling strategies and rate adopted in the control stope are listed Table 8. The monitoring point is located at the stope floor.

4.4. Effect of Operation Time. Due to staged placement of CPB into stope and drainage through barricade, the internal stress (effective stress, total stress, and PWP) can

TABLE 8: Backfilling conditions adopted in the control stope.

Parameters	Control stope
Length of stope L_A (m)	15
Width of stope L_B (m)	7.5
Height of stope H (m)	36
Filling rate (m/d)	12
Filling strategy	Two-stage filling with 1-day rest time
Width of barricade l_a (m)	6
Height of barricade l_b (m)	6
Thickness of barricade W_b (m)	0.3

demonstrate strongly time-dependent characteristics [2, 47]. As indicated in equation (32), the developed model incorporates the evolution of PWP (including both positive and negative PWP) and total stress (i.e., different unit weight of CPB in saturated and unsaturated states) into the prediction of effective stress in CPB. Hence, the variation of effective stress with time can be described by the developed model. In this study, the control stope is chosen to assess the change of internal stress in CPB with time. The evolution of internal stress in CPB is plotted in Figure 5. From this figure, it can be observed that (1) the effective stress gradually increases during the filling stage and postfilling stage, which is mainly attributed to the increase in total vertical stress with the fresh CPB poured into stope and to the water drainage through barricade and (2) during the rest period (from 1 day to 2 days), the effective stress shows an increasing trend although no fresh CPB is placed into stope during this stage. This is because of the pore-water loss by barricade drainage. As shown in Figure 5, the PWP decreases from 86 kPa to 64 kPa during the rest period, which contributes to the enhancement of effective stress in CPB. Therefore, the staged filling operation with a specified rest time is favorable to the improvement of stability of CPB structure. The obtained results indicate that the developed model is able to describe the change of internal stress in CPB with operation time.

Moreover, due to the water drainage through barricade, negative PWP will be generated in CPB. Therefore, it is necessary to investigate the spatial distribution of PWP in CPB with operation time. The comparison of PWP versus stope height for different operation time is plotted in Figure 6. From this figure, it can be observed that during the filling stage (from 0 to 4 days), the PWP shows an increase for a given stope elevation. As discussed previously, this is due to the continuous placement of fresh CPB into stope. Moreover, the location of water table also increases with time during the filling stage. However, the PWP shows an opposite trend during the postfilling stage. Specifically, PWP becomes more negative for a given elevation, and the water table decreases with time. Therefore, the obtained results indicate that filling operation and water drainage through barricade can significantly affect the distribution of PWP in CPB. The developed model is able to characterize the spatial evolution of PWP in CPB.

4.5. Effect of Stope Geometry. As aforementioned, the stope geometry may differ from one stope to another due to the irregularities of ore body and various stoping methods. To
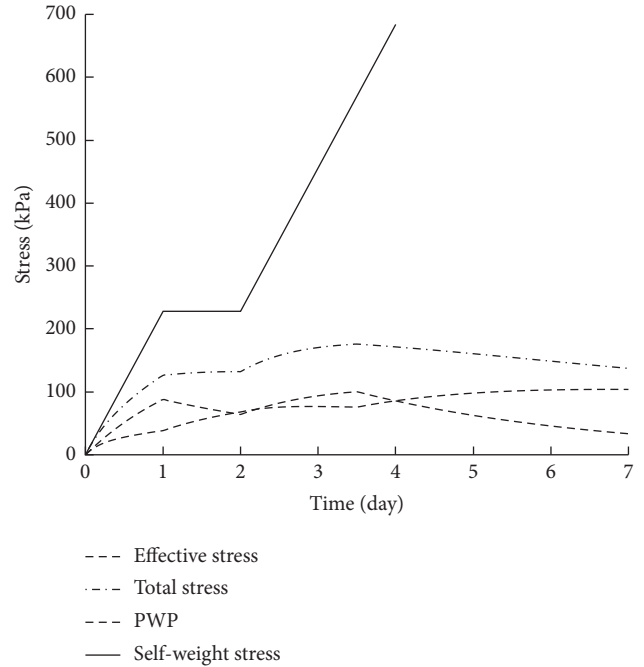
FIGURE 5: Effect of operation time on the variation of internal stress in CPB.
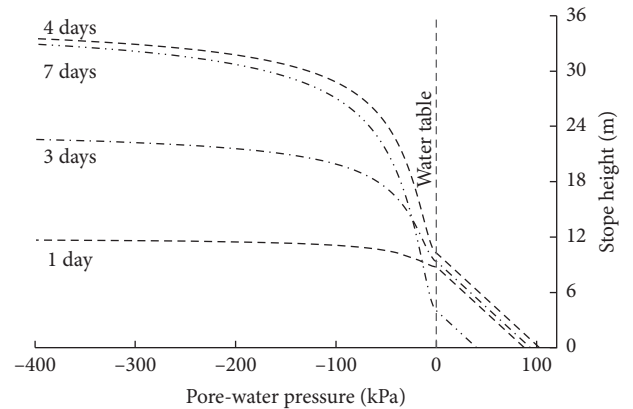
FIGURE 6: PWP versus stope height for different operation times.

investigate the effect of stope geometry, three different stope heights including 15m, 30m, and 45m were selected. In this case, the values of model parameters are same to those adopted in control stope. Figure 7 presents the development of internal stress for different stope heights. The results show, as expected, that stope height (i.e., the backfilling heights) has a significant effect on the variation of internal stress in CPB. Specifically, a higher level of effective stress is obtained in the CPB with a higher stope height (see Figure 7(a)) after the filling completion. This is due to the larger total stress developed in CPB with higher filling height (see Figure 7(b)). However, the contribution of filling height to effective stress becomes progressively smaller with the increase in stope height. For example, at the end of filling operation in these three stopes, the effective stress for 30m and 45m cases, respectively, increases by 40% (163 kPa) and

(a)

(b)

(c)
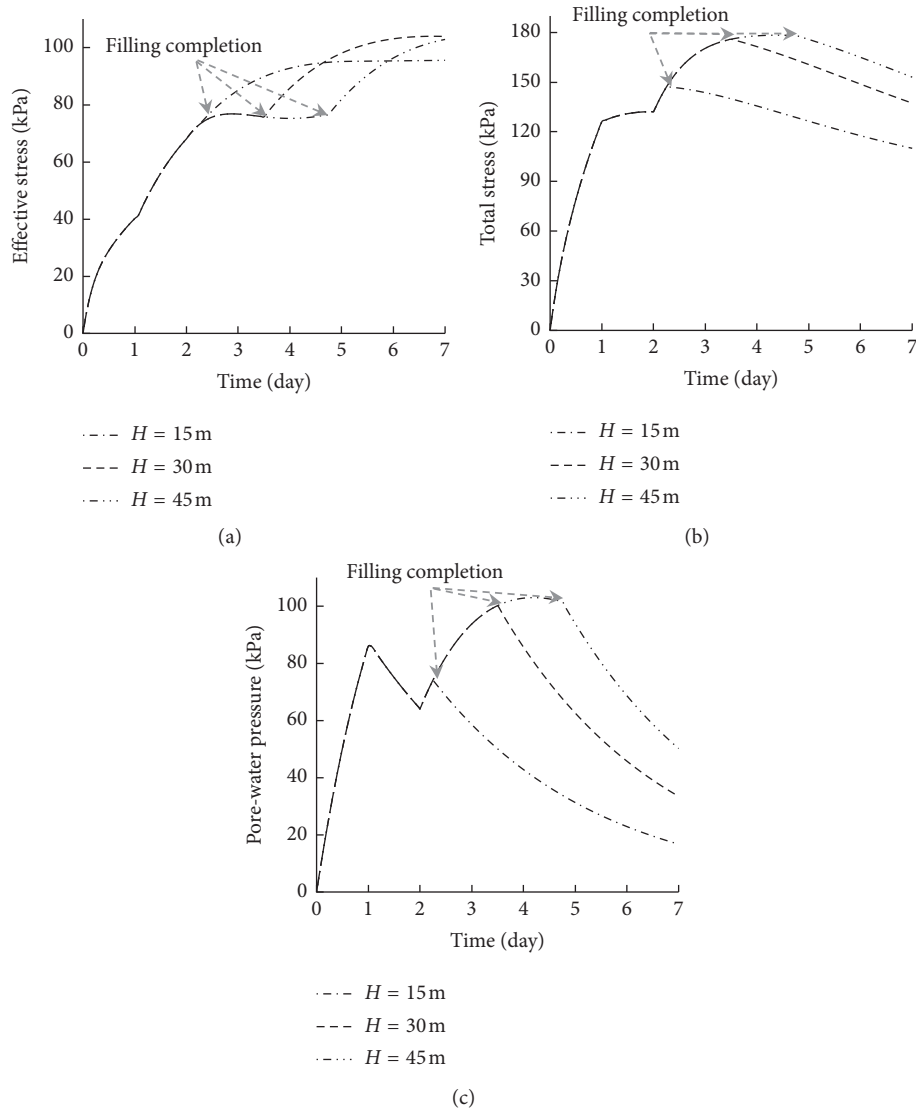
Figure 7: Effect of stope geometry on the variation of internal stress: (a) effective stress; (b) total stress; (c) PWP.

52% (178 kPa) with respect to the counterpart (117 kPa) obtained in stope with a height of 15 m. This is partly because the arching effect can reduce the total stress to a larger extent for CPB with higher height and partly because higher PWP is observed after filling operation for higher filling height case (see Figure 7(c)). The increased PWP can reduce the development of effective stress and thus further contribute to the nonlinear variation of effective stress in CPB. The obtained results are consistent with the previous study [38] on the variation of internal stress in CPB.

4.6. Effect of Rock/CPB Interface Adhesion. Due to the rock/CPB interface resistance, the resultant total vertical stress in CPB is less than its self-weight stress, namely, the arching effect is attributed to the interface interaction. The rock/CPB interface interaction consists of two components including interface friction stress and adhesion. From a mathematical point of view, the contribution of interface friction angle and

adhesion to the arching effect is same. Hence, only the interface adhesion c is selected to investigate the effect of rock/CPB interface interaction on the internal stress in CPB. For this purpose, a range of interface adhesion values: 10 kPa, 15 kPa, and 20 kPa were chosen in this study. The comparison of internal stress in CPB with different interface adhesion is presented in Figure 8. It can be observed that lower total stress is obtained in CPB with higher interface adhesion (see Figure 8(a)), namely, the arching effect is enhanced by the increased interface adhesion. Moreover, it should be noted that as indicated in equation (32), the interface adhesion only affects total stress, which means the resultant PWP is same for these three cases. Consequently, with the change of interface adhesion, the development of effective stress is dominated by the variation of total stress. Hence, the lower total stress can reduce the level of effective stress in CPB (Figure 8(b)). The obtained results show that the change of interface adhesion can significantly affect the internal stress in CPB. Therefore, the interface interaction
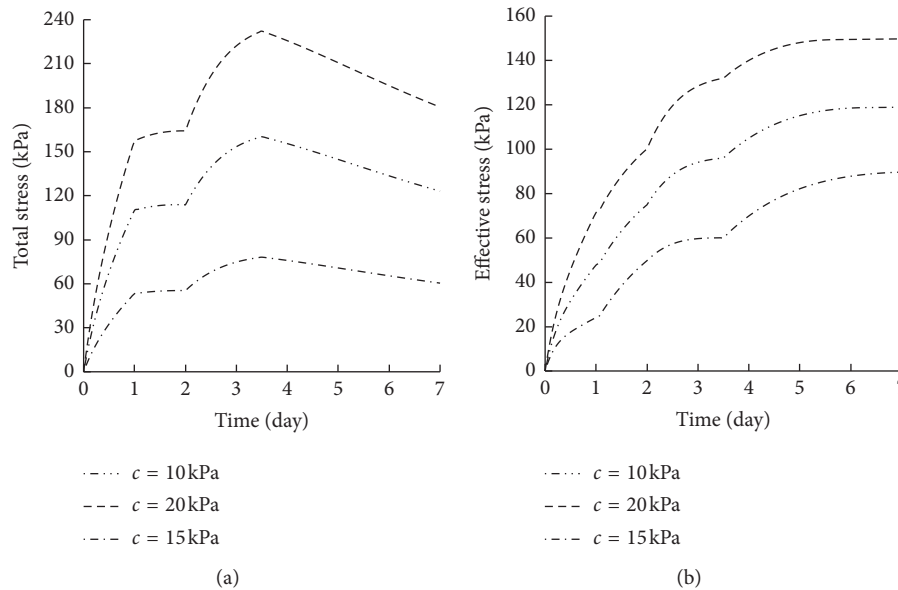
FIGURE 8: Effect of interface adhesion on the development of (a) total stress and (b) effective stress.

should be incorporated into the optimal design of CPB structure.

5. Discussion

As complex reactive porous media, the behaviour and performance of CPB are strongly affected by arching effect [48], curing conditions (e.g., temperature of surrounding rock and water drainage) [49], mix recipe (cement content, tailings types, and water-to-cement ratio) [50], and backfilling operation (filling rate and sequences) [51]. The focus of the present study is on the effect of rock/CPB interface behaviour on the internal stresses. The analytical model (equation (32)) was developed based on limit equilibrium analysis and several assumptions (including constant material properties and uniformly distributed stresses in the horizontal direction). Therefore, it is necessary to identify the associated limitations of the developed model for its engineering application and future study.

First, constant material properties are assumed in the present study. Therefore, this model is not applicable for the prediction of internal stresses under the effects of (1) binder hydration on the improvement of material properties such as the CPB cohesion and interface adhesion and (2) volume change on the porosity-dependent material properties such as hydraulic conductivity and associated development of excess PWP in CPB. Second, to perform equilibrium analysis on the representative thin-layer CPB, uniformly distributed stresses (total stress, effective stress, and PWP) are assumed in the horizontal direction. However, due to differential settlement [52] and the rock/CTB interface interaction [38] in CPB, especially for the CPB in narrow stope, the non-uniform distribution of internal stresses may develop in CPB mass. Consequently, the proposed model (equation (32)) may overestimate the arching effect in stopes. Third, it is assumed that the change of PWP is attributed to the water

drainage through the barricade. However, there exist several additional contributors (e.g., water consumption by binder hydration, water evaporation through top surface of CPB, and water exchange between CPB and fractured rock walls) to the variation of PWP in the field [51]. Consequently, the obtained results from this equation (10) may underestimate the change of PWP in CTB. The abovementioned aspects will require more work related to advanced mathematical modelling (especially the multiphysics modelling) for the reactive CPB.

6. Conclusions

Based the limit equilibrium analysis, a new 3D analytical solution was developed to predict the internal stresses (total stress, effective stress, and PWP) under the influence of rock/CPB interface interaction. In this model, the changes of the saturation state in CPB due to the water drainage through barricade and rock/CPB interface behaviour were taken into account. The model parameters were determined in terms of measurable model parameters. The uncertainties induced by model parameters were assessed by the sensitivity analysis. Moreover, the developed model was applied to address the practical problems including the effects of operation time, stope geometry, and rock/CPB interface properties on the internal stress in CPB. Based on the obtained results in the present study, the following conclusions were drawn:

(1) A 3D effective stress model is developed in this study to assess the evolution of internal stress in CPB. The model fully considers the influence of rock/CPB interface interaction, backfilling conditions, and barricade drainage.

(2) The variation of internal stress (effective stress, total stress, and PWP) in CPB can demonstrate strongly nonlinear and time-dependent characteristics.

(3) The effect of stope geometry on the total stress becomes progressively weak with the increase in filling height, which can further affect the enhancement of effective stress in CPB and thus its stability.

(4) The rock/CPB interaction significantly affects the arching effect and thus the variation of internal stress in CPB. The obtained results show that the total stress and effective stress are sensitive to the change of interface adhesion. With the increase in interface adhesion, the arching can develop to a larger extent.

(5) The reaction coefficient can affect the interface shear stress and thus the internal stress in CPB. The decreased reaction coefficient can reduce the contribution of interface shear stress to the arching effect.

The proposed analytical model can be used as a helpful tool to assess the effects of interaction between CPB mass and surrounding rock, backfilling conditions (e.g., filling strategies and stope geometry), and drainage conditions for both filling and postfilling stages. Hence, the developed model can be employed as an effective tool for the optimal design of CPB structure.

Data Availability

The data used to support the findings of this study are available from the corresponding author upon request.

Conflicts of Interest

The authors declare that they have no conflicts of interest regarding the publication of this paper.

Acknowledgments

References

[1] E. Yilmaz, T. Belem, B. Bussière, M. Mbonimpa, and M. Benzaazoua, "Curing time effect on consolidation behaviour of cemented paste backfill containing different cement types and contents," *Construction and Building Materials*, vol. 75, pp. 99–111, 2015.

[2] L. Cui and M. Fall, "An evolutive elasto-plastic model for cemented paste backfill," *Computers and Geotechnics*, vol. 71, pp. 19–29, 2016.

[3] W. Li and M. Fall, "Sulphate effect on the early age strength and self-desiccation of cemented paste backfill," *Construction and Building Materials*, vol. 106, pp. 296–304, 2016.

[4] E. Yilmaz and M. Fall, *Paste Tailings Management*, Springer International, Berlin, Germany, 2017.

[5] I. L. S. Libos and L. Cui, "Effects of curing time, cement content, and saturation state on mode-I fracture toughness of cemented paste backfill," *Engineering Fracture Mechanics*, vol. 235, p. 107174, 2020.

[6] T. Yılmaz, B. Ercikdi, and H. Deveci, "Utilisation of construction and demolition waste as cemented paste backfill material for underground mine openings," *Journal of Environmental Management*, vol. 222, pp. 250–259, 2018.

[7] Y. Wang, Y. Cao, L. Cui, Z. Si, and H. Wang, "Effect of external sulfate attack on the mechanical behavior of cemented paste backfill," *Construction and Building Materials*, vol. 263, p. 120968, 2020.

[8] T. Yılmaz, B. Ercikdi, and F. Cihangir, "Evaluation of the neutralization performances of the industrial waste products (IWPs) in sulphide-rich environment of cemented paste backfill," *Journal of Environmental Management*, vol. 258, p. 110037, 2020.

[9] T. Yılmaz, B. Ercikdi, and H. Deveci, "Evaluation of geochemical behaviour of flooded cemented paste backfill of sulphide-rich tailings by dynamic-tank leaching test," *International Journal of Mining, Reclamation and Environment*, pp. 1–20, 2020.

[10] L. Cui and M. Fall, "A coupled thermo-hydro-mechanical-chemical model for underground cemented tailings backfill," *Tunnelling and Underground Space Technology*, vol. 50, pp. 396–414, 2015.

[11] G. Lu, M. Fall, and L. Cui, "A multiphysics-viscoplastic cap model for simulating blast response of cemented tailings backfill," *Journal of Rock Mechanics and Geotechnical Engineering*, vol. 9, no. 3, pp. 551–564, 2017.

[12] M. Kermani, F. P. Hassani, E. Aflaki, M. Benzaazoua, and M. Nokken, "Evaluation of the effect of sodium silicate addition to mine backfill, Gelfill - Part 2: effects of mixing time and curing temperature," *Journal of Rock Mechanics and Geotechnical Engineering*, vol. 7, no. 6, pp. 668–673, 2015.

[13] B. Ercikdi, H. Baki, and M. İzki, "Effect of desliming of sulphide-rich mill tailings on the long-term strength of cemented paste backfill," *Journal of Environmental Management*, vol. 115, pp. 5–13, 2013.

[14] O. Nasir and M. Fall, "Shear behaviour of cemented pastefill-rock interfaces," *Engineering Geology*, vol. 101, no. 3-4, pp. 146–153, 2008.

[15] N. El Mkadmi, M. Aubertin, and L. Li, "Effect of drainage and sequential filling on the behavior of backfill in mine stopes," *Canadian Geotechnical Journal*, vol. 51, no. 1, pp. 1–15, 2013.

[16] E. Yilmaz, T. Belem, and M. Benzaazoua, "Effects of curing and stress conditions on hydromechanical, geotechnical and geochemical properties of cemented paste backfill," *Engineering Geology*, vol. 168, pp. 23–37, 2014.

[17] S. Cao, W. Song, and E. Yilmaz, "Influence of structural factors on uniaxial compressive strength of cemented tailings backfill," *Construction and Building Materials*, vol. 174, pp. 190–201, 2018.

[18] J. Fu, W. Song, and Y. Tan, "Study on microstructural evolution and strength growth and fracture mechanism of cemented paste backfill," *Advances in Materials Science and Engineering*, vol. 2016, Article ID 8792817, 13 pages, 2016.

[19] J. Wu, M. Feng, G. Han, X. Ni, and Z. Chen, "Experimental investigation on mechanical properties of cemented paste backfill under different gradations of aggregate particles and types and contents of cementing materials," *Advances in Materials Science and Engineering*, vol. 2019, Article ID 9456861, 11 pages, 2019.

[20] S. Cao and W.-d. Song, "Effect of filling interval time on long-term mechanical strength of layered cemented tailing

backfill," *Advances in Materials Science and Engineering*, vol. 2016, 2016.

[21] M. Helinski, M. Fahey, and A. Fourie, "Behavior of cemented paste backfill in two mine stopes: measurements and modeling," *Journal of Geotechnical and Geoenvironmental Engineering*, vol. 137, no. 2, pp. 171–182, 2010.

[22] J. P. Doherty, A. Hasan, G. H. Suazo, and A. Fourie, "Investigation of some controllable factors that impact the stress state in cemented paste backfill," *Canadian Geotechnical Journal*, vol. 52, no. 12, pp. 1901–1912, 2015.

[23] P. Yang, L. Li, and M. Aubertin, "A new solution to assess the required strength of mine backfill with a vertical exposure," *International Journal of Geomechanics*, vol. 17, no. 10, Article ID 04017084, 2017.

[24] L. Li, "Generalized solution for mining backfill design," *International Journal of Geomechanics*, vol. 14, no. 3, Article ID 04014006, 2014.

[25] M. Soltani and K. Maekawa, "Numerical simulation of progressive shear localization and scale effect in cohesionless soil media," *International Journal of Non-linear Mechanics*, vol. 69, pp. 1–13, 2015.

[26] L. Cui, "M. Fall, "Multiphysics model for consolidation behavior of cemented paste backfill," *International Journal of Geomechanics*, vol. 17, no. 3, Article ID 04016077, 2016.

[27] A. W. Bishop, "The principle of effective stress," *Teknisk Ukeblad*, vol. 106, no. 39, pp. 859–863, 1955.

[28] I. Vlahinić, H. M. Jennings, J. E. Andrade, and J. J. Thomas, "A novel and general form of effective stress in a partially saturated porous material: the influence of microstructure," *Mechanics of Materials*, vol. 43, no. 1, pp. 25–35, 2011.

[29] N. Khalili and M. Khabbaz, "A unique relationship for chi for the determination of the shear strength of unsaturated soils," *Geotechnique*, vol. 52, no. 1, pp. 76-77, 2002.

[30] N. Abdul-Hussain and M. Fall, "Unsaturated hydraulic properties of cemented tailings backfill that contains sodium silicate," *Engineering Geology*, vol. 123, no. 4, pp. 288–301, 2011.

[31] D. G. Fredlund and H. Rahardjo, *Soil Mechanics for Unsaturated Soils*, John Wiley & Sons, Hoboken, NJ, USA, 1993.

[32] L. Cui and M. Fall, "Numerical simulation of consolidation behavior of large hydrating fill mass," *International Journal of Concrete Structures and Materials*, vol. 14, no. 23, pp. 1–16, 2020.

[33] M. T. Van Genuchten, "A closed-form equation for predicting the hydraulic conductivity of unsaturated soils," *Soil Science Society of America Journal*, vol. 44, no. 5, pp. 892–898, 1980.

[34] N. J. F. Koupouli, T. Belem, P. Rivard, and H. Effenguet, "Direct shear tests on cemented paste backfill-rock wall and cemented paste backfill-backfill interfaces," *Journal of Rock Mechanics and Geotechnical Engineering*, vol. 8, no. 4, pp. 472–479, 2016.

[35] M. Fall and O. Nasir, "Mechanical behaviour of the interface between cemented tailings backfill and retaining structures under shear loads," *Geotechnical and Geological Engineering*, vol. 28, no. 6, pp. 779–790, 2010.

[36] L. Cui and M. Fall, "Mechanical and thermal properties of cemented tailings materials at early ages: influence of initial temperature, curing stress and drainage conditions," *Construction and Building Materials*, vol. 125, pp. 553–563, 2016.

[37] A. Ghirian and M. Fall, "Coupled thermo-hydro-mechanical-chemical behaviour of cemented paste backfill in column experiments," *Engineering Geology*, vol. 170, pp. 11–23, 2014.

[38] L. Cui and M. Fall, "Multiphysics modeling of arching effects in fill mass," *Computers and Geotechnics*, vol. 83, pp. 114–131, 2017.

[39] C. Benson, G. Bohnhoff, P. Apiwantragoon et al., "Comparison of model predictions and field data for an ET cover," in *Proceedings of Tailings And Mine Waste*, Vail, Colorado, USA, November 2004.

[40] G. H. Suazo, "Effects of Dynamic Loading on the Geomechanical Behaviour of Cemented Paste Backfill," Ph.D. Thesis, University of Western Australia, Perth, Austrailia, 2016.

[41] N. Sivakugan, R. Rankine, K. Rankine, and K. Rankine, "Geotechnical considerations in mine backfilling in Australia," *Journal of Cleaner Production*, vol. 14, no. 12-13, pp. 1168–1175, 2006.

[42] K. J. Rankine, "An Investigation into the Drainage Characteristics and Behaviour of Hydraulically Placed Mine Backfill and Permeable Minefill Barricades," Ph.D. thesis, James Cook University, Queensland, Australia, 2005.

[43] C. C. Berndt, K. J. Rankine, and N. Sivakugan, "Materials properties of barricade bricks for mining applications," *Geotechnical and Geological Engineering*, vol. 25, no. 4, pp. 449–471, 2007.

[44] M. Aubertin, B. Bussiere, and R. P. Chapuis, "Hydraulic conductivity of homogenized tailings from hard rock mines," *Canadian Geotechnical Journal*, vol. 33, no. 3, pp. 470–482, 1996.

[45] Z. Xu, X. Yang, J. Chai, Y. Qin, and Y. Li, "Permeability characteristics of tailings considering chemical and physical clogging in lixi tailings dam, China," *Journal of Chemistry*, vol. 2016, Article ID 8147845, 8 pages, 2016.

[46] V. Banks and M. Kirkham, *Hydraulic Characterisation of the Tailings Associated with the Abandoned Mine at Frongoch, Mid-Wales*, N.E.R. Council, Nottingham, UK, 2011.

[47] B. D. Thompson, W. F. Bawden, and M. W. Grabinsky, "In situ measurements of cemented paste backfill at the Cayeli Mine," *Canadian Geotechnical Journal*, vol. 49, no. 7, pp. 755–772, 2012.

[48] E. Yilmaz, "Stope depth effect on field behaviour and performance of cemented paste backfills," *International Journal of Mining, Reclamation and Environment*, vol. 32, no. 4, pp. 273–296, 2018.

[49] H. Jiang, M. Fall, and L. Cui, "Freezing behaviour of cemented paste backfill material in column experiments," *Construction and Building Materials*, vol. 147, pp. 837–846, 2017.

[50] L. Cui, "M. Fall, "Multiphysics modeling and simulation of strength development and distribution in cemented tailings backfill structures," *International Journal of Concrete Structures and Materials*, vol. 12, no. 1, p. 25, 2018.

[51] L. Cui and M. Fall, "Modeling of pressure on retaining structures for underground fill mass," *Tunnelling and Underground Space Technology*, vol. 69, pp. 94–107, 2017.

[52] E. Yilmaz, "One-dimensional consolidation parameters of cemented paste backfills," *Mineral Resources Management*, vol. 28, no. 4, pp. 29–45, 2012.

Research Article

Removal of Pb (II) from Synthetic Solution and Paint Industry Wastewater Using Activated Carbon Derived from African Arrowroot (*Canna indica*) Stem

Takele Sime Tessema [1,2] **Amare Tiruneh Adugna** [1,2] **and M. Kamaraj** [2,3]

[1]*Department of Environmental Engineering, College of Biological and Chemical Engineering, Addis Ababa Science and Technology University, Addis Ababa 16417, Ethiopia*
[2]*Bioprocess and Biotechnology Center of Excellence, Addis Ababa Science and Technology University, Addis Ababa 16417, Ethiopia*
[3]*Department of Biotechnology, College of Biological and Chemical Engineering, Addis Ababa Science and Technology University, Addis Ababa 16417, Ethiopia*

Correspondence should be addressed to Amare Tiruneh Adugna; amardugna@yahoo.com

This study aimed to investigate the potential of *Canna indica* stem-based activated carbon (CISAC) for the removal of Pb (II) ions from synthetic solution and paint industry wastewater. The effects of pH, initial Pb (II) ion concentration, and adsorbent dose were studied using an aqueous solution prepared using pure lead nitrate ($Pb(NO_3)_2$) on a batch mode. Dried *Canna indica* stem (CIS) was carbonized in a rectangular furnace at 500°C for 2 h and treated with phosphoric acid (H_3PO_4) at a ratio of 1 : 1 (w/v). Results showed that the CISAC had 5.4% of moisture, 5.0% of ash, 26.7% of volatile matter, 62.9% of fixed carbon, and 797.5 mg/g of iodine number. The Fourier Transform Infrared (FTIR) results showed that the hydroxyl, carboxyl, and phenolic functional groups were dominant in the CISAC surface. Physicochemical characteristics revealed that raw wastewater had a concentration of 4.6 mg/L Pb (II), 3 mg/L Cu (II), 171 mg/L BOD_5, 2402 mg/L COD, and 619 mg/L TSS. Better removal of Pb (II) ion from aqueous solution was achieved at a pH of 5.5, initial Pb (II) concentration of 102.4 mg/L, and an adsorbent dose of 1.4 g using response surface methodology. The highest removal efficiencies of Pb (II) which was achieved from aqueous solution and paint wastewater were 98% and 70%, respectively. The experimental data are fitted with Langmuir and Freundlich isothermic models. The results suggested CISAC as a promising adsorbent to remove Pb (II) ion from paint industry wastewater.

1. Introduction

Water and land contamination by heavy metals discharged from industrial wastes has become a global problem during the current years [1]. The rapid development of various industrial activities and technologies discharged heavy metals into the environment which highly affected the environment and human health due to their toxicity, bioaccumulation, and bioaugmentation in the food chain and persistence in nature [2]. Heavy metals like arsenic, chromium, copper, mercury, nickel, and silver are among the most widely known toxins found in modern effluents [3].

However, lead is a substantial heavy metal found in wastewater from the paint industry which is toxic to life, even at low concentrations, and can affect the nervous and reproductive system [3, 4]. To remove heavy metals from industrial effluent, precipitation, ion exchange, coagulation, electrodialysis, etc. are the most commonly used technologies [5]. These technologies have numerous disadvantages such as incomplete metal ion removal, high energy and reagent costs, and toxic sludge [6]. However, adsorption techniques look to be more attractive due to their simplicity, ease of use, high efficiency, and being economical in the removal of heavy metals from wastewater [7].

Commercial activated carbon is the most commonly used adsorbent but not cost-effective [8]. Therefore, many researchers were prompted to search for low cost and equally workable adsorbents. Conversion of lignocellulose content to activated carbon is a possible and feasible approach [1]. Some previous studies have reported the production of activated carbon from agricultural residues and other materials for removing Pb (II) ions from wastewater, for instance, Banana steam [9], Apricot stone [10], Almond shell [11], winemaking waste [12], and pine cone [13]. However, the *Canna indica* found in Ethiopia (which is planted to decorate homes and public parks) is not yet studied for its potential as an adsorbent. This research investigated the potential of *Canna indica* stem activated carbon to determine its Pb (II) ion adsorption capacity from aqueous solution and paint wastewater.

2. Materials and Methods

2.1. Preparation of the Adsorbent.
The experiment was conducted in an environmental engineering laboratory at Addis Ababa Science and Technology University. The *Canna indica* stems were collected from the locally available *canna indica* garden in Addis Ababa city, Ethiopia. Then, the stems were reduced from 1.5 to 3 cm using a knife and sun-dried for 5 days. The dirt was removed by washing with distilled water and dried in an oven at 105°C for 24 h. Then, it was ground using pestle and mortar, and a 100 g sample was taken and mixed with 100 ml of concentrated phosphoric acid (85% w/w) for 12 h. After that, it was dried in an oven at 105°C for 24 h and carbonized using a rectangular electrical muffle furnace (Nabertherm F 330) at 500°C with a heating rate of 25°C/min for 1 h [14]. The carbonized sample was then taken out of the furnace and cooled in a desiccator and continuously washed with distilled water until a neutral solution was achieved. Finally, it was dried in an oven at 105°C for 24 h, ground and sieved using 125 μm sieve, and stored in plastic bottles for further use.

2.2. Characterization of the Adsorbent.
The proximate analysis (moisture, volatile matter, ash, and fixed carbon content) and iodine number were determined with ASTM (D 2866–2869) and (D4607-94) method, respectively. The functional groups on the prepared adsorbent were determined using a Fourier Transform Infrared (Shimadzu IRAffinity-1s) spectrometer in the spectral range of 4000–400 cm^{-1} and the data were analyzed by using standard software (Origin 2018 Version 9.55). The X-ray diffraction analysis was also determined using X-ray diffraction (Rigaku Miniflex 600 diffractometer). The XRD was operated at Cu Ka, 40 kV/40 mA, and a current of 15 mA. The X-ray diffraction patterns were collected with a scan rate of 4.2°C/min and the results were analyzed using standard software (Origin 2018 Version 9.55).

2.3. Preparation of Aqueous Solution.
The lead (II) stock solution (1000 mg/L) was prepared by dissolving 1.5985 g of Pb $(NO_3)_2$ (99.8%) with 1000 ml distilled water. The lead standard working solution was prepared by using the following equation:

$$C_1 V_1 = C_2 C_2, \tag{1}$$

where C_1 is the initial concentration, C_2 is the final concentration, V_1 is the initial volume, and V_2 is the final volume

2.4. Collection and Processing of the Paint Industry Effluent.
Polythene bottle (1500 ml) was washed with tap water, thoroughly cleaned with hydrochloric acid, and resined with distilled water to make it acid-free, being used to collect the samples. The effluent samples were collected from the paint industry in Addis Ababa (the subcity of Nefas Silk Lafto (latitude: 8°58′50.29″, longitude: 38°44′57.6″)). The effluent was taken in the morning and afternoon for three days during the first week of July, as there was no further treatment. The sample was immediately transported to the laboratory allowed to settle the solids for 1 h and analyzed within 24 h. The heavy metals (Pb (II), Cu (II)) and physicochemical characteristics (BOD_5, COD, TSS, turbidity, pH, and temperature) of the effluent before and after adsorption were characterized using the APHA (2010) method.

2.5. Experimental Methods.
The experiments were done to optimize the influence of experimental factors such as pH (3, 5.5, and 8), adsorbent dose (0.5, 1, and 1.5 g), and initial concentration of Pb (II) ions (50, 100, and 150 mg/L) for the removal efficiency of Pb (II) ion from aqueous solution. Using the optimal experimental conditions, the real paint industry wastewater was examined for the removal efficiency of Pb (II) ion. The experiments were conducted in a 250 ml Erlenmeyer flask with a constant speed of 250 rpm and a contact time of 120 min at room temperature [15] on a batch basis. Then, it was filtered using 0.45 μm Whatman filter paper to separate from the adsorbent. The residual Pb (II) ion concentration was determined by using Microwave Plasma Atomic Emission Spectrometry (Agilent mp-aes 4200). All of the experiments were performed in triplicate. The removal efficiency and adsorption capacity qe (mg/g) were calculated using the following equations, respectively:

$$R = \frac{C_o - C_e}{C_o} * 100, \tag{2}$$

$$q_e = (C_o - C_e)\frac{v}{m}, \tag{3}$$

where C_o and C_e are the initial and the final Pb (II) ion concentration (mg/L), respectively, V is the adsorbate volume (L), and m is the mass of adsorbent (g).

2.6. Experiment Design and Optimization.
The experimental design for process optimization and its statistical analysis was carried out using Design Expert ® software version 7.0.0. The relationship between dependent response variables and a set of quantitative experimental factors (independent

variables) was analyzed by using the Box–Behnken factorial surface (3 levels and 3 factors). This design was utilized to determine the effect of three factors initial Pb (II) ion concentration, adsorbent dosage, and pH on the removal efficiency of Pb (II) ion using *Canna indica*-activated carbon over three levels. The ranges and levels of the experimental parameters are shown in Table 1.

The total number of experiments was determined using the following equation:

$$N = 2^F + 2F + x_o, \tag{4}$$

where N is the number of experimental runs, F represents the factor number, and x_o is the number of replicates at the central point. In this study, the values of N, F, and xo were 17, 3, and 5, respectively. The relationship between coded and actual values of variables was measured using the following equation:

$$x_i = x_i = \frac{X_i - X_o}{\Delta x}, \tag{5}$$

where x_i is the dimensionless coded value of the ith independent variable, X_o is the value of X_i at the center point, and Δx is the step change value. A second-order polynomial response surface model for the fitting of experimental data was calculated using the following equation:

$$y = b_o + \sum_i^n b_i x_i + \sum_i^n b_{ii} x^2 i \Big) + \sum_i^n b_{ij} x_{iX_j}, \tag{6}$$

where y, x_i, b_o, and b_i represent the predicted response, independent variables, constant offset term, and linear coefficients, respectively. Furthermore, b_{ii} represents the regression coefficients for the quadratic and b_{ij} represents interaction effects.

2.7. Adsorption Isotherms.
Langmuir and Freundlich isotherm models were used in this work: the Langmuir isotherm theory assumes monolayer adsorbent distribution over a homogeneous adsorbent surface. The Langmuir isotherm is presented in the following equation:

$$\frac{Ce}{qe} = \frac{Ce}{qm} + \frac{1}{K_L qm}, \tag{7}$$

where q_m is the maximum amount of metal ion adsorbed capacity (mg/g), qe is the amount of metal ion per unit mass of adsorbent at equilibrium (mg/g), K_L is a constant related to the binding energy of adsorption, and the other constants can be estimated by plotting Ce versus qe.

The Freundlich isotherm is an empirical equation describing heterogeneous surface adsorption. The Freundlich isotherm is commonly presented as shown in the following equation:

$$q_e = kfce^{1/n} \tag{8}$$

where k_f is the Freundlich constant related to adsorption capacity (mg/g) and n is the Freundlich exponent (dimensionless). By taking the logarithmic function of equation (8), it is simplified to the following equation:

Table 1: Coded and real values of operational parameters for the Box–Behnken statistical design.

Factors	Levels of Box–Behnken		
	Low (−1)	Middle (0)	High (+1)
pH (x_1)	3	5.5	8
Adsorbent dose (x_2)	0.5	1	1.5
Initial concentration (x_3)	50	100	150

$$Log q_e = Log k_f \frac{1}{n} Log c_e. \tag{9}$$

3. Results and Discussion

3.1. Proximate and Iodine Number Analysis. The results of proximate and iodine number analysis values are presented in Table 2. In observation of the data of proximate analysis, CISAc shows low ash content (5%), medium content of volatile matter (26.7%), low moisture content (5.4%), and a high percentage of fixed carbon (62.9%). The moisture content value was lower than the values reported by Olugbenga et al. [16] and Ozdemir et al. [36] while studying the activated carbon from Pawpaw (*Carica papaya*) leaf and grape stalk, respectively. This indicates that CISAC may have better removal potential due to its lower moisture content [17]. However, the volatile matter contents of this were more than the value obtained from Banana (*Musa paradisiaca*) stalk-based activated carbon [18]. The fixed carbon for CISAC was better than the activated carbons made from Banana empty fruit bunch, *Delonix regia* fruit pod [19], and pumpkin seed shell [20]. The medium content of volatile matter and the low ash content usually increase the solid yield of the carbon and produce high fixed carbon [21]. Better performance was obtained when there is a high microstructure which is directly correlated with the iodine value. The higher number of carbons in iodine was due to the presence of a large structure of micropores and the high likelihood of carbons having a large surface area due to the enlargement of their pore structure [22]. The iodine value is significantly affected by activation temperature and time (Mopoung et al. [14]) and Kumar et al. [23] reported an activation time of 1 to 2 hr, and the activation temperature within 500 to 600°C increases the microstructure.

The iodine number of the CISAC was greater than a value obtained from activated carbon from Cassava peels [24] and Lapsi (*Choerospondias axillaris*) seed stone [25]. This shows that CISAC has a better removal capacity as a higher iodine number of carbons credited to the nearness of large micropore shape and to have expansive surface vicinity due to the broadening of their pore structure [26].

3.2. FTIR Analysis of CISAC. Table 3 presents the FTIR spectral characteristics of CISAC based on pH (7 and 5.5), initial Pb (II) ion concentration (0 and 50 mg/L), and adsorbent dosage (1 and 1.5) before and after Pb (II) ion adsorption, respectively. The FTIR spectrum of the activated carbon shows a significant difference in peak frequencies due

TABLE 2: The proximate and iodine number analysis for CISAC.

Parameters	Value (%)
Moisture	5.4
Ash	5.0
Volatile matter	26.7
Fixed carbon (%)	62.9
Iodine number (mg/g)	797.5

TABLE 3: FTIR spectral characteristics of CISAC before and after Pb (II) ion adsorption.

FTIR peak	Assigned functional groups	Band wave number (cm^{-1})		
		Before	After	Shift differences
1	Hydroxyl (O-H)	3450	3394	56
2	Methyl and methylene (C-H)	2374	2368	6
3	Methyl and methylene (C-H)	2291	2291	0
4	Acetyl (C=O)	1620	1606	14
5	Carbonyl (CC)	1383	1320	63
6	Nitrate (NO_2)	1313	1236	77
7	Aryl (C-O)	1166	1152	14
8	Aryl (C-O)	1040	398	642

to the binding of Pb (II) ion with active sites of the activated carbon indicating the presence of ionizable functional groups on the activated carbon which has the potential to interact with other cations [4].

The FTIR spectra of CISAC before and after adsorption of Pb (II) ion are revealed in Figure 1. The recorded spectra give different adsorption peaks which represent the presence of various functional groups in the CISAC. The spectra of CISAC before adsorption of Pb (II) ion band at $3450\,cm^{-1}$ representing stretching vibrations of O-H in hydroxyl group and band at $2374\,cm^{-1}$ assigned to C-H stretching indicate the methyl and methylene [27]. Besides band at $1620\,cm^{-1}$ stretching of the acetyl group in hemicellulose, band at $1383\,cm^{-1}$ indicated stretching in the aromatic ring, band at $1313\,cm^{-1}$ attributed to N-O stretching vibration, and band at $1166\,cm^{-1}$ and $1040\,cm^{-1}$ associated with the C-O stretching of the aryl group in lignin, respectively [21]. All of the assigned wave numbers of CISAC after adsorption are different from before adsorption except for one of them where many wavenumbers shift during the adsorption process.

3.3. XRD Analysis.

X-ray diffraction was used to assess the presence of amorphous and crystalline between the matrixes of carbon. The X-ray powder diffraction spectra are presented in Figure 2. According to the powder diffraction results, the CISAC shows two broad intense peaks at $2\Theta = 23°$ and $2\Theta = 24°$. These were a sign of crystalline graphite formation inside the carbon [28]. The spectra pattern exhibits a persistent decrease in crest concentration as a result collapse of the graphite layers. This can be an ordinary amorphous carbon arrangement [29].

3.4. Paint Industry Untreated and Treated Wastewater Characteristics.

Table 4 presents the untreated and treated wastewater characteristics collected from the paint industry. The concentrations of most parameters for the untreated wastewater, except for pH and temperature, were above the WHO standard. Particularly, the Pb (II) ions concentration was 46 times higher than the standard; hence, it must be removed to avoid environmental risks.

The treated wastewater characteristics were below the standard set by WHO (2017) except for COD and TSS. Hence, further treatment is needed to remove the excess COD and TSS before disposing to the environment. Though the research was concentrated on Pb (II) removal, [30] reported the biochar made from *Canna indica* has the potential to remove cadmium from an aqueous solution which shows that it might have a potential to remove other heavy metals.

3.5. Effects of Individual Factors on Pb (II) Ion Removal Efficiency

3.5.1. Effects of pH.

The influences of pH were investigated in the range of 3–8 under constant initial Pb (II) concentration of 100 mg/L, a contact time of 120, and an adsorbent dose of 1.5 g. Figure 3(a) displays the Pb (II) ions removal efficiency was increased when the solution of pH increased from 3 to 5.5. The better removal of Pb (II) ion was achieved at pH 5.5 while the removal decreased under highly acidic and moderate basic conditions. A similar finding was reported by Gundogdu et al. [31]. At a highly acidic pH, the overall surface charge on the active site becomes positive and metal cations and protons compete for the binding site of the adsorbent [32]. The removal efficiency was decreased when the values of pH increased from 5.5 to 8. In this condition, Pb (II) ions were precipitated in the form of Pb $(OH)_2$ [33]. Related trends were reported for the adsorption of Pb (II) ions on the activated carbon prepared from coconut shell [34].

3.5.2. Effects of Initial Pb (II) Ions Concentration.

The better removal was achieved at the initial Pb (II) ion concentration of 50 mg/L (Figure 3(b)). The elimination of Pb (II) ion was decreased with the increase in concentration from 50 to 150 mg/L; because of low concentration, there is a low number of lead ions to the ration of the surface-active site found in the adsorbent surface. Therefore, all of the lead ions may interact with the active site. In contrast when higher initial concentration proved more lead ion for being attached on the adsorbent surface, as a result, the active site is not sufficient and saturation in the adsorbent has happened which resulted in the reduction of removal efficiency.

3.5.3. Effects of Adsorbent Dosage.

The effect of an adsorbent dose was investigated by altering the adsorbent in the range of 0.5–1.5 g/100 ml. The fixed parameters were pH of 5.5, a contact time of 120 min, and an initial Pb (II) ion concentration of 100 mg/L. Figure 3(c) shows the removal of Pb (II) ion was increased while the adsorbent dose increased

(a)

(b)
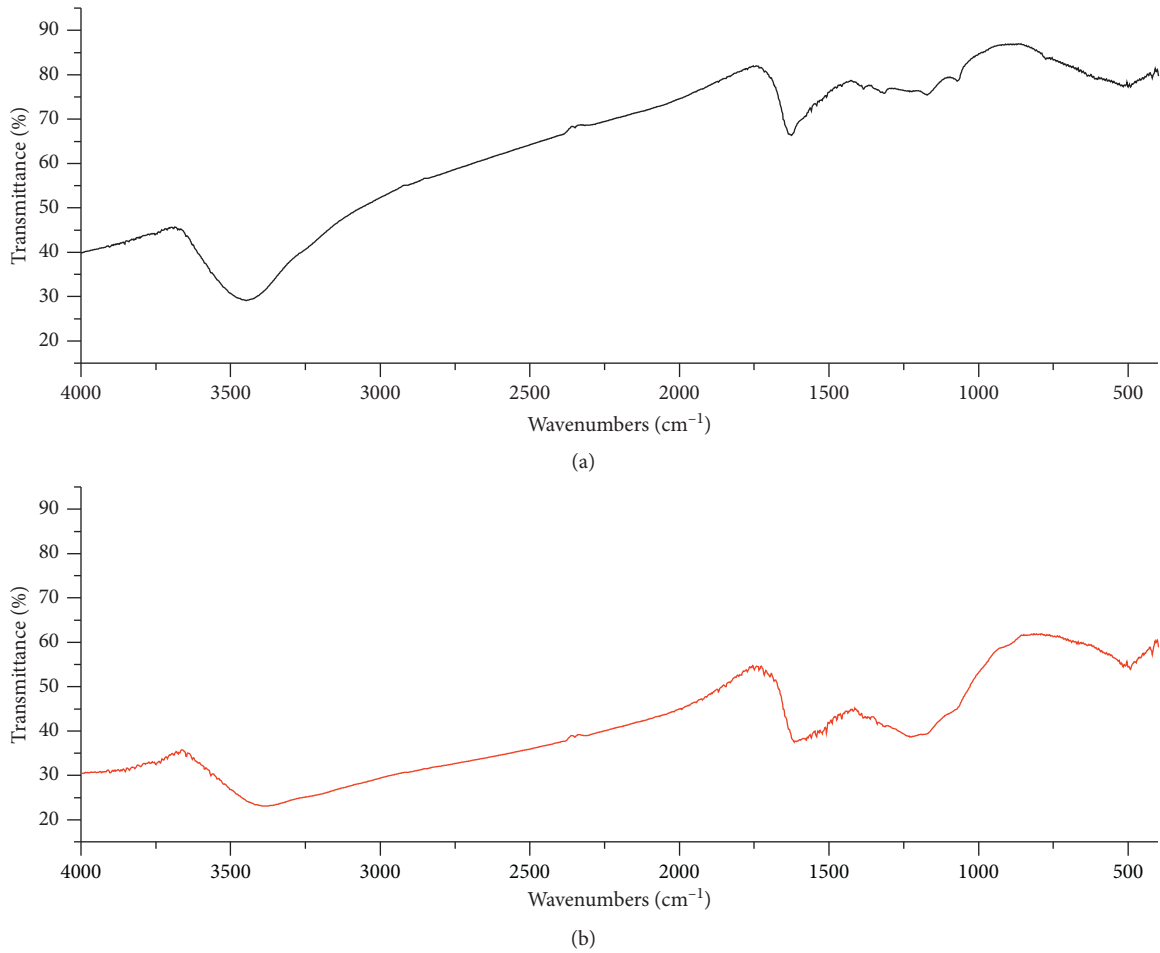
FIGURE 1: FTIR analysis of CISAC before (a) and after (b) Pb (II) ion adsorption.
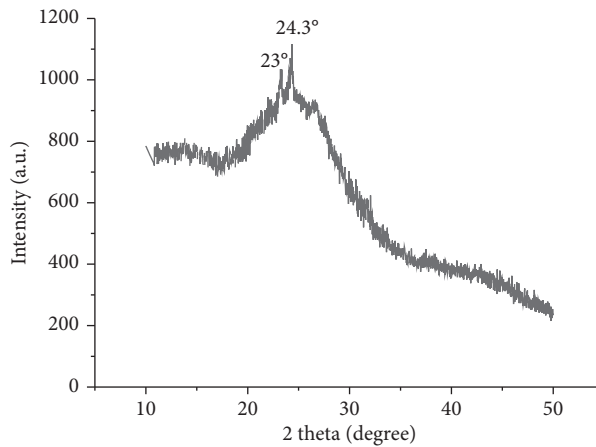
FIGURE 2: XRD analysis of CISAC.

from 0.5 to 1.5 g. It is due to a constant initial concentration whilst growing the adsorbent dose gives a higher adsorption surface area. However, a reverse trend was observed for adsorption capacity. A similar result was reported in the elimination of Pb (II) ion from aqueous solution using bamboo-based activated carbon as adsorbent [35]. The elimination of lead (II) increased with an increase in the adsorbent dosage and then it remains almost constant which leads to better removal at 1.5 g of adsorbent.

3.6. Process Optimization and Effects of Factors Interaction Response Surface Methodology. 3D plots can be drawn for a different combination of parameters which show the trend of

TABLE 4: Paint industry wastewater (untreated and treated) characteristics.

Parameters	Unit	Untreated wastewater	Treated wastewater	Maximum limited value (WHO, 2017)
pH	pH unit	5.3	6.5	6.5–9.2
Temperature	°C	20.6	20	40
Turbidity	NUT	255	10	—
BOD_5	mg/L	171	25	40
COD	mg/L	2402	150	120
TSS	mg/L	619	138	45
Pb (II)	mg/L	4.6	0.428	0.1
Cu (II)	mg/L	3	0.268	1
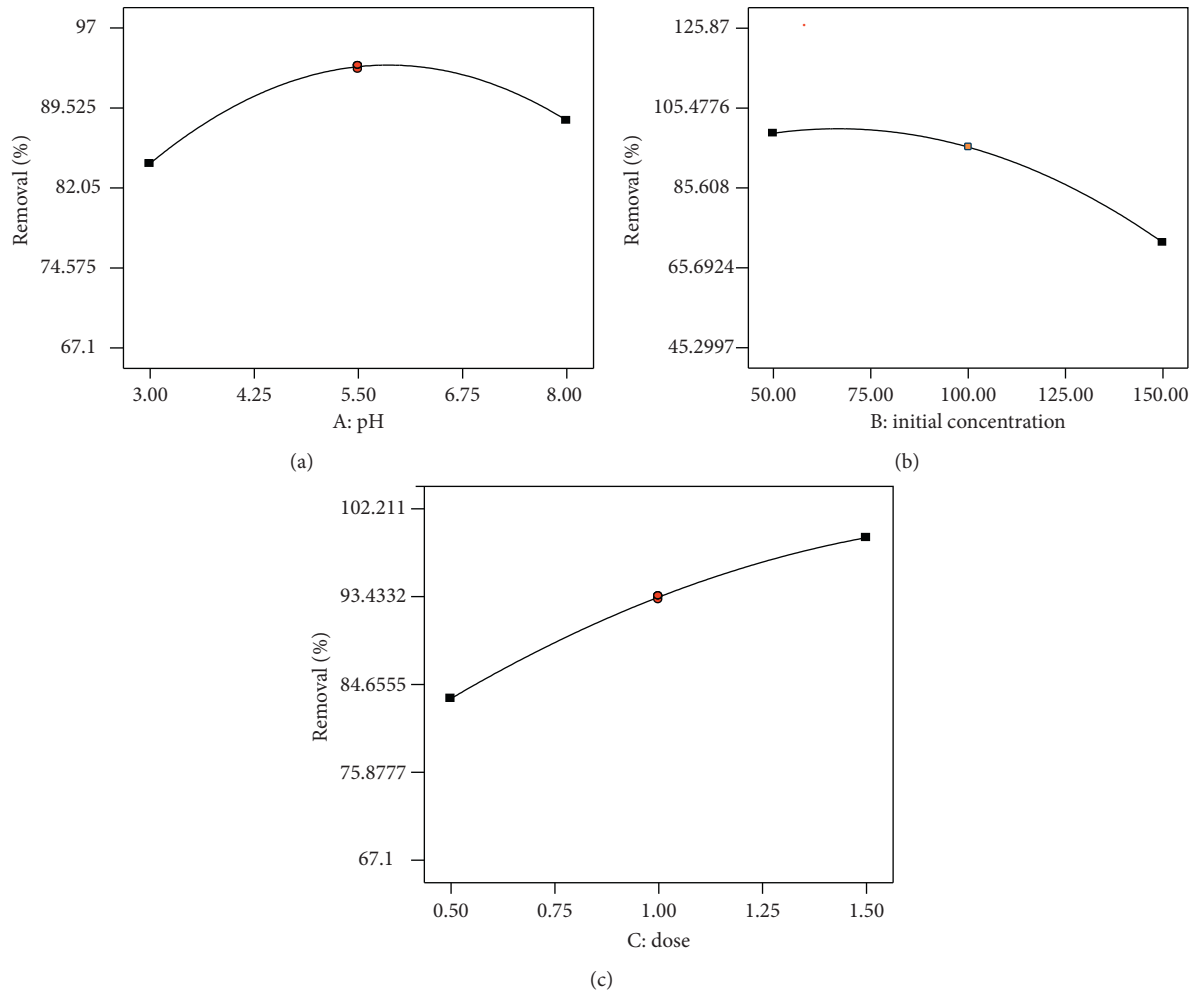
FIGURE 3: Individual effects of pH (a); initial Pb (II) ions concentration (b); and adsorbent dosage (c) on Pb (II) adsorption by CISAC.

variation of response within the selected range of input factors ((pH, initial Pb (II) ions concentration, and an adsorbent dose) and the influence of each parameter over the other parameters. Few such typical plots are shown in Figure 4.

Figure 4(a) shows the 3D plot, the combined effects of pH (x_1), and initial Pb (II) ion concentration (x_2) on the elimination efficiency of Pb (II) ion by keeping the adsorbent dose constant. The result from Figure 4(a) indicates that the elimination efficiency was increased with an increase in the solution of pH from 3 to 5.5 with decreasing the Pb (II) ion concentration from 150 to 50 mg/L and then decreased when further increasing pH from 5.5 to 8.

The 3D surface plot in Figure 4(b) displays the Pb (II) ion removal efficiency as the combined effects of adsorbent dose (x_3) and pH (X_1) in maintaining the initial Pb (II) ion concentration constant. The removal of Pb (II) ion decreased when the pH decreased from 5.5 to 3 with the decrease in the adsorbent dose from 1.5 to 0.5 g. Then, the removal efficiency increased when the pH decreased from 8 to 5.5 and the adsorbent dose increased from 0.5 to 1.5 g.

The 3D plot which was constructed to show the most significant two factors of adsorbent dose (X_3) and initial Pb (II) ion concentration (x_2) with keeping pH constant is revealed in Figure 4(c). From Figure 4(c), it can be observed

(a)

(b)

(c)
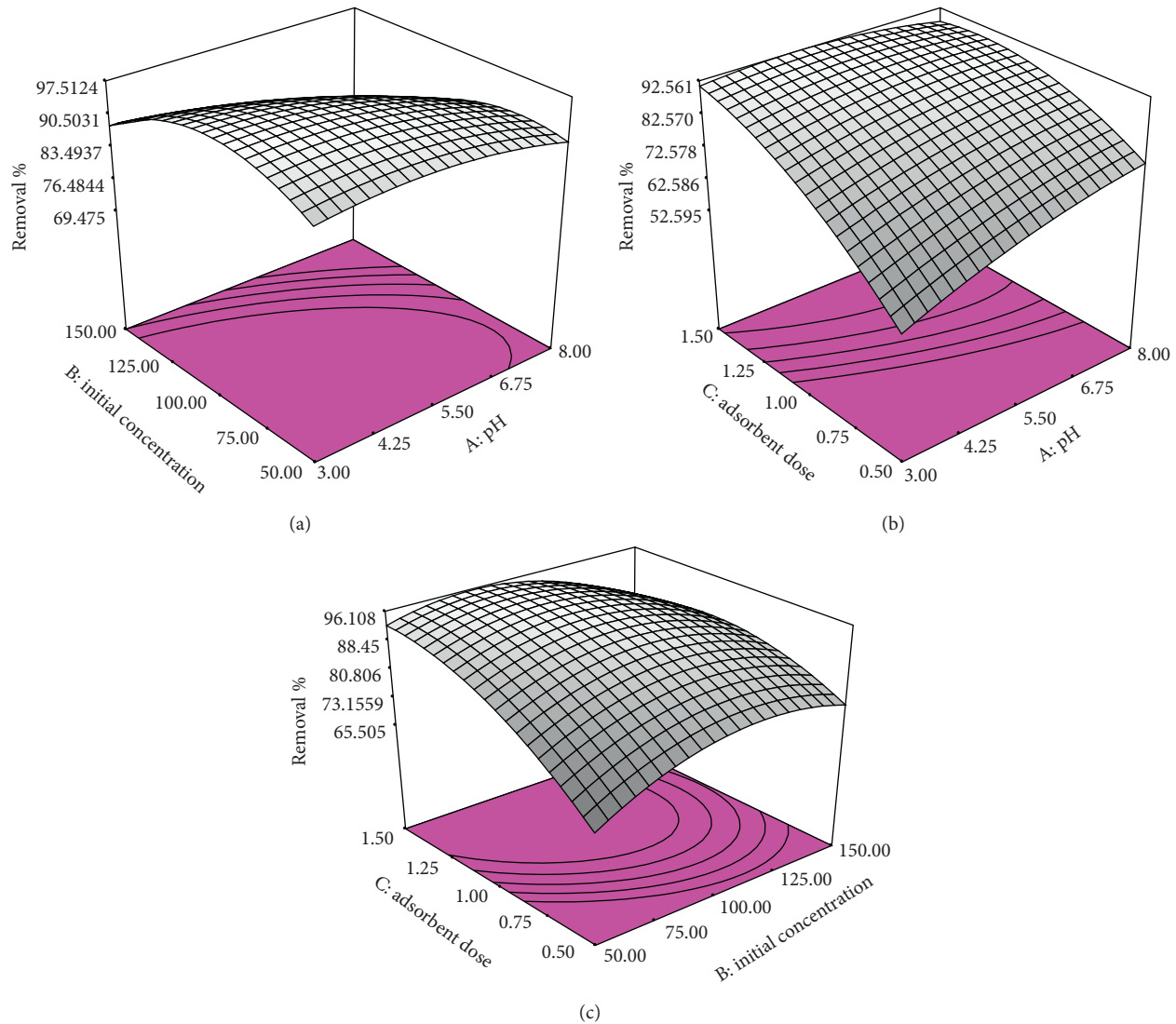
Figure 4: Surface plots for the effects of (a) the solution of pH and initial Pb (II) ion concentration; (b) initial Pb (II) ion concentration and (c) adsorbent dose; and (c) adsorbent dose and initial Pb (II) concentration on the removal (%).

that the adsorption capacity increased when the adsorbent dose increased from 0.5 to 1.5 g and the initial Pb (II) ion concentration decreased from 150 to 50 mg/L. The increase in the adsorbent dose provided a greater surface area or increased available adsorptions sites which increased the amount of Pb (II) adsorbed.

The optimization process was performed by numerical optimization defined in the Design-Expert software. In numerical optimization, the program seeks to maximize the desirability function to create the optimal condition. All the three factors and Pb (II) removal efficiency were set in experimental ranges for the maximum desirability. Optimization was done by considering the values of parameters for better removal for Pb (II) ion from aqueous solution using CISAC, that is, pH value of 5.5, adsorbent dose of 1.35 g, and initial Pb (II) ions concentration of 102.37 mg/L with the desirability of 1 (Figure 5). Therefore, using these values, the removal efficiencies of Pb (II) ion from aqueous solution and paint industry wastewater were found to be

98% and 70%. Pb (II) ion removal efficiency of CISAC in paint wastewater was much lower than in aqueous solution because paint industry wastewater contained different types of heavy metals (Cu^{+2}, Cr^{+3}, and Zn^{+2}), binders, additives, biological oxygen demand (BOD_5), chemical oxygen demand (COD), total suspended solids and turbidity that affected the Pb (II) ion removal efficiency by competing one another in the adsorbent site.

3.7. Adsorption Equilibrium Isotherm Studies. The equilibrium isotherm experiments were carried out using 1.5 g/100 ml of *Canna indica* activated carbon with pH of 5.5 and the initial Pb (II) ions concentrations (50, 100, and 150 mg/L) under room temperature. The adsorbate-adsorbent solutions were mixed at a constant speed of 250 rpm for an equilibrium time of 120 min. Figures 6(a) and 6(b) represent the Langmuir and Freundlich isotherm adsorption of Pb (II) ion on CISAC, and Table 5 shows the parameters of these
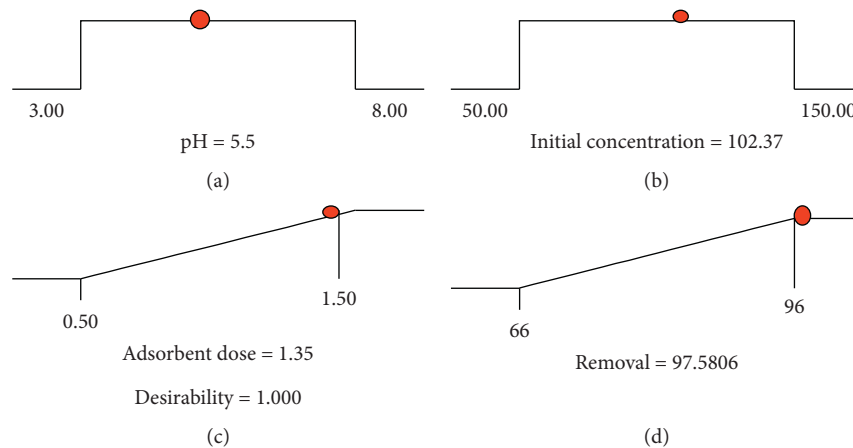
FIGURE 5: Desirability ramp for numerical optimization of four goals, namely, the solution pH (a), initial Pb (II) ion concentration (b), adsorbent dose (c), and removal efficiency (d).
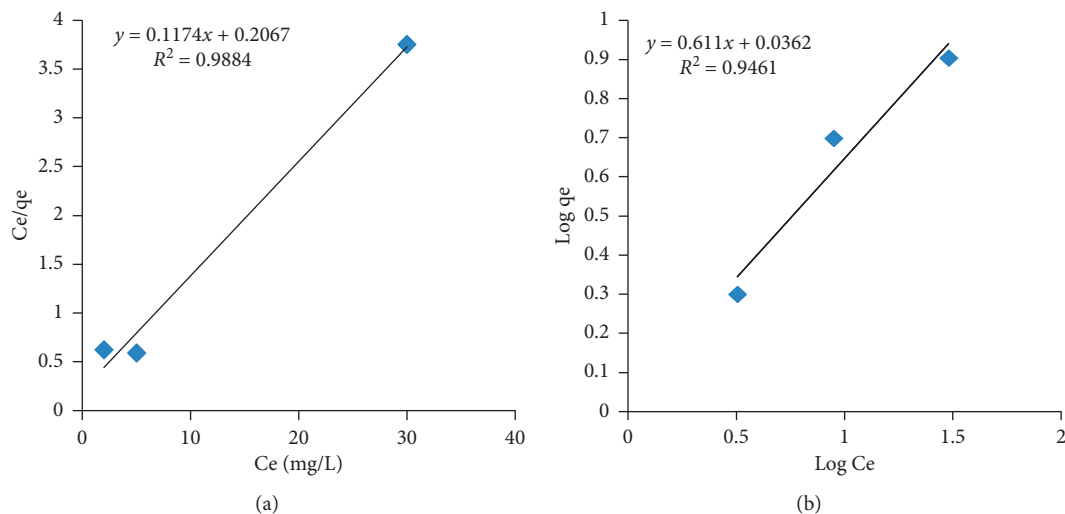
FIGURE 6: Langmuir plot (a) and Freundlich plot (b) for Pb (II) ion adsorption on CISA.

TABLE 5: The isotherm parameters of Langmuir and Freundlich for Pb (II) adsorption by CISAC.

Langmuir parameters			Freundlich parameters			
q_m (mg/g)	K_L (L/mg)	R^2	k_f (mg/g)	n	$1/n$	R^2
8.52	0.57	0.9884	1.44	1.64	0.61	0.9461

isotherms. The correlation coefficients (R^2) of Langmuir and Freundlich isotherms models are 0.9884 and 0.9461, respectively. Thus, the adsorption of Pb (II) on CISAC fits the model of Langmuir very well.

4. Conclusion

The present study shows that CISAC is a good adsorbent for the removal of Pb (II) ions from aqueous solution and paint industry wastewater. Better removal (98%) was achieved at an initial Pb (II) ion concentration of 102.4 mg/L, an adsorbent dosage of 1.4 g, and pH of 5.5. With the same

condition, 69.7% of Pb (II) ion was removed from the paint industry wastewater. The performance of the CISAC for the removal of Pb (II) ion in the paint industry wastewater was much lower than in aqueous because the paint industry wastewater contains various types of pollutants. Adsorption isotherm showed that the Langmuir isotherm model provides the best correlation of R^2 (0.9884). The treated wastewater characteristics were below the standard set by WHO (2017) except for COD and TSS. Hence, further treatment is needed to remove the excess COD and TSS before disposing to the environment. The findings of the current study suggest that the adsorption process using

CISAC is an environmentally friendly and effective adsorbent for the removal of Pb (II) ions from aqueous solution and paint industry wastewater. However, it is suggested that CISAC might have the potential to remove other heavy metals, and further studies are recommended for the authentication.

Data Availability

The information used in this study can be obtained from the corresponding author upon request.

Conflicts of Interest

The authors have no conflicts of interest.

Acknowledgments

References

[1] J. Ocreto, C. I. Go, J. C. Chua, C. J. Apacible, and A. Vilando, "Competitive effects for the adsorption of copper, cadmium and lead ions using modified activated carbon from bambo," *MATEC Web of Conferences*, vol. 268, Article ID 6021, 2019.

[2] J. He and J. P. Chen, "A comprehensive review on biosorption of heavy metals by algal biomass: materials, performances, chemistry, and modeling simulation tools," *Bioresource Technology*, vol. 160, pp. 67–78, 2014.

[3] E. Bernard, A. Jimoh, and J. Odigure, "Heavy metals removal from industrial wastewater by activated carbon prepared from coconut shell," *Research Journal of Chemical Sciences*, vol. 2231, p. 606x, 2013.

[4] M. Sobh, M. A. Moussawi, W. Rammal et al., "Removal of lead (ii) ions from waste water by using lebanese cymbopogon citratus (lemon grass) stem as adsorbent," *American Journal of Phytomedicine and Clinical Therapeutics*, vol. 2, pp. 1070–1080, 2014.

[5] A. M. El-wakil, E. M. W. M. Abou, and F. S. Awad, "Removal of lead from aqueous solution on activated carbon and modified activated carbon prepared from dried water hyacinth plant," *Journal of Analytical & Bioanalytical Techniques*, vol. 5, pp. 1–14, 2014.

[6] Z.-J. Yi, J. Yao, Y.-F. Kuang, H.-L. Chen, F. Wang, and Z.-M. Yuan, "Removal of pb (ii) by adsorption onto Chinese walnut shell activated carbon," *Water Science and Technology*, vol. 72, pp. 983–989, 2015.

[7] I. C. Chukwujike, C. Ewulonu, S. C. Nwanonenyi, and I. Uche, "Adsorption treatment of industrial paint effluent for the removal of pollutants by local clays," *International Journal of Scientific and Engineering Research*, vol. 6, no. 10, pp. 690–703, 2015.

[8] M. Auta and B. H. Hameed, "Preparation of waste tea activated carbon using potassium acetate as an activating agent for adsorption of acid blue 25 dye," *Chemical Engineering Journal*, vol. 171, no. 2, pp. 502–509, 2011.

[9] O. Ogunleye, O. Adio, and T. Salawudeen, "Removal of lead (ii) from aqueous solution using banana (musa paradisiaca) stalk-based activated carbon," *Chemical and Process Engineering Research*, vol. 28, pp. 45–59, 2014.

[10] L. Mouni, D. Merabet, A. Bouzaza, and L. Belkhiri, "Adsorption of Pb (II) from aqueous solutions using activated carbon developed from Apricot stone," *Desalination*, vol. 276, no. 1–3, pp. 148–153, 2011.

[11] P. V. Thitame and S. R. Shukla, "Removal of lead (ii) from synthetic solution and industry wastewater using almond shell activated carbon," *Environmental Progress & Sustainable Energy*, vol. 36, pp. 1628–1633, 2017.

[12] F. Alguacil, l. Alcaraz, I. García-Díaz, and F. López, "Removal of pb2+ in wastewater via adsorption onto an activated carbon produced from winemaking waste," *Metals*, vol. 8, no. 9, p. 697, 2018.

[13] M. Momčilović, M. Purenović, A. Bojić, A. Zarubica, and M. Ranđelović, "Removal of lead (ii) ions from aqueous solutions by adsorption onto pine cone activated carbon," *Desalination*, vol. 276, pp. 53–59, 2011.

[14] S. Mopoung, P. Moonsri, W. Palas, and S. khumpai, "Characterization and properties of activated carbon prepared from tamarind seeds by koh activation for fe (iii) adsorption from aqueous solution," *The Scientific World Journal*, vol. 2015, Article ID 415961, 9 pages, 2015.

[15] S. Uwadiae and O. Edokpiawe, "Modelling and optimization of lead adsorption from aqueous solution using groundnut shell," *Acta Technica Corvininesis-Bulletin of Engineering*, vol. 12, 2019.

[16] O. S. Bello, A. Inyinbor, A. O. Dada, and A. A. Kayode, "Preparation and characterization of modified adsorbents derived from pawpaw (carica papaya) leaf," *International Proceedings of Chemical, Biological and Environmental Engineering*, vol. 96, pp. 64–70, 2016.

[17] S. M. Anisuzzaman, C. G. Joseph, W. M. A. B. W. Daud, D. Krishnaiah, and H. S. Yee, "Preparation and characterization of activated carbon from typha orientalis leaves," *International Journal of Industrial Chemistry*, vol. 6, no. 1, pp. 9–21, 2015.

[18] O. O. Ogunleye, M. A. Ajala, and S. E. Agarry, "Evaluation of biosorptive capacity of banana (<i>Musa paradisiaca</i>) stalk for lead (ii) removal from aqueous solution," *Journal of Environmental Protection*, vol. 5, pp. 1451–1465, 2014.

[19] P. Sugumaran, V. P. Susan, P. Ravichandran, and S. Seshadri, "Production and characterization of activated carbon from banana empty fruit bunch and delonix regia fruit pod," *Journal of Sustainable Energy & Environment*, vol. 3, pp. 125–132, 2012.

[20] I. Demiral and C. Şamdan, "Preparation and characterisation of activated carbon from pumpkin seed shell using h3po4," *Anadolu University Journal of Science and Technology-A Applied Sciences and Engineering*, vol. 17, no. 1, pp. 125–138, 2016.

[21] M. S. Shamsuddin, N. R. N. Yusoff, and M. A. Sulaiman, "Synthesis and characterization of activated carbon produced from kenaf core fiber using H_3PO_4 activation," *Procedia Chemistry*, vol. 19, pp. 558–565, 2016.

[22] O. A. Ekpete, A. C. Marcus, and V. Osi, "Preparation and characterization of activated carbon obtained from plantain (Musa paradisiaca) fruit stem," *Journal of Chemistry*, vol. 2017, Article ID 8635615, 6 pages, 2017.

[23] B. P. Kumar, K. Shivakamy, L. R. Miranda, and M. Velan, "Preparation of steam activated carbon from rubberwood sawdust (Hevea brasiliensis) and its adsorption kinetics," *Journal of Hazardous Materials*, vol. 136, no. 3, pp. 922–929, 2006.

[24] I. R. Ilaboya, E. Oti, G. Ekoh, L. Umukoro, and A. Ibiam, "Performance of activated carbon from cassava peels for the treatment of effluent wastewater," *Iranica Journal of Energy and Environment*, vol. 4, no. 4, pp. 361–370, 2013.

[25] S. Joshi and B. P. Pokharel, "Preparation and characterization of activated carbon from lapsi (choerospondias axillaris) seed stone by chemical activation with potassium hydroxide," *Journal of the Institute of Engineering*, vol. 9, pp. 79–88, 2013.

[26] S. Adhikaria, B. Pokharel, V. Gurung, R. M. Shrestha, and R. Rajbhandari, "Preparation and characterization of activated carbon from walnut (jaglansregia) shells by chemical activation with zinc chloride (ZnCl2)," in *Proceedings of the IOE Graduate Conference*, Kathmandu, Nepal, December 2019.

[27] J. Chen, L. Zhang, G. Yang, Q. Wang, R. Li, and L. A. Lucia, "Preparation and characterization of activated carbon from hydrochar by phosphoric acid activation and its adsorption performance in prehydrolysis liquor," *BioResources*, vol. 12, no. 3, pp. 5928–5941, 2017.

[28] X. S. Wang, H. J. Lu, L. Zhu, F. Liu, and J. J. Ren, "Adsorption of lead (ii) ions onto magnetite nanoparticles," *Adsorption Science & Technology*, vol. 28, pp. 407–417, 2010.

[29] M. Om Prakash, G. Raghavendra, S. Ojha, and M. Panchal, "Characterization of porous activated carbon prepared from arhar stalks by single step chemical activation method," *Materials Today: Proceedings*, 2020.

[30] X. Cui, S. Fang, Y. Yao et al., "Potential mechanisms of cadmium removal from aqueous solution by Canna indica derived biochar," *Science of the Total Environment*, vol. 562, pp. 517–525, 2016.

[31] A. Gundogdu, D. Ozdes, C. Duran, V. N. Bulut, M. Soylak, and H. B. Senturk, "Biosorption of Pb (II) ions from aqueous solution by pine bark (Pinus brutia Ten.)," *Chemical Engineering Journal*, vol. 153, no. 1–3, pp. 62–69, 2009.

[32] Y. Li, Q. Du, X. Wang et al., "Removal of lead from aqueous solution by activated carbon prepared from Enteromorpha prolifera by zinc chloride activation," *Journal of Hazardous Materials*, vol. 183, no. 1–3, pp. 583–589, 2010.

[33] M. A. Khan, A. Alemayehu, R. Duraisamy, and A. K. Berekete, "Removal of lead ion from aqueous solution by bamboo activated carbon," *International Journal of Water Research*, vol. 5, pp. 33–46, 2015.

[34] M. Sekar, V. Sakthi, and S. Rengaraj, "Kinetics and equilibrium adsorption study of lead (ii) onto activated carbon prepared from coconut shell," *Journal of Colloid and Interface Science*, vol. 279, pp. 307–313, 2004.

[35] N. Udeh and J. Agunwamba, "Equilibrium and kinetics adsorption of cadmium and lead ions from aqueous solution using bamboo based activated carbon," *The International Journal Of Engineering and Science*, vol. 6, pp. 17–26, 2017.

[36] I. Ozdemir, M. Sahin, R. Orhan, and M. Erdem, "Preparation and characterization of activated carbon from grape stalk by zinc chloride activation," *Fuel Processing Technology*, vol. 125, pp. 200–206, 2014.

Research Article

Valorization of Food Waste to Produce Eco-Friendly Means of Corrosion Protection and "Green" Synthesis of Nanoparticles

Georgii Vasyliev [ID] **and Victoria Vorobyova** [ID]

Department of Chemical Technology, National Technical University of Ukraine "Igor Sikorsky Kyiv Polytechnic Institute", Kyiv 03056, Ukraine

Correspondence should be addressed to Georgii Vasyliev; g.vasyliev@kpi.ua

Agrifood by-products are a key element within Europe's sustainable strategies. Valorization and reuse of zero-waste technologies are becoming more popular, and they are commonly named as "second-generation food waste management." The present study is directed to the valuable extracts of "green" organic compounds from the by-products of fruit and berry/vegetable crops, which can be revalorized in sustainable chemical technology and engineering, namely, in the production of "green" synthesis of nanoparticles and for the inhibition of corrosion and scaling of metals in corrosive media. Numerous types of agrifood by-products (rapeseed pomace, sugar beet pulp, fodder radish cake, grape pomace, and pomegranate peels) were investigated. The waste extracts for corrosion and scale inhibitors of mild steel in tap water were prepared by the conventional extraction method that uses 2-propanol and characterized by gas chromatography-mass spectroscopy (GC-MS). Inhibition of scaling and corrosion was investigated in thermal scaling conditions on the surface of the electrode manufactured from mild steel. The LPR technique was applied to measure the corrosion rate, and the scaling rate was determined gravimetrically. The extracts were found to inhibit the corrosion rate 2-3 times, while only radish cake extract inhibited both the corrosion and scaling rates. The waste extracts to produce nanoparticles were prepared by the ultrasound-assisted water extraction with subsequent oxidation by oxygen purge and characterized by liquid chromatography-mass spectroscopy (LC-MS). The aqueous grape pomace and pomegranate peel extracts were screened for total phenolic content (TPC) and total flavonoid content (TFC). The reduction capacity of the extracts was assessed using ferric reducing power (FRAP) and phosphomolybdenum (PM) assays. AgNPs were characterized by UV-Vis spectroscopy, dynamic light scattering (DLS), Fourier transform infrared spectroscopy (FT-IR), scanning electron microscope (SEM), and energy-dispersive X-ray spectroscopy (EDX) analysis. The particle size of AgNPs ranged between 40 and 50 nm. The antimicrobial activity of AgNPs was tested against *Escherichia coli* using the agar diffusion method and optical density.

1. Introduction

Integrated utilization or recycling of food waste is a progressive direction of resource conservation. In almost every country in the world, the most important advances in scientific and technological progress and worldwide experience in the recycling of household and vegetable waste are used [1]. Within this direction is the idea of introducing into production not only low-waste but also zero-waste technologies. Involvement of waste in chemical technology production processes as a secondary raw material makes it possible to turn it into a valuable product, followed by its

widespread use in the chemical materials industry [2–5], pharmaceutical, and cosmetic industries [6]. A significant amount of waste is generated in the processing of vegetable, fruit, and berry crops. Almost all these wastes are valuable secondary raw materials because they contain natural organic compounds. Therefore, the priority direction for the development of green chemical technology and engineering is the search and use of recycling materials for the receiving of organic compounds (plant extracts) from the waste of vegetable raw materials as well as the study of their composition and physicochemical properties. Further obtained extracts of "green" organic compounds can be used in the

production of "green" synthesis of nanoparticles [7–11], for inhibition of corrosion and scaling of metals in corrosive media [12–16] and production of food additives and valuable nutrients, as a natural preservative and antioxidant in cosmetic products [17–19].

The food industry is an integrated branch of the agro-industrial sector and includes the processing of fruit, berry, and vegetable crops. Most waste is generated in the production of food products and in the beverage industry, which include pomaces of berries and vegetable and skins and stems of vegetable raw materials. The grape and pomegranate are widely cultivated in Ukraine and other European countries. Besides being consumed fresh, these are grown commercially to be processed into juices, jams, jellies, and nutraceutical ingredients. Similarly, pomace accounts for approximately 30% of the total waste of juice industry. After juice pressing, the waste pomegranate peels account for 12 wt% of the fruit. In the grape juice industry, about 45% of grape is utilized for juice and the remained part constitutes grape pomace. Moreover, several studies have demonstrated that fruit pomaces display antioxidant and radical scavenging activity. According to the composition of grape pomace and pomegranate peel extracts, they contain a large amount of phenolic compounds, flavonoids, and organic acids; thus, the extracts are promising antioxidants and "green reductants" to obtain nanoscale materials.

The process of Ag^+ cation reduction and nanoparticle formation may require a significant amount of time (12–150 hours) [20–22]. The reason for this can be the chemical modification of the plant extract with time that increases its reduction ability. Recent studies report the use of oxidized amylose as reducing agents [20]. Chemical transformations that require several hours or days can be accelerated and completed in few minutes by oxygen purge of the prepared extract. It was established that silver nanoparticles can be synthesized using previously oxidized extract of black currant and apricot pomaces as a reducing and capping agent [21, 22]. So, the search for the ways to intensify the "green" synthesis is a challenging task. In view of the effective synthesis of AgNPs using previously oxidized extract, it is important to investigate the efficiency of this approach for other types of plant raw materials.

Another popular area in the field of cost-effective treatment of industrial waste research is the development of "green," environmentally friendly, biodegradable reagents (anticorrosion and antiscale reagents) based on organic compounds extracted from food and agricultural products processing. The antiscalant effect of naturally occurring plant extracts (*Bistorta officinalis*, *Azadirachta indica*, *Punica granatum* hull and leaf, seaweeds, palm leaves, *Aloe vera*, corn stalks, *Momordica charantia*, *Paronychia argentea*, *Spergularia rubra*, and *Parietaria officinalis*) for cooling systems was studied by many authors [23–25]. The authors suggested that the scale inhibition efficiency of these extracts may be due to the involvement of phenolic compounds or polysaccharides. In particular, by-products of sugar production, industrial radish, and rape processing result in the generation of by-products containing valuable anticorrosion and antiscale compounds that can be extracted and further

valorized as anticorrosion products. According to the literature, radish seed extract was tested as a mild steel corrosion inhibitor in $1 MH_2SO_4$ solution [26]. The inhibitory effect of radish leaf extract (RLE) on mild steel corrosion in $0.5 MH_2SO_4$ was studied by the weight loss and electrochemical techniques [27]. Furthermore, the black radish juice was found to inhibit tin corrosion which was studied by Radojčić et al. [28]. In another study, Selvi et al. evaluated the corrosion inhibition behavior of beetroot extract in well water in the presence of Zn^{2+} [29]. The significant inhibition performance of the rape grist extract for steel corrosion in neutral media was observed [30]. At the same time, extracts of these by-products have not ever been studied as both corrosion and scale inhibitors. It is worse to point out that many extracts provide corrosion inhibition effects but do not have antiscale properties.

Thus, the study of the possibility to use plant waste in different areas of chemical technology and to create zero-waste technologies by the use of food waste is an urgent issue. For European countries, the most typical types of waste were identified: grape, pomegranate processing residues (pomace and peels), and processing residues of radish, rape, and beetroots.

The aims of the present study are as follows:

(1) To investigate the natural raw materials from agricultural and food industry (rapeseed pomace, sugar beet pulp, and fodder radish cake) as potential sources of corrosion and scale inhibitors for mild steel in tap water

(2) To assess the prospects of the use of plant extracts (grape pomace and pomegranate peels) as a reducing agent in nanoparticle production

2. Materials and Methods

2.1. Extract Preparation. The raw material powder and ethanol were mixed in the weight ratio of 1 : 10. The rapeseed pomace, sugar beet pulp, and fodder radish cake extracts were prepared by maceration for 24 h in ethanol. The resulted mixture was filtered with a Whatman filter grade 3 paper to remove solid contents.

In the second case, the grape pomace (GPE) and pomegranate peel extract (PPE) were obtained from the pomaces remained after mechanical pressing of the fresh fruits to produce juices. The grape pomace and pomegranate peels were mixed with distilled water in the 1 : 10 (w/v) ratio at 25°C. The mixture was placed in the ultrasound bath. The ultrasound of 27 kHz frequency and 6 W/cm^2 intensity was applied for 2 hours. The sonication process was coupled with air bubbling through the solution to intensify extract oxidation [21, 22]. The oxidized extract appeared to be highly efficient in AgNPs synthesis compared to nonoxidized extract. During the sonication, the air was continuously bubbled through the solution. Due to the high intensity of sonication, the ultrasound cavitation occurs in the solution intensifying the extraction process. At the end of the process, the temperature of the solution reached 40°C due to the influence of ultrasound. After the extraction, the solution was filtered through a paper filter.

2.2. GC-MS and LC-MS Extract Composition Analyses.
The obtained extracts were analyzed with LC-MS and GC-MS techniques. A detailed description of the protocol of the chromatography mode is presented in previously published works [15, 23].

2.3. Total Polyphenol and Flavonoid Contents in the Extracts.
The total polyphenol content (TPC) was determined using the Folin–Ciocalteu assay according to the method of Sánchez-Rangel et al. [31]. The results were expressed as milligrams of gallic acid equivalent per gram of the extract (mg GAE/g).

The total flavonoid content (TFC) was determined by the aluminum chloride assay according to the method of Arvouet-Grand et al. [32]. The final values were expressed as milligrams of quercetin equivalent per gram of the extract (mg QCE/g).

2.4. Antioxidant Capacity of the Extracts.
The total antioxidant activity of the extracts was determined by the phosphomolybdenum reduction assay described by Prieto et al. [33]. The antioxidant activity is expressed as milligrams of ascorbic acid equivalent per gram of the extract (mg ASE eq/g extract).

Scavenging of 2, 2-diphenyl-1-picrylhydrazyl (DPPH) radicals and 2, 2′-azino-bis-(3-ethylbenzothiazoline-6-sulfonic acid) (ABTS) were performed according to the method of Taipong et al. [34].

The FRAP assay was performed as described by the method of Rhimi et al. [35]. The FRAP assay was determined based on the method that involves assessing the ability of the test extract to reduce ferricyanide (Fe^{3+}) to form potassium ferrocyanide (Fe^{2+}), which then reacts with ferric chloride to form a ferric ferrous complex that has an absorption maximum at 700 nm.

2.5. Characterization of Anticorrosion and Antiscalant Properties of the Extracts.
Antiscalant efficiency of the extract was tested in thermal scaling conditions according to the method that was described in previously published works [36]. Corrosion inhibition efficiency of the extract was determined with linear polarization resistance technique (LPR) in thermal scaling conditions [37–39]. The morphology of the surface after thermal scaling was studied with the use of a SEM-106I Selmi microscope (Ukraine) operated at 20 kV. The steel rings were removed from the Pyrex tube, dried, and sent to analyses.

2.6. Synthesis of AgNPs Using the Extracts.
Synthesis of AgNPs using the extracts was performed as described in previously published works [21, 22]. The previously oxidized grape pomace and pomegranate peel extracts were used as environmentally friendly reducing and capping agents to synthesize silver nanoparticles for the first time.

2.7. UV-Visible Spectroscopy of AgNPs.
The synthesized silver nanoparticles were investigated using an UV-Vis spectrophotometer (Shimadzu-2450 UV-Vis spectrophotometer) in the range between 200 and –800 nm according to the method of Ankamwar et al. [4]. The samples were diluted with deionized water, and UV-visible spectra were recorded using a 1 cm quartz cuvette at 25°C.

2.8. Dynamic Light Scattering (DLS) of AgNPs.
Characterization of the particle size and zeta potential of the AgNPs were carried out according to the method described previously [5, 8]. The particle size and zeta potential of the AgNPs were carried out by Zetasizer (Malvern Zetasizer Nano-ZS, Malvern Instruments, UK). The sample was prepared by diluting the 10 ml of the AgNPs solution in 10 ml of distilled water. After that, 10 ml of sample solution was put in the cuvette. The cuvette was placed in the cell holder and scanned in the range of 1–100 nm using a fixed angle of 173°.

2.9. Scanning Electron Microscopy of AgNPs.
A scanning electron microscope (SEM) was used to examine the morphology of the synthesized AgNPs. A drop of colloidal system of extract-AgNPs was applied on the carbon-coated copper plate, and an image was taken at an acceleration voltage of 10 kV. EDX analysis was conducted with the same instrument to confirm the elemental composition of the sample.

2.10. Fourier Transform Infrared Spectroscopy (FT-IR) of AgNPs.
FT-IR spectroscopy measurements were carried out to identify the functional groups which were responsible for capping the AgNPs and involved in the synthesis of AgNPs. FT-IR spectra of extracts and extract-AgNPs were measured by using a Bruker Tensor 27 FTIR spectrometer with a diamond crystal accessory in a spectral range of $4000–600 \, cm^{-1}$ with a resolution of $4 \, cm^{-1}$.

2.11. Antibacterial Assay of AgNPs.
The minimum bactericidal concentration (MBC) was determined as the lowest concentration of AgNPs solution in the tube that caused no significant changes of turbidity, and no colony was found in Endo agar [35]. Minimum inhibitory concentration (MIC) was estimated as a concentration in the tube in which turbidity (optical density) was doubly decreased. Low values of optical density, at least less than 0.07, as well as the control absence of bacterial growth on Endo agar allowed us to determine the minimal bactericidal concentration of each sample of AgNPs solution.

3. Results and Discussion

3.1. By-Products of Plant Food Processing as Corrosion and Scale Inhibitors.
The priority area of reducing the material consumption is to involve waste in the chemical production process of corrosion and scale inhibitors [37–40]. Three industry by-products were used, rapeseed pomace from the wastes of production of edible oil, sugar beet pulp from the wastes from sugar production, and fodder radish cake.

The key factor that determines the effectiveness of using a plant extract as corrosion or scale inhibitor of mild steel in natural water is the component composition of them [15]. Gas chromatography-mass spectrometry (GC-MS) analysis was carried out to analyze the chemical composition of extracts. The results of the GC-MS analysis of the radish cake extract (RCE) are presented in Table 1. This extract is characterized by the presence of anthocyanidins including cyanidin (6.7%) and pelargonidin (6.9%), isothiocyanates such as 3-(methylthio)propyl isothiocyanate (iberverin) (4.2%), 4-pentenyl isothiocyanate (8.3%), 4-methylpentyl isothiocyanate (3.1%), 3-butenyl isothiocyanate (3.9%), 4-(methylthio)-3-butenyl isothiocyanate (5.2%), 4-(methylthio)butyl isothiocyanate (erucin) (6.4%), 5-(methylthio)pentyl isothiocyanate (berteroin) (6.9%), and L-sulforaphane (1.1%). In addition, other major compounds included phenolic compounds such as pyrogallol, vanillic, and gallic acids, and eugenol. In addition, fatty acids were detected in a considerable amount (8.9%) in the extract.

The main compounds extracted from the rape cake are given in Table 2. A total of 18 compounds were identified, including saturated and unsaturated fatty acids, aldehydes, ketones, terpenes, and glycosides. The major phytocompounds identified in the rape cake extract are $3',5'$-dimethoxyacetophenone (28.3%), 4-hydroxy-3,5-dimethoxybenzaldehyde (20.5%), and (9Z)-octadec-9-enoic acid (12.2%). Other 15 compounds were present in 39.7% of the total compounds.

The GC-MS analysis of the sugar beet pulp extract revealed the presence of six compounds (Table 3). The maximum amount of the components present in the sugar beet pulp extract are sugar acid ((2S, 3R, 4S, 5R)-2, 3, 4, 5-tetrahydroxy-6-oxo-hexanoic acid) (36.9%) and sophorose (11.2%). These compounds represented over 48% of the total compounds in the extract.

3.2. Thermal Scaling Test.

The scale mass growth rate on the surface of mild steel is given in Figure 1. The deposition rate in tap water is $7.5\,\mu g/(h \cdot cm^2)$. It remains constant during the test. In contrast to tap water, when the radish cake extract is added, the scale deposition is reduced to $1.6\,\mu g/(h \cdot cm^2)$ meaning that the antiscaling efficiency is 78.7%. Rape pomace extract does not cause any influence on the scale deposition rate, and the scaling rate is the same as in the tap water. Sugar beet pulp extract appears to accelerate scaling. The scale deposition rate in tap water exceeds $20\,\mu g/(h \cdot cm^2)$. Such a high deposition rate is probably caused by the deposition of extract components on the electrode surface, simultaneously with calcium carbonate. So, only RCE slows down the deposition of calcium carbonate even at the temperature of 100°C.

Possible mechanism of scale inhibition could be the formation of soluble complexes with calcium ions. Such complexes prevent the deposition of calcium carbonate, keeping calcium ions in the soluble form. The mechanisms for scale inhibition by the extract are associated with the active functional groups (C=O, −OH, and −COOH groups) of the main compounds of the extract [41–47]. These substances, which have hydroxyl and/or carboxyl functional groups that interact with divalent ions such as Ca^{2+}, are known to form water-soluble complexes with calcium ions [15, 23–25]. In addition to this, carboxyl-terminated anthocyanidins have a larger surface area, which can chelate with more Ca^{2+}.

According to GC-MS, phenolic compounds such as anthocyanidins, phenolic acids, polysaccharides, sugar acids, and saturated and unsaturated fatty acids were found in the rape pomace and sugar beet pulp extract, while the radish cake extract additionally contains isothiocyanates with N=C=S functional groups that can dimerize [15]. The mechanisms for scale inhibition of the radish cake extract have been associated with both the formation of the protective film on the surface of steel by compounds such as isothiocyanates and saturated fatty acids and the formation of water-soluble complexes of phenolic derivatives (pyrogallol, vanillic, and gallic acids, eugenol, and polysaccharides) with divalent ions such as Ca^{2+}.

3.3. Corrosion Inhibition.

The instantaneous corrosion rate of mild steel determined with LPR technique in thermal scaling conditions is given in Figure 2. In tap water, the corrosion rate of mild steel right after immersion is around 0.8 mm/year and decreases with the boiling time due to the formation of the scale layer that acts as a diffusion barrier and reduces oxygen supply to the surface. In tap water with added extracts, the corrosion rate decreases in the first hours. The corrosion rate reduction with radish cake and sugar beet pulp extracts is very close; however, rape pomace extract appears to be a more efficient corrosion inhibitor. In the first 10 hours, corrosion rate reaches 0.1 mm/year. As scale deposition progresses, the corrosion rate in both tap water and inhibited solutions decreases; however, in tap water, the decrease is faster because more scale is deposited. The thicker the scale layer, the less porous it becomes, and thus, the corrosion rate is lower. After 80 h of boiling, the corrosion rate in the solutions coincides at 0.2 mm/year and continued to decrease till the corrosion rate of 0.1 mm/year is reached.

3.4. Surface Film Formation.

The SEM images of the scaled steel surface are given in Figure 3. The scale deposited from tap water has a regular structure. The crystals are 60–80 μm, and the layer is uniform. In the presence of RCE, the crystals are much smaller, and the presence of the organic film is clearly observed on the surface. Figure 3(c) demonstrates the charging effect of SEM when the electrons are accumulated in the organic film. SEM analysis clearly demonstrates the formation of the organic surface film that acts as a barrier level to reduce the supply of oxygen and calcium carbonate, thus reducing scaling and corrosion. The scale crystals formed in tap water containing rape cake extract are significantly larger. At the same time, the crystals in sugar beet pulp extract solution are smaller compared to the crystals obtained in tap water, but an amorphous surface film is

TABLE 1: GC-MS analysis results of radish cake extract.

RT (min)[a]	Compound	RI[b]	Percentage (%)
2.91	3-(Methylthio)propyl isothiocyanate[a,b]	1305	4.2
3.02	Pyrogallol acids[a,b]	1370	2.9
6.96	4-Pentenyl isothiocyanate[a,b]	1075	8.3
7.31	4-Methylpentyl isothiocyanate[a,b]	1139	3.1
10.02	Undecane[a,b]	1100	1.9
10.41	2-Methoxy-4-(prop-2-en-1-yl)phenol[a,b]	1340	2.5
10.62	4-Hydroxy-3-methoxybenzoic acid[a,b]	1636	2.8
10.92	Dodecane[a,b]	1200	1.0
12.42	4-(Methylthio)-3-butenyl isothiocyanate[a,b]	1433	5.2
12.73	4-(Methylthio)butyl isothiocyanate[a,b]	1408	6.4
12.99	Gallic acid[a,b]	1943	2.7
13.78	5-(Methylthio)pentyl isothiocyanate[a,b]	1250	6.9
14.24	L-Sulforaphane[a]	—	1.1
15.27	Dextrose[a]	—	3.7
15.49	Tridecane[a,b]	1300	1.9
16.11	Dodecanoic acid[a,b]	1645	0.8
16.33	Cyanidin[a]		6.7
18.77	Hexadecanoic acid[a,b]	2059	2.2
19.92	Pelargonidin[a]	—	6.9
21.00	Octadecanoic acid[a,b]	2157	5.9
24.11	Methyl linoleate[a,b]	2133	5.1
25.16	Sophorose[a]	—	7.1

[a]RT: retention time; STD: standard compound; NIST 14. [b]RI: Kovats retention indices (RI) determined using a commercial hydrocarbon mixture (C9–C25) on the HP-5MS column.

TABLE 2: GC-MS analysis results of rape pomace extract.

RT (min)[a]	Compound	RI[b]	Percentage (%)
8.41	Guanosine[a]	—	10.4
8.57	Sucrose[a]	—	1.2
8.92	Xanthosine[a,b]	1758	4.3
9.48	4-Hydroxy-3, 5-dimethoxybenzoic acid[a,b]	1893	28.3
10.37	4-Hydroxy-3, 5-dimethoxybenzaldehyde[a,b]	1662	20.5
10.42	Acetic acid[a,b]	1090	1.6
15.14	n-Cyclohexyl-4-hydroxybutyramide[a,b]		1.6
16.33	(9Z, 12Z)-9, 12-Octadecadienoic acid[a,b]	2129	4.8
16.88	Hexadecanoic acid[a,b]	2059	4.1
18.76	(9Z)-Octadec-9-enoicacid[a,b]	2134	12.2
19.92	Octadecanoic acid[a,b]	2157	2.0
22.75	Pyrrolidine, 1-(1-oxo-7,10-hexadecadienyl)[a]	—	0.9
22.97	Ethanamine, 2, 2′-oxybis[N, N-dimethyl]-[a]	—	0.9
23.37	7-Dehydrodiosgenin[a]	—	2.1
23.87	Campesterol[a]	—	1.1
23.99	γ-Sitosterol[a,b]	3299	1.2
24.56	β-Sitosterol[a,b]	3299	1.1
25.03	Ergosta-5, 22-dien-3-ol	—	2.4

[a]RT: retention time; STD: standard compound; NIST 14. [b]RI: Kovats retention indices (RI) determined using a commercial hydrocarbon mixture (C9–C25) on the HP-5MS column.

found around them, probably due to the deposition of extract components.

3.5. By-Products of Plant Food Processing for the Manufacture of Nanomaterials.

The synthesis of metal nanoparticles using environmentally friendly "green" compounds extracted from wastes and serving as both reducing and capping agent is especially promising for the cost-effective treatment/valorization of industrial wastes. Different wastes have been used for the synthesis of AgNPs, such as banana and orange peel, papaya peel, tea and grape wastes, and sugarcane bagasse. However, further search for large tonnage waste is promising for the production of nanomaterials which is an important task, both from the side of creating resource-saving technologies for waste processing and for the development of sustainable chemistry concepts in the field of chemical synthesis of nanomaterials. For Ukraine and other countries, it is interesting to use the waste generated during the processing of fruit and berry crops, such as apricot, grapes, pomegranate, and currant. These agroindustrial

TABLE 3: GC-MS analysis results of the sugar beet pulp extract.

RT (min)[a]	Compound	RI[b]	Percentage (%)
5.21	1-Methyl-4-(prop-1-en-2-yl)cyclohex-1-ene[a]	—	3.7
5.79	Unknown		—
6.96	(2S, 3R, 4S, 5R)-2, 3, 4, 5-Tetrahydroxy-6-oxo-hexanoic acid[a]	—	36.9
9.24	(E)-3-(4-Hydroxy-3-methoxy-phenyl)prop-2-enoic acid[a,b]	2091	4.4
10.32	Sophorose[a]	—	11.2
10.48	Unknown	—	—
12.51	Unknown	—	—

[a]RT: retention time; STD: standard compound; NIST 14. [b]RI: Kovats retention indices (RI) determined using a commercial hydrocarbon mixture (C9–C25) on the HP-5MS column.
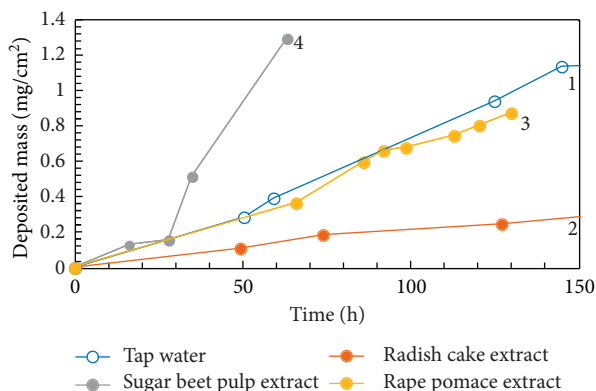

FIGURE 1: Scaling rate of mild steel in tap water at 100°C: (1) blank; (2) with 10 mL/L of radish cake extract; (3) with 10 mL/L of rape pomace extract; (4) with 10 mL/L of sugar beet pulp extract.
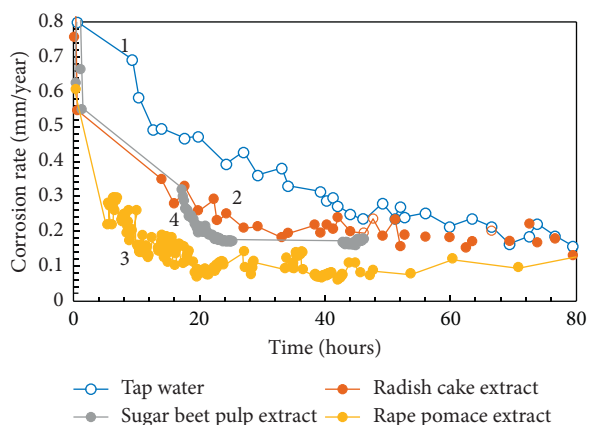

FIGURE 2: LPR corrosion rate of mild steel in tap water at 100°C: (1) blank; (2) with 10 mL/L of radish cake extract; (3) with 10 mL/L of rape pomace extract; (4) with 10 mL/L of sugar beet pulp extract.

wastes are readily available, eco-friendly, cost-effective, and can be easily reused. Agrofood wastes are regarded as a highly multicomponent system for nanoparticle synthesis because they contain a wide range of green organic compounds with high reducing potential. Usually, for the synthesis of nanoparticles, aqueous and alcoholic extracts of plant materials are used. These are the classic solvents that were initially used in the extraction process and further to obtain nanoparticles. However, it was found that the preliminary modified extract through oxidation

modification (oxygen purge) increases its reduction ability [21, 22].

The prospects of the use of plant extracts (grape pomace and pomegranate peels) as a reducing and capping agent to produce nanoparticles were investigated (Table 4). In particular, the component composition and radical scavenging of the grape pomace and pomegranate peel extracts, obtained by ultrasound-assisted water extraction, were studied. The obtained extracts were used to obtain silver nanoparticles through "green" synthesis, and the antibacterial properties of the nanoparticles were estimated.

Characterization of the plant extracts that were previously oxidized is an essential requirement to have information on the chemical composition and reducing power. To our knowledge, this is the first application of the method of preliminary modification extract through oxidation and the next analysis of the extracts by the LC-MS method.

The extracts from grape pomace and pomegranate peels were analyzed by liquid chromatography-mass spectrometry (LC-MS). The main groups both quantitatively and qualitatively of the compounds in grape pomace extract were phenolic acids, anthocyanins, and stilbenes. The major percentage corresponded to phenolic compounds. p-Coumaric acid, 3, 4-dimethoxyphenylacetic acid, and delphinidin-3-O-glucoside were found in large amounts in the grape pomace extract. The results of the chemical analysis of previously oxidized grape pomace extract are shown in Table 4, and a comparative analysis of the major components with respect to studies reported in the literature [47, 48] indicates that oxidation products prevail in the composition.

Table 5 shows the composition of the pomegranate peel extract. Pomegranate peel extract mainly consists of phenolic compounds, predominantly chlorogenic acid (7.5%), ellagic acid (7.8%), and caffeic acid (4.7%), and major quantities of punicalagin (granatin A and granatin B) (13.4%). The results of LC-MS analyses of the extracts are in agreement with the literature data [7, 49–51].

Several articles described the significant role of phenolic compounds in the reduction capacity of plant extracts [51, 52]. Therefore, the total phenolic (TPC) and flavonoid contents of the extracts were investigated (Figure 4). The total polyphenol content was determined using the Folin–Ciocalteu assay according to the method of Sánchez-Rangel et al. [31].
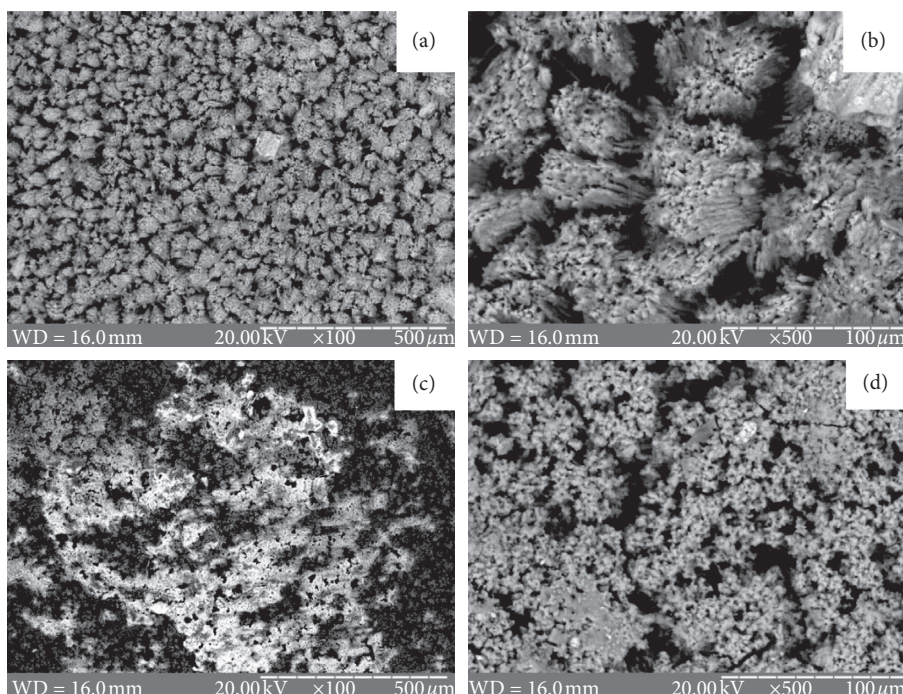
FIGURE 3: SEM images of steel scaled surface after 150 h of boiling in tap water with addition: (a) blank; (b) 10 mL/L of rape pomace extract; (c) 10 mL/L of radish cake extract; (d) 10 mL/L of sugar beet pulp extract.

It was found that the pomegranate peel extract had higher phenolic content of 108.5 ± 1.8 mg GAS/100 g extract while grape pomace extract phenolic content was 64.2 ± 1.8 mg GAS/100 g extract. The total flavonoid content of the extracts is shown in Figure 4. The total flavonoid content of the extracts was increased in the direction as the total polyphenol content. This finding was also confirmed by the chromatographic analysis, which indicated that the pomegranate peels contained more phenolic compounds than the grape pomace extract.

Similar findings were also observed in the reducing power assay (FRAP) (Figure 5) and by the phosphomolybdenum method (Figure 6) where the pomegranate peel extract was more active. The highest total antioxidant capacity (571.25 mg GAE/g extract) was obtained for grape pomace extract. Figure 6 shows the dose-response relation for the reducing power of the extracts. Reducing powers of the extracts were found to increase with increasing concentrations.

The reducing activity of the extract is generally associated with the presence of compounds, which has been proven to exert reduction reaction and formation of Ag^+ cations in the process of NPs synthesis. Total reducing activities of grape pomace and pomegranate peel extracts are given in Figure 6. It was shown that the contents of reductive substances in the extracts were abundant, which was beneficial to the formation of silver nanoparticles.

3.6. Determination of the Synthesis Efficiency.
The potential of the $Ag^+|Ag$ electrode variation with time is given in Figure 7. The electrode potential corresponds to Ag^+ concentration in the solution, and thus, the synthesis process

can be monitored. A sharp decrease of the potential is caused by $AgNO_3$ mixing with the extract and the beginning of the synthesis.

Calculated degree of conversion of Ag in the "green" synthesis with extracts is given in Table 6. The highest yield of AgNPs was obtained with pomegranate extract (99.7%). The higher abundance of phenolic acids in the pomegranate peel aqueous extract may be responsible for the improved AgNPs synthesis with it.

3.7. Spectrophotometric Characterization of Ag-NPs.
The synthesis of the AgNPs in liquid solution was observed by measuring the absorption spectra at a wavelength range of 200–1100 nm. In the UV-Vis spectrum, a single, strong, and broad surface plasmon resonance peak was observed at 440 nm that confirmed the synthesis of AgNPs (Figure 8).

The DLS measurements revealed that the average hydrodynamic size of the synthesized GPE-AgNPs was 34.68 ± 4.95 nm, and the average zeta potential was -25.31 mV (Table 7). The average particle size was found to be higher for GPE-AgNPs in comparison with the samples of PPE-AgNPs. AgNPs prepared by pomegranate peel extracts most often are negatively charged. Several reports demonstrated similar negative values of zeta potential for metallic nanoparticles stabilized with different polyphenols [53, 54]. These results are consistent with the earlier results of the plant-mediated synthesis of AgNPs, including orange peel and others.

The EDX spectra of "green" synthesized nanoparticles are depicted in Figure 9. AgNPs display typical peaks in the range 2.7–3.4 keV. The presence of another peak in the

TABLE 4: LC-MS analysis results of the aqueous grape pomace extract.

RT[a] (min)	Compound	RI[b]	[M-H][−c]	Percentage (%)
2.26	Benzoic acid[a,b,c]	1162	121	4.1
5.81	3-Hydroxybenzoic acid[a,b,c]	1563	137	5.2
6.01	4-Hydroxybenzoic acid[a,b,c]	1625	137	5.5
8.49	(2E)-3-(4-Hydroxyphenyl)prop-2-enoic acid (p-coumaric acid)[a,b,c]	1938	163	10.6
8.42	3, 4, 5-Trihydroxybenzoic acid (gallic acid)[a,b,c]	1943	169	5.5
10.37	(2E)-3-(4-Hydroxy-3-methoxyphenyl)prop-2-enoic acid (ferulic acid)[a,b,c]	2091	193	3.7
10.42	3-(3, 4-Dihydroxyphenyl)-2-propenoic acid (caffeic acid)[a,b,c]	2130	179	3.9
11.81	3-(4-Hydroxy-3, 5-dimethoxyphenyl)prop-2-enoic acid (sinapic acid)[a,b,c]	2241	223	3.2
12.74	Delphinidin-3-O-glucoside[a,c]	—	464	8.5
12.99	Cyanidin-3-O-glucoside[a,c]	—	457	6.6
15.27	Malvidin-3-O-glucoside[a,c]	—	491	6.4
16.33	(2R,2'R,3R,3'S,4R)-2, 2'-Bis(3, 4-dihydroxyphenyl)-3, 3',4, 4'-tetrahydro-2H,2'H-4,8'-bichromene-3, 3',5, 5',7, 7'-hexol (procyanidin B1)[a,c]	—	579	8.8
16.88	(2R,3S)-2-(3, 4-Dihydroxyphenyl)-3, 4-dihydro-2H-chromene-3, 5, 7-triol (catechin)[a,b]	2859	289	1.8
18.76	Epicatechin[a,b,c]	2836	289	2.7
19.92	Quercetin-3-O-galactoside[a,c]	—	363	4.9
21.46	Kaempferol-3-O-glucoside[a,c]	—	447	5.9
21.85	2-(3, 4-Dihydroxyphenyl)-3, 5, 7-trihydroxy-4H-chromen-4-one (quercetin)[a,b,c]	3163	301	4.6
21.98	3, 5, 7-Trihydroxy-2-(4-hydroxyphenyl)-4H-chromen-4-one (kaempferol)[a,c]	—	285	2.1

[a]RT: retention time; STD: standard compound; NIST 14 (compound identified by RI comparison with library). [b]RI: Kovats retention indices (RI) determined using a commercial hydrocarbon mixture (C9–C25) on the HP-5MS column (compound identified by Kovats retention indices comparison with literature values). [c]MS: compound identified by mass spectra comparison with the Wiley library.

TABLE 5: LC-MS analysis results of the pomegranate peel extract.

RT[a] (min)	Compound	RI[b]	[M-H][c]	Percentage (%)
2.25	Butanoic acid 2-hydroxymethylestera[b]	1361	—	3.1
2.91	Pyridine[a,b,c]	1172	80	2.4
3.27	2, 3, 7, 8-Tetrahydroxy-chromeno[5 ,4, 3-cde]chromene-5, 10-dione (ellagic acid)[a,b,c]	3292	300	7.8
4.01	1-Deoxy-2, 4-O,O-methylene-d-xylitol	—	—	1.2
4.45	Gallic acid[a,b,c]	1943	169	5.9
5.01	3-(3, 4-Dihydroxyphenyl)-2-propenoic acid (caffeic acid)[a,b,c]	2130	179	4.7
6.99	n-Heptyl acrylate[a,b,c]	1489	—	2.1
7.45	Benzoyl bromide[a,b,c]	—	—	1.4
7.77	1, 2-Di(2-furyl)-1, 2-ethanedione[a,b,c]	—	—	1.1
8.00	Delphinidin 3, 5-diglucoside[a]	—	—	8.8
8.42	(1S, 3R, 4R, 5R)-3-{[(2E)-3-(3, 4-Dihydroxyphenyl)prop-2-enoyl]oxy}-1, 4, 5-trihydroxycyclohexanecarboxylic acid (chlorogenic acid)[a,b,c]	3098	353	7.5
10.92	2, 5-Furandicarboxaldehyde[a,b]	2467	—	3.2
11.86	2-Furancarboxaldehyde 5-(hydroxymethyl)[a,b]	2509	—	2.8
12.73	Valoneic acid dilactone[a]	—	—	5.1
16.33	Catechin[a,b,c]	2859	289	10.2
16.88	Epicatechin[a,b,c]	2836	289	7.5
18.77	Rutin[a,c]	—	465	2.2
24.11	Granatin A[a]	—	—	6.5
25.16	Granatin B[a]	—	—	6.9

[a]RT: retention time; STD: standard compound; NIST 14 (compound identified by RI comparison with library). [b]RI: Kovats retention indices (RI) determined using a commercial hydrocarbon mixture (C9–C25) on the HP-5MS column (compound identified by Kovats retention indices comparison with literature values). [c]MS: compound identified by mass spectra comparison with the Wiley library.

spectra suggests that the AgNPs were capped by organic constituents of the black currant, apricot, grape pomace, and pomegranate peel extracts.

FT-IR measurements were carried out to identify the possible compounds in the extracts responsible for capping leading to efficient stabilization of the silver nanoparticles (Figure 10). The FT-IR spectrum of the samples under the study had almost the same set of absorption bands and differed only in the intensity and slight shift of some bands. FT-IR spectra of grape pomace and pomegranate peel extracts before reaction showed several peaks at around $3400 \, cm^{-1}$ which can be assigned to ν (OH) vibrations of polyphenols [4, 9, 52]. The peaks at $1620 \, cm^{-1}$, $1140 \, cm^{-1}$, $1360 \, cm^{-1}$, and $1050 \, cm^{-1}$ corresponds to the ν (C=O), while
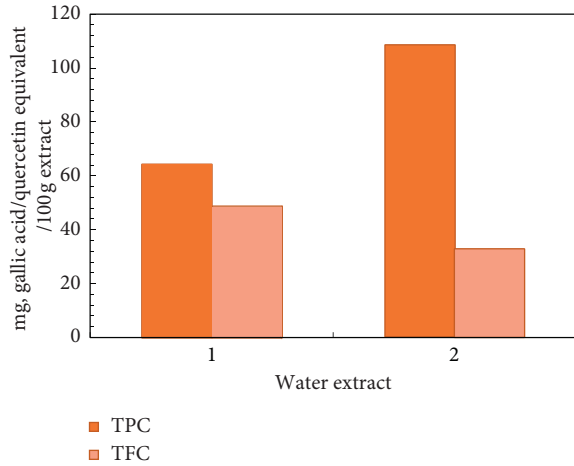
FIGURE 4: Total phenolic (TPC) and flavonoid (TFC) contents of the aqueous grape pomace (1) and pomegranate peel (2) extracts.
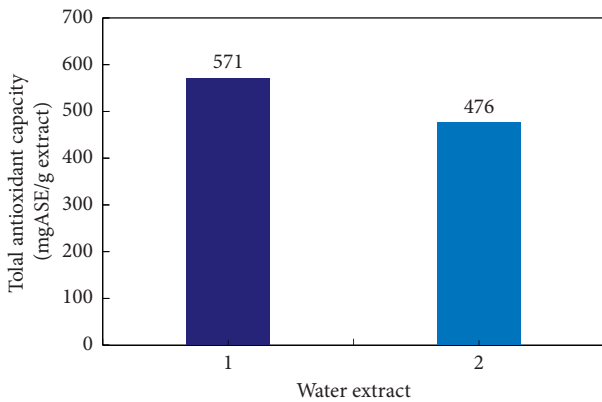

FIGURE 5: Total antioxidant capacity (mg ASE/g extract) of the aqueous grape pomace (1) and pomegranate peel (2) extracts were evaluated by the phosphomolybdenum method.
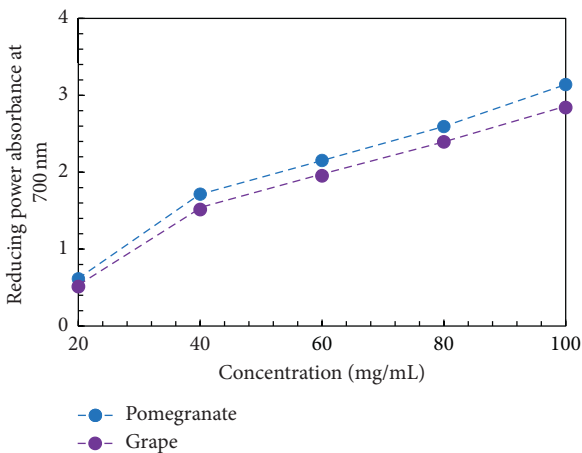

FIGURE 6: Reducing power of the aqueous grape pomace and pomegranate peel extracts was evaluated by the FRAP assay.

the absorptions at $1652 \, cm^{-1}$ may be referred to C=C vibrations or aromatic ring ν (C=C). Absorption bands at $2910 \, cm^{-1}$ are attributed to C-H bonds in aldehydes [31, 52].
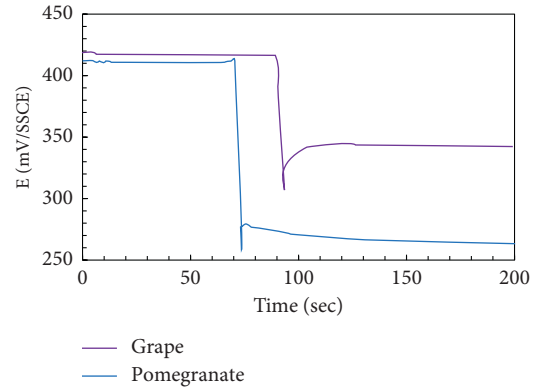

FIGURE 7: The $Ag^+|Ag$ electrode potential variation with time during the "green" synthesis with extracts at $80°C$.

TABLE 6: The degree of conversion of Ag in the "green" synthesis.

	Extract	Degree of conversion (%)
1	Grape pomace	93.3
2	Pomegranate peels	99.7

Comparison of the FTIR spectra of the extracts and sample AgNPs synthesis with the extract showed a significant difference between the type and intensity of the observed peaks. The shift of peaks and reduction in bands in the range 1500–1600, 1000–1200, and $3500–3200 \, cm^{-1}$ after reduction indicates the oxidation of the corresponding functional groups and may be attributed to the reduction of Ag^+ ions to Ag^0 nanoparticles. The FT-IR spectrum of the synthesized GPE-AgNPs and PPE-AgNPs showed absorption peaks at $1645 \, cm$ and $3440 \, cm^{-1}$. The weak peak detected at $1645 \, cm^{-1}$ was assigned as carbonyl groups that were almost decreased in the FT-IR band. It could indicate that the carbonyl groups might participate in the reduction of $AgNO_3$. The absence of peaks at $1264 \, cm^{-1}$, $1289 \, cm^{-1}$, and $1347 \, cm^{-1}$ may be due to the capping action of the C–O group in the synthesis of AgNPs.

The results of SEM analyses are presented in Figure 11. The SEM analysis provides further information about the morphology of the synthesized AgNPs. The SEM images revealed the formation of individual silver nanoparticles as well as several aggregates. Spherical nanoparticles were evidenced from the SEM image with few agglomerations, which may be because of the stabilization of the organic compounds present in the extracts. More agglomeration was observed in the suspensions of nanoparticles derived from pomegranate peel extract as the reductant, which indicates lower stability of the system. In meantime, the AgNPs obtained with GPE do not tend to agglomerate even when the solution is diluted before SEM. This confirms the higher stabilization properties of GPE compared to PPE.

The antibacterial properties of GPE-AgNPs and PPE-AgNPs were evaluated using the agar well diffusion method and the results were expressed as a zone of inhibition in mm
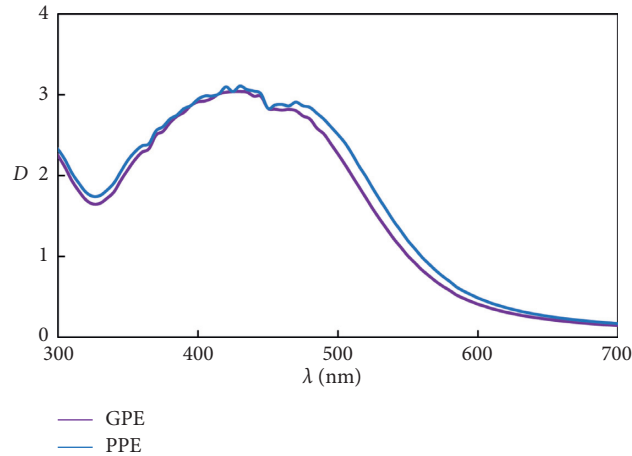
FIGURE 8: UV-Vis absorption spectra of GPE-AgNPs and PPE-AgNPs after 30 min of reaction displaying the characteristic surface plasmon resonance band at 440 nm.

TABLE 7: Characteristics of AgNPs synthesized using black currant, apricot, grape pomace, and pomegranate peel extracts.

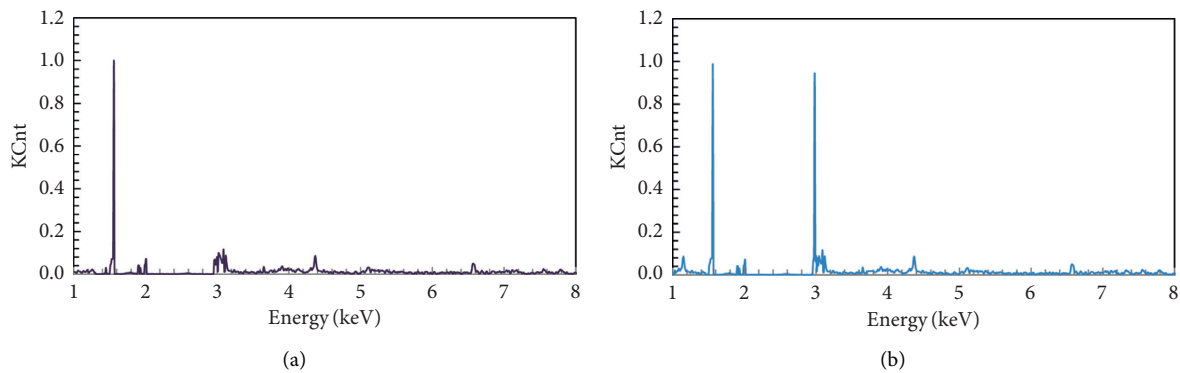| System	Average particle-sized AgNPs (nm)	Zeta potential
GPE-AgNPs	50–90 nm	−25.31
PPE-AgNPs	40–54 nm	−38.82

(a)

(b)

FIGURE 9: EDX spectra of GPE-AgNPs and PPE-AgNP.

(Table 8). The Gram-negative bacteria showed a lower zone of inhibition, while Gram-positive bacteria showed better results. The inhibitory effect of GPE-AgNPs and PPE-AgNPs on the growth of bacteria was observed after incubation at 37°C for 24 h. After 24 h of incubation, the observed zones of growth inhibition treated by GPE-AgNPs were 3.9 ± 0.1 mm (*B. subtilis*) and 2.1 ± 0.1 (*E. coli*), respectively. After 24 h of incubation, the observed zones of growth inhibition treated by PPE-AgNPs were 2.7 ± 0.1 mm (*B. subtilis*) and 2.2 ± 0.1 (*E. coli*), respectively.

As a general result, it was observed that the GPE-AgNPs and PPE-AgNPs showed higher activity against *B. subtilis* compared with *E. coli*. Two primary mechanisms of antimicrobial action of AgNPs have been recognized: (1) contact killing and (2) ion-mediated killing [55, 56]. Antibacterial mechanisms through direct contact occur by adhesion of

AgNPs onto the surface of the cell wall and penetration into it. Connecting AgNPs to proteins in bacteria membranes leads to membrane damage that can cause leakage of cellular contents and bacterial death. After penetrating the membrane, AgNPs can also enter the bacterial cytoplasm.

Additionally, the antibacterial properties of GPE-AgNPs and PPE-AgNPs were evaluated using a liquid medium. As shown in Figure 12, the synthesized GPE-AgNPs and PPE-AgNPs exhibited significant antibacterial activity in a concentration-dependent manner against *E. coli*. The inhibitory efficacy (MIC) assay demonstrated a reduction in *E. coli* at AgNPs concentrations above 7.5% and 10% solutions of GPE-AgNPs and PPE-AgNPs, respectively. Thus, the synthesized AgNPs could be a good antimicrobial agent.

Although the wastes of the above-studied extracts have already been used for the synthesis of silver nanoparticles
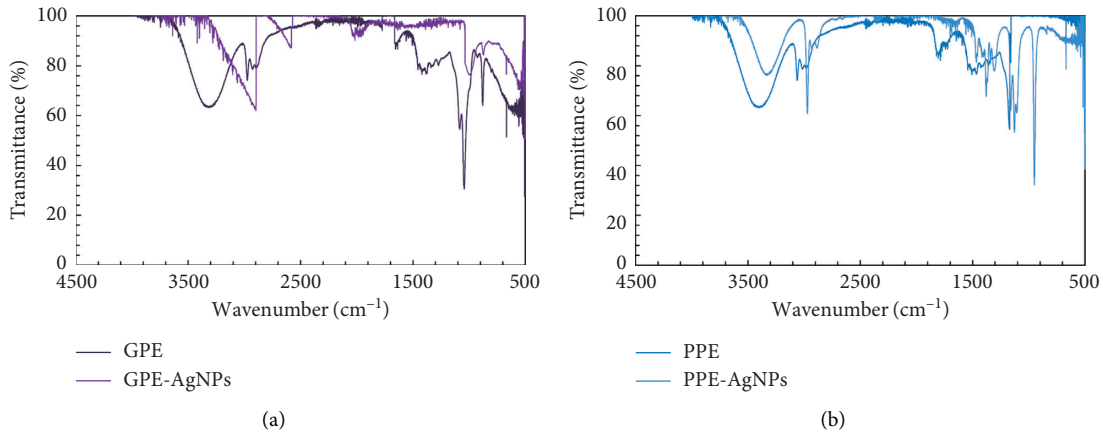
FIGURE 10: FT-IR spectra of aqueous black currant, apricot, grape pomace, and pomegranate peel extracts and GPE-AgNPs and PPE-AgNP.
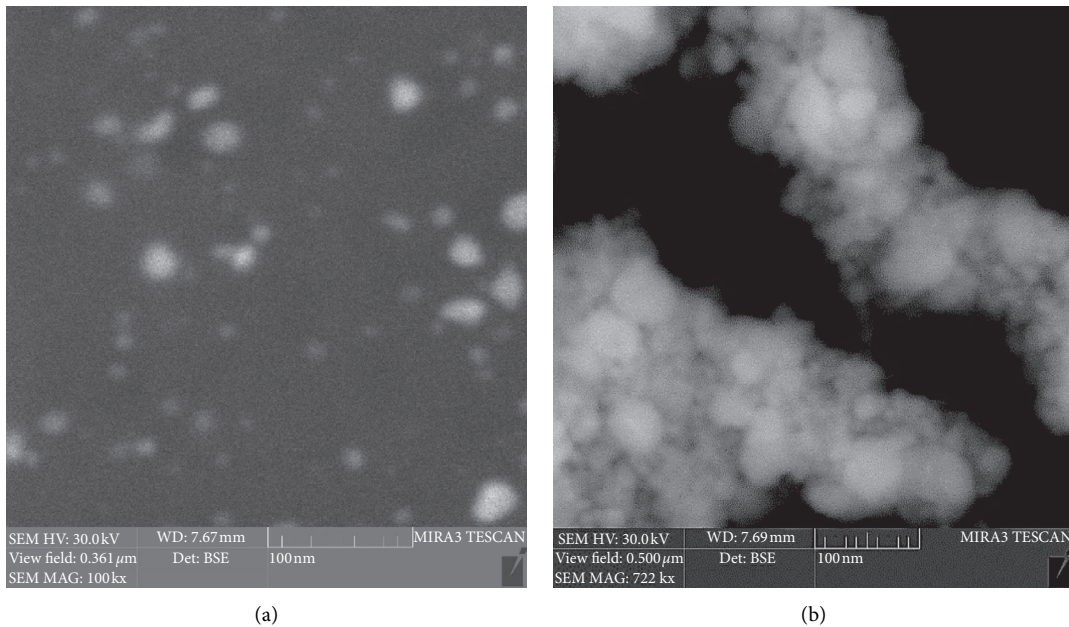
FIGURE 11: SEM images of silver nanoparticles (C (Ag$^+$) = 10 mmol/L, τ = 30 min, and ratio AgNO$_3$: extract of grape pomace (a) and pomegranate peel (b) extracts (mL) = 1 : 1).

TABLE 8: Antibacterial activity of GPE-AgNPs and PPE-AgNPs.

| Bacteria strains | Stirred heater | Zone of inhibition (mm) | | | |
| | | 24 h | | 48 h | |
		GPE-AgNPs	PPE-AgNPs	GPE-AgNPs	PPE-AgNPs
E. coli	—	2.9 ± 0.1	2.2 ± 0.1	3.4 ± 0.1	3.1 ± 0.1
B. subtilis	—	3.9 ± 0.1	2.7 ± 0.1	4.6 ± 0.1	3.4 ± 0.1

and are presented in the literature, their preliminary oxidation makes it possible to reduce the synthesis time and to limit the use of an ecologically safe extractant (water) instead of organic solvents. To illustrate the important benefits of the utilization of preoxidized extract for the synthesis of AgNPs, it was compared with other studies, and the recent
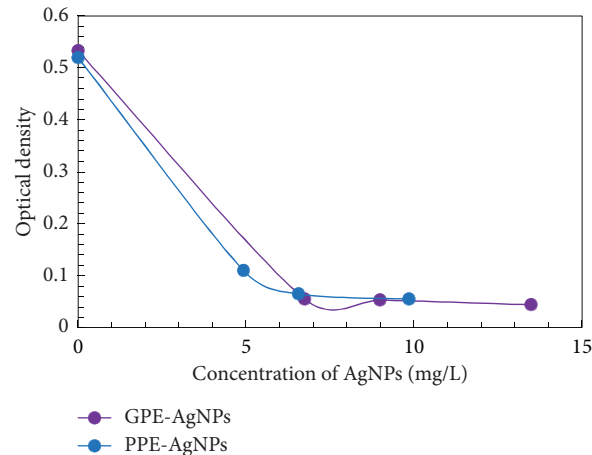
FIGURE 12: Optical density of test tubes with *E. coli* culture and different concentrations of AgNP grape pomaces and pomegranate peel extracts after 24 hours of cultivation.

TABLE 9: A summary of plant-based extracts as Ag reducing agent.

Plant/Fruit	Time of the synthesis AgNPs	Extractant	Reference
Peels of *Punica granatum*	10–15 min	Boiled for water	[8, 9]
	24 h	Water	[51]
	15 min	Plasma chemical treatment	[5]
Grape pomace	24 h	Ethanol	[56]
	48 h	Aqueous solution of Na_2CO_3 (2.5%) and Na_2SO_3 (2.5%)	[57]

outcomes to produce the AgNPs by extract are summarized in Table 9.

Table summarized the application of plant-based extracts as AgNPs reducing agents. Clearly, the oxidized extracts show the shortest time of reduction of Ag^+ cations to the NPs in comparison with the extracts described in the literature.

4. Conclusions

The obtained results show high potential for the usage of wastes in corrosion and scale inhibition or nanomaterial development and production processes.

(1) Inhibition of scaling and corrosion was investigated in thermal scaling conditions on the surface of the electrode manufactured from mild steel. The LPR technique was applied to measure the corrosion rate, and the scaling rate was determined gravimetrically. The extracts were found to inhibit the corrosion rate 2-3 times, while only radish cake extract inhibited both the corrosion and scaling rates.

(2) The result obtained in this investigation is remarkably interesting in terms of the identification of potential fruit and berry crops for the synthesis of silver nanoparticles. The present study firstly documented the synthesis and characterization of silver nanoparticles by using previously oxidized aqueous black currant, apricot, grape pomace, and pomegranate peel extracts.

(3) Detailed gas chromatography-mass spectrometry (LC-MS) results established that polyphenolic compounds

and flavonoids predominate in the apricot, grape, black currant pomace, and pomegranate peel extracts. The pomegranate peel and grape pomace extracts contained higher amounts of phenolics and flavonoids when compared with the black currant and apricot pomace extract. The grape pomace and pomegranate peel extract showed higher reducing power measured by the spectrophotometry method, as well as higher efficiency for "green" synthesis of silver nanoparticles. In summary, SEM, EDX, and UV-Vis spectroscopy confirmed the successful eco-friendly method for the synthesis of AgNPs using extracts. The synthesized GPE-AgNPs and PPE-AgNPs exhibit mainly a spherical shape with small size (40 to 60 nm). The sharp peak detected near 3 keV approves the successful synthesis of AgNPs by the use of the extracts. The AgNPs showed antimicrobial activity against common pathogenic bacteria *E. coli.* and *B. subtilis.*

Data Availability

All data generated or analyzed during this study are included within the article.

Conflicts of Interest

The authors declare that they have no conflicts of interest.

Acknowledgments

References

[1] C. M. Ajila, S. K. Brar, M. Verma, and U. J. S. Prasada Rao, "Sustainable solutions for agro processing waste management: an overview," *Strategies for Sustainability. Environmental Protection Strategies for Sustainable Development*, pp. 65–109, Springer, Dordrecht, Netherlands, 2011.

[2] T. Quang Huy, N. van Quy, and L. Anh-Tuan, "Silver nanoparticles: synthesis, properties, toxicology, applications and perspectives," *Advances in Natural Sciences: Nanoscience and Nanotechnology*, vol. 4, no. 3, Article ID 033001, 2013.

[3] M. Darroudi, M. B. Ahmad, A. H. Abdullah, N. A. Ibrahim, and K. Shameli, "Effect of accelerator in green synthesis of silver nanoparticles," *International Journal of Molecular Sciences*, vol. 11, no. 10, pp. 3898–3905, 2010.

[4] B. Ankamwar, C. Damle, A. Ahmad, and M. Sastry, "Biosynthesis of gold and silver nanoparticles using emblica officinalis fruit extract, their phase transfer and transmetallation in an organic solution," *Journal of Nanoscience and Nanotechnology*, vol. 5, no. 10, pp. 1665–1671, 2005.

[5] M. Skiba and V. Vorobyova, "Green synthesis of silver nanoparticles using grape pomace extract prepared by plasma-chemical assisted extraction method," *Molecular Crystals and Liquid Crystals*, vol. 671, no. 1, pp. 142–151, 2018.

[6] S. Pimentel-Moral, M. d. l. L. Cádiz-Gurrea, C. Rodríguez-Pérez, and A. Segura-Carretero, "Recent advances in extraction technologies of phytochemicals applied for the revaluation of agri-food by-products," in *Functional and Preservative Properties of Phytochemicals*, pp. 209–239, Elsevier, Amsterdam, Netherlands, 2020.

[7] K. V. G. Ravikumar, S. V. Sudakaran, K. Ravichandran, M. Pulimi, C. Natarajan, and A. Mukherjee, "Green synthesis of NiFe nano particles using *Punica granatum* peel extract for tetracycline removal," *Journal of Cleaner Production*, vol. 210, pp. 767–776, 2019.

[8] N. Ahmad and S. Sharma, "Biosynthesis of silver nanoparticles from biowaste pomegranate peels," *International Journal of Nanoparticles*, vol. 5, no. 3, pp. 185–195, 2012.

[9] N. Ahmad, S. Sharma, and R. Rai, "Rapid green synthesis of silver and gold nanoparticles using peels of *Punica granatum*," *Advanced Materials Letters*, vol. 3, no. 5, pp. 376–380, 2012.

[10] S. S. Shankar, A. Rai, A. Ahmad, and M. Sastry, "Rapid synthesis of Au, Ag, and bimetallic Au core-Ag shell nanoparticles using Neem (*Azadirachta indica*) leaf broth," *Journal of Colloid and Interface Science*, vol. 275, no. 2, pp. 496–502, 2004.

[11] H. I. Abdel-Shafy and M. S. M. Mansour, "Green synthesis of metallic nanoparticles from natural resources and food waste and their environmental application," *Green Metal Nanoparticles*, vol. 117, pp. 321–385, 2018.

[12] E. Alibakhshi, M. Ramezanzadeh, S. A. Haddadi, G. Bahlakeh, B. Ramezanzadeh, and M. Mahdavian, "*Persian Liquorice* extract as a highly efficient sustainable corrosion inhibitor for mild steel in sodium chloride solution," *Journal of Cleaner Production*, vol. 210, pp. 660–672, 2019.

[13] V. I. Vorobyova, M. I. Skiba, and I. M. Trus, "Apricot pomaces extract (*Prunus armeniaca l.*) as a highly efficient sustainable corrosion inhibitor for mild steel in sodium chloride solution," *International Journal of Corrosion and Scale Inhibition*, vol. 8, no. 4, pp. 1060–1083, 2019.

[14] P. Refait, C. Rahal, and M. Masmoudi, "Corrosion inhibition of copper in 0.5 M NaCl solutions by aqueous and hydrolysis acid extracts of olive leaf," *Journal of Electroanalytical Chemistry*, vol. 859, Article ID 113834, 2020.

[15] G. Vasyliev, V. Vorobyova, and T. Zhuk, "*Raphanus sativus* L. extract as a scale and corrosion inhibitor for mild steel in tap water," *Journal of Chemistry*, vol. 2020, Article ID 5089758, 2020.

[16] V. Vorob'iova, O. Chyhyrynets, and O. Vasyl'kevych, "Mechanism of formation of the protective flms on steel by volatile compounds of rapeseed cake," *Materials Science*, vol. 50, no. 5, pp. 726–735, 2015.

[17] O. V. Zillich, U. Schweiggert-Weisz, P. Eisner, and M. Kerscher, "Polyphenols as active ingredients for cosmetic products," *International Journal of Cosmetic Science*, vol. 37, no. 5, pp. 455–464, 2015.

[18] G.-F. Deng, X. Lin, X.-R. Xu, L.-L. Gao, J.-F. Xie, and H.-B. Li, "Antioxidant capacities and total phenolic contents of 56 vegetables," *Journal of Functional Foods*, vol. 5, no. 1, pp. 260–266, 2013.

[19] M. Castrica, R. Rebucci, C. Giromini, M. Tretola, D. Cattaneo, and A. Baldi, "Total phenolic content and antioxidant capacity of agri-food waste and by-products," *Italian Journal of Animal Science*, vol. 18, no. 1, pp. 1–6, 2018.

[20] Y. Lyu, M. Yu, Q. Liu et al., "Synthesis of silver nanoparticles using oxidized amylose and combination with curcumin for enhanced antibacterial activity," *Carbohydrate Polymers*, vol. 230, Article ID 115573, 2019.

[21] V. Vorobyova, G. Vasyliev, and M. Skiba, "Eco-friendly "green" synthesis of silver nanoparticles with the black currant pomace extract and its antibacterial, electrochemical and antioxidant activity," *Applied Nanoscience*, vol. 10, 2020.

[22] G. Vasyliev, V. Vorobyova, M. Skiba, and L. Khrokalo, "Green synthesis of silver nanoparticles using waste products (apricot and black currant pomace) aqueous extracts and their characterization," *Advances in Materials Science and Engineering*, vol. 2020, no. 3, Article ID 4505787, 11 pages, 2020.

[23] M. Chaussemier, E. Pourmohtasham, D. Gelus et al., "State of art of natural inhibitors of calcium carbonate scaling. a review article," *Desalination*, vol. 356, pp. 47–55, 2015.

[24] Z. Belarbi, J. Gamby, L. Makhloufi, B. Sotta, and B. Tribollet, "Inhibition of calcium carbonate precipitation by aqueous extract of Paronychia argentea," *Journal of Crystal Growth*, vol. 386, pp. 208–214, 2014.

[25] H. Cheap-Charpentier, D. Gelus, N. Pécoul et al., "Antiscalant properties of *Spergularia rubra* and Parietaria officinalis aqueous solutions," *Journal of Crystal Growth*, vol. 443, pp. 43–49, 2016.

[26] E. A. Noor, "The impact of some factors on the inhibitory action of Radish seeds aqueous extract for mild steel corrosion in 1M H_2SO_4 solution," *Materials Chemistry and Physics*, vol. 131, no. 1-2, pp. 160–169, 2011.

[27] D. Li, P. Zhang, X. Guo, X. Zhao, and Y. Xu, "The inhibition of mild steel corrosion in 0.5 M H_2SO_4 solution by radish leaf extract," *RSC Advances*, vol. 9, no. 70, pp. 40997–41009, 2019.

[28] I. Radojčić, K. Berković, S. Kovač, and J. Vorkapić-Furač, "Natural honey and black radish juice as tin corrosion inhibitors," *Corrosion Science*, vol. 50, no. 5, pp. 1498–1504, 2008.

[29] J. A. Selvi, S. Rajendran, V. G. Sri, A. J. Amalraj, and B. Narayanasamy, "Corrosion inhibition by beet root extract," *Portugaliae Electrochimica Acta*, vol. 27, no. 1, 2009.

[30] G. Vasyliev and V. Vorobiova, "Rape grist extract (*Brassica napus*) as a green corrosion inhibitor for water systems," *Materials Today: Proceedings*, vol. 6, pp. 178–186, 2019.

[31] J. C. Sánchez-Rangel, J. Benavides, J. B. Heredia, L. Cisneros-Zevallos, and D. A. Jacobo-Velázquez, "The *Folin-Ciocalteu* assay revisited: improvement of its specificity for total

phenolic content determination," *Analytical Methods*, vol. 5, no. 21, p. 5990, 2013.

[32] A. Arvouet-Grand, B. Vennat, A. Pourrat, and P. Legret, "Standardization of propolis extract and identification of principal constituents," *Journal of Pharmacy Belgium*, vol. 49, pp. 462–468, 1994.

[33] P. Prieto, M. Pineda, and M. Aguilar, "Spectrophotometric quantitation of antioxidant capacity through the formation of a phosphomolybdenum complex: specific application to the determination of vitamin E," *Analytical Biochemistry*, vol. 269, no. 2, pp. 337–341, 1999.

[34] K. Taipong, U. Boonprakob, K. Crosby, L. Cisneros-Zevallos, and D. Hawkins Byrne, "Comparison of ABTS, DPPH, FRAP, and ORAC assays for estimating antioxidant activity from guava fruit extracts," *Journal of Food Composition and Analysis*, vol. 19, no. 6-7, pp. 669–675, 2006.

[35] W. Rhimi, R. Hlel, I. Ben Salem, A. Boulila, A. Rejeb, and M. Saidi, "*Dittrichia viscosa* L. ethanolic extract based ointment with antiradical, antioxidant, and healing wound activities," *BioMed Research International*, vol. 2019, Article ID 4081253, 10 pages, 2019.

[36] H. S. Vasyl'Ev, "Measurement of polarization resistance with computer logging of results," *Materials Science*, vol. 48, no. 5, pp. 694–696, 2013.

[37] H. S. Vasyl'ev and Y. S. Herasymenko, "Corrosion meters of new generation based on the improved method of polarization resistance," *Materials Science*, vol. 52, no. 5, pp. 722–731, 2017.

[38] G. Vasyliev, "Polarization resistance measurement in tap water: the influence of rust electrochemical activity," *Journal of Materials Engineering and Performance*, vol. 26, no. 8, pp. 3939–3945, 2017.

[39] Y. S. Herasymenko and H. S. Vasyl'ev, "A two-step method for the evaluation of corrosion rate in metals," *Materials Science*, vol. 45, no. 6, pp. 899–904, 2009.

[40] G. Vasyliev, S. Vasylieva, A. Novosad, and Y. Gerasymenko, "Ultrasonic modification of carbonate scale electrochemically deposited in tap water," *Ultrasonics Sonochemistry*, vol. 48, pp. 57–63, 2018.

[41] O. E. Chyhyrynets, Y. F. Fateev, V. I. Vorobiova, and M. I. Skyba, "Study of the mechanism of action of the isopropanol extract of rapeseed oil cake on the atmospheric corrosion of copper," *Materials Science*, vol. 51, no. 5, pp. 644–651, 2016.

[42] V. Vorobyova, M. Skiba, and O. Chygyrynets', "A novel eco-friendly vapor phase corrosion inhibitor of mild steel," *Pigment & Resin Technology*, vol. 48, no. 2, pp. 137–147, 2019.

[43] V. Vorobyova, O. Chygyrynets, M. Skiba, T. Zhuk, I. Kurmakova, and O. Bondar, "A comprehensive study of grape cake extract and its active components as effective vapour phase corrosion inhibitor of mild steel," *International Journal of Corrosion and Scale Inhibition*, vol. 7, pp. 185–202, 2018.

[44] V. Vorobyova, O. Chygyryneť, M. Skiba, I. Kurmakova, and O. Bondar, "Self-assembled monoterpenoid phenol as vapor phase atmospheric corrosion inhibitor of carbon steel," *International Journal of Corrosion and Scale Inhibition*, vol. 6, no. 4, pp. 485–503, 2017.

[45] V. I. Vorobyova, M. I. Skiba, A. S. Shakun, and S. V. Nahirniak, "Relationship between the inhibition and antioxidant properties of the plant and biomass wastes extracts—a review," *International Journal of Corrosion and Scale Inhibition*, vol. 8, pp. 150–178, 2019.

[46] V. Vorobyova, O. Chygyrynets, and M. Skiba, "4-hydroxy-3-methoxybenzaldehyde as a volatile inhibitor on the atmospheric corrosion of carbon steel," *Journal of Chemical Technology and Metallurgy*, vol. 53, pp. 336–345, 2018.

[47] V. Vorobyova, M. Skiba, O. Chygyrynets', M. Skiba, I. Trus, and S. Frolenkova, "Grape pomace extract as green vapor phase corrosion inhibitor," *Chemistry & Chemical Technology*, vol. 12, no. 3, pp. 410–418, 2018.

[48] E. Bruno Romanini, L. Misturini Rodrigues, A. Finger, T. Perez Cantuaria Chierrito, M. Regina da Silva Scapim, and G. Scaramal Madrona, "Ultrasound assisted extraction of bioactive compounds from BRS Violet grape pomace followed by alginate-Ca^{2+} encapsulation," *Food Chemistry*, vol. 338, p. 128101, 2021.

[49] J. E. Young, Z. Pan, H. E. Teh et al., "Phenolic composition of pomegranate peel extracts using an liquid chromatography-mass spectrometry approach with silica hydride columns," *Journal of Separation Science*, vol. 40, no. 7, pp. 1449–1456, 2017.

[50] N. Swilam and K. A. Nematallah, "Polyphenols profile of pomegranate leaves and their role in green synthesis of silver nanoparticles," *Scientific Reports*, vol. 10, p. 14851, 2020.

[51] T. J. I. Edison and M. G. Sethuraman, "Biogenic robust synthesis of silver nanoparticles using *Punica granatum* peel and its application as a green catalyst for the reduction of an anthropogenic pollutant 4-nitrophenol," *Spectrochimica Acta Part A: Molecular and Biomolecular Spectroscopy*, vol. 104, pp. 262–264, 2013.

[52] M. F. Zayed, W. H. Eisa, S. M. El-kousy, W. K. Mleha, and N. Kamal, "Ficus retusa-stabilized gold and silver nanoparticles: controlled synthesis, spectroscopic characterization, and sensing properties," *Spectrochimica Acta Part A: Molecular and Biomolecular Spectroscopy*, vol. 214, pp. 496–512, 2019.

[53] M. Skiba, V. Vorobyova, A. Pivovarov, A. Shakun, E. Gnatko, and I. Trus, ""Green" synthesis of nanoparticles of precious metals: antimicrobial and catalytic properties," *Eastern-European Journal of Enterprise Technologies*, vol. 5, no. 6 (95), pp. 51–58, 2018.

[54] P. Chettri, V. S. Vendamani, A. Tripathi, M. K. Singh, A. P. Pathak, and A. Tiwari, "Green synthesis of silver nanoparticle-reduced graphene oxide using *Psidium guajava* and its application in SERS for the detection of methylene blue," *Applied Surface Science*, vol. 406, pp. 312–318, 2017.

[55] S. Devanesan, M. S. AlSalhi, R. V. Balaji et al., "Antimicrobial and cytotoxicity effects of synthesized silver nanoparticles from *Punica granatum* peel extract," *Nanoscale Research Letters*, vol. 13, p. 315, 2018.

[56] G. D. Saratale, R. G. Saratale, D.-S. Kim, D.-Y. Kim, and H.-S. Shin, "Exploiting fruit waste grape pomace for silver nanoparticles synthesis, assessing their antioxidant, antidiabetic potential and antibacterial activity against human pathogens: a novel approach," *Nanomaterials*, vol. 10, no. 8, p. 1457, 2020.

[57] N. Hashim, M. Paramasivam, J. S. Tan et al., "Green mode synthesis of silver nanoparticles using *Vitis vinifera*'s tannin and screening its antimicrobial activity/apoptotic potential versus cancer cells," *Materials Today Communications*, vol. 25, Article ID 101511, 2020.

Research Article

Microwave Heating Characteristics of Emulsified Asphalt Repair Materials Incorporated with Steel Slag

Yongfeng Wei,[1,2] Jinyang Huo,[3] Zhenjun Wang [ID],[3] and Jiangtao Gao[1]

[1]*Research and Development Center of Transport Industry of Technologies,*
 Materials and Equipments of Highway Construction and Maintenance (Gansu Province Traffic Construction Group),
 Lanzhou 730030, China
[2]*Gansu Road and Bridge Construction Group, Lanzhou 730030, China*
[3]*School of Materials Science and Engineering, Chang'an University, Xi'an 710061, China*

Correspondence should be addressed to Zhenjun Wang; zjwang@chd.edu.cn

Emulsified asphalt needs to be cured for a certain age after demulsification to produce strength, which seriously affects the traffic opening time. In this work, microwave heating technology was applied for emulsified asphalt repair materials. Steel slag with high microwave activity was adopted to improve the performance of emulsified asphalt repair materials by microwave heating. Effects of steel slag sizes and contents on the heating rate, temperature distribution, and thermal performance of emulsified asphalt repair materials were analyzed by close microwave heating, open microwave heating, and repair simulation tests. Results show that the temperature of emulsified asphalt repair materials presents three different heating stages under microwave irradiation. The "critical point of phase transition" in the three stages is gradually advanced with the increase in steel slag content. The core temperature and maximum temperature of emulsified asphalt repair materials with different steel slag sizes are basically the same; however, the heat distribution of emulsified asphalt repair materials is significantly different. In contrast to conventional asphalt mixture, there exists a smaller temperature difference. The temperature of repairing materials can reach above 80°C. The interface area can form an embedded interface structure. Incorporation of steel slag and adoption of microwave heating are effective to improve the performance of emulsified asphalt repair materials.

1. Introduction

Emulsified asphalt repair materials are a mixture of emulsified asphalt as a binder and are mixed according to a certain proportion, which is used to treat asphalt pavement potholes and other diseases. They have the advantages of energy saving and environmental protection, low pollution, wide application, simple construction, and less external influence [1–3]. However, as emulsified asphalt is a water-based emulsified material, the internal free water is difficult to volatilize and exists for a long time [4–6]. This results in low interfacial adhesion, low strength, and poor flexibility of the emulsified asphalt mixture [7–9].

In recent years, microwave heating technology has been applied to asphalt and cement pavement engineering

[10, 11]. Microwave heating technology has the characteristics of fast heating rate, uniform heating, and environment friendly for asphalt mixture [12]. Microwave heating technology is suitable for the repair of asphalt pavement cracks and depressions. Notably, microwave treatment of metal factory waste (such as steel slag and cooper slag) is very effective in asphalt mixture crack repair [13, 14]. Furthermore, the mixture heated by microwave has better high-temperature rutting resistance, low-temperature crack resistance, and water stability [15]. In addition, microwave heating technology has been applied in the chemical field of crude oil demulsification [16–18]. In contrast to traditional methods, such as thermal demulsification and stable emulsion demulsification, microwave heating technology has a higher demulsification rate, higher dehydration rate,

and better demulsification effect [19–22]. Based on the advantages of microwave heating technology, it is feasible to introduce microwave heating technology into an emulsified asphalt mixture.

At present, the influence of microwave heating on the performance of emulsified asphalt mixture has been studied [23, 24]. The results show that microwave heating is beneficial to improve the mechanical properties of emulsified asphalt mixture. Microwave heating can rapidly increase the temperature in a short period of time to quickly destroy the electrical double layer structure of emulsified asphalt. At the same time, the repulsive force between the emulsified asphalt particles decreases, and the water in the emulsion is released quickly to demulsify the asphalt emulsion. However, the microwave heating time of emulsified asphalt mixture without high microwave active materials is relatively long.

In this work, the emulsified asphalt repair materials based on microwave heating were developed. It can be mixed at room temperature on a construction site, produce strength quickly, and has good interface performance. The heating efficiency and temperature distribution of emulsified asphalt repair materials with different steel slag sizes and contents were studied by heating tests. In addition, the effects of steel slag sizes and contents on microwave heating performance of emulsified asphalt repair materials were analyzed through X-ray diffraction (XRD) test and environmental scanning electron microscopy (ESEM) test.

2. Experimental

2.1. Materials. The material selection and experiments are based on the Standard Test Methods of Bitumen and Bituminous Mixtures for Highway Engineering (JTG E20-2011). Tables 1 and 2 show properties of cationic emulsified asphalt and steel slag (the tail slag of steelworks), respectively. Figure 1 shows aggregate gradation used for emulsified asphalt repair mixture.

2.2. Mix Proportion Design. In this work, the single grade aggregate was selected for the mix proportion verification test to ensure the stability of the mix proportion. According to the Marshall test result, the optimum asphalt-aggregate ratio was 4.8%, and the volume content of steel slag was 10%. Tables 3 and 4 show the mix proportion of emulsified asphalt mixture with different steel slag contents and emulsified asphalt mixture with different steel slag sizes, respectively.

2.3. Preparation of Specimens. Figure 2 shows the preparation and test flow chart of the emulsified asphalt mixture with steel slag. First, aggregate, water, mineral powder, and emulsified asphalt were weighed. Their total mass is 1250 g. Then, these raw materials were put into the mixture mixer and mixed for 120 s. Second, the mixture was poured into round molds with the diameter of 101.5 mm and the height of 63.5 mm to prepare the specimens. Then, these molds with mixtures were heated in a microwave. Third, the surface temperature and internal temperature of specimens were tested by using an infrared thermal imager.

2.4. Test Methods

2.4.1. Close Microwave Heating Test. In the indoor heating efficiency test, the civil microwave was used to conduct a close microwave heating test on emulsified asphalt repair materials in ceramic containers. The core temperature, overall infrared thermal imaging, and thermal distribution tests were conducted at different test points. The output frequency and output power of the microwave were 2.45 GHz and 0.7 kW, respectively.

2.4.2. Open Microwave Heating Test. In the simulation test of emulsified asphalt repair, self-prepared open microwave heating equipment (Figure 3) was used to conduct field simulation heating test. According to the Industrial Microwave Heating Installations-Test Methods for the Determination of Power Output (IEC 61307-2011) and Safety in Electroheat Installations-Part 6 and Specifications for Safety in Industrial Microwave Heating Equipment (IEC 60519-6-2011), Table 5 shows the specific parameters of self-prepared open microwave heating equipment.

2.4.3. Repair Simulation Test. Figure 4 shows the simulation test process of emulsified asphalt repair. The new-old mixture bonding model was used in the repair simulation test. The rutting plate of ordinary asphalt mixture was used to repair the old mixture. Firstly, the old mixture is drilled with a rotary drilling rig, and then, the core drilling position of the old mixture was filled with emulsified asphalt repair materials. Secondly, the plate was heated to the design temperature of 140°C in self-prepared open microwave heating equipment. Finally, the plate was rolled and formed.

2.4.4. Microstructure Tests of Steel Slag. In this work, an X-ray diffraction (XRD) test and environmental scanning electron microscopy (ESEM) test were conducted. For the XRD test, first, the steel slag aggregate was crushed into small pieces (4-6 mm) and immersed in ethanol absolute for 24 h. Then, the small piece of steel slag aggregate was dried in a vacuum drying oven at 80°C for 12 h to achieve a constant mass. Second, the small piece of steel slag aggregate was ground into powder (<80 μm). Finally, the powder was tested by using X-ray diffractometer at a scanning range of 5°–80°, a scanning speed of 5°/min, and a step size of 0.02°.

For the ESEM test, the steel slag aggregate was crushed into small pieces (about 5 mm). Then, the small piece was tested by S-4800 cold-field ESEM at an applied accelerating voltage of 7.0 kV and temperature of 20°C.

3. Results and Discussion

3.1. XRD Analyses of Steel Slag. Figures 5 and 6 show the XRD and microstructure of steel slag, respectively. Figure 5 shows that the steel slag contains a variety of minerals, especially magnetite. Magnetite has a strong microwave absorption capacity [25, 26]. As can be seen from Figure 6(a), there are tiny pits and cracks on the steel slag surface. These cracks can be used to fill asphalt to increase

TABLE 1: Properties of emulsified asphalt.

Test items		Unit	Specification	Test results
Residue percentage (1.18 mm sieve)		%	<0.1	0.03
Viscosity	Engra viscosity E25	—	2–30	8.12
	25°C Saybolt viscosity	s	7–100	55
Evaporated residue	Residual content	%	>62	64
	Solubility	%	>97.5	100
	Needle penetration (25°C)	0.1 mm	50–300	65
	Ductility (15°C)	cm	>40	79
Adhesion to coarse aggregate		—	2/3	2/3
Mixing test with aggregate			Even	Even
Storage	1 d	%	<1%	0.3
Stability	5 d		<5%	2.0

TABLE 2: Properties of steel slag.

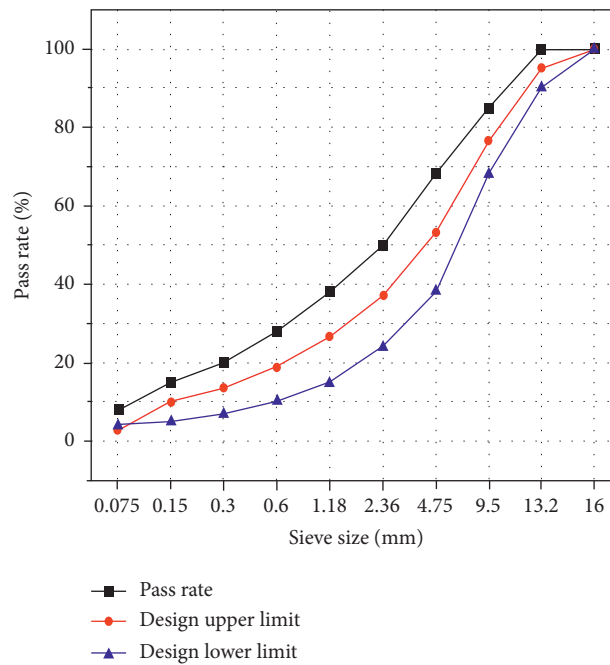| Test items	1.18 mm	2.36 mm	4.75 mm	9.5 mm
Apparent relative density	3.420	3.380	3.320	3.310
Water absorption (%)	1.57	1.61	1.58	1.60
Polished value (%)		67		
Los Angeles attrition (%)		13.0		
Crushing value (%)		12.1		
Adhesion		Level 5		

FIGURE 1: Aggregate gradation chart of emulsified asphalt mixture.

TABLE 3: Mix proportion of emulsified asphalt mixture with different steel slag contents.

Mix proportion	13.2	9.5	Aggregate percentage (%)							Mineral powder	Asphalt-aggregate ratio (%)
			4.75	2.36	1.18	0.6	0.3	0.15	0.075		
0-0-0	5	18.5	23.5	16	10.5	7.5	5.5	3.5	7	3	4.8
1-2-1	5	18.5	18.5 + 5*	16	10.5	7.5	5.5	3.5	7	3	4.8
1-2-2	5	18.5	13.5 + 10*	16	10.5	7.5	5.5	3.5	7	3	4.8
1-2-3	5	18.5	8.5 + 15*	16	10.5	7.5	5.5	3.5	7	3	4.8

Note: $X + 5^*$ (10^* or 15^*) represents equal substitution of 5% (10% or 15%) ordinary aggregate with steel slag of the same size.

TABLE 4: Mix proportion of emulsified asphalt mixture with different steel slag sizes.

Mix proportion	13.2	9.5	4.75	2.36	1.18	0.6	0.3	0.15	0.075	Mineral powder	Asphalt-aggregate ratio (%)
1-1-2	5	8.5 + 10*	23.5	16	10.5	7.5	5.5	3.5	7	3	4.8
1-2-2	5	18.5	13.5 + 10*	16	10.5	7.5	5.5	3.5	7	3	4.8
1-3-2	5	18.5	23.5	6 + 10*	10.5	7.5	5.5	3.5	7	3	4.8
1-4-2	5	18.5	23.5	16	0.5 + 10*	7.5	5.5	3.5	7	3	4.8

Note: $X + 5^*$ (10^* or 15^*) represents equal substitution of 5% (10% or 15%) ordinary aggregate with steel slag of the same size.
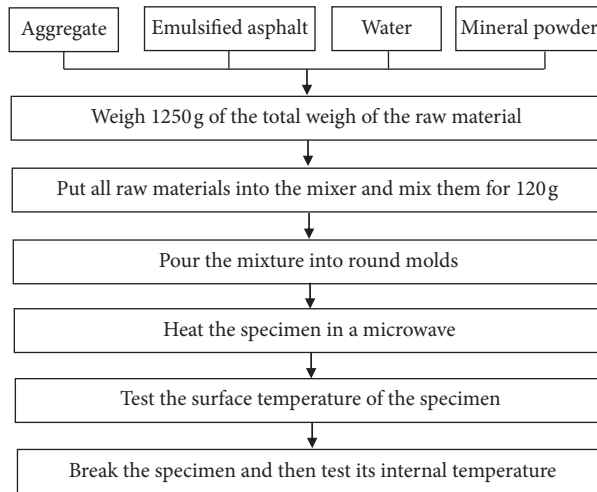

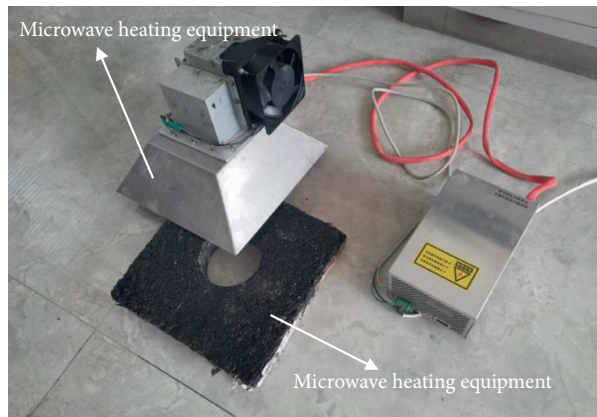FIGURE 2: Preparation and test flow of emulsified asphalt mixture with steel slag.

FIGURE 3: Self-prepared microwave heating equipment.

TABLE 5: Technical parameters of self-prepared open microwave heating equipment.

Parameters	Size (cm × cm)	Input voltage (V)	Output frequency (GHz)	Output power (kW)
Results	30 × 30	220	2.45	1.5

the depth of embedding on the steel slag surface. The stress area of steel slag can increase, which enhances its resistance to external forces. Therefore, the physical structure characteristics of the steel slag surface provide a skeleton-like effect for the asphalt-aggregate interface [27]. In addition, Figure 6(b) shows that the main elements in the slag are Si (SiO_2), O (SiO_2), Fe (Fe), Mg (MgO), and Ca (wollastonite). It is the presence of Fe element that increases the electromagnetic loss of emulsified asphalt repair materials with steel slag. This can enhance the microwave absorption capacity of emulsified asphalt repair materials to improve its heating efficiency [28].
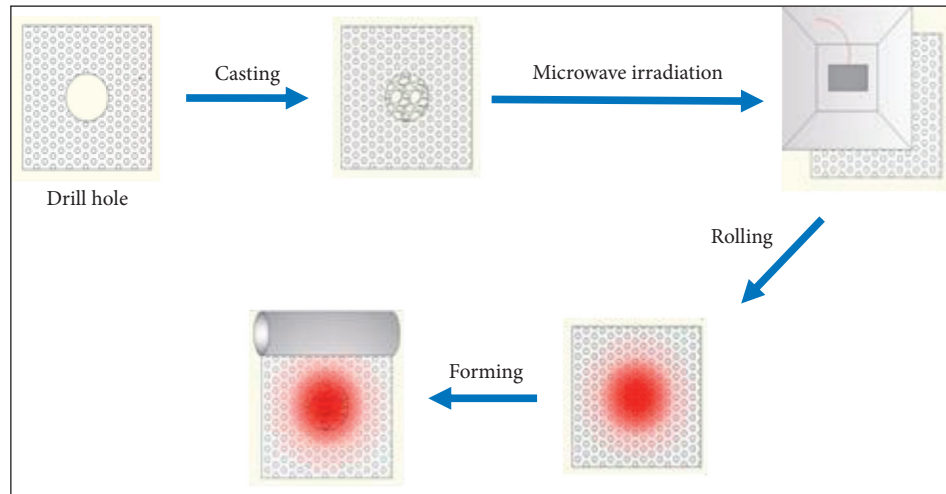
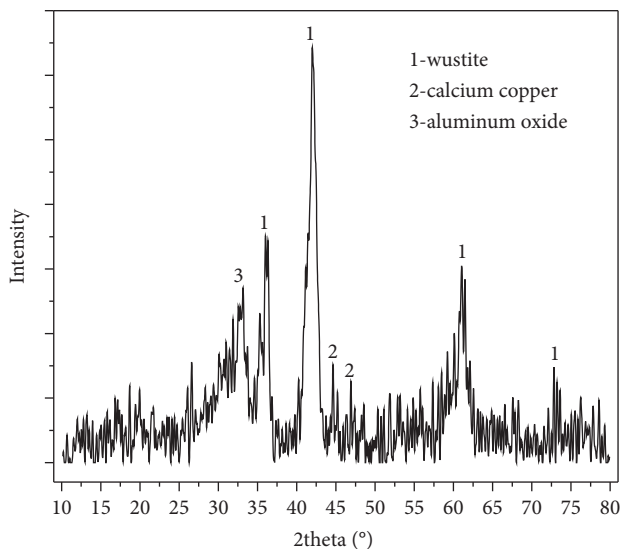FIGURE 4: Simulation test process of emulsified asphalt repair.

FIGURE 5: XRD spectrum of steel slag.

3.2. Effects of Steel Slag on Heating Rate of Emulsified Asphalt Repair Materials

3.2.1. Temperature Changes in Emulsified Asphalt Repair Materials. Figure 7 shows the temperature curve of emulsified asphalt repair materials with different steel slag contents under microwave heating (the size of steel slag is 4.75 mm). The heating rate of emulsified asphalt repair materials increases gradually with the increase in steel slag content. This shows that steel slag can greatly shorten microwave heating time. The higher the content, the higher the temperature of emulsified asphalt repair materials. In addition, Figure 7 shows the curve of temperature change (Figure 8). The heating stage can be divided into three stages: initial rapid rising stage (stage I: ≤95°C), medium stable stage (stage II: 95°C–100°C), and late rapid rising stage (stage III: ≥100°C). Figures 7 and 8 show that the heating trend of all samples is roughly the same. However, the transformation

points of the three stages are slightly different due to the content of steel slag.

In emulsified asphalt repair materials with steel slag, water and steel slag are the main microwave absorbing materials. They produce a large number of molecular friction and collision under the microwave heating, which makes the temperature of emulsified asphalt repair materials rise rapidly. Thus, it presents an "initial rapid rising stage" (stage I: ≤95°C). The water in emulsified asphalt evaporates, when the internal temperature of emulsified asphalt repair materials increases close to 100°C. In a long period of time, the core temperature of emulsified asphalt repair materials is basically stable, thus forming a "medium stable stage" (stage II: 95°C–100°C). As the microwave heating continues, a large amount of moisture in the emulsified asphalt repair materials evaporates. The main microwave absorbing materials in the emulsified asphalt repair materials change from water and steel slag to steel slag. The core temperature of emulsified asphalt repair materials increased rapidly for the second time, thus forming a "late rapid rising stage" (stage III: ≥100°C). In the emulsified asphalt repair materials without steel slag, water and aggregates are the main microwave absorbing materials. The temperature rise range of emulsified asphalt repair materials without steel slag is less than that of emulsified asphalt repair materials with steel slag.

3.2.2. Temperature Distribution of Emulsified Asphalt Repair Materials. Figure 9 shows the infrared thermograms of the surface temperature of emulsified asphalt repair materials without steel slag and with 5% steel slag heated by microwave for 15 min, respectively. Based on the observation in Figures 9(a) and 9(b), the average surface temperature of emulsified asphalt repair materials with steel slag is 140°C, while emulsified asphalt repair materials without steel slag are 84°C. This shows that steel slag can significantly increase the surface temperature of emulsified asphalt repair materials.
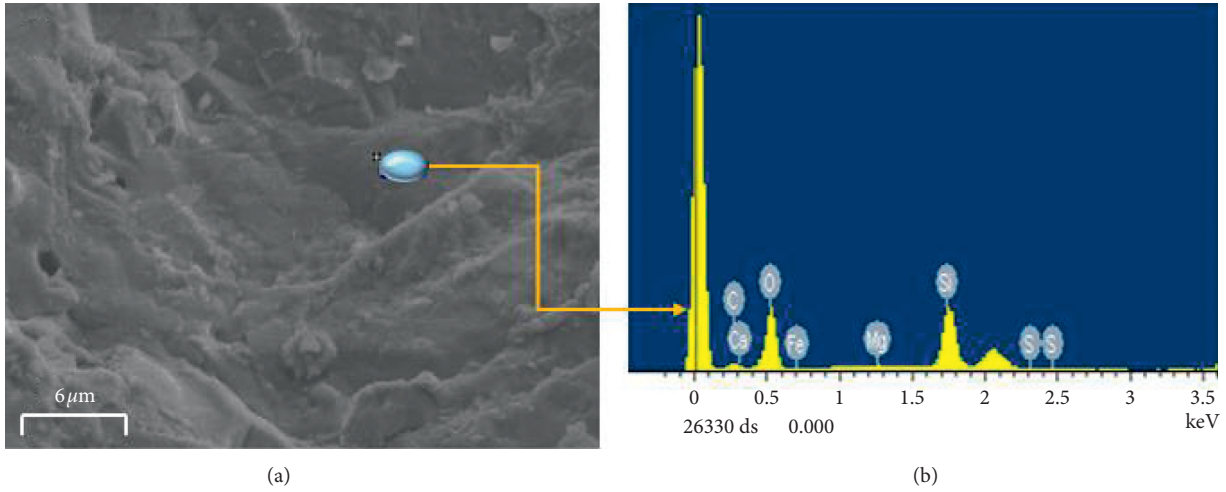
(a)

(b)

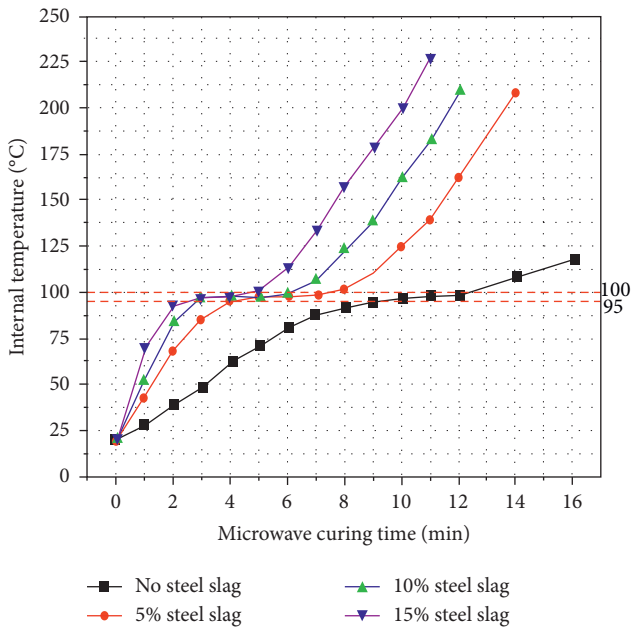FIGURE 6: The ESEM results of steel slag: (a) microstructures; (b) main elements.

FIGURE 7: Temperature curve of emulsified asphalt repair materials with different steel slag contents.
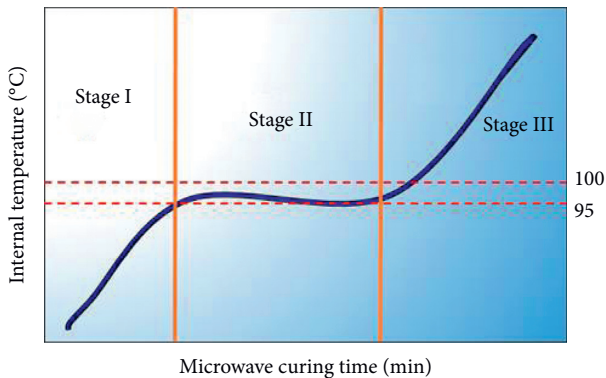

FIGURE 8: Temperature changes in emulsified asphalt repair materials under microwave heating.

In addition, the temperature distribution of emulsified asphalt without steel slag is uneven, the temperature of the middle part is significantly higher than that of the surrounding, and the temperature difference is about 20°C. The surface temperature distribution of emulsified asphalt repair materials with steel slag is more uniform (Figure 9(b)). This shows that the steel slag is evenly distributed in the emulsified asphalt repair materials, and it is conducive to improve the uniformity of temperature distribution of emulsified asphalt repair materials.

Figure 10 shows the internal temperature of emulsified asphalt repair materials. The average internal temperature of emulsified asphalt repair materials with steel slag is 150°C. The average internal temperature of emulsified asphalt repair materials without steel slag is 113°C. This shows that steel slag can significantly increase the internal temperature of emulsified asphalt repair materials. At the same time, the temperature distribution of emulsified asphalt repair materials with steel slag is approximately uniform, but the temperature at the edge of the mixture is hierarchical. The temperature limit of emulsified asphalt repair materials without steel slag is not obvious. It shows that the internal temperature distribution of emulsified asphalt repair materials without steel slag is more uniform.

In addition, in contrast to the internal temperature and the surface temperature (Figures 9(b) and 10(b)), the internal and external temperature difference in emulsified asphalt repair materials with steel slag is 7°C, while the internal and external temperature difference in emulsified asphalt repair materials without steel slag is 30°C. Therefore, steel slag has a positive effect on reducing the internal and external temperature difference in emulsified asphalt repair materials after microwave heating.

3.3. Effect of Steel Slag Size on Heating Rate of Emulsified Asphalt Repair Materials

3.3.1. Temperature Changes in Emulsified Asphalt Repair Materials. Figure 11 shows the temperature change trend of emulsified asphalt repair materials with different steel slag
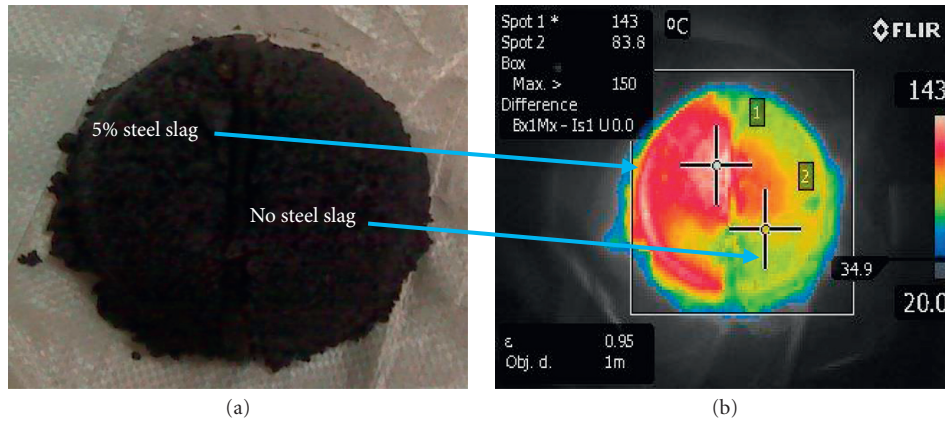
(a)

(b)

FIGURE 9: Surface infrared thermogram of emulsified asphalt repair materials: (a) mixture sample; (b) infrared thermogram.
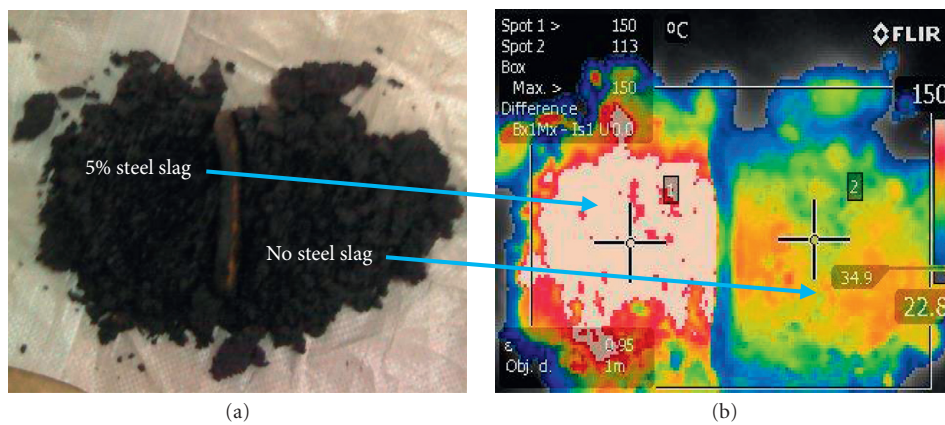

(a)

(b)

FIGURE 10: Internal infrared thermogram of emulsified asphalt repair materials: (a) mixture sample; (b) infrared thermogram.
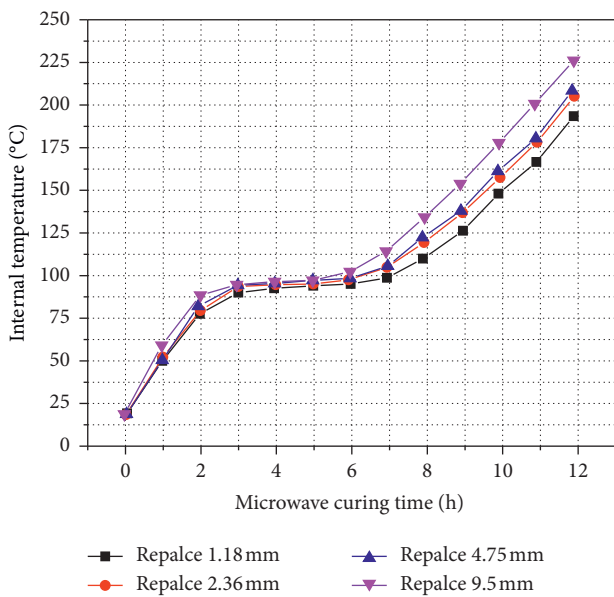

FIGURE 11: Temperature change trend of emulsified asphalt repair materials with different steel slag sizes under microwave heating.

sizes under microwave heating. The temperature rising rate of emulsified asphalt repair materials with different steel slag sizes is different, but the difference is not significant. According to the size, the order of temperature rising rate of emulsified asphalt repair materials is 9.5 mm > 4.75 mm > 2.36 mm > 1.18 mm. In contrast to Figures 11 and 7, the influence of steel slag sizes on the temperature of emulsified asphalt repair materials is weak. At the same time, the change in the heating curve in Figure 11 is consistent with that of the heating curve in Figure 7, including the initial rapid rising stage ($\leq 95°C$), medium stable stage ($95°C–100°C$), and late rapid rising stage ($\geq 100°C$).

Figure 12 shows the distribution results of the main elements in steel slag. The corresponding elements are marked and distinguished with points of different colors. The distribution of Ca, Si, and O in steel slag is uniform, while Fe is uneven and discontinuous. Therefore, the steel slag size has an effect on the heating rate of emulsified asphalt repair materials.

3.3.2. Temperature Distribution of Emulsified Asphalt Repair Materials with Different Steel Slag Sizes. Figure 13 shows the infrared thermogram of emulsified asphalt repair materials with different steel slag sizes. The surface temperature and internal temperature of emulsified asphalt repair materials can be improved rapidly. Compared with the internal temperature, the surface temperature is higher. The maximum surface temperature is 95.4°C, and the maximum internal temperature is 80.3°C. Due to the short microwave heating time, the temperature of emulsified asphalt repair
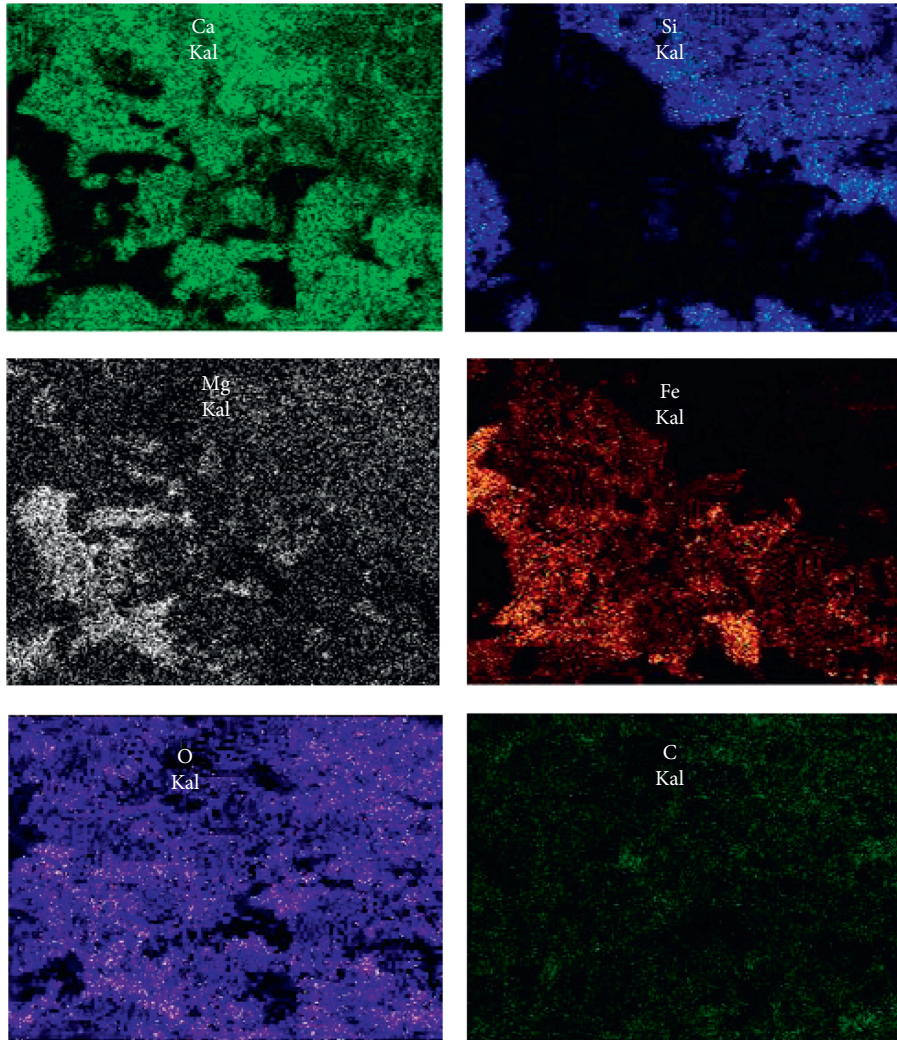
FIGURE 12: Distribution of main elements in steel slag.

materials is lower. In the process of crushing, emulsified asphalt repair materials dissipate a part of heat, resulting in a large temperature gradient inside and outside. However, the core temperature and maximum temperature of emulsified asphalt repair materials with different steel slag sizes are basically the same, and there is no significant difference. The average surface temperature is about 83°C, and the internal temperature is about 68°C.

In addition, the temperature distribution of emulsified asphalt repair materials is different. The larger the steel slag size, the more uneven the surface temperature and internal temperature. The surface and internal temperature distributions of emulsified asphalt repair materials with a steel slag size of 9.5 mm have a high range of color differences, indicating that the temperature distribution is uneven. However, the surface and internal colors of emulsified asphalt repair materials with 2.36 mm and 1.18 mm steel slags are basically the same, indicating that the temperature distribution is relatively uniform.

Figure 14 shows the simulation diagram of emulsified asphalt repair materials with different steel slag sizes under

microwave heating. The distribution of steel slag in emulsified asphalt repair materials is different when the size of steel slag changes (the content of steel slag remains unchanged). The steel slag is distributed in the form of coarse aggregate in the emulsified asphalt repair materials, when the steel slag size is larger. The microwave absorption capacity of large volume steel slag (9.5 mm) is higher than that of small volume steel slag (2.36 mm and 1.18 mm).

Therefore, the heating rate of emulsified asphalt repair materials with large volume steel slag is higher than that of emulsified asphalt repair materials with a small volume steel slag. Notably, the small volume steel slag has the function of fine aggregate. It can fill the gap and disperse evenly in the emulsified asphalt repair materials. Thus, the overall temperature distribution of emulsified asphalt repair materials with small volume steel slag is more uniform under microwave heating [29].

3.4. Analyses of the Effect of Repair Methods. Figure 15 shows the infrared thermogram of the repair model of the
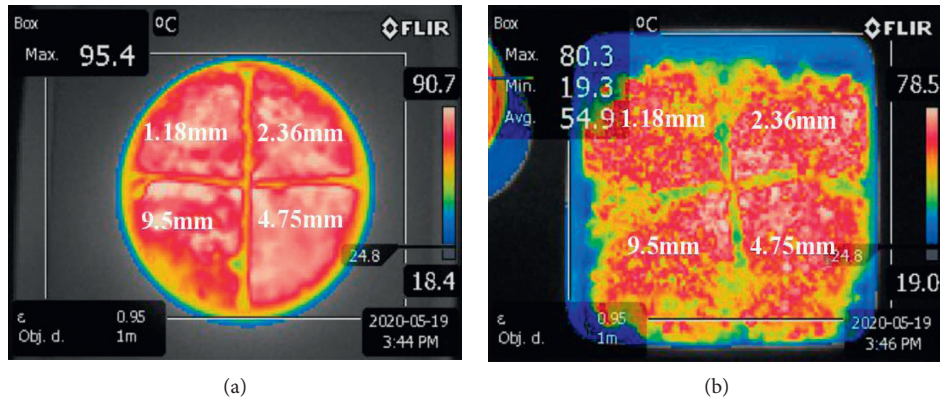
Figure 13: Infrared thermography of emulsified asphalt repair materials with different steel slag sizes: (a) surface temperature distribution; (b) internal temperature distribution.
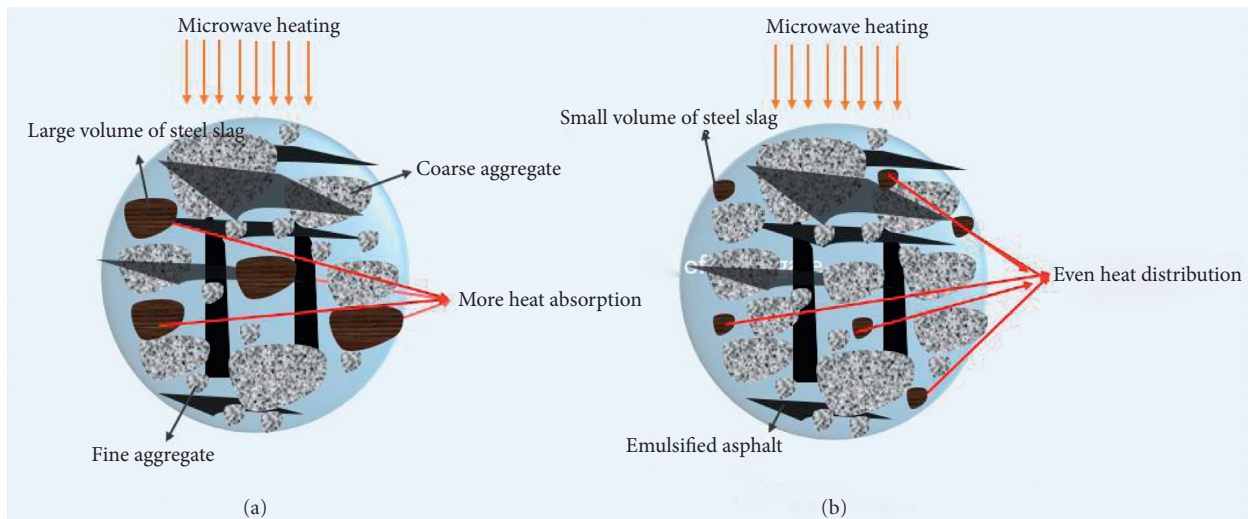

Figure 14: Simulation diagram of emulsified asphalt repair materials with different steel slag sizes under microwave heating: (a) bulk steel slag instead of aggregate; (b) small steel slag instead of aggregate.

conventional asphalt mixture. Based on the observation in Figure 15, the average temperature of the matrix is 20°C, when the conventional asphalt mixture is used to repair the potholes of the asphalt pavement. The average temperature of hot mix asphalt mixture is 125°C. There is a significant temperature difference in the interface transition zone. Excessive temperature difference is not conducive to repair. At the same time, it can be seen from Figure 15(b) that the heat loss in the high temperature zone of the asphalt mixture is large after the mixture is rolled. The temperature difference between after rolling and before rolling is 30°C. However, the temperature of the matrix is not significantly increased, which is only 28.1°C. This shows that the heat loss of conventional asphalt mixture is less absorbed by the matrix. Most of the heat is dissipated, and the energy utilization efficiency is low. Therefore, the temperature difference between the matrix and the hot mix asphalt mixture is high.

Figure 16 shows the infrared thermogram of the repair model based on microwave heating emulsified asphalt mixture. Based on the observation in Figure 16, the average

temperature of the matrix and emulsified asphalt mixture is 85°C and 141°C, respectively, when the asphalt pavement potholes are repaired by microwave heating emulsified asphalt mixture. The temperature difference in the transition zone is small (<60°C). At the same time, it can be seen from Figure 16(b) that the heat loss in the high-temperature zone is small after rolling the emulsified asphalt mixture. The temperature difference between after rolling and before rolling is 10°C.

However, the temperature of the matrix has dropped slightly, which indicates that a part of the heat has been lost and has not been fully utilized. In addition, compared with Figures 15 and 16, the heat dissipation part is obviously reduced, and the energy utilization rate is relatively high when microwave heating emulsified asphalt mixture is used to repair asphalt pavement potholes. Thus, microwave heating has a positive effect on reducing the temperature gradient.

Figure 17 shows the mixture repair interface with different repair methods. There are obvious voids and defect areas at
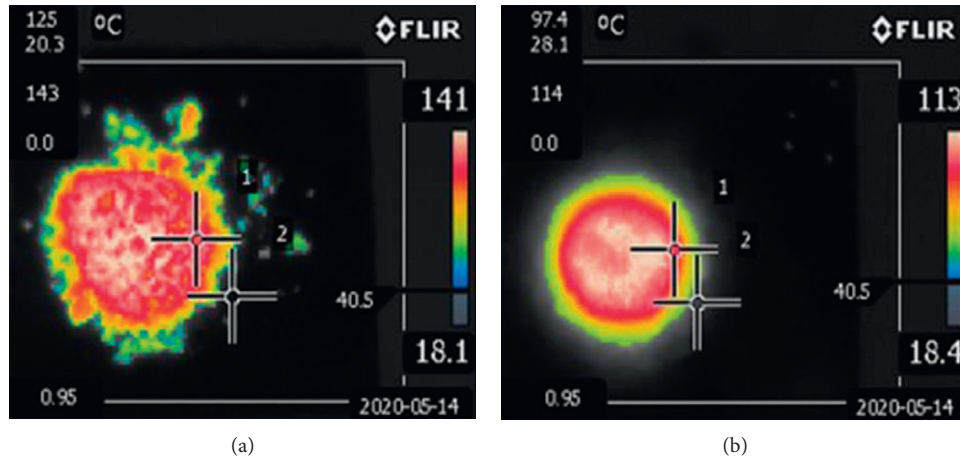
(a)

(b)

FIGURE 15: Infrared thermography of conventional asphalt mixture repair method: (a) temperature distribution before rolling; (b) temperature distribution after rolling.

(a)

(b)
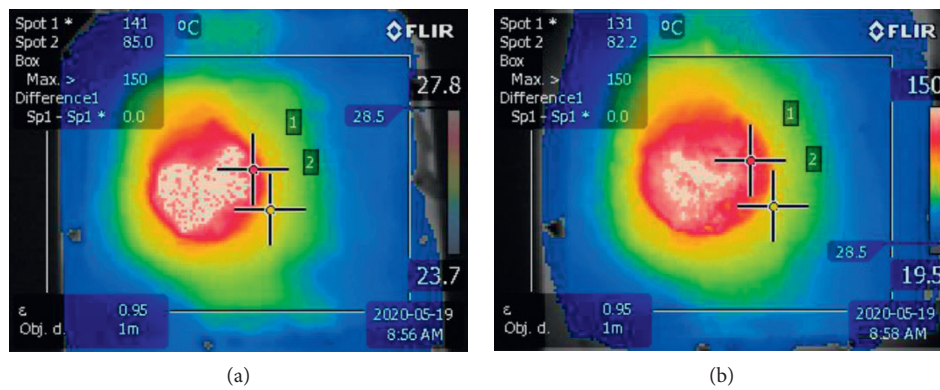
FIGURE 16: Infrared thermography of microwave heating emulsified asphalt mixture repair method: (a) temperature distribution before rolling; (b) temperature distribution after rolling.
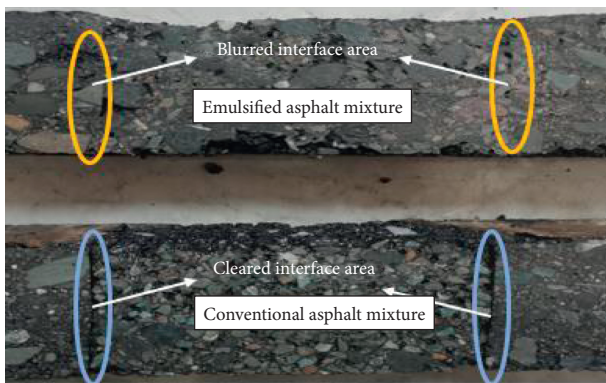
FIGURE 17: Interface repair with different asphalt mixtures.

the repair interface when the conventional asphalt mixture is used to repair the potholes of the asphalt pavement. The interface zone has a great influence on the fatigue life of mixture, and the interface bonding joint greatly reduces the overall service life of asphalt pavement [30]. The interface transition zone is not obvious when the emulsified asphalt mixture with microwave heating is used to repair asphalt

pavement potholes. Therefore, the defect area is reduced, and the combination of repair material and old material is closer, which is beneficial to the service life of asphalt pavement.

4. Conclusions

In this work, the microwave heating efficiency and temperature distribution of emulsified asphalt repair materials with different steel slag sizes and contents were studied by the heating test and simulation test. In addition, the effects of steel slag sizes and contents on microwave heating performance of emulsified asphalt repair materials were analyzed by the X-ray diffraction (XRD) test and environmental scanning electron microscopy (ESEM) test. The following conclusions can be drawn:

(1) Under the microwave heating, the heating stage of emulsified asphalt repair materials can be divided into three stages: initial rapid rising stage (stage I: $\leq 95°C$), medium stable stage (stage II: $95°C–100°C$), and late rapid rising stage (stage III: $\geq 100°C$).

(2) With the increase in steel slag content, the "critical point of phase transition" in the three stages of

temperature rise of emulsified asphalt repair material is gradually advanced and the duration of "initial rapid rising stage" and "medium stable stage" is also gradually shortened.

(3) The core temperature of the emulsified asphalt repair materials with different steel slag sizes under the microwave heating has basically the same change trend, showing a typical three-stage change rule. The temperature distribution of emulsified asphalt repair materials with steel slag is obviously different. The larger the steel slag size, the more uneven the surface and the internal temperatures.

(4) In contrast to the conventional asphalt mixture repair method, the temperature difference in the interface zone is smaller. The temperature of repairing materials can reach above 80°C. The temperature loss is small after rolling. The interface area can form an embedded interface structure.

Data Availability

The data used to support the findings of this study are included within the article.

Conflicts of Interest

The authors declare that they have no conflicts of interest.

Acknowledgments

References

[1] J. Ouyang, L. Hu, W. Yang, and B. Han, "Strength improvement additives for cement bitumen emulsion mixture," *Construction and Building Materials*, vol. 198, pp. 456–464, 2019.

[2] Y. Kim and H. D. Lee, "Performance evaluation of Cold In-Place Recycling mixtures using emulsified asphalt based on dynamic modulus, flow number, flow time, and raveling loss," *KSCE Journal of Civil Engineering*, vol. 16, no. 4, pp. 586–593, 2012.

[3] M. Lambert, J.-M. Piau, V. Gaudefroy et al., "Modeling of cold mix asphalt evolutive behaviour based on nonlinear viscoelastic spectral decomposition," *Construction and Building Materials*, vol. 173, pp. 403–410, 2018.

[4] T. Ma, H. Wang, Y. Zhao, X. Huang, and Y. Pi, "Strength mechanism and influence factors for cold recycled asphalt mixture," *Advances in Materials Science and Engineering*, vol. 2015, Article ID 181853, 10 pages, 2015.

[5] A. Graziani, C. Iafelice, S. Raschia, D. Perraton, and A. Carter, "A procedure for characterizing the curing process of cold recycled bitumen emulsion mixtures," *Construction and Building Materials*, vol. 173, pp. 754–762, 2018.

[6] T. Chen, Y. Luan, T. Ma, J. Zhu, X. Huang, and S. Ma, "Mechanical and microstructural characteristics of different interfaces in cold recycled mixture containing cement and asphalt emulsion," *Journal of Cleaner Production*, vol. 258, Article ID 120674, 2020.

[7] S. Du, "Interaction mechanism of cement and asphalt emulsion in asphalt emulsion mixtures," vol. 47, no. 7, pp. 1149–1159, 2014.

[8] N. F. Moghadas Habibi, M. Hosseini, P. Jahanbakhsh, and J. Hamid, "Investigating the mechanical and fatigue properties of sustainable cement emulsified asphalt mortar," *Journal of Cleaner Production*, vol. 156, pp. 717–728, 2017.

[9] O. Xu, Z. Wang, and R. Wang, "Effects of aggregate gradations and binder contents on engineering properties of cement emulsified asphalt mixtures," *Construction and Building Materials*, vol. 135, pp. 632–640, 2017.

[10] J. Gao, H. Guo, X. Wang et al., "Microwave deicing for asphalt mixture containing steel wool fibers," *Journal of Cleaner Production*, vol. 206, pp. 1110–1122, 2019.

[11] H. Guo, Z. Wang, D. An, and J. Huo, "Collaborative design of cement-based composites incorporated with cooper slag in considerations of engineering properties and microwave-absorbing characters," *Journal of Cleaner Production*, Article ID 124614, 2020, In press.

[12] B. Lou, A. Sha, Y. Li et al., "Effect of metallic-waste aggregates on microwave self-healing performances of asphalt mixtures," *Construction and Building Materials*, vol. 246, Article ID 118510, 2020.

[13] J. Norambuena-Contreras, A. Gonzalez, J. L. Concha, I. Gonzalez-Torre, and E. Schlangen, "Effect of metallic waste addition on the electrical, thermophysical and microwave crack-healing properties of asphalt mixtures," *Construction and Building Materials*, vol. 187, pp. 1039–1050, 2018.

[14] T. M. Phan, D.-W. Park, and T. Ho Minh Le, "Crack healing performance of hot mix asphalt containing steel slag by microwaves heating," *Construction and Building Materials*, vol. 180, pp. 503–511, 2018.

[15] H. Guo, Z. Wang, J. Huo, X. Wang, Z. Liu, and G. Li, "Microwave heating improvement of asphalt mixtures through optimizing layer thickness of magnetite and limestone aggregates," *Journal of Cleaner Production*, vol. 273, Article ID 123090, 2020.

[16] C. S. Fang and P. M. C. Lai, "Microwave heating and separation of water-in-oil emulsions," *Journal of Microwave Power and Electromagnetic Energy*, vol. 30, no. 1, pp. 46–57, 2016.

[17] W. Liu, B. Xiao, G. Yang, Y. Bi, and F. Chen, "Rapid salt-assisted microwave demulsification of oil-rich emulsion obtained by aqueous enzymatic extraction of peanut seeds," *European Journal of Lipid Science and Technology*, vol. 122, no. 2, Article ID 1900120, 2020.

[18] R. Zolfaghari, A. Fakhru'l-Razi, L. C. Abdullah, S. S. E. H. Elnashaie, and A. Pendashteh, "Demulsification techniques of water-in-oil and oil-in-water emulsions in petroleum industry," *Separation and Purification Technology*, vol. 170, pp. 377–407, 2016.

[19] R. Martínez-Palou, R. Cerón-Camacho, B. Chávez et al., "Demulsification of heavy crude oil-in-water emulsions: a comparative study between microwave and thermal heating," *Fuel*, vol. 113, pp. 407–414, 2013.

[20] C.-C. Chan and Y.-C. Chen, "Demulsification of W/O emulsions by microwave radiation," *Separation Science and Technology*, vol. 37, no. 15, pp. 3407–3420, 2002.

[21] N. H. Abdurahman, R. M. Yunus, N. H. Azhari, N. Said, and Z. Hassan, "The potential of microwave heating in separating water-in-oil (w/o) emulsions," *Energy Procedia*, vol. 138, pp. 1023–1028, 2017.

[22] A. Hamid Nour, S. F. Pang, and M. S. Omer, "Demulsification of water-in-crude oil (W/O) emulsion by using microwave radiation," *Journal of Applied Sciences*, vol. 10, no. 22, p. 2395, 2010.

[23] Z. Wang, N. Dai, X. Wang, G. Li, and H. Guo, "Early-stage road property improvements of cold recycled asphalt emulsion mixture with microwave technology," *Journal of Cleaner Production*, vol. 263, Article ID 121451, 2020.

[24] Z. Wang, N. Dai, X. Wang, J. Zhang, and H. Guo, "Laboratory investigation on effects of microwave heating on early strength of cement bitumen emulsion mixture," *Construction and Building Materials*, vol. 236, Article ID 117439, 2020.

[25] J. Wan, S. Wu, Y. Xiao, Z. Chen, and D. Zhang, "Study on the effective composition of steel slag for asphalt mixture induction heating purpose," *Construction and Building Materials*, vol. 178, pp. 542–550, 2018.

[26] L. Mo, S. Yang, B. Huang, L. Xu, S. Feng, and M. Deng, "Preparation, microstructure and property of carbonated artificial steel slag aggregate used in concrete," *Cement and Concrete Composites*, vol. 113, Article ID 103715, 2020.

[27] W. Liu, H. Li, H. Zhu, and P. Xu, "The interfacial adhesion performance and mechanism of a modified asphalt-steel slag aggregate," *Materials*, vol. 13, no. 5, p. 1180, 2020.

[28] J. Gao, A. Sha, Z. Wang, Z. Tong, and Z. Liu, "Utilization of steel slag as aggregate in asphalt mixtures for microwave deicing," *Journal of Cleaner Production*, vol. 152, pp. 429–442, 2017.

[29] B. H. Dinh, D.-W. Park, and T. M. Phan, "Healing performance of granite and steel slag asphalt mixtures modified with steel wool fibers," *KSCE Journal of Civil Engineering*, vol. 22, no. 6, pp. 2064–2072, 2018.

[30] J. Liu, B. Yu, and Q. Hong, "Molecular dynamics simulation of distribution and adhesion of asphalt components on steel slag," *Construction and Building Materials*, vol. 255, Article ID 119332, 2020.

Research Article

Shear-Dependent Yield Stress of Iron Ore Fine Tailings in Two-Step Flocculation Process

Ying Yang [ID],[1] **Hongjiang Wang** [ID],[1] **Bern Klein,**[2] **and Aixiang Wu**[1]

[1]*School of Civil and Resource Engineering, University of Science and Technology Beijing, Beijing 100083, China*
[2]*Norman B. Keevil Institute of Mining Engineering, University of British Columbia, Vancouver V6T 1Z4, Canada*

Correspondence should be addressed to Hongjiang Wang; wanghj1988@126.com

Both shear and flocculation have a significant influence on the rheological behavior of tailings, especially the yield stress. In the two-step flocculation process, the above two kinds of actions exist at the same time, and they influence each other. In order to explore the change rule of the yield stress and its internal causes, a two-step flocculation process of the iron ore fine tailings with different shear conditions in the four different phases was designed. In the primary flocculation phase, tailing particles combined with the primary flocculant and formed a primary floc network structure. In the primary broken phase, shear destroyed the primary floc network structure and decreased the average floc size, so the shear-dependent yield stress, the floc strength factor, and the fractal dimension decreased. In the secondary flocculation phase, broken floc combined with the secondary flocculant and produced a more compact floc network structure which had a better shear resistance. Therefore, in the secondary broken phase, with the increase of shear, the decrease of yield stress, the floc strength factor, and fractal dimension were less obvious than that in the primary broken phase. In both two broken phases, the yield stress of the secondary flocculating slurry was always higher than that of the primary flocculating slurry, but with the increase of shear, the difference became smaller. The floc strength and fractal dimension also showed the same rule. The internal reasons for the stronger shear resistance of the secondary flocculating slurry were the increase of the number of binding sites, the electric neutralization between the two flocculants, and the steric hindrance effect of the flocculants.

1. Introduction

For mineral processing and tailings disposal, dual polymer systems have been a research focus due to its significant advantages over the use of single polymers [1–3]. A dual polymer system can rapidly improve the dehydration capacity and rheological properties of the slurry. In mineral processing, rheological parameters, especially yield stress, directly affect energy consumption [4], separation efficiency [5], and sedimentation stability [6]. For tailings disposal, the physical stability of tailings, backfill, and paste are also dependent on rheological properties [7]. Therefore, it is necessary to fully understand the variation of rheology and the internal mechanism in a dual polymer system.

The interaction between particles and aqueous phases is the reason for rheological properties of slurry, which is dependent on physical characteristics and chemical characteristics of the constituents, such as mineralogical content [8], particle volume fraction φ [9], particle size distribution [10], and chemical additives [11]. It is also affected by the external effect, such as shear action [12]. Therefore, rheological properties are a complex function of physical and chemical properties and of processes that occur at the scale of the suspended particles. In order to further understand rheological properties and its mechanisms, many pieces of research focused on the variation of rheological behavior under different conditions, such as shear, particle size distribution, floc structure, and maximum particle packing fraction.

In terms of minerals slurry, shear has an essential impact both on dual polymer systems and its rheological properties. Shear rate and shear time are considered to be the most

important factors. For dual polymer systems, some researchers have used the product of shear rate and shear time as the index of shear action because this product is closely related to the rate of orthokinetic flocculation, which has a direct impact on the flocculation effect [13, 14]. For rheological properties, shear action affects the rheological properties by changing the particle size distribution and the interaction of particles and the aqueous phase. For relatively small shear rates, the fine particles are controlled by Brownian motion effects or colloidal forces, while coarse particles are generally faced with frictional or collisional contacts or hydrodynamic forces [15]. However, for relatively high shear rates, the colloidal fine fraction and coarse fraction are assumed to act independently and the coarse fraction mainly contributes to increased viscosity through hydrodynamic dissipation [16, 17].

Apart from shear action, the rheological properties are closely related to floc structure and floc strength [18–21]. Nasser and James [22] found that the magnitude of the yield stress and viscous modulus is strongly dependent upon the floc structure. When shear exceeds the particle interactions, the floc network structure is disrupted, and the pulp yield stress decreases, which shows clear links between shear, floc structure, and dewaterability [23]. Furthermore, Farrokhpay [24] proposed that the rheological behavior of mineral slurries indicates the level of particle interaction or aggregation and disaggregation is a balance between floc formation and floc breakage [25–29]. In other words, the shear-dependent yield stress of slurry indicates the shear resistance of the floc network structure in the process of flocculation and shear disruption. And in the field of water treatment, the floc strength factor demonstrates the shear resistance of flocs in the process of floc formation and floc breakage. Therefore, the floc strength factor can be considered as a unit of shear resistance of the floc network, and it can also be used as an important indicator of the variation of the shear-dependent yield stress. However, there is not enough information on the relationship between yield stress, floc structure, and floc strength factor in the two-step flocculation process.

In the paper, a two-step flocculation process of the iron ore fine tailings under different shear conditions was designed so as to explore the change rule of the yield stress with shear. This two-step flocculation process included the primary flocculation phase, the primary broken phase, the secondary flocculation phase, and the secondary broken phase. In order to explain the variation of the shear-dependent yield stress in this process and its internal causes, the floc size, floc strength factors, and the fractal dimension will be calculated and analyzed.

2. Materials and Methods

2.1. Tailings.
The tailings used in this study were iron ore tailings originally supplied by ArcelorMittal USA, a steel and mining company operating in the USA. The tailings preparation process is comprised of a number of steps. Firstly, taking a 45 kg wet sample of +4.0 mm feed size from the tailings and passing it through a vibrating screen. The

portion of the tailings that did not pass through the screen was crushed using gyratory and cone crushers and subsequently mixed with the portion of the sample that had filtered through. Secondly, the combined sample was then mixed with water to bring its concentration to 60% prior to grounding it in a rod mill for 66 mins. Through preexperiments, the relation curve between the particle size distribution of tailings and grinding time was obtained and the grinding time was determined to be 66 mins with the 80th percentile of the cumulative particle size distribution of $70\,\mu m$ as the target. Then, the sample was subsequently dried in a drying box until the tailings were completely dry so as to obtain the working sample that would be used in this study. The working sample particle size distribution was measured using a Malvern Mastersizer 2000 Laser Diffraction Particle Size Analyser. The 50th and 80th percentile of the cumulative particle size distribution was $60.2\,\mu m$ and $70.2\,\mu m$, respectively (Figure 1). The specific gravity of the tailings was $2.326\,\text{g/cm}^3$, and the result of the X-ray diffraction is shown in Table 1.

2.2. Flocculants.
Through single flocculation preexperiments and combined flocculation preexperiments, the optimal flocculant combination was selected (923VHM and 4800SSH). These two kinds of commercial flocculants were used in this study, supplied by SNF Canada. The anionic polyacrylamide, 923VHM, was used as the primary flocculant and the cationic polyacrylamide, 4800SSH, was used as the second flocculant. Both of them have high molecular weight and good water solubility. To prevent mineral impurities from affecting test results, deionized water was used in all water-based tests.

2.3. Suspension Preparation.
A slurry of 15% solids (w/v %) was prepared in a 1 L beaker using 150 g tailings and 850 ml deionized water. The slurry was homogenized by agitating at a rotational speed of approx. 600 rpm for 30 seconds, and at 280 rpm for 10 mins. Then 2 ml of the anionic PAM flocculant solution with the concentration of 0.15% was added to the slurry (corresponding to the polymer optimum dosage of 20 g/t, determined from previous experimentation) and agitation was ceased immediately to avoid breaking the flocs. Following agitation, the beaker containing the slurry was allowed to rest for 5 mins prior to removing the supernatant from the solution by pouring (it out of the beaker). The average particle size, d_0, of the underflow was measured by using the Malvern Mastersizer 2000 Laser Diffraction Particle Size Analyser.

2.4. Rheology Tests in Two-step Flocculation Process.
The time-dependent rheological behavior of the slurry was characterized using a shear rheometer (Thermo Haake VT 550, Germany). The rheometer was also used as a power device to provide floc shear disruption during the two-step flocculation process. The cup and bob fixture was a concentric cylinder geometry of which the radius of the fixed outer cylinder and the rotatable inner cylinder was 21.00 mm
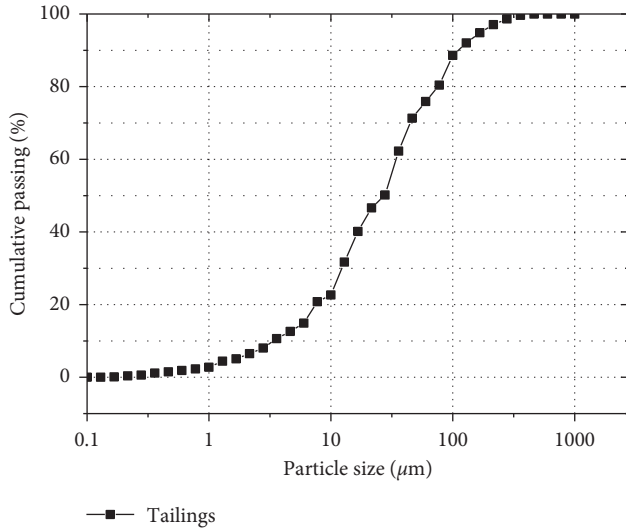
FIGURE 1: Granularity composition of tailings.

TABLE 1: Parameter design of floc shear disruption.

Primary broken phase		Secondary broken phase	
Shear rate	Shear time	Shear rate	Shear time
200	30	200	30
400	30	400	30
600	30	600	30
800	30	800	30
200	60	200	60
400	60	400	60
600	60	600	60
800	60	800	60
200	120	200	120
400	120	400	120
600	120	600	120
800	120	800	120
200	240	200	240
400	240	400	240
600	240	600	240
800	240	800	240

and 20.04 mm, respectively, so there was a gap between the cup and bob fixture to minimize non-Newtonian shear rate effects, particle bridging across the shear surfaces, and the magnitude of wall slip errors [30–32]. For each test, 34 ml samples were required and the temperature was fixed at 23°C by the Poly science 9100 constant temperature circulator from the USA.

The rheological tests were conducted including four phases, primary flocculation phase, primary broken phase, secondary flocculation phase, and secondary broken phase, as shown in Figure 2.

Firstly, in the primary flocculation phase, the tailings slurry and the primary flocculant solution were mixed as shown previously, to prepare the primary flocculated suspension. The yield stress of the primary flocculated

suspension was measured with the increase of shear rate from 0 to $300 \, s^{-1}$ and the decrease from $300 \, s^{-1}$ to 0 within 120 seconds. In addition, the primary particle size distribution, d_1, was obtained using the Malvern Mastersizer 2000 Laser Diffraction Particle Size Analyser.

Secondly, in the primary broken phase, the tests were implemented at a constant shear rate for a desired period (Table 1), during which the rheometer was only used as a floc shear disruption device. Subsequently, the yield stress and the particle size distribution, d_2, of the primary broken suspension was measured with the same method in the primary flocculation phase.

Then, in the secondary flocculation phase, 0.4 ml flocculant solution of the cationic PAM with the concentration of 0.15% (corresponding to the polymer optimum dosage of 20 g/t, determined from previous experimentation) was added to the suspension in the cup and the slurry was stirred until it was homogeneous. Then, the measurement of the yield stress and the particle size distribution, d_3, of the secondary flocculated slurry was carried out.

Finally, in the secondary broken phase, adjusting the shear rate and shear time to the same values with those in the primary broken phase (Table 1), prior to measuring the yield stress and the particle size, d_4, of the secondary broken suspension.

2.5. Floc Structure Measurement.

At the end of each phase of the experiments, samples were taken from the main suspensions. The microstructure of flocs was observed by SEM. In order to make the images obtained clearly reflect the changes of the floc microstructure, with the help of ImageJ2X software, the images were binarized by gray histogram method.

2.6. Data Treatment Methods

2.6.1. Floc Strength Factor in Two-Step Flocculation.

Floc strength factor demonstrates the shear resistance of flocs in the process of floc formation and floc breakage, while shear-dependent yield stress of slurry indicates the shear resistance of the floc network in the process of flocculation and shear disruption. Therefore, floc strength factor can be considered as a unit of shear resistance of the floc network and it can also be used as an important indicator of the variation of the shear-dependent yield stress.

In the paper, the floc strength factor was introduced from the water treatment field to explore the relationship between floc strength factor and shear-dependent yield stress of the slurry in the two-step flocculation process. The formulas were listed as follows [33]:

Strength factor:

$$F_1 = \frac{d_2}{d_1}. \tag{1}$$

Here d_1 is the average flocs size before breakage, μm, d_2 is the average flocs size after breakage, μm.
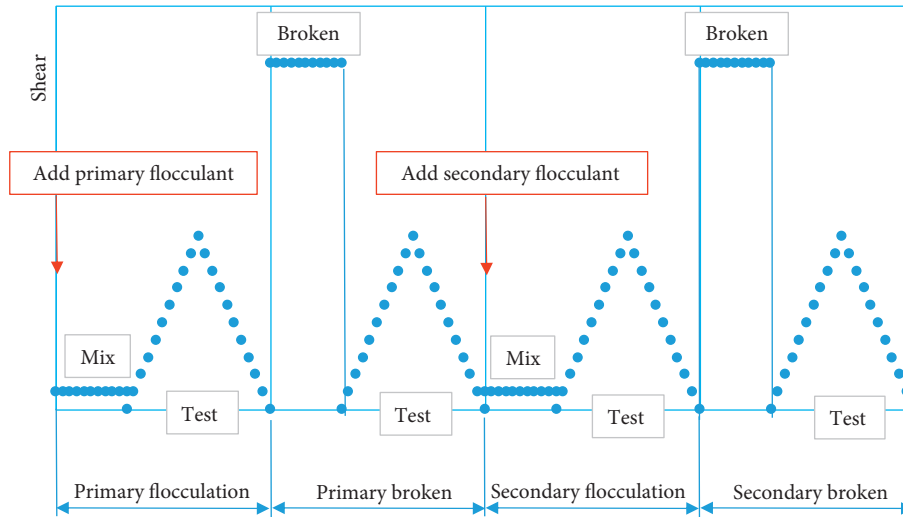
FIGURE 2: A scheme of rheological tests.

2.6.2. Floc Fractal Dimension in Two-Step Flocculation. Floc fractal dimension is an important parameter of floc structure, floc strength, and flocculation effect. It can also be used as an important indicator to explain the variation of the shear-dependent yield stress in the two-step flocculation.

With the help of FractalFox image fractal processing software, the box counting dimension method was used to calculate the fractal dimension of floc structure in the two-step flocculation experiments. The basic principle was as follows. The small box with side length r was used to cover the fractal curve, and the number of small boxes covering the fractal curve was $N(r)$. Then, the box side length r was continuously reduced. When r infinitely approached zero, the fractal dimension D was obtained.

$$D = -\lim_{r \longrightarrow 0} \frac{\log N(r)}{\log r}. \tag{2}$$

3. Results

3.1. Yield Stress in the Primary and Secondary Broken Phases. The Bingham model was used to fit the measurement results of the rheometer to obtain the yield stress of the slurry in the four different phases. They were the first phase (primary flocculation phase), the second phase (primary broken phase), the third phase (secondary flocculation phase), and the fourth phase (secondary broken phase), and the calculated coefficient of determination R^2 was >0.95, which shows that the Bingham model can accurately reflect the change of the rheological properties in different phases.

The variation of yield stress in the primary flocculation and primary broken phases with a shear rate under different shearing time is shown in Figure 3. In the primary broken phase, the yield stress gradually decreased with the increase of shear rate and shear time and the minimum value was about 80% of the yield stress without shear disruption. The increase of shear rate led to a more significant decrease in yield stress than that of shear time. The failure of the floc network structure was a possible reason for this

phenomenon. The increasing shear action aggravated the disruption of the floc network structure, resulting in the continuous reduction of the yield stress in the broken phase. In addition, the increasing shear rate could overcome the stronger internal effect of floc structure and change the failure mode of floc structure, while the increase of shear time could enlarge the damage degree of floc structure.

As shown in Figures 4(a)–4(d), in the primary and secondary broken phases, the yield stress obviously decreased with the increase of shear rate and shear time. However, the yield stress in the secondary broken phase decreased more slowly than that in the primary broken phase. Taking Figure 4(d) as an example, when the shear time was 240 s, with the increase of shear rate from 200 s^{-1} to 400 s^{-1}, the yield stress in the primary broken phase decreased by 3.5 Pa, while that in the secondary broken phase decreased by 1.5 Pa.

In addition, the yield stress in the secondary broken phase was always larger than that in the primary broken phase and the gap became smaller with the increase of shear rate and shear time. In other words, secondary flocculation increased the yield stress and shear resistance of the slurry. This could be explained by the increase of the floc strength and the density of floc structure in the secondary flocculation process, which will be further analyzed in Sections 3.3 and 3.4. Furthermore, with the increase of shear action, the smaller gap of the yield stress between the primary broken phase and the secondary broken phase indicated that the stronger shear resistance of the secondary flocculation slurry was more obvious under low shear action and it was weakened under high shear action.

For dual polymer systems, the product of shear rate and shear time is regarded as the index of shear action because it is closely related to the rate of orthokinetic flocculation, which has a direct impact on the flocculation effect [13, 14]. Therefore, in this paper, the product of shear rate and shear time was used as a shear index to explore the variation of yield stress in the primary broken and secondary broken phases.
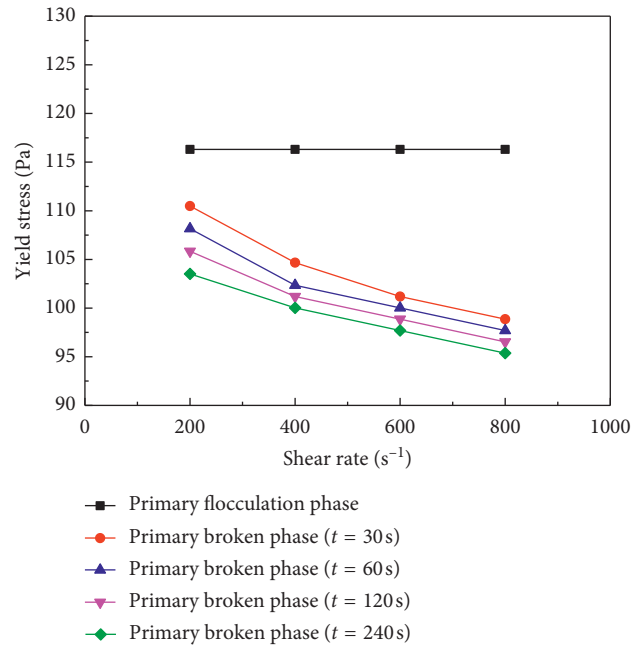
FIGURE 3: The variation of yield stress with shear rate during different shear times in the primary flocculation and primary broken phases.
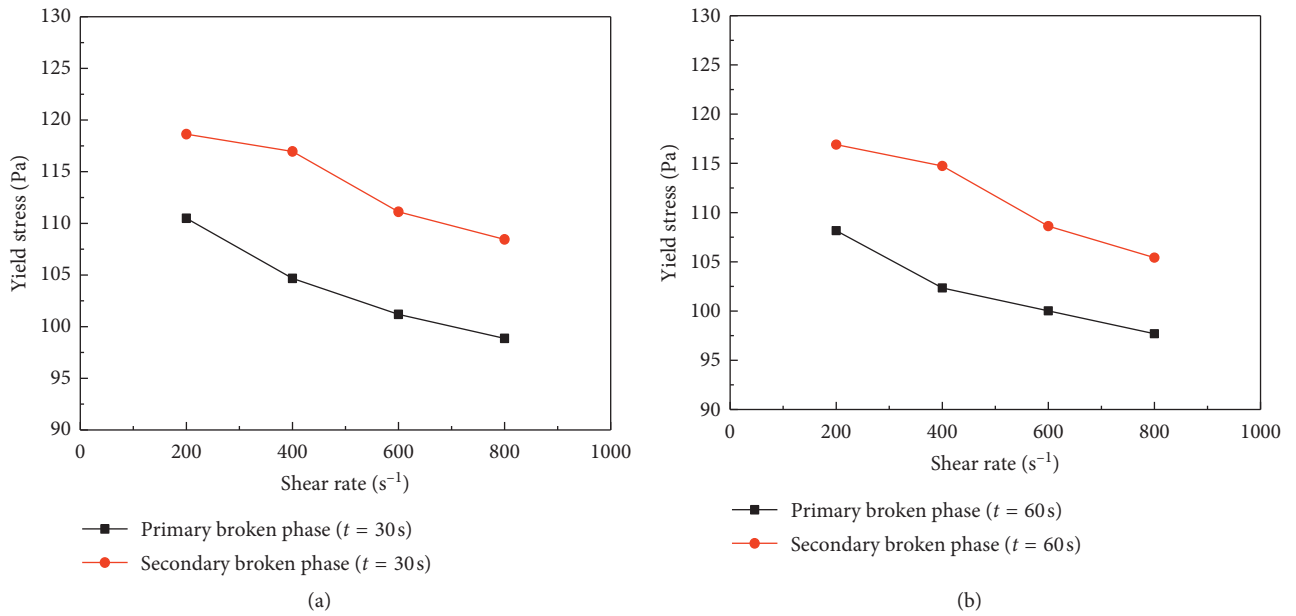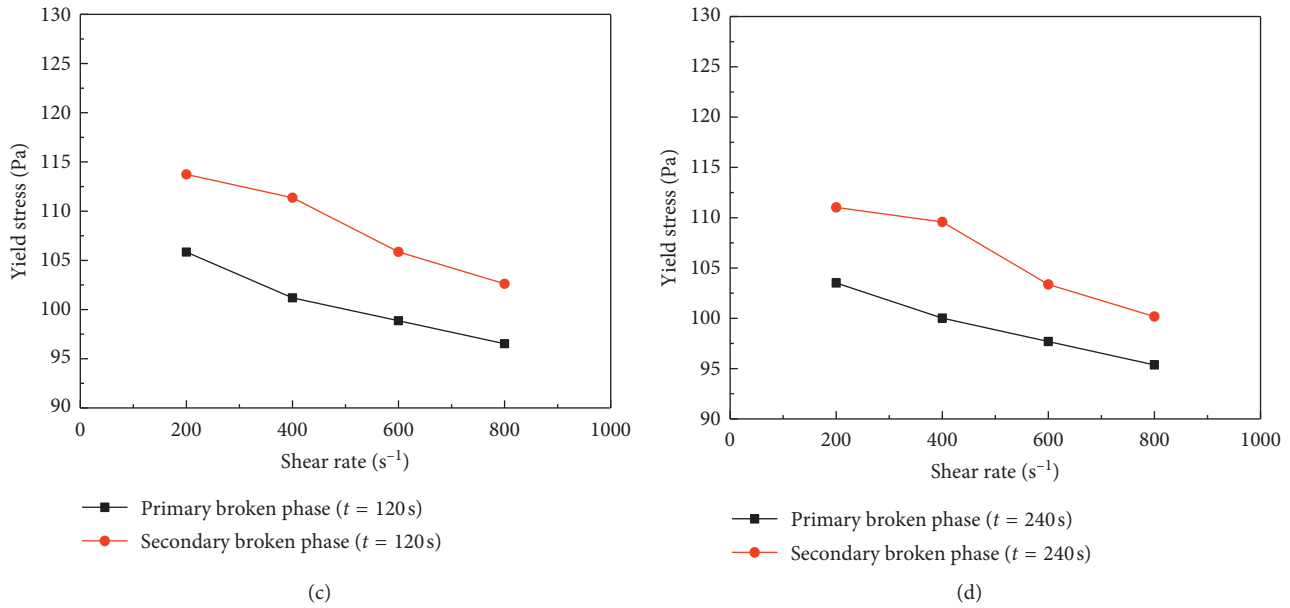

(a)

(b)

FIGURE 4: Continued.

(c)

(d)

FIGURE 4: The variation of yield stress with shear rate during different shear times in the primary broken and secondary broken phases.
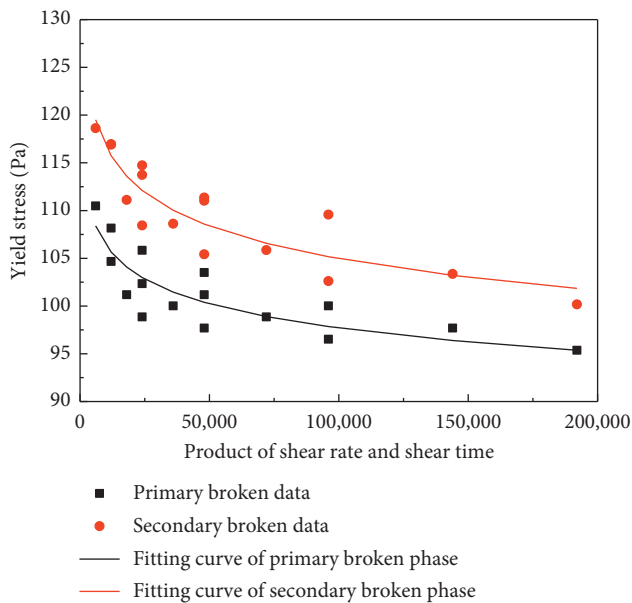

FIGURE 5: The variation of yield stress with the product of shear rate and shear time in the primary and secondary flocculation phases.

As shown in Figure 5, the yield stress in the primary and secondary broken phases showed a similar change trend, but the value in the secondary broken phase was always higher than that in the primary broken phase. When the product of shear rate and shear time was between 0 and 100,000, the yield stress in the primary broken and secondary broken phases decreased significantly. When the value was higher than 100,000, the yield stress in the two broken phases tended to be stable. The probable reason for this phenomenon was the shear was easier to overcome the weak connections of floc structure, and it had a more obvious effect on the yield stress of slurry. The higher yield stress in the secondary broken phase was probably because secondary flocculation formed a more compact floc network structure and higher floc strength.

3.2. Floc Size in the Two-Step Flocculation.

The variation of average floc size in the primary flocculation and primary broken phases with a shear rate under different shearing time is shown in Figure 6. In the primary broken phase, the average floc size gradually decreased with the increase of shear rate and shear time, and the minimum value was about 80% of the average floc size without shear disruption in the primary flocculation phase. The increase of shear rate led to a more significant decrease in yield stress than that of shear time.

The possible reason for this phenomenon was that the complete floc network structure formed in the primary flocculation phase was too loose. There were some weak connections in the primary floc network structure, so the shear resistance of the whole structure was low. In the primary broken phase, even in the face of low shear, the structural integrity was significantly damaged, which led to the average floc size decreasing rapidly.

As shown in Figure 7, compared with the primary floc, the average size of secondary floc increased significantly. In the secondary broken phase, with the increase of shear rate and shear time, the average size of secondary floc also decreased gradually, but the size of secondary broken floc after shear was still larger than that of primarily broken floc. The minimum size of the secondary broken floc was 83% of the secondary floc without shear failure. In other words, secondary flocs had higher floc strength. This may be because in the primary broken phase, the shear action destroyed the weak connection parts in the loose primary floc network structure, and the internal effect of the remaining flocs was strong. At the same time, the secondary flocculation
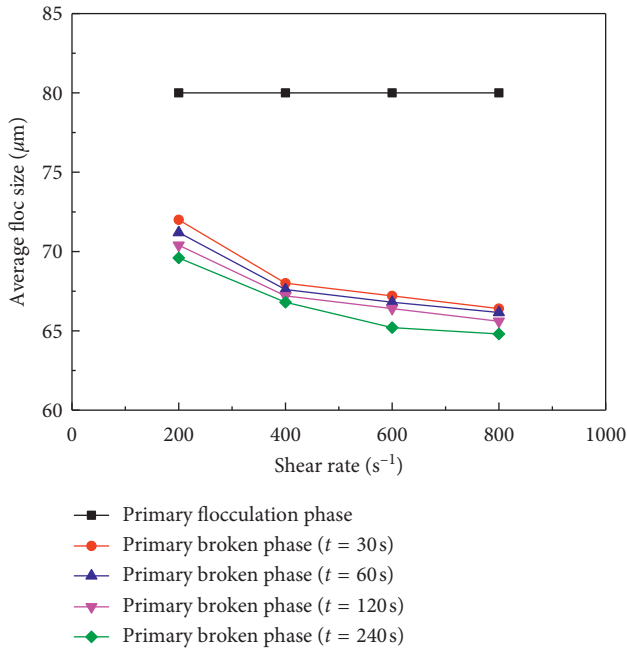
FIGURE 6: The variation of average floc size with shear rate during different shear times in the primary flocculation and primary broken phases.
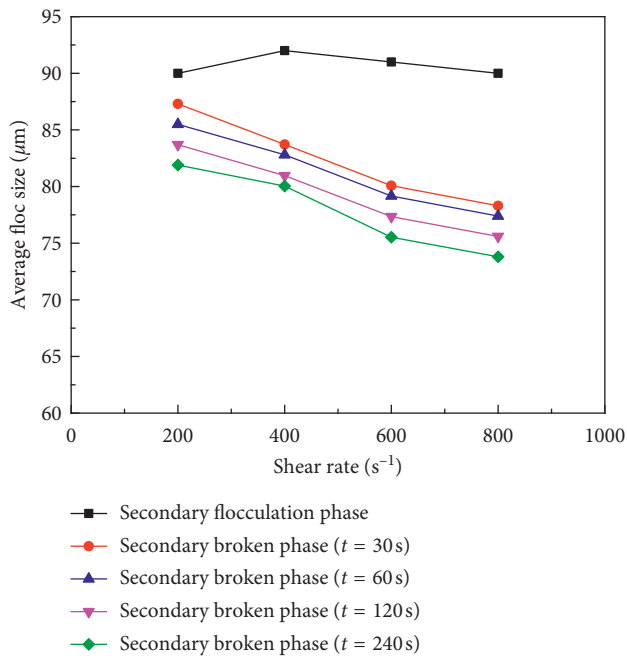

FIGURE 7: The variation of average floc size with shear rate during different shear times in the secondary flocculation and secondary broken phases.

FIGURE 8: The variation of average floc size with a product of shear rate and shear time in the primary and secondary broken phases.

produced a dense structure, which not only increased the shear resistance of the whole structure but also increased the strength of the internal flocs.

As shown in Figure 8, with the increase of the product of shear rate and shear time, the change trend of the average floc size in the primary and secondary broken phases was consistent with that of yield stress. The average floc size in the two broken phases decreased rapidly and then tended to be stable when the product of shear rate and shear time was higher than 100,000. The average floc size decreased rapidly probably because lower shear overcame weaker connections of floc structure, which caused a large-scale structural fracture of floc structure, the integrity of the floc network structure was significantly damaged. In addition, the average floc size in the secondary broken phase was also always higher than that in the primary broken phase. It means that the strength of the secondary floc was higher than that of the primary floc.

3.3. Floc Strength Factor in the Primary and Secondary Broken Phases. According to equation (1), the floc strength factors were calculated using the results of the average floc sizes. As shown in Figure 9, the secondary floc strength factors were always larger than the primary ones and the gap became smaller with the increase of shear rate and shear time. In other words, both the shear disruption prior to the secondary flocculation and secondary flocculation process enhanced the floc shear resistance and formed the stronger secondary flocs.

With the increase of shear disruption, the primary and secondary floc strength factors decreased gradually and finally tended to be stable. The variation of the floc strength factors could be explained by analyzing the change of the average floc sizes. As shown in Figures 6 and 7, the difference between the average sizes of the flocs and the broken flocs in the primary flocculation process was always larger than that in the secondary flocculation process. It led to the secondary floc strength factors being larger than the primary ones. In addition, secondary flocculation enhanced the floc sizes and further widened the difference

(a)

(b)

(c)

(d)
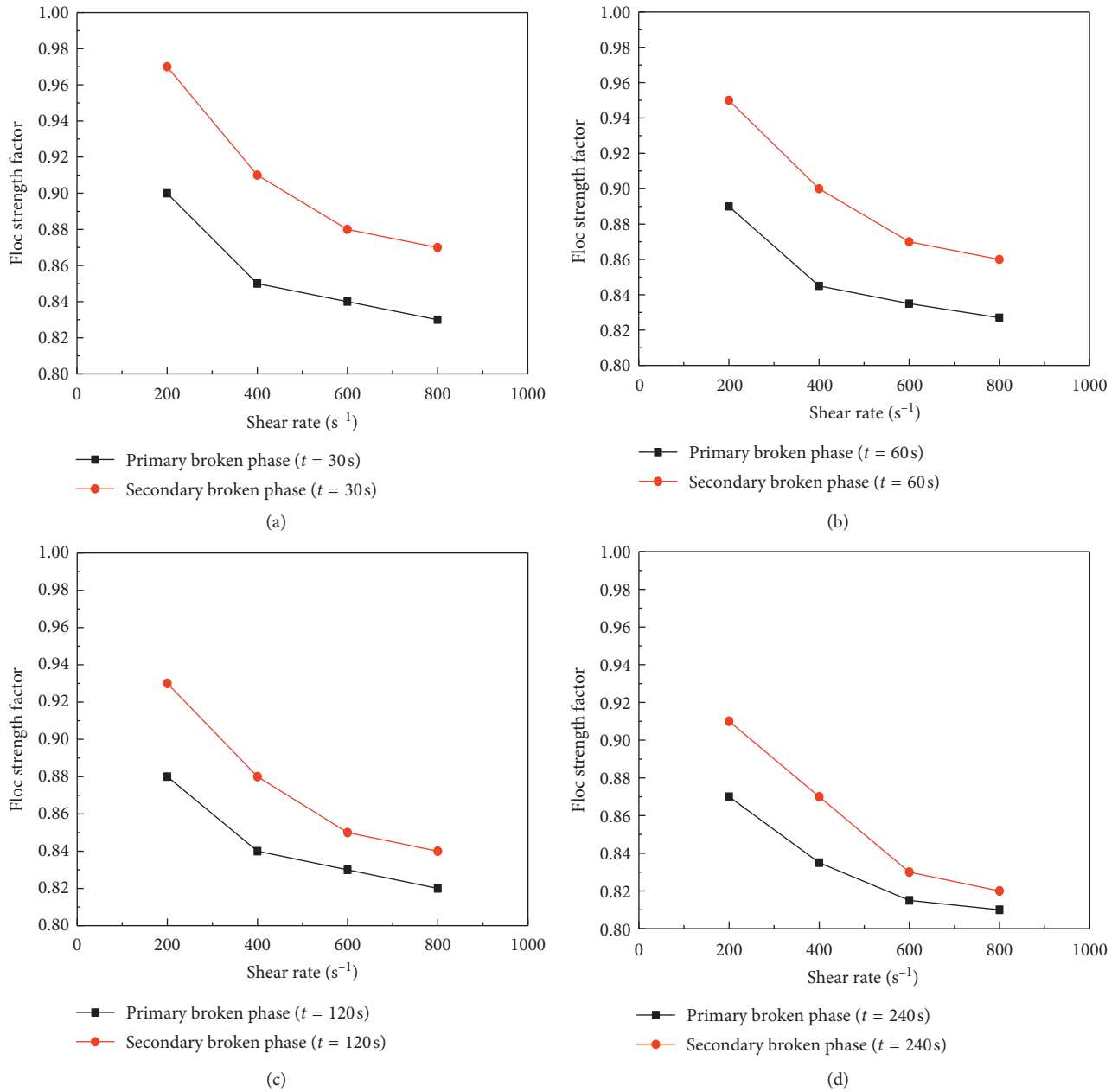
FIGURE 9: The variation of floc strength factor with shear rate during different shear times in the primary broken and secondary broken phases.

between the floc strength factors in the primary and secondary broken phases.

The variation of floc strength factors with the product of shear rate and shear time in the primary and secondary broken phases is shown in Figure 10. When the product of shear rate and shear time was between 0 and 100,000, the floc strength factors decreased significantly. When the value was higher than 100,000, the floc strength factors tended to be stable. The secondary floc strength factors were always larger than the primary ones, and the gap became smaller under higher shear. The variation of floc strength could also be explained by the failure mode of floc structure under shear and the strengthening floc in the secondary flocculation.

It is worth mentioning that the variation of yield stress, floc size, and floc strength with the product of shear rate and shear time in the primary and secondary broken phases being basically consistent (Figures 5, 8, and 10). Their inflection points from a rapid decrease to stabilization were all around the product value of 100,000. This could be explained by the increase of the strength of floc or floc structure in the secondary flocculation process. The strengthening effect was more obvious under lower shear stress. According to the definition of floc strength, the change of floc size was the reason for the change of floc strength. In other words, secondary flocculation increased the yield stress of the slurry by enhancing the floc strength. However, the change of the floc strength was not the only reason for the variation of the
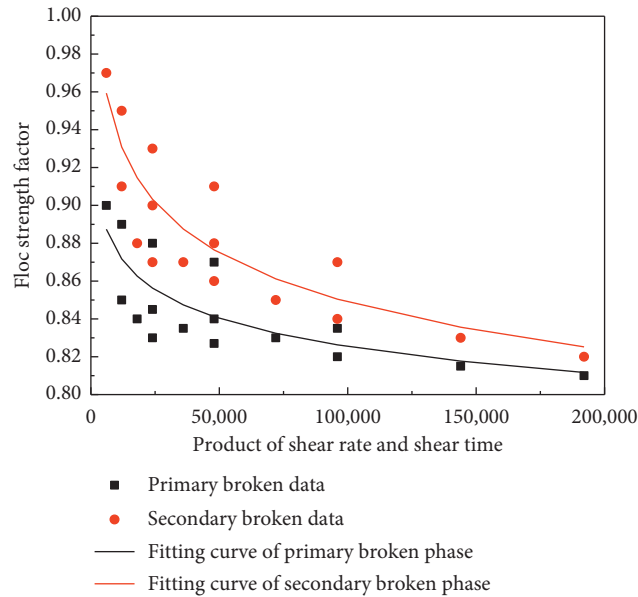
FIGURE 10: The variation of floc strength factor with the product of shear rate and shear time in the primary and secondary broken phases.

yield stress. It was also related to the floc network structure, which will be explained in Section 3.4.

3.4. Floc Fractal Dimension in the Two-Step Flocculation.

With the help of the box counting dimension method, the fractal dimensions of floc structure were calculated in the two-step flocculation experiments. The curve of the shearing time of 120 s was taken as an example. The variation of fractal dimensions of floc structure with the increase of shear rate and shear time was shown in Figure 11. Compared with the primary and secondary flocculation, the secondary floc fractal dimensions were all higher than the primary ones. Similarly, the fractal dimensions of the secondary broken floc were also higher than those of the primary broken ones. In addition, under higher shear, the difference between the fractal dimension in the primary (broken) and secondary (broken) phases became smaller.

As shown in Figure 12, the floc structure in different phases was significantly different. In the primary flocculation phase, there were many "cavities" in the floc network structure, which led to loose floc structure, low shear strength, and small fractal dimension. In the primary broken phase, shear destroyed the floc structure and produced a large number of small flocs. In the secondary flocculation phase, the floc size increased significantly, the structure became more compact, which led to high floc strength and large fractal dimensions. In the secondary broken phase, under the same shear action, the scale of broken floc structure was smaller and the sizes of broken flocs were larger compared with the primary broken phase.

As shown in Figure 13, in the primary and secondary broken phases, the change trend of fractal dimension of floc structure was consistent with that of yield stress with the increase of shear rate and shear time. In other words, the variation of the floc fractal dimension could also be another reason for the change of yield stress in the two-step
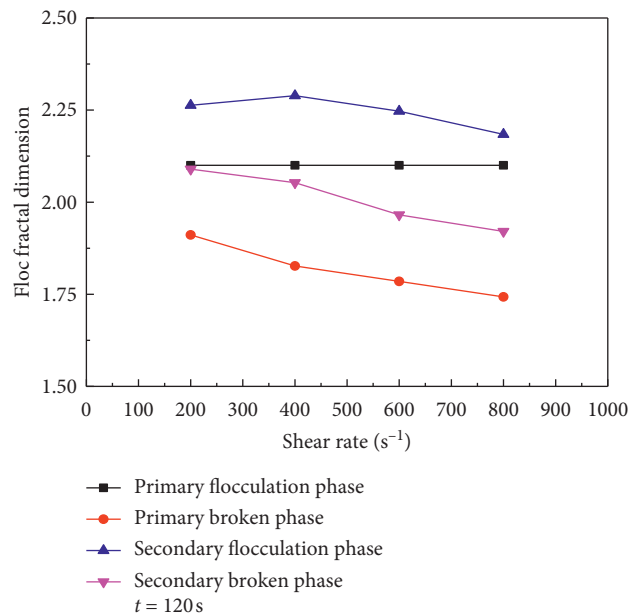
FIGURE 11: The variation of floc fractal dimension with a shear rate in the four phases (shear time = 120 s).

flocculation. Therefore, secondary flocculation increased the yield stress of the slurry by enhancing the floc strength and the density of the floc structure.

3.5. Discussion.

Through analyzing the variation of yield stress, floc size, floc strength, and fractal structure with the increase of shear rate and shear time, comparing the change rule of the above parameters in the primary broken phase with that in the secondary broken phase, it is found that the secondary flocculation slurry had better shear resistance. This may be because of the following (Figure 14):

(a)

(b)

(c)

(d)
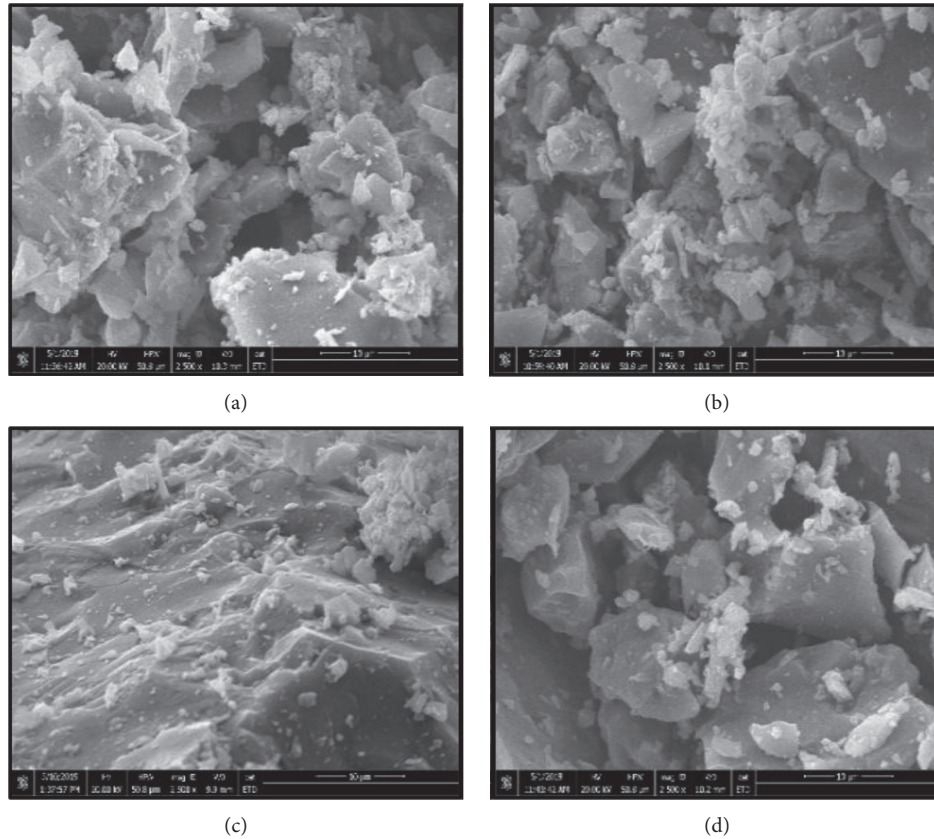
FIGURE 12: The SEM of floc structure in the four phases (shear rate = 400 s^{-1} and shear time = 120 s): (a) primary flocculation, (b) primary broken, (c) secondary flocculation, and (d) secondary broken.
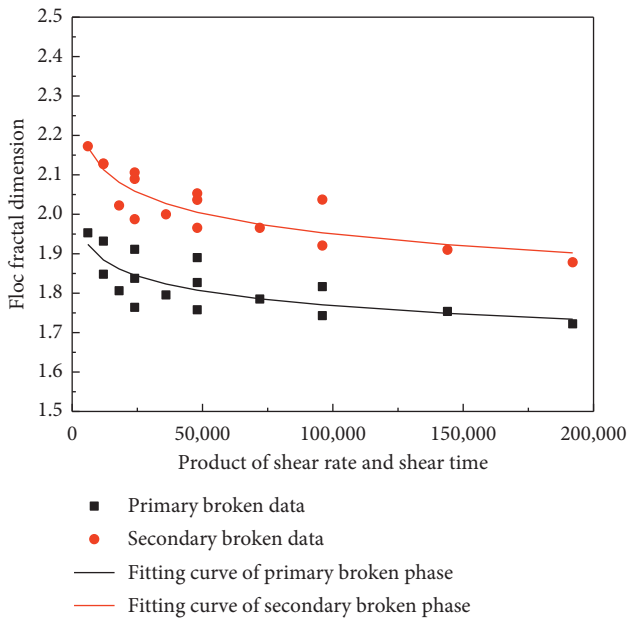
FIGURE 13: The variation of floc fractal dimension with the product of shear rate and shear time in the primary and secondary broken phases.
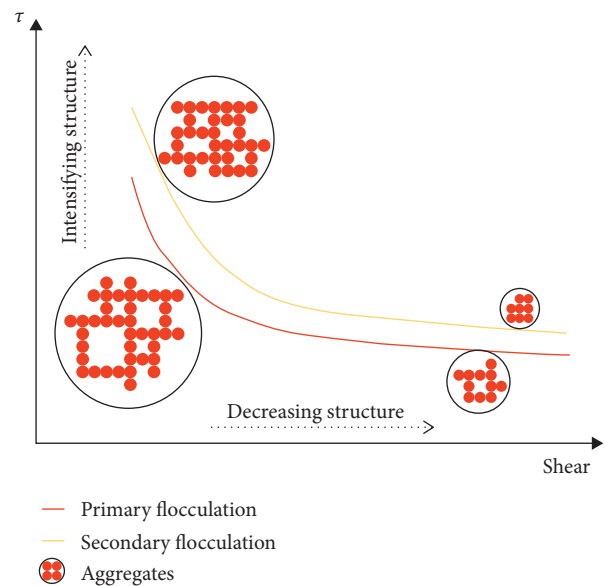
FIGURE 14: A schematic for the variation of shear-dependent yield stress with shear in the two-step flocculation process.

(1) The addition of primary flocculant increased the number of binding sites on the surface of tailings particles; in the primary broken phase, shear disruption promoted the release of binding sites on the surface of broken flocs. Therefore, in the secondary flocculation phase, the binding probability of

broken flocs and secondary flocculant molecules increased.

(2) In this experiment, the anionic flocculant was used as the primary flocculant, and the cationic flocculant was used as the secondary flocculant. Through the electric neutralization of the two kinds of flocculants, secondary flocculation formed a more compact floc network structure. Compared with the primary floc network structure formed by bridging, the internal force of the secondary floc network structure was stronger which showed stronger shear resistance.

(3) The steric hindrance effect of the two polymeric flocculants gave them higher bridging probability, which was conducive to the formation of dense floc network structure.

4. Conclusions

The variation of the yield stress, the floc strength factor, and the fractal dimension of the iron ore fine tailings under different shear conditions in a two-step flocculation process was studied in the research through analyzing the change of floc network structure and floc size distribution. The main conclusions are as follows:

(1) Shear destroyed the floc network structure, so the yield stress gradually decreased with the increase of shear rate and shear time in the primary and secondary broken phases. Secondary flocculation increased the yield stress, so the yield stress in the secondary flocculation phase was always higher than that in the primary flocculation phase. However, with the increase of shear action, the gap of the yield stress reduced in the two broken phases.

(2) Shear disruption decreased the average floc size and further decreased the floc strength factors in the broken phases. Secondary flocculation increased the floc strength. However, under high shear disruption, the difference between floc size and floc strength in the primary and secondary broken phases was small.

(3) The floc structure and its fractal dimensions in the four different phases were compared. It is found that the loose primary floc structure was the internal cause of its low shear resistance. Therefore, the sizes of the primarily broken flocs were smaller. Secondary flocculation enhanced the density of the floc structure, and the fractal dimensions were also larger.

(4) Through analyzing the variation of the yield stress, the floc strength factor, and the floc fractal dimension under different shearing conditions, it is found that their variation trend was essentially similar to the increase of shear. In other words, it can be considered that secondary flocculation increased the yield stress of the slurry by enhancing the density of the floc network structure and the floc strength.

(5) The internal reasons for the stronger shear resistance of the secondary flocculating slurry were the increase of the number of binding sites, the electric neutralization between the two flocculants, and the steric hindrance effect of the flocculants.

Data Availability

All data, models, and code generated or used during the study appear in the submitted article. No additional data are available.

Conflicts of Interest

The authors declare that they have no conflicts of interest.

Acknowledgments

References

[1] J. Gregory and S. Barany, "Adsorption and flocculation by polymers and polymer mixtures," *Advances in Colloid and Interface Science*, vol. 169, no. 1, pp. 1–12, 2011.

[2] C. H. Lee and J. C. Liu, "Sludge dewaterability and floc structure in dual polymer conditioning," *Advances in Environmental Research*, vol. 5, no. 2, pp. 129–136, 2001.

[3] G. Petzold, M. Mende, K. Lunkwitz, S. Schwarz, and H.-M. Buchhammer, "Higher efficiency in the flocculation of clay suspensions by using combinations of oppositely charged polyelectrolytes," *Colloids and Surfaces A: Physicochemical and Engineering Aspects*, vol. 218, no. 1–3, pp. 47–57, 2003.

[4] M. G. Vieira and A. E. C. Peres, "Effect of rheology and dispersion degree on the regrinding of an iron ore concentrate," *Journal of Materials Research and Technology*, vol. 2, no. 4, pp. 332–339, 2013.

[5] Z. Ding, Z. Yin, L. Liu, and Q. Chen, "Effect of grinding parameters on the rheology of pyrite-heptane slurry in a laboratory stirred media mill," *Minerals Engineering*, vol. 20, no. 7, pp. 701–709, 2007.

[6] J. Yue, *Rheological effects on ultra-fine grinding in stirred mills*, Ph.D. Dissertation, University of British Columbia, Vancouver, Canada, 2003.

[7] Q. D. Nguyen and D. V. Boger, "Application of rheology to solving tailings disposal problems," *International Journal of Mineral Processing*, vol. 54, no. 3-4, pp. 217–233, 1998.

[8] E. Burdukova, M. Becker, B. Ndlovu, B. Mokgethi, and D. A. Deglon, "Relationship between slurry rheology and its mineralogical content," in Proceedings of the 24th InternationalMinerals Processing Congress, China Scientific Book Service Co. Ltd., Beijing, China, pp. 2169–2178, September 2008.

[9] D. J. Jeffrey and A. Acrivos, "The rheological properties of suspensions of rigid particles," *AIChE Journal*, vol. 22, no. 3, pp. 417–432, 1976.

[10] F. Boylu, H. Dinçer, and G. Ateşok, "Effect of coal particle size distribution, volume fraction and rank on the rheology of coal-water slurries," *Fuel Processing Technology*, vol. 85, no. 4, pp. 241–250, 2004.

[11] E. S. Mosa, M. Abdel-Hady, T. A. T. Saleh, and A. M. El-Molla, "Effect of chemical additives on flow characteristics of

coal slurries," *Physicochemical Problems of Mineral Processing*, vol. 42, pp. 107–118, 2008.

[12] R. F. Probstein, M. Z. Sengun, and T. C. Tseng, "Bimodal model of concentrated suspension viscosity for distributed particle sizes," *Journal of Rheology*, vol. 38, no. 4, pp. 811–829, 1994.

[13] T. R. Camp, D. A. Root, and B. V. Bhoota, "Effects of temperature on rate of floc formation," *American Water Works Association*, vol. 32, no. 11, pp. 1913–1927, 1940.

[14] T. R. Camp, "Velocity gradients and internal work in fluid motion," *Boston Society of Civil Engineers*, vol. 30, pp. 219–230, 1943.

[15] C. Ancey and H. Jorrot, "Yield stress for particle suspensions within a clay dispersion," *Journal of Rheology*, vol. 45, no. 2, pp. 297–319, 2001.

[16] M. Z. Sengun and R. F. Probstein, "Bimodal model of slurry viscosity with application to coal-slurries. Part 1. Theory and experiment," *Rheologica Acta*, vol. 28, no. 5, pp. 382–393, 1989.

[17] M. Z. Sengun and R. F. Probstein, "Bimodal model of slurry viscosity with application to coal-slurries. Part 2. High shear limit behavior," *Rheologica Acta*, vol. 28, no. 5, pp. 394–401, 1989.

[18] P. Ofori, A. V. Nguyen, B. Firth, C. McNally, and O. Ozdemir, "Shear-induced floc structure changes for enhanced dewatering of coal preparation plant tailings," *Chemical Engineering Journal*, vol. 172, no. 2-3, pp. 914–923, 2011.

[19] M. J. McGuire, J. Addai-Mensah, and K. E. Bremmell, "Improved dewaterability of iron oxide dispersions: the role of polymeric flocculant type, pH and shear," *Asia-Pacific Journal of Chemical Engineering*, vol. 3, no. 1, pp. 18–23, 2008.

[20] B. Gladman, R. G. De Kretser, M. Rudman, and P. J. Scales, "Effect of shear on particulate suspension dewatering," *Chemical Engineering Research and Design*, vol. 83, no. 7, pp. 933–936, 2005.

[21] K. Scales, A. Puisto, J. Paltakari, M. Alava, and T. Maloney, "The influence of shear on the dewatering of high consistency nanofibrillated cellulose furnishes," *Cellulose*, vol. 20, no. 4, pp. 1853–1864, 2013.

[22] M. S. Nasser and A. E. James, "Effect of polyacrylamide polymers on floc size and rheological behaviour of kaolinite suspensions," *Colloids and Surfaces A: Physicochemical and Engineering Aspects*, vol. 301, no. 1–3, pp. 311–322, 2007.

[23] A. J. McFarlane, K. E. Bremmell, and J. Addai-Mensah, "Optimising the dewatering behaviour of clay tailings through interfacial chemistry, orthokinetic flocculation and controlled shear," *Powder Technology*, vol. 160, no. 1, pp. 27–34, 2005.

[24] S. Farrokhpay, "The importance of rheology in mineral flotation: a review," *Minerals Engineering*, vol. 36–38, pp. 272–278, 2012.

[25] D. S. Parker, W. J. Kaufman, and D. Jenkins, "Floc breakup in turbulent flocculation processes," *Journal of the Sanitary Engineering Division*, vol. 98, pp. 79–99, 1972.

[26] R. J. François, "Strength of aluminium hydroxide flocs," *Water Research*, vol. 21, no. 9, pp. 1023–1030, 1987.

[27] P. T. Spicer and S. E. Pratsinis, "Shear-induced flocculation: the evolution of floc structure and the shape of the size distribution at steady state," *Water Research*, vol. 30, no. 5, pp. 1049–1056, 1996.

[28] J. J. Ducoste and M. M. Clark, "The influence of tank size and impeller geometry on turbulent flocculation: I. Experimental," *Environmental Engineering Science*, vol. 15, no. 3, pp. 215–224, 1998.

[29] C. Biggs and P. A. Lant, "Activated sludge flocculation: on-line determination of floc size and the effect of shear," *Water Research*, vol. 34, no. 9, pp. 2542–2550, 2000.

[30] R. J. Farris, "Prediction of the viscosity of multimodal suspensions from unimodal viscosity data," *Transactions of the Society of Rheology*, vol. 12, no. 2, pp. 281–301, 1968.

[31] J. A. Mangels and R. M. Williams, "Injection molding ceramics to high green densities," *American Ceramic Society Bulletin*, vol. 62, pp. 601–606, 1983.

[32] R. E. Johnson and W. H. Morrison, "Ceramic powder dispersion in nonaqueous systems," *Advances in Ceramics*, vol. 21, p. 323, 1987.

[33] M. A. Yukselen and J. Gregory, "The reversibility of floc breakage," *International Journal of Mineral Processing*, vol. 73, no. 2–4, pp. 251–259, 2004.

Research Article

Effect of the Initial Air Content in Fresh Slurry on the Compressive Strength of Hardened Cemented Paste Backfill

Youzhi Zhang [ID],[1] **Deqing Gan** [ID],[1] **Zhenlin Xue,**[1] **Xun Chen,**[2] **and Sheng Hu**[2]

[1]*College of Mining Engineering, North China University of Science and Technology, Tangshan 063210, China*
[2]*School of Civil and Resource Engineering, University of Science and Technology Beijing, Beijing 100083, China*

Correspondence should be addressed to Deqing Gan; 17330544396@163.com

Filling mining method can dispose of the tailings into filling slurry, which can be transported to the stope through pipelines to manage the ground pressure and protect the environment. To improve the flowability of filling slurry, additives are used more and more widely. However, some additives can increase the air content in the slurry. The air in the slurry will become pores in the hardened cemented paste backfill (CPB). Therefore, it is necessary to explore the influence of initial air content in fresh slurry on the compressive strength of CPB. In this paper, sodium dodecyl sulfate (SDS) was used to regulate the air content in the fresh slurry. After measuring the initial air content, the slurry was made into test blocks. Then, the uniaxial compressive strength (UCS) of CPB at 28 d age was tested, and the distribution of CPB microscopic pores was observed by scanning electron microscope (SEM). The results show that as the initial air content in fresh slurry increases, the UCS of CPB first increases and then decreases. Before the initial air content in fresh slurry is 6.03%, the CPB pores distribution is relatively uniform. However, after exceeding this value, "discontinuous contact" structures, pore groups, and macropores occur in CPB. Through the CPB microscopic force analysis, the mathematical model describing the effect of initial air content on UCS of CPB should be a combination of logarithmic function and quadratic polynomial. This work can provide a supplement to the theory of CPB strength.

1. Introduction

Filling mining method can discharge all or most of the tailings into the underground stope, which can not only effectively manage the ground pressure of stope, but also relieve the environmental and economic pressure of tailings surface depositing [1–7]. Under this background, the mechanical properties (i.e., compressive strength, tensile strength, and flexural strength) of cemented paste backfill (CPB) have attracted wide attention. The compressive strength is the most concerned property among all of them [8–10]. Generally, filling slurry is composed of aggregates, binders, water, and other additives [11]. After stirring by a mixer, the slurry will contain a certain amount of air, so that there will be some pores in the hardened CPB [12, 13]. The slurry is transported into the stope through a pipeline, so the slurry flowability has an important influence on the filling mining efficiency. Low-concentration slurry has good

flowability, but the strength of hardened CPB is poor (caused by cement segregation). High-concentration slurry can effectively improve the CPB strength, but the flowability is poor. In order to improve the flowability of high-concentration slurry, pumping agents are widely used in slurry pipeline transportation. The pumping agent is generally mainly composed of water-reducing agent and air-entraining agent (AEA). Air-entraining agent will increase the air content (the percentage in air volume/total slurry volume) in the slurry, thereby increasing the pores in the CPB, which will have a certain impact on the CPB strength [14, 15].

Traditional studies on initial air content in fresh slurry tend to focus on its influence on material durability, frost resistance, and thermal conductivity of concrete or CPB [16–18]. However, in recent years, scholars have also carried out a large number of studies to investigate the relationship between initial air content and compressive strength of

concrete or CPB. In the first place, according to chemical composition, AEA can be divided into type rosin, alkyl, saponins, etc. The air entrainment effect of different AEA is different, and the AEA dosage for different properties of materials (i.e., surface chemical properties of materials, grain size distribution, and the concentration of slurry) is also different [19]. Secondly, literatures [20, 21] showed that the pores in CPB introduced by surfactants or hydrolyzed protein solutions are usually in the micron range, and the size, spacing, and connectivity of the pores are also important. Besides, Özcan and Emin Koç [22] used image processing technology to find that the compressive strength of aerated concrete is inversely proportional to the air content of the fresh slurry and the pores area of the hardened concrete cutting surface. On the contrary, Hilal et al. [23] believed that although some additives increased the porosity of the concrete cutting surface, they achieved higher strength due to the reduced connectivity.

It can be seen that past researches have analyzed the relationship between porosity and compressive strength from a qualitative perspective. However, they did not propose a mathematical model that can use the initial air content in fresh slurry to quantitatively analyze the CPB strength. In engineering, it is easier to test the initial air content in a fresh slurry, but it is relatively difficult to test the porosity of CPB. Therefore, this paper will carry out the experimental research on the effect of initial air content in fresh slurry on the UCS of CPB. Combined with the CPB microscopic force analysis under compression, a quantitative mathematical model will be proposed. This work will make a useful supplement to the theory of CPB strength.

2. Materials and Methods

2.1. Materials and Equipment. The full tailings are taken from an iron ore tailings reservoir in Hebei Province, China. The particle size distribution curve of full tailings is shown in Figure 1. The important tailings particle size parameters are as follows: d (av) = 37.58 μm, d (50) = 20.33 μm, and d (90) = 98.96 μm. The specific gravity is 2.62 g·cm^{-3}. The chemical composition analysis of full tailings is shown in Table 1. The cementing agent is Portland slag cement P.S.A 32.5 (granulated blast furnace slag accounts for 50%). The water is ordinary city tap water, and AEA is sodium dodecyl sulfate (SDS), which belongs to the type alkyl. The CA-3 digital concrete air content tester, with a range of 10%, was used to test the air content in fresh slurry. For the observation of the CPB microstructure, the JEOL JSM-6390A scanning electron microscope (SEM) was selected. The uniaxial compressive strength (UCS) test adopted the WHY-600 single-axis press with a range of 600 kN and an accuracy of 0.01 kN.

The components of the air content tester are shown in Figure 2. The first step when measuring is to put the fresh slurry into the device and then use a vibrating table to vibrate to a dense state (the frequency of the vibrating table is 50 Hz). If the slurry is lower than the bottom chamber sealing plane, it should be added to be a little higher than the sealing plane. After vibrating again, use a scraper to scrape off the excess slurry on the sealing surface. Next, close the lid,
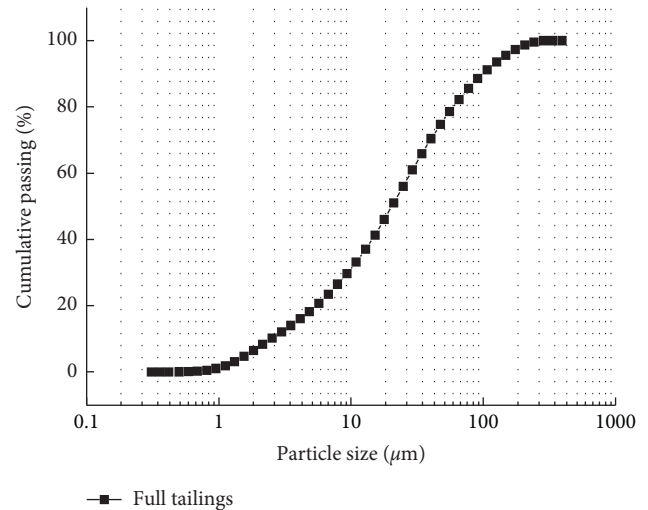
Figure 1: Particle size distribution curve of full tailings.

Table 1: Chemical composition of full tailings

Component	TFe	SiO$_2$	CaO	MgO	Al$_2$O$_3$	Others
Content (%)	4.29	74.24	2.96	3.34	7.65	7.52
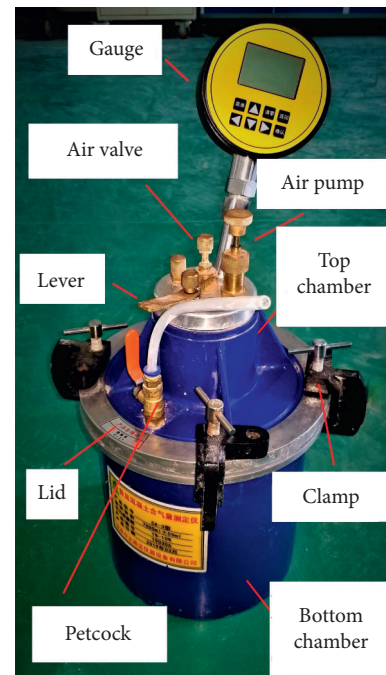
Figure 2: Air content tester for fresh slurry.

and clamp it with clamps. A bubble level is used to check the device. Then, open the petcock to fill water, and close the petcock and air valve when the water flows out from the air valve. Next, pressurize to 0.1 MPa with an air pump. Then, press the lever 2–3 times, and use a wooden hammer to hit the bottom chamber to distribute the pressure evenly to all parts of the sample. The gauge can directly display the air content value. When the data in the gauge is stable, record

the air content value. A calibration experiment is needed before the formal experiment. Each experiment is executed twice. If the measured values differ by more than 0.5%, a new experiment is needed. Until the measured values differ by less than 0.5%, take the average value as the final value.

2.2. Test Scheme.

In this study, the mass concentration of slurry used in the experiment was set to 70%, and the cement/sand ratio was 1 : 4. The volume of the air content tester bottom chamber is 7 L. Considering the richness factor, the volume of slurry in each experiment was set at 7.5 L. SDS was added to water to complete dissolution, and then the tailings, cement, and water were mixed in a mixing tank for 1 minute to ensure the slurry uniform preparation. The SDS dosage was set to 0.01%–0.06% of the quality of cement, and we set up a control experiment without SDS. Since it usually takes 3–5 minutes for the slurry from the mixing tank to filling drilling in a mine, the air content test is carried out 3 minutes after the slurry is prepared. Then, the slurry was made into $70.7 \times 70.7 \times 70.7$ mm standard test blocks (Chinese industry-standard, JGJ/T70-2009). Each slurry was made into 6 blocks. After 24 hours, the mold was removed, and the blocks were put into the curing box. The curing temperature was 20°C, and the humidity was 90%. When the curing age was 28 d, the UCS test of blocks was carried out. Among the six test blocks, the repeatable test value was considered as the 28 d strength value. Finally, the SEM experiments were carried out to observe the failure surface. The mixing ratio of fresh filling slurry is shown in Table 2.

3. Results and Discussion

3.1. Effect of SDS Dosage on Initial Air Content in Fresh Slurry.

According to the test results of each experiment, the relationship between the SDS dosage and the initial air content in fresh slurry is drawn, as shown in Figure 3. It can be seen that the air content in fresh slurry increases steadily with the SDS dosage increase. From experiment A to experiment B, when the SDS dosage is from 0 to 0.01%, the initial air content increases from 2.40% to 4.62%, with the biggest increase amplitude of 2.22%. From experiment B (air content 4.62%) to experiment C (air content 6.03%), the increased amplitude is 1.41%, and it is lower than 2.22%. The lowest increase amplitude is 0.58%, which occurs from experiment F (air content 8.31%) to experiment G (air content 8.89%). It is showing an obvious quadratic polynomial relationship between SDS dosage and initial air content. The fitting equation is $y = -1516.7x^2 + 193.1x + 2.6$ (x represents the SDS dosage, and y represents the initial air content in fresh slurry). The adjustment coefficient of determination (R^2) is 0.9904, indicating that the fitting equation has high credibility and can truly reflect the effect of SDS dosage on initial air content in a fresh slurry.

3.2. Effect of Initial Air Content on UCS.

Figure 4 shows the stress-displacement curve of each experiment in the UCS test when curing for 28 days. The stress-displacement curve of some experiments in Figure 4 shows fluctuation around the peak value. This phenomenon is caused by local pores collapse when the test block is compressed under the conditions of constant loading rate and random pore distribution. In the vicinity of the pores, where the stress concentration is high, the particle bonding contact loss leads to local softening and collapse. This collapse will cause local densification, thereby hardening the material and increasing the stress. After the sample is compacted, the stress concentration will appear in another new position until it forms new cracks. This process may be repeated two or more times, then several macroscopic cracks are formed, resulting in complete destruction. Besides, it can be seen from Figure 4 that this kind of fluctuations mostly appeared in experiments A, B, C, and D, and experiments E, F, and G, and by contrast, they are not obvious. The 28 d age UCS of all test blocks are shown in Figure 5. It can be seen that the strength of the control block is 1.15 MPa. The strength of experiment C (6.03% initial air content) is the highest, which is 1.54 MPa. The strength of experiments F and G (8.31% and 8.89% initial air content, respectively) is lower than that of the control experiment, while that of the other experiments was between 1.15 MPa and 1.54 MPa. It can be seen that the initial air content in fresh slurry has a nonmonotonic effect on the 28 d age UCS. This result can provide some explanation for the different views of Özcan and Emin Koç [22] and Hilal et al. [23]. For these experimental materials, the initial air content of 6.03% is the most beneficial to the 28 d age strength.

3.3. Effect of Initial Air Content on Pores Distribution.

The SEM photos are shown in Figure 6, which shows that as the initial air content in fresh slurry gradually increases, the pores structure in hardened 28 d age CPB is more and more developed. The pores distribution of Figure 6(b) is more uniform than that of the control experiment, shown in Figure 6(a), and the structure formed by calcium silicate hydrate (C-S-H) and tailings particles in Figure 6(b) is also denser than that shown in Figures 6(a), 6(c), and 6(d), respectively, representing that the initial air content in fresh slurry is 6.03% and 6.94%, which are close to three times of the control experiment. After being hardened, the dense area is denser than that of experiments A and B, but there are already a few large pores formed. Figure 6(e) shows that, due to the increase of the initial air content in fresh slurry, the inside of CPB has shown "discontinuous contact" structures. Figures 6(f) and 6(g) represent that pore groups and macropores begin to appear, and the diameter of the macropore approaches 200 μm. This is because SDS is an anionic surfactant. When the SDS dosage is small, the entrained bubbles will have a "wall effect" on the surface, which has a certain hindering ability to reduce the bubbles combination. When the dosage increases to a certain value, with too many bubbles entrained, the bubbles begin to break through this "wall effect." They have a tendency to gather together, forming a certain amount of pore groups, and even fusion phenomenon occurs, resulting in large bubbles, which appear as macropores after solidification. The

TABLE 2: Mixing ratio of the fresh filling slurry.

Serial number	SDS dosage (%)	SDS dosage (g)	Cement/sand ratio	Volume of slurry (L)	Mass concentration (%)	Cement (kg)	Full tailings (kg)	Water (kg)
A	0	0	0.25	7.5	70	1.93	7.70	4.13
B	0.01	0.193	0.25	7.5	70	1.93	7.70	4.13
C	0.02	0.385	0.25	7.5	70	1.93	7.70	4.13
D	0.03	0.578	0.25	7.5	70	1.93	7.70	4.13
E	0.04	0.770	0.25	7.5	70	1.93	7.70	4.13
F	0.05	0.963	0.25	7.5	70	1.93	7.70	4.13
G	0.06	1.155	0.25	7.5	70	1.93	7.70	4.13
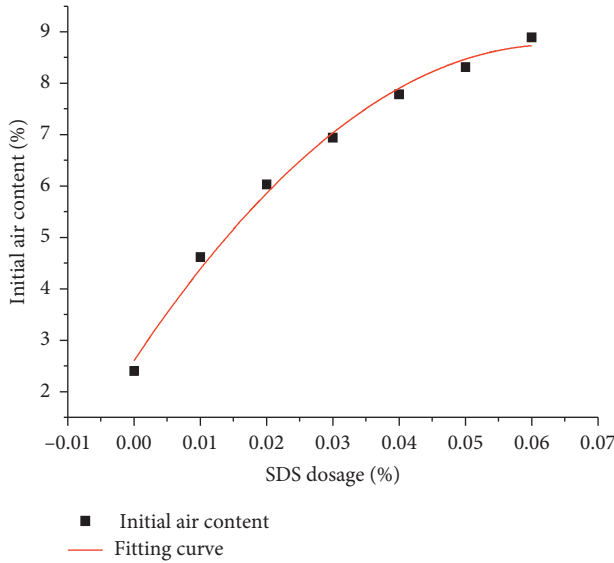
FIGURE 3: Relationship between the SDS dosage and the initial air content in fresh slurry.

FIGURE 5: The relationship between initial UCS with different initial air content air content and 28 d age UCS.

lost its load-bearing capacity. This is also the reason why the experimental curves of E, F, and G in Figure 4 have not obvious fluctuations.

3.4. Mathematical Model and Its Evaluation. Given the characteristic that the 28 d age strength first increases and then decreases with the increase of initial air content, a quadratic polynomial fitting was performed for the 28 d age strength. The fitting result is $y = -0.052x^2 + 0.535x + 0.134$ (x represents initial air content, and y represents 28 d age UCS), and the R^2 is 0.889, which is lower than 0.9, with low credibility. Therefore, it is necessary to carry out in-depth mechanical analysis to find a mathematical model that can accurately describe the effect of initial air content in fresh slurry on 28 d age UCS.

The hardened CPB can be simplified into the following model [24]: (i) Tiny particles gather together to form a unit-body; (ii) The gaps between the particles are filled with C-S-H; (iii) Numerous unit-bodies constitute the entire CPB. The macroscopic mechanical properties of CPB are the sum of the unit-bodies mechanical properties. Figure 7 shows the contact relationship between the particles in the unit-body when the CPB is compressed.

Figure 7(a) is a unit-body. A fixed particle i in the unit-body will have a contact relationship with multiple particles. According to Newton's second law, the equation of motion can be described as

FIGURE 4: Stress-displacement curves of 28 d age.

"discontinuous contact" structures, pore groups, and macropores will still soften and collapse when the block is compressed, but before compaction occurs, the block has

Figure 6: Pores distribution of 28 d age CPB formed by slurry with different initial air content. (a) 2.40%. (b) 4.62%. (c) 6.03%. (d) 6.94%. (e) 7.78%. (f) 8.31%. (g) 8.89%.

FIGURE 7: Schematic diagram of the contact relationship between the particles when the CPB is compressed. (a) The unit-body. (b) Two contacting particles in the unit-body.

$$F_i = m_i u_i, \tag{1}$$

where F_i is the vector force of particle i, m_i is the particle mass, and u_i is the displacement vector of the centroid of particle i, namely, acceleration. Considering the relationship between multiple particles, equation (1) can become
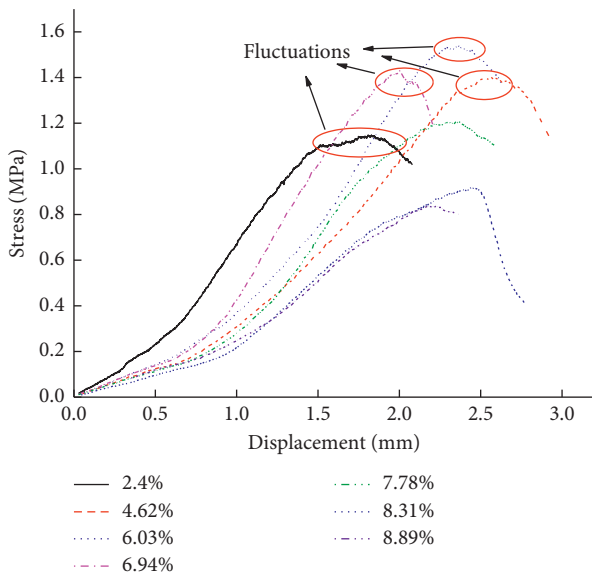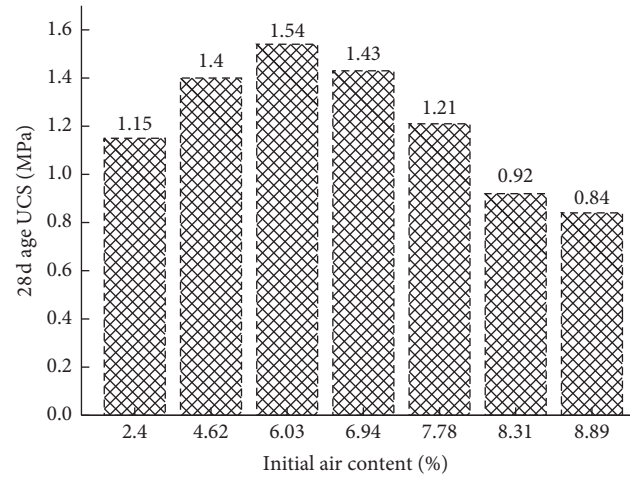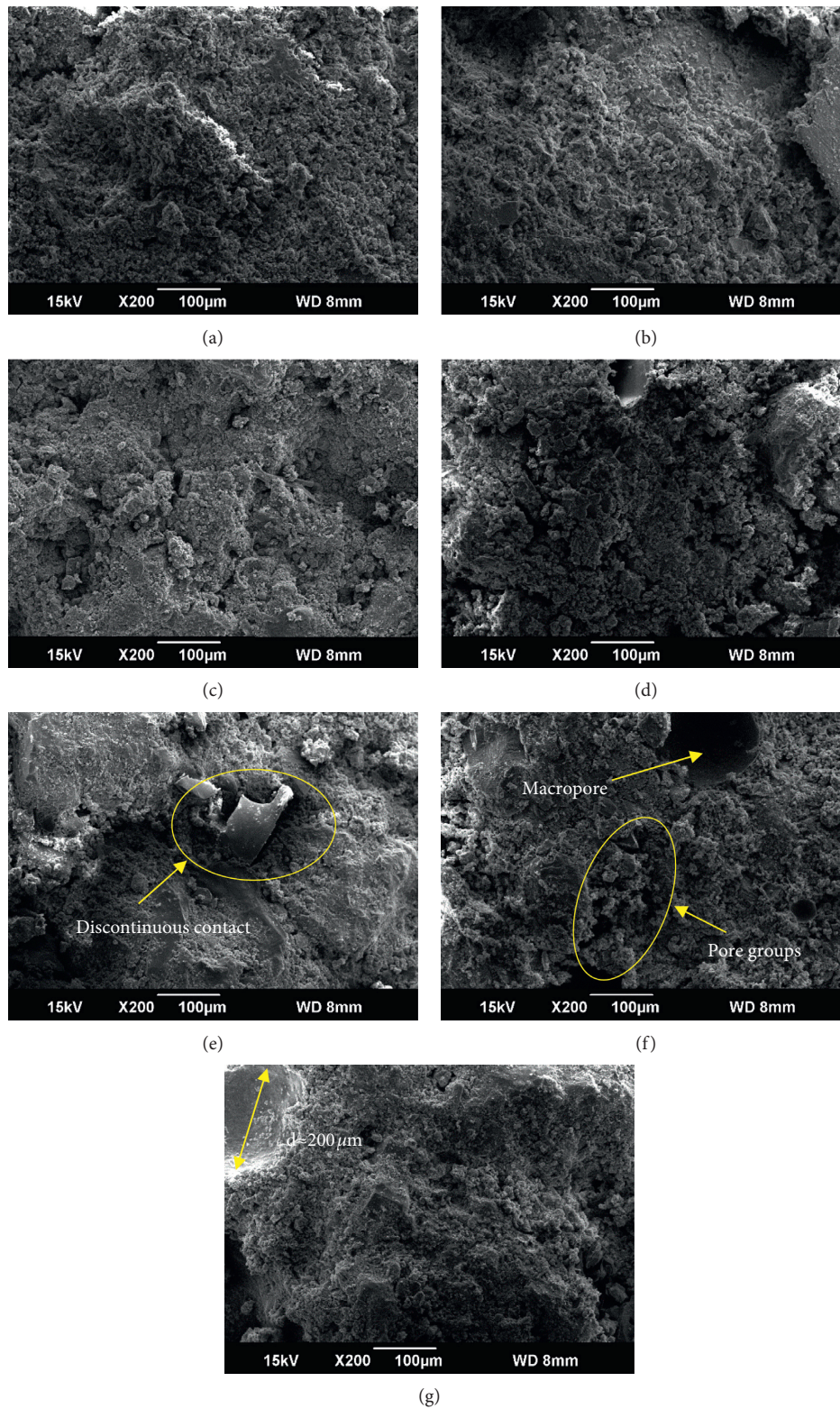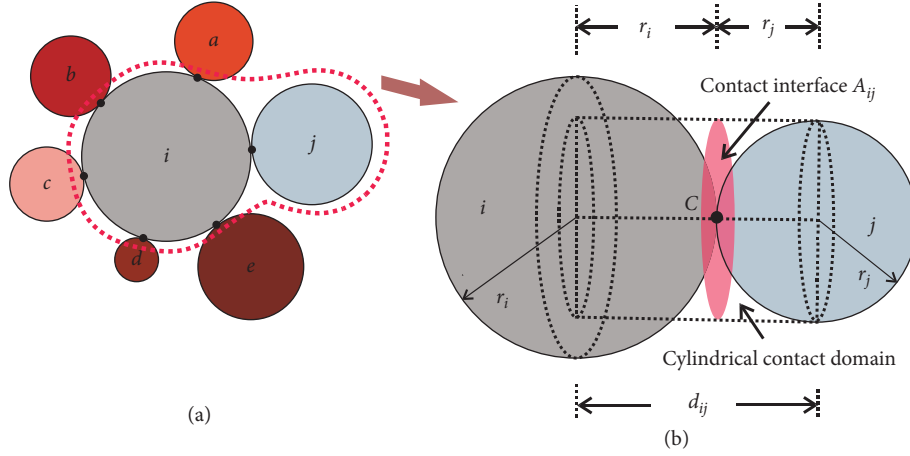
$$F_i = F_i^{\text{ext}} + \sum_{j=1}^{n_i^c} F^{ij} + F_i^{\text{damp}}, \tag{2}$$

where n_i^c is the number of particles in contact with particle i, F_i^{ext} represents the external field force, F^{ij} refers to the contact force between particle i and particle j, and F_i^{damp} represents the force generated by the particle external damping, which comes from the contact between particle and C-S-H. Assuming that the particles are spherical and only a slight overlap between the particles is allowed, the contact condition between particle i and particle j is

$$d_{ij} = r_i + r_j. \tag{3}$$

Therefore, the contact interface of two adjacent particles is a circular surface, as shown by A_{ij} in Figure 7(b), and the area of the circle is

$$A_{ij} = \pi r_c^2, \tag{4}$$

$$r_c = \min(r_i, r_j). \tag{5}$$

When two spherical particles are in contact, the contact force F^{ij} is composed of the normal force F_n^{ij} and the shear force F_s^{ij}. Then, the contact force can be decomposed into

$$F^{ij} = F_n^{ij} + F_s^{ij}. \tag{6}$$

F_n^{ij} and F_s^{ij} are derived from the normal stress σ_n and the shear stress σ_s. F_n^{ij} and F_s^{ij} can be calculated by the following formula through the contact area:

$$F_n^{ij} = A_{ij}\sigma_n, \tag{7}$$

$$F_s^{ij} = A_{ij}\sigma_s. \tag{8}$$

For a fixed unit-body, assuming that the number of solid particles and their distribution is fixed, the initial air content only changes the distribution of C-S-H. Then, the higher the initial air content in fresh slurry, the more the C-S-H space occupied by the pores. This will cause the following effects: (i) The damping force F_i^{damp} on the particles is reduced because the particles are exposed to less C-S-H. (ii) The decrease of C-S-H results in the increase of σ_n and σ_s when particles are under pressure, while the contact interface A_{ij} does not change. Therefore, it can be seen from equations (6), (7), and (8) that F^{ij} increases. Besides, F_i^{ext} can be considered unchanged in the gravity field. In summary, under the same pressure, as the initial air content in fresh slurry increases, F_i^{damp} decreases, F^{ij} increases, and F_i^{ext} does not change. It can be concluded that the effect of initial air content in fresh slurry on UCS of CPB must be composed of two parts.

Assuming that two functions affect F_i^{damp} and F^{ij}, respectively, so from a macro perspective, the effect of initial air content on strength is also composed of two functions. Given the characteristic that the strength first increases and then decreases, in general, there are quadratic function, exponential function, and logarithmic function that can be referred to. Then, the mathematical model should be composed of a pair-wise combination of the three. After screening, it is found that the combination of logarithmic function and quadratic polynomial is the best. The function is $y = -2.90 \ln x - 0.106x^2 + 1.732x + 0.143$ (x represents the initial air content in fresh slurry, and y represents the 28 d age UCS of CPB), as shown in Figure 8. The R^2 is 0.968, so the reliability is greatly improved compared with single quadratic polynomial ($R^2 = 0.889$), which has a greater reference value.

In order to verify the validity of the mathematical model, another two experiments were performed. The air-entraining agent dosage was 0.5 g (0.026%) and 1 g (0.052%), respectively, which were different from any experiment in Table 2. The other ratios were the same as Table 2. The results showed that the air content was 6.52%, 8.53% and the 28 d UCS was 1.46 MPa and 0.90 MPa, respectively. The strength
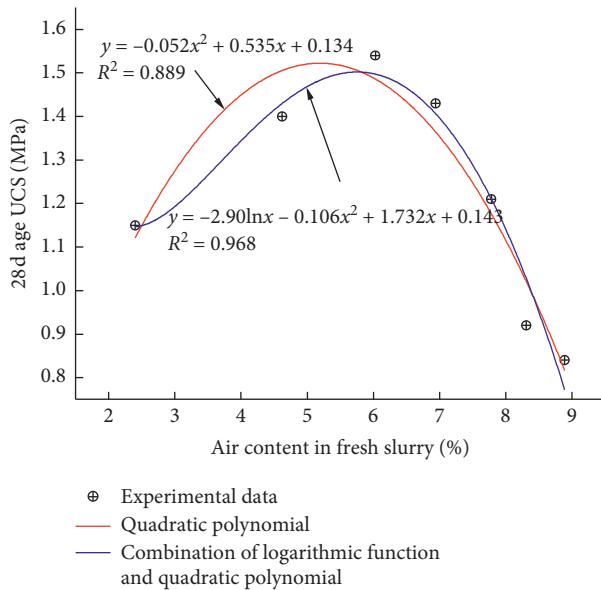
FIGURE 8: Comparison of two mathematical models.

calculated using this model is 1.49 MPa and 0.98 MPa, respectively. The error between the calculated value and the test value is calculated by equation (9):

$$k = \frac{|\sigma_c - \sigma_t|}{\sigma_t},\tag{9}$$

where k represents the error, σ_c represents the calculated value by this model, and σ_t represents the experimental test value. The error is 2.1% and 8.9%, respectively, both within 10%, indicating that the model has good practicability.

4. Conclusions

The main conclusions of this paper are as follows:

(1) The influence of SDS dosage on the initial air content in fresh slurry is a quadratic polynomial.

(2) In the UCS experiment, some samples show fluctuations near the peak of the stress-displacement curve, and this phenomenon does not become obvious after the initial air content is higher than 6.94%.

(3) As the initial air content in fresh slurry increases, the 28 d age UCS of CPB first increases and then decreases, and the initial air content of 6.03% can provide the optimal UCS for CPB.

(4) Before the initial air content of 6.03%, the microstructure of CPB is relatively compact. After this value, "discontinuous contact" structure, pore groups, and macropores will appear inside the CPB. The diameter of the largest pore can reach 200μm. These are the reasons to reduce the UCS of CPB.

(5) The mathematical model to describe the effect of initial air content in fresh slurry on the 28 d age UCS of CPB is composed of a logarithmic function and a quadratic polynomial. However, this mathematical

model does not include changes in gradation, concentration, and cement/sand ratio. The next work is to incorporate more factors into the model.

Data Availability

The data supporting the findings of this study are included in the article. Additionally, raw data generated during the study are available from the corresponding author upon request.

Conflicts of Interest

The authors declare that they have no conflicts of interest.

Acknowledgments

References

[1] Z. Xue, D. Gan, Y. Zhang, and Z. Liu, "Rheological behavior of ultrafine-tailings cemented paste backfill in high-temperature mining conditions," *Construction and Building Materials*, vol. 253, Article ID 119212, 2020.

[2] M. Fall, M. Benzaazoua, and S. Ouellet, "Experimental characterization of the influence of tailings fineness and density on the quality of cemented paste backfill," *Minerals Engineering*, vol. 18, no. 1, pp. 41–44, 2005.

[3] X. Chen, X. Shi, J. Zhou, X. Du, Q. Chen, and X. Qiu, "Effect of overflow tailings properties on cemented paste backfill," *Journal of Environmental Management*, vol. 235, pp. 133–144, 2019.

[4] L. Yang, H. Wang, A. Wu et al., "Effect of mixing time on hydration kinetics and mechanical property of cemented paste backfill," *Construction and Building Materials*, vol. 247, Article ID 118516, 2020.

[5] S. Yin, Y. Shao, A. Wu, H. Wang, X. Liu, and Y. Wang, "A systematic review of paste technology in metal mines for cleaner production in China," *Journal of Cleaner Production*, vol. 247, Article ID 119590, 2020.

[6] F. Cihangir and Y. Akyol, "Effect of desliming of tailings on the fresh and hardened properties of paste backfill made from alkali-activated slag," *Advances in Materials Science and Engineering*, vol. 2020, Article ID 4536257, 11 pages, 2020.

[7] F. Wang, G. Chen, L. Ji, and Z. Yuan, "Preparation and mechanical properties of cemented uranium tailing backfill based on alkali-activated slag," *Advances in Materials Science and Engineering*, vol. 2020, Article ID 6345206, 7 pages, 2020.

[8] X. Zhou, S. Hu, G. Zhang, J. Li, D. Xuan, and W. Gao, "Experimental investigation and mathematical strength model study on the mechanical properties of cemented paste backfill," *Construction and Building Materials*, vol. 226, pp. 524–533, 2019.

[9] J. Wu, M. Feng, G. Han, X. Ni, and Z. Chen, "Experimental investigation on mechanical properties of cemented paste backfill under different gradations of aggregate particles and types and contents of cementing materials," *Advances in*

Materials Science and Engineering, vol. 2019, Article ID 9456861, 11 pages, 2019.

[10] Y.-y. Tan, X. Yu, D. Elmo, L.-h. Xu, and W.-d. Song, "Experimental study on dynamic mechanical property of cemented tailings backfill under SHPB impact loading," *International Journal of Minerals, Metallurgy, and Materials*, vol. 26, no. 4, pp. 404–416, 2019.

[11] B. Yan, F. Ren, M. Cai, and C. Qiao, "Influence of new hydrophobic agent on the mechanical properties of modified cemented paste backfill," *Journal of Materials Research and Technology*, vol. 8, no. 6, pp. 5716–5727, 2019.

[12] R. Gao, K. Zhou, W. Liu, and Q. Ren, "Correlation between the pore structure and water retention of cemented paste backfill using centrifugal and nuclear magnetic resonance methods," *Minerals*, vol. 10, no. 7, p. 610, 2020.

[13] H. Rong, M. Zhou, and H. Hou, "Pore structure evolution and its effect on strength development of sulfate-containing cemented paste backfill," *Minerals*, vol. 7, no. 1, p. 8, 2017.

[14] J. H. Hu, Y. Kuang, T. Zhou, and F. Zhao, "Influence of air entraining agent on strength and microstructure properties of cemented paste backfill," *IEEE Access*, vol. 7, pp. 140899–140907, 2019.

[15] J. Hu, F. Zhao, Y. Kuang, D. Yang, M. Zheng, and L. Zhao, "Microscopic characteristics of the action of an air entraining agent on cemented paste backfill pores," *Alexandria Engineering Journal*, vol. 59, no. 3, pp. 1583–1593, 2020.

[16] E. K. K. Nambiar and K. Ramamurthy, "Air-void characterisation of foam concrete," *Cement and Concrete Research*, vol. 37, no. 2, pp. 221–230, 2007.

[17] Y. Xie, J. Li, Z. Lu, J. Jiang, and Y. Niu, "Effects of bentonite slurry on air-void structure and properties of foamed concrete," *Construction and Building Materials*, vol. 179, pp. 207–219, 2018.

[18] P. Du, Y. Yao, L. Wang et al., "Using strain to evaluate influence of air content on frost resistance of concrete," *Cold Regions Science and Technology*, vol. 157, pp. 21–29, 2019.

[19] Q. Yang, P. Zhu, X. Wu, and S. Huang, "Properties of concrete with a new type of saponin air-entraining agent," *Cement and Concrete Research*, vol. 30, no. 8, pp. 1313–1317, 2000.

[20] T. S. Yun, K. Y. Kim, and D. H. Kang, "Quantifying the distribution of paste-void spacing of hardened cement paste using X-ray computed tomography," *Materials Characterization*, vol. 73, pp. 137–143, 2012.

[21] H. Jianhua, Q. Jiang, and Q. Ren, "Cross scale correlation characteristics of pore structure and meso parameters of filling body," *The Chinese Journal of Nonferrous Metals*, vol. 28, no. 10, pp. 2154–2163, 2018.

[22] F. Özcan and M. Emin Koç, "Influence of ground pumice on compressive strength and air content of both non-air and air entrained concrete in fresh and hardened state," *Construction and Building Materials*, vol. 187, pp. 382–393, 2018.

[23] A. A. Hilal, N. H. Thom, and A. R. Dawson, "On void structure and strength of foamed concrete made without/with additives," *Construction and Building Materials*, vol. 85, pp. 157–164, 2015.

[24] T. T. Nguyen, H. H. Bui, T. D. Ngo, and G. D. Nguyen, "Experimental and numerical investigation of influence of air-voids on the compressive behaviour of foamed concrete," *Materials & Design*, vol. 130, pp. 103–119, 2017.

Research Article

Experimental Study on the Evolution Law of Mesofissure in Full Tailing Cemented Backfill

Yufan Feng ![ORCID], **Guanghua Sun** ![ORCID], **Xuejian Liang** ![ORCID], **Chenyang Liu** ![ORCID], **and Yue Wang** ![ORCID]

College of Mining Engineering, North China University of Science and Technology, Tangshan, Hebei 063210, China

Correspondence should be addressed to Guanghua Sun; czsgh110@163.com

To understand the mechanical properties of the backfill, to reveal the evolvement of micromechanical fissure of backfill, a uniaxial compression experiment was carried out for the full tailing cemented backfill. After loading, the microstructure of the specimens was observed by microscope and the pore characteristic parameters were analyzed. The results showed that the diameter of the initial damage hole of the backfill was mostly between 0 and 40 μm, the hole diameter increases gradually with the increase of pressure, and the hole diameter reached more than 5000 μm in the postpeak damage stage. The upper structure of the backfill specimen is compact while the lower structure is relatively loose. The cracks and interfaces between tailings particles and cement paste are mechanical weak surfaces, where the cracks are mainly generated and propagated. The tip of microfractures in the backfill is damaged by the influence of stress concentration. In the failure process, both surface porosity and fracture density decrease first and then increase, and the average pore diameter increases gradually. The results have guiding significance for the study of backfill mechanical properties and goaf filling design.

1. Introduction

The filling mining method uses tailings to fill goaf, which not only protects the mine surrounding environment but also reduces the discharge of tailings. Full tailing cemented backfill is an aggregate composed of tailings and cement cemented with different properties. Complex microscopic structures such as the size and composition of tailings, particles, structural surfaces, and microcracks directly affect the macroscopic mechanical properties, thus affecting the mine production safety. Therefore, it is helpful to understand the backfill mechanical properties and provide a certain basis for the safety of filling mining by exploring the mesofracture evolution law of backfill mesostructure.

Some scholars [1–4] have made great contributions to crack propagation and closure under uniaxial compression. Ghazvinian et al. [5] studied the thresholds for crack initiation (CI) and crack propagation (CD) in brittle rocks. Xue et al. [6] applied acoustic emission technology to study the damage stress threshold of different types of rock cracks under uniaxial compression. Rodríguez and Paola et al. [7]

studied fracture microcrack propagation in marble and pyromanganese ore by acoustic emission technology. Kumari et al. [8] used acoustic emission to study the corresponding fracture propagation patterns in the microstructure of rocks. Liu et al. [9] analyzed the failure mechanism of tailing cemented backfill with different gray-sand ratios and its mechanical properties under different ratios. Most of these studies are based on acoustic emission (AE). The temporal and spatial evolution of crack damage can be well described by AE technology, but the mesoscopic structure cannot be described in detail.

With the development of CT technology, it has been applied increasingly in geotechnical engineering. Ren et al. [10] analyzed the microcrack behavior between cement slurry and aggregate interface through CT. Shang et al. [11] and Hu and Yang [12] studied the relationship between rock porosity change and rock damage under uniaxial load by using nuclear magnetic resonance (NMR) to determine the porosity inside the rock. Zhang et al. [13] obtained the hole distribution of asphalt mixture by CT. Liang et al. [14] studied the internal void and aggregate distribution

characteristics of cement-stabilized macadam (CSM) through CT. Wang et al. [15, 16] proposed a Monte Carlo simulation method for the study of concrete microstructures and size effects and obtained the initiation and propagation of concrete microcracks. Kupwade-Patil et al. [17] used a variety of pore and microstructure characterization techniques such as X-ray and infrared spectroscopy to study the pore and microstructure of pozzolan in cement hardening. Sun et al. [18] conducted a real-time uniaxial compression scanning test using CT and a small loading device and discussed the pore evolution law during the bearing failure of cemented backfill (CPB). Through CT research, we can have a deeper understanding of the microscopic structure of rock and soil. Due to the limitations of CT images obtained through computer processing, the microstructure of backfill samples cannot be directly observed.

As conventional equipment for rock and ore identification in mineralogy and petrology, polarized light microscope is used to obtain two-dimensional petrographic photos of different scales. It can identify mineral particles with naked eyes and accurately quantify the structural characteristics of rocks with image processing and structural analysis software. Yang et al. [19] analyzed the structure and composition of granite. Higgins et al. [20] studied the volcanic activities of Quizapu and the cracks under the volcano through the analysis of andesite. O′Driscoll et al. [21] conducted an in-depth study on the genesis of the Bon Accord nickel deposit and believed that it might be related to the nickel oxide sulfide deposit related to the explosion of the Undersea Koma iron mine. Hepworth et al. [22] and Bradshaw [23] studied the origin of peridot crystals in peridot magma by observing a series of rock structures and geochemistry, respectively. Soulié et al. [24] studied the dissolution of magnesium-rich olivine at high temperature. Cheng et al. [25] discussed the source of potash feldspar crystal by analyzing the composition of the rhyolite in Emei Mountain. However, polarized light microscopy has rarely been reported in the field of mining and backfill research. Therefore, the microscopic images of backfill under uniaxial loading were observed by a polarized light microscope. The pore characteristic parameters and crack propagation forms of backfill were analyzed to understand the mechanical properties and reveal the mesofracture evolution law of backfill.

2. Test Design and Process

2.1. Sample Making. The aggregate was made of full tailings from an iron ore mine in Jidong, and the cementing agent was made of 42.5# Portland cement. The specimens with a concentration of 70% and a size of 200 mm × 200 mm × 200 mm were prepared according to a gray-sand ratio of 1 : 10 annd maintained in the standard maintenance box for 28 days. The mechanical properties of the same batch of specimens are also different due to the influence of the size and composition of tailings particles and the structural surface between particles and microcracks. To ensure that the original damage structure and basic mechanical properties of the specimens are

consistent, the stability of the test results can be guaranteed to the greatest extent by taking the same specimen for testing. After curing, the use of core drilling in backfill specimen of nine Φ = 50 mm core, according to sequence numbers 1∼9 for use in subsequent tests. Then, polish the upper and lower ends of specimen nos. 1∼8, leaving 100 mm in the middle. Specimen no. 9 was not polished for comparative analysis. The flowchart of sample preparation is shown in Figure 1.

2.2. Uniaxial Compression Test. The mechanical properties of the backfill at each stage of the loading process can be expressed by the stress-time curve. Therefore, in order to obtain the stress-time curve of the backfill under uniaxial loading, to divide the middle moment of the loading stage, uniaxial compression tests were carried out for the three specimens numbered 1∼3 by uniaxial testing machine. To ensure full contact between the press and the sample, preloading was carried out before the test, with a limit of 10 kN and a moving speed of 2 mm/min. After the end of preloading, axial equivalent displacement loading was adopted with a loading rate of 0.15 mm/min. After the completion of the loading of specimen nos. 1∼3, we obtain the stress-time curve as shown in Figure 2. The backfill loading stage is divided into compaction stage (stage I), elastic deformation stage (stage II), plastic deformation stage (stage III), and postpeak failure stage (stage IV) by dotted line. Find out the specific intermediate time corresponding to each stage as shown in Table 1. Stage 0 represents the raw specimen that has not been treated.

To study the evolution law of mesoscopic fracture in the whole loading, uniaxial loading test was carried out to obtain the failure of mesoscopic fracture at each stage. To maintain the initial damage of the backfill specimen and protect the original mesocrack, specimen no. 4 was not loaded. Then, specimens 5 to 8 were loaded according to the timetable in Table 1, respectively, and then the specimens were removed. The results of specimen treatment are shown in Table 2.

To facilitate the grease injection test and subsequent data analysis, specimens nos. 4∼9 to be processed were renumbered first, and the numbering rules were shown in Table 3.

The first letter C represents the backfill, the second digit 10 represents the gray-sand ratio of 1 : 10, and the third digits 0, 1, 2, 3, and 4 represent the original specimen of the backfill, compaction stage, elastic deformation stage, plastic deformation stage, and postpeak failure stage, respectively. d stands for specimen no. 9 as the comparison specimen.

2.3. Vacuum Grease Injection Test. Thin section analysis can clearly observe the form and evolution process of mesocracks in each loading stage of the backfill. For this reason, BROT vacuum casting gauge in France was used to inject colored epoxy resin into the specimen. The principle is to pump the laboratory chamber into a vacuum and at the same time extract the air in the crack of the specimen. The resin enters into the crack to replace the air in the crack, to ensure that the cracks and pores in the specimen are not damaged
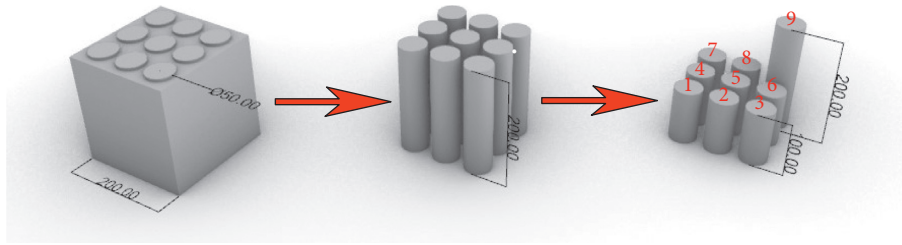
Figure 1: Schematic diagram for making backfill specimen.
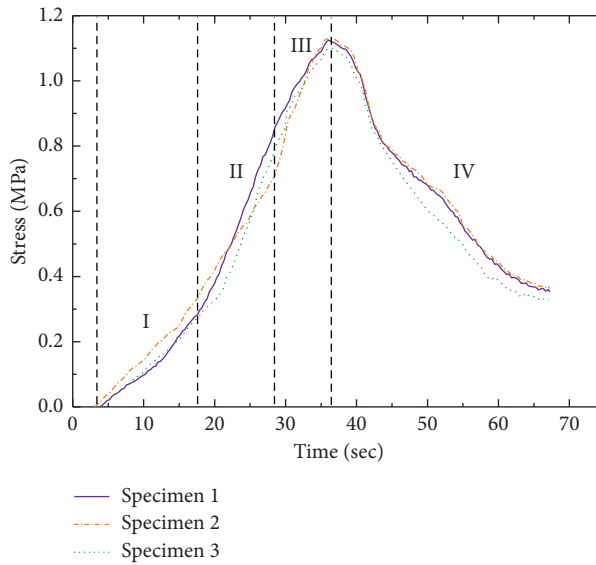
Figure 2: Stress-time curve of backfill under uniaxial compression.

Table 1: Intermediate schedule of backfill loading stage.

In the loading stage	Stage 0	Stage I	Stage II	Stage III	Stage IV
Intermediate time interval (sec)	0	10~12	23~25	32~33	50~60

Table 2: Treatment table of backfill specimen.

Specimen number	Take down the test piece time (sec)	In the loading stage
4	00	Original specimen
5	12	Compaction stage
6	24	Elastic deformation stage
7	33	Plastic deformation stage
8	55	Postpeak failure stage

Table 3: Number table of backfill.

Stratification	Number					
	4	5	6	7	8	9
Above	C-10-0-a	C-10-1-a	C-10-2-a	C-10-3-a	C-10-4-a	C-10-d-a
Middle	C-10-0-m	C-10-1-m	C-10-2-m	C-10-3-m	C-10-4-m	C-10-d-m
Below	C-10-0-b	C-10-1-b	C-10-2-b	C-10-3-b	C-10-4-b	C-10-d-b

during the grinding process and the morphology is preserved. Dyes are added to the resin to facilitate the resolution of solid particles and pores under a microscope under strong light.

First, the backfill was marked and stratified from top to bottom and put into the experimental chamber. Then the epoxy resin and curing agent were mixed at a ratio of 2 : 1, the catalyst and a small amount of blue dye were added, and

the evenly mixed glue solution was heated in a water bath at 80°C. After the system is vacuumed, the resin was injected into the laboratory, and samples were taken out and dried after pressurization. After drying, the samples were cut into cuboids with a size of 3 cm × 2 cm × 1 cm along the axial direction of the backfill and then ground into backfill casting slices with a thickness of 0.03 mm. A total of 18 backfill casting slices are made for slice analysis. See Figure 3 for the schematic diagram of test section making. Figure 4 shows the test process.

To ensure that the section would not affect the crack of the specimen during the test, first, the resin was injected after stratification to protect the crack inside the specimen from being destroyed. And then, the specimen is then cut after drying. At this point, any operation will not affect the cracks of the specimen, because the cracks are protected by resin. Finally, the reason why the blue part in the center of the specimen was selected for cutting was to avoid possible cracks in the stratification process, to ensure the accuracy of the test.

3. Test Results and Analysis

3.1. Evolution Characteristics of Mesoscopic Fissure. The "color image analysis system for pore characteristics and grain size of rock thin sections" developed by Sichuan University was used to process and calculate the parameters of the image of backfill cast thin sections obtained by Zeiss polarizing microscope, and then the pore distribution of backfill was quantitatively analyzed. The magnification of the image determines the number of microcracks observed in an image. If the multiple is too large, the microcracks are not complete. If the multiple is too small, the microcracks are not obvious in the image, and the image information will be lost during the image processing. To avoid this situation, the magnification is determined to be 100 times after comprehensive consideration. The middle position of the backfill was selected for observation and analysis of backfill casting thin section images. The gray part is the hardened set cement, the blue part is the dyed epoxy resin, and the others are tailing particles. The field of vision of the sample observed under the microscope is limited, and improper observation position will lead to errors in the analysis results. Therefore, images of the sample with typical characteristics are selected. To obtain enough microfracture information, the pore statistics are statistical histograms obtained from the same thin section based on multiple cross-section images.

(1) In the unloaded stage, the slice image and the histogram of pore statistics are shown in Figure 5. In Figure 5(a), it can be seen that there are already initial microcracks in the backfill. In Figure 5(b), the area frequency of hole diameter reaches the maximum in the range of 0~40 μm, and the cumulative area frequency is nearly 80%, indicating that there are a large number of microcracks and bubbles at the beginning, which constitute the initial damage of the backfill.

(2) In the compaction stage, the slice image and the histogram of pore statistics are shown in Figure 6. In Figure 6(a), the backfill begins to be pressurized, the specimen is basically without infiltration of dyed epoxy resin, and the microcrack closes under pressure. In Figure 6(b), the frequency of the hole diameter area significantly disappears in the range of 40~60 μm and increases in the range of 20~40 μm, indicating that the microcrack and bubble in the filling are closed under pressure, and the specimen is in the compaction stage.

(3) In the elastic deformation stage, the slice image and the histogram of pore statistics are shown in Figure 7. In Figure 7(a) the specimen was subjected to increased pressure, and the dyed epoxy resin entered the backfill and filled with microcracks, indicating that the backfill was reopened by the compaction cracks. The microcracks' tip was subjected to great concentrated stress, and the microcracks tip began to break, In Figure 7(b), the frequency of hole diameter area decreased in the range of 0~40 and increased in the range of, 40~100 μm, indicating that the crack gradually expanded at this stage.

(4) In the plastic deformation stage, the slice image and the histogram of pore statistics are shown in Figure 8. In Figure 8(a), as can be seen from the area occupied by the epoxy resin (the blue part in the figure), the microcracks develop into larger cracks, while the contact part between the two cracks produces microcracks but does not connect. In Figure 8(b), the frequency of the hole diameter area significantly increases further, reaches more than 160 μm.

(5) In the postpeak failure stage, the slice image and the histogram of pore statistics are shown in Figure 9. In Figure 9(a), in the postpeak failure stage, the backfill has clearly produced the through crack. In Figure 9(b), the frequency of hole diameter area increases between 180 and 200 μm. The through crack reduces the strength of the backfill, and the proportion above 5000 μm increases sharply, indicating that the macrocrack has been formed and the backfill has lost its bearing capacity after complete destruction.

The microcracks and bubbles constitute the initial damage of the backfill, which is mainly in the range of 0~40 μm. The 40~60 μm with large fissure was closed in the compaction stage, and with the increasing pressure, the reexpansion development increased from 40~100 μm to 160 μm to above 5000 μm. Therefore, a large number of microfractures are first distributed in the backfill. Under the action of pressure, some of these fractures expand and develop under pressure, leading to macroscopic failure of backfill. However, the stress of some fractures is not significant and the development of fractures is not obvious.
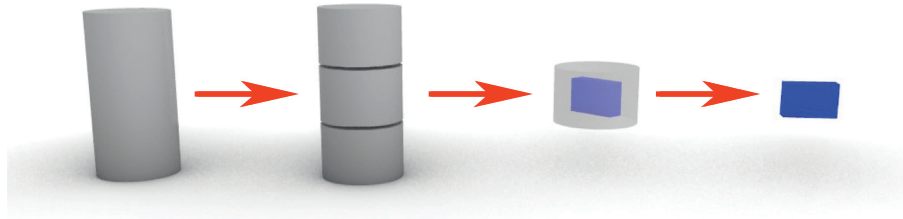
Figure 3: Schematic diagram of test slice cutting.
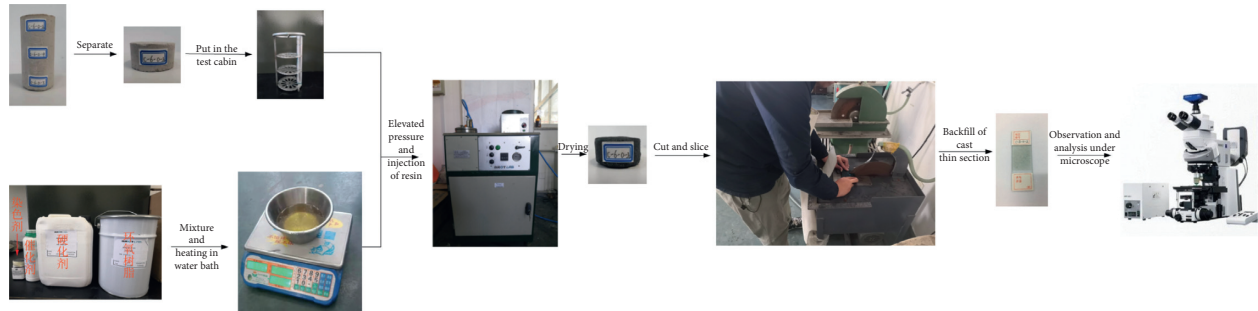
Figure 4: Flowchart of lipid injection test.
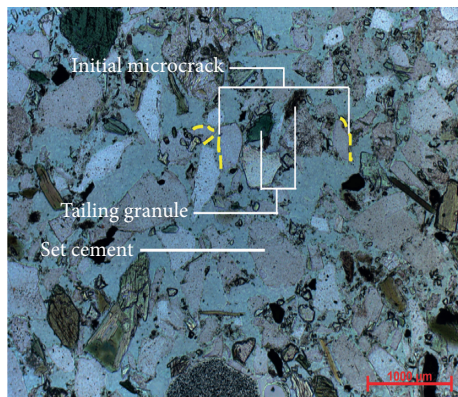
(a)
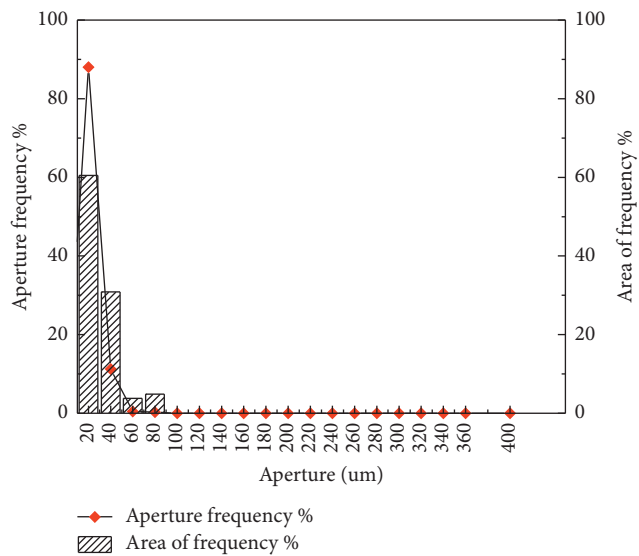
(b)

Figure 5: Original specimen of the cast thin section. (a) Slice image. (b) Pore statistical histogram.

3.2. Characteristics of Backfill in the Direction of Gravity.
The filling slurry is uniform under ideal conditions without segregation and precipitation. However, segregation and settlement still exist in practice because of the fluidity of the filling slurry in the pipe. In addition, before the consolidation of filling slurry, the hydration reaction of cement has not been completely completed, and the consolidation force of cement on tailings particles is too weak. Figure 10 shows the upper, middle, and lower castings of the specimen with no. 9 backfill.

It can be seen from Figure 10(a) that there are many types of set cement and a large area. The upper layer of backfill is mostly cement with a tight structure. The lower layer, as shown in Figure 10(c), has more tailing particles and looser structure. As shown in Figure 10(b), the proportion of middle set cement and tailings particles is between the upper and lower layers. This phenomenon is obvious from the perspective of gravity analysis. Due to the different particle sizes of tailings, during the consolidation process of backfill, the coarsest particles firstly settle and accumulate in the

(a)   (b)

FIGURE 6: Compaction stage of the cast thin section. (a) Slice image. (b) Pore statistical histogram.

(a)   (b)
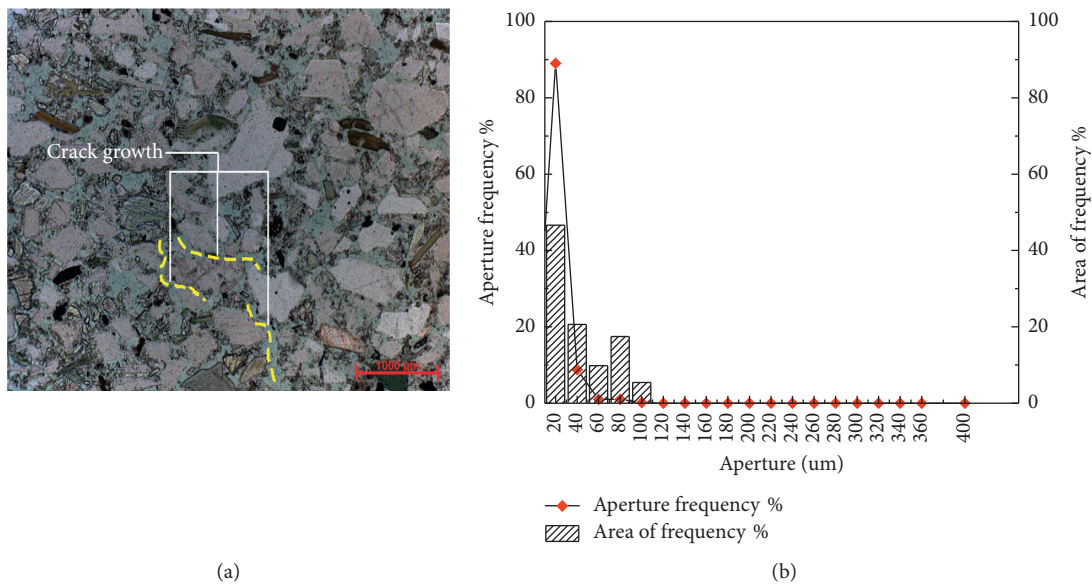
FIGURE 7: Elastic deformation stage of the cast thin section. (a) Slice image. (b) Pore statistical histogram.

lower end of backfill, while the unhydrated cement is on the upper layer of backfill. Therefore, this phenomenon will result in different mechanical strength of upper and lower ends of backfill under uniaxial compression. Therefore, in the pretreatment of Section 2.1 sample making, the upper and lower ends of the backfill were polished, the middle section is selected for the test, which reduces the influence to a certain extent, and the test results are more persuasive.

3.3. Propagation Law of Mesoscopic Fissure. To explore the propagation direction of mesoscopic fractures in the backfill, the cast slices of the backfill numbered "C-10-2-middle"

were observed under a microscope, and the picture shown in Figure 11 was obtained.

It can be clearly seen from the pictures that the microcracks in the backfill occur at the contact surface between tailing particles and set cement and are distributed and developed along the edge of tailing particles. Then, under the action of stress, the microcracks on the edge of the particles gradually develop and expand and then deflate and expand toward the cement stone area, finally forming the through cracks.

Under the action of pressure, the crack tip produces concentrated stress, which promotes the crack surface and microcrack propagation. The fracture and interface between

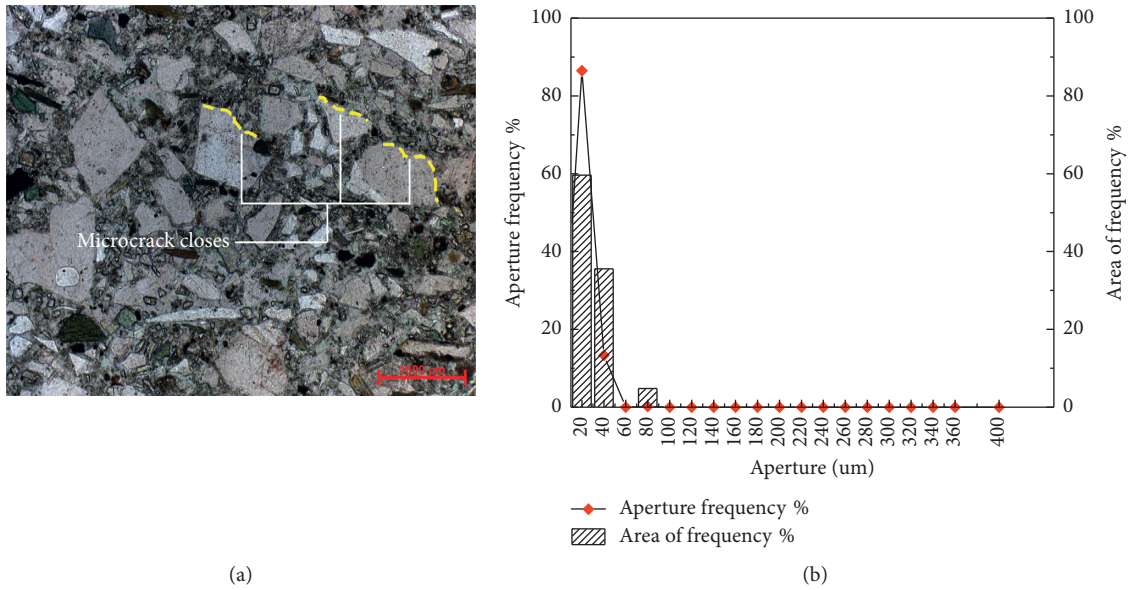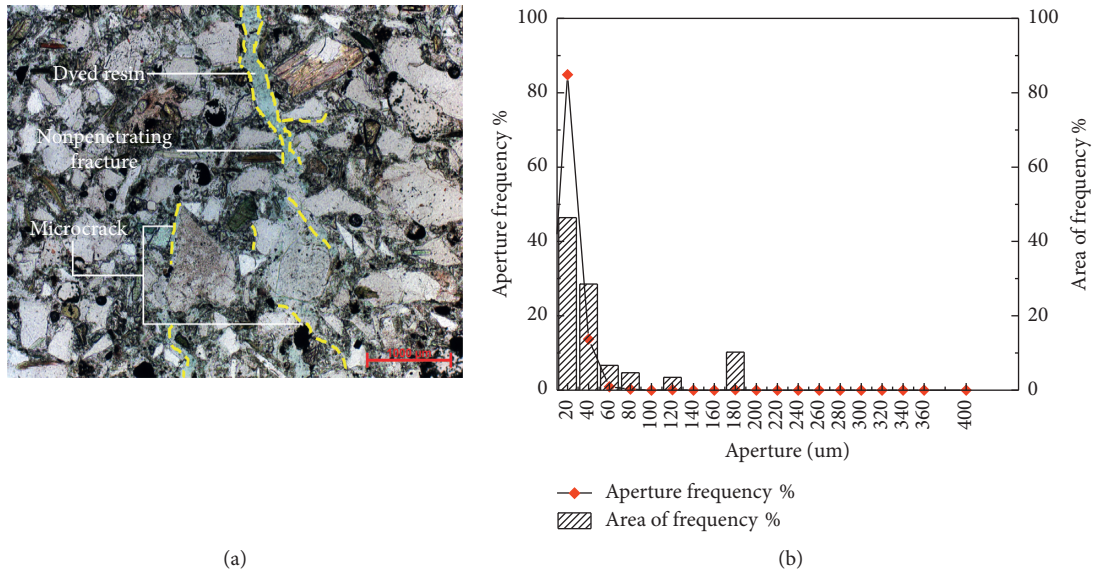FIGURE 8: Plastic deformation stage of the cast thin section. (a) Slice image. (b) Pore statistical histogram.
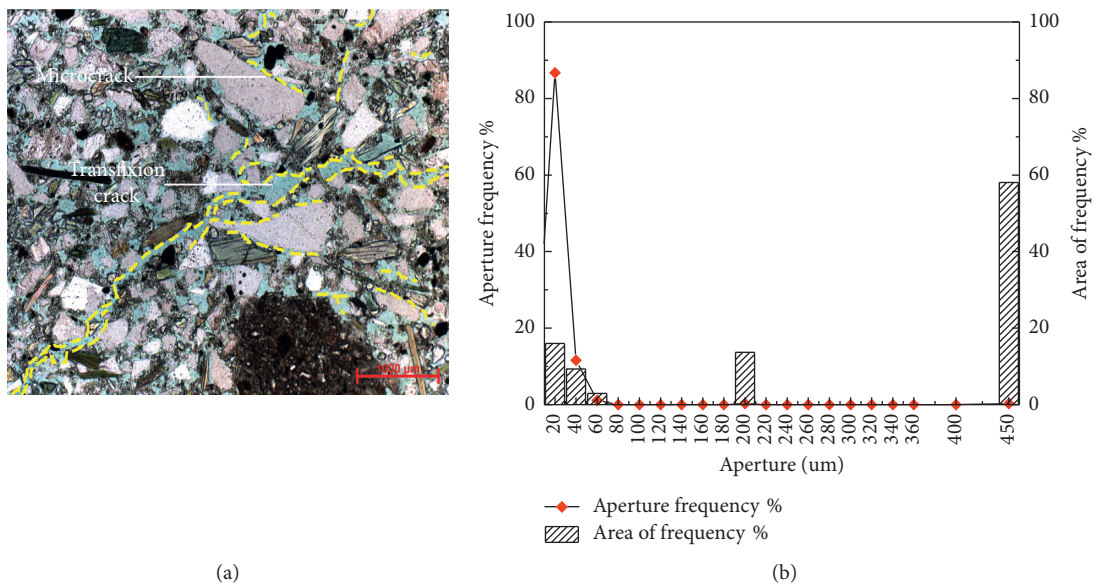
FIGURE 9: Postpeak failure stage of the cast thin section. (a) Slice image. (b) Pore statistical histogram.

tailing particles and set cement are the mechanical weak surfaces. This is because of their different hardness and the stress propagates at the interface between them. The difference in hardness leads to the formation of microcracks on the interface, which propagate on the interface and eventually develop into cracks throughout the backfill.

4. Discussion

As a composite material, full tailing cementing backfill is composed of full tailings, cement, water, bubbles, initial cracks, and so on. The early hydration slurries consist of needles or sheets of fibers, which are not solid, but fine tubular and dendritic interlaced. Therefore, the backfill contains a large number of microcracks in a disorderly direction. Griffith failure criterion believes that there are many fine cracks in the material; under the action of force, the surrounding of these fine cracks, especially the crack end, can produce stress concentration phenomenon. Damage to the material often starts at the end of the crack and the crack spreads and eventually leads to complete damage to the material. The pore characteristic parameters of backfill under uniaxial loading are shown in Table 4.

(a)

(b)

(c)
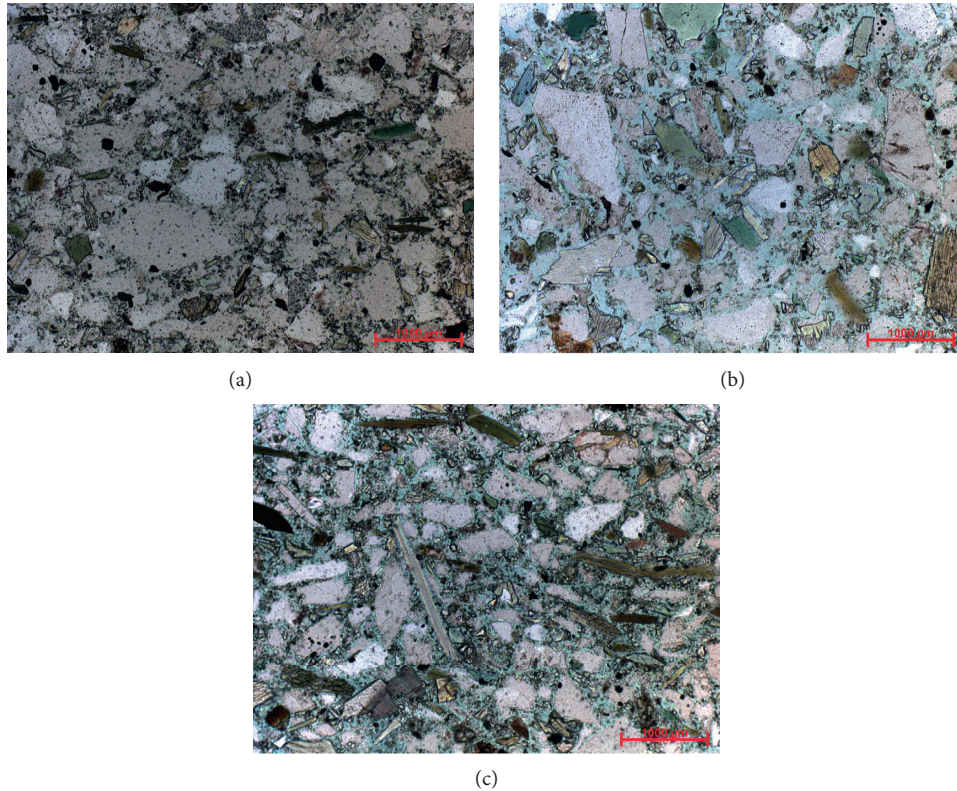
FIGURE 10: The cast thin slices in different positions of specimen no. 9. (a) C-10-d-above slice image (b) C-10-d-middle slice image. (c) C-10-d-below slice image.
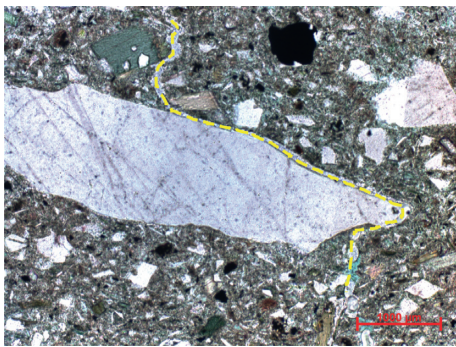
FIGURE 11: "C-10-2- middle" backfill casting thin section image.

Both the physics experiment of Chen et al. [26] and the simulation experiment of Xu et al. [27] show that cracks usually appear at the tip of cracks and then gradually expand around cracks. In their papers, they both mentioned that rock bridge (the rock mass between fractures that has not been penetrated), where the inner tip of the two fractures converge during the loading process,thus connecting the two fractures Their research results and the research content of this paper can be well verified: in the elastic deformation stage, the fracture ends of microcracks begin to expand to the surrounding due to stress concentration; in the plastic deformation stage, the fracture is enlarged, but the fracture is not connected; it can be regarded as a "bridge" in the backfill. In the subsequent postpeak failure stage, the fracture is connected. In this paper, the characteristics of crack evolution described by them are described in detail at different loading stages.

In the unloaded stage, the face rate and fracture density of the backfill are 8.77% and 2.32 mm/mm², respectively, which are mainly the initial cracks formed on the interface between tailings particles and the set cement of the backfill and the undischarged bubbles. According to the Griffith failure criterion, it is assumed that the cracks are open and elliptically shaped and begin to crack at the tip edge wall of the open crack [28–31]. In the compaction stage, the backfill face rate and fracture density were reduced to 7.28% and 1.62 mm/mm², respectively. The reason for the fracture closure of the backfill was that the compaction was worse than that of the rock. Under the action of external forces, the internal microcracks and bubble compression stress of the specimen led to compaction and closure, and the pore characteristic parameters were relatively reduced. In elastic deformation stage, face filling rate and fracture density were increased to 9.24%, 3.22 mm/mm², with the increase of pressure, the microcracks after undergoes compression,new microcracks start to emerge at the seam end on the basis of the initial cracks, and the new cracks are mainly distributed between the tailing particles and the cement stone or around the larger tailing particles In the plastic deformation stage, the face rate and fracture density of backfill increased significantly, which were 17.11% and 6.54 mm/mm², respectively, indicating that the internal stress continued to increase, the cracks expanded rapidly, mainly along the edge

TABLE 4: Pore characteristic parameters of backfill.

In the loading stage	Characteristic parameter		
	Face rate (%)	Fracture density (mm/mm^2)	Average pore size (μm)
Original specimen	8.77	2.32	21.37
Compaction stage	7.28	1.62	22.05
Elastic deformation stage	9.24	3.22	34.53
Plastic deformation stage	17.11	6.54	42.54
Postpeak failure stage	25.44	14.66	266.41

of tailings particles to set cement, and a large number of microcracks were connected to form larger pores. In the postpeak failure stage, a large area of damage occurred inside the sample, and the face rate and fracture density of the backfill further increased, which were 25.44% and 14.66 mm/mm^2, respectively, indicating that the through crack had formed the bearing capacity of the macroscopic crack backfill. In summary, under uniaxial compression, the mesoscopic crack of the backfill body is damaged under the influence of tensile stress. However, the average pore size is increasing from 21.37 μm to 266.41 μm, indicating that the volume of the mesocrack of the backfill is increasing, the contact between tailings particles becomes less due to the propagation of cracks, the structure inside the specimen becomes loose, the cementing capacity of cement begins to decline, and the carrying capacity of the backfill decreases.

5. Conclusion

(1) During the consolidation of backfill, due to the action of gravity, large tailings particles sink to the bottom, so the upper structure of consolidated backfill is compact, while the lower structure is relatively loose.

(2) In the unloaded stage, the diameter of the initially damaged pores was mostly between 0 and 40 μm. With the increase of load, the diameter of the holes in the compaction stage decreased slightly, while the diameter of the holes in the elastic deformation stage increased in the range of 40~100 μm, and microcracks began to form and develop. In the plastic deformation stage, the diameter of the hole reaches more than 160 μm, and the crack expands rapidly. In the postpeak failure stage, the pore diameter is above 5000 μm, the crack is connected to the macrocrack, and the backfill is destroyed.

(3) The fracture and interface of tailings particles and set cement are the weak mechanical surface and the weak position of the backfill. The generation and propagation of cracks mainly occur here.

(4) In the failure process, the pore characteristic parameters, face rate and fracture density, both decrease first and then increase, and the average pore diameter gradually increases. The tip of the microcrack is destroyed by the influence of stress concentration, the crack volume increases gradually, the specimen structure becomes loose, and the carrying capacity of the backfill decreases.

Data Availability

All data, models, or codes generated or used during the study are available from the corresponding author or author upon request (Guanghua Sun, email:czsgh110@163.com).

Conflicts of Interest

The authors declare that there are no conflicts of interest regarding the publication of this paper.

Acknowledgments

References

[1] C. H. Park and A. Bobet, "Crack initiation, propagation and coalescence from frictional flaws in uniaxial compression," *Engineering Fracture Mechanics*, vol. 77, no. 14, pp. 2727–2748, 2010.

[2] P.-Q. Ji, X.-P. Zhang, and Q. Zhang, "A new method to model the non-linear crack closure behavior of rocks under uniaxial compression," *International Journal of Rock Mechanics and Mining Sciences*, vol. 112, 2018.

[3] Y. Wang, X. Zhou, and Y. Shou, "The modeling of crack propagation and coalescence in rocks under uniaxial compression using the novel conjugated bond-based peridynamics," *International Journal of Mechanical Sciences*, vol. 128-129, pp. 614–643, 2017.

[4] Y. Niu, X.-P. Zhou, and F. Berto, "Evaluation of fracture mode classification in flawed red sandstone under uniaxial compression," *Theoretical and Applied Fracture Mechanics*, vol. 107, Article ID 102528, 2020.

[5] E. Ghazvinian, M. S. Diederichs, D. Labrie, and C. D. Martin, "An investigation on the fabric type dependency of the crack damage thresholds in brittle rocks," *Geotechnical and Geological Engineering*, vol. 33, no. 6, 2015.

[6] L. Xue, S. Qin, Q. Sun, Y. Wang, M. Lee, and W. Li, "A study on crack damage stress thresholds of different rock types based on uniaxial compression tests," *Rock Mechanics and Rock Engineering*, vol. 47, no. 4, 2014.

[7] P. Rodríguez, B. A. Paola, and T. B. Celestino, "Characterization of rock cracking patterns in diametral compression tests by acoustic emission and petrographic analysis," *International Journal of Rock Mechanics and Mining Sciences*, vol. 83, pp. 73–85, 2016.

[8] W. G. P. Kumari, P. G. Ranjith, M. S. A. Perera, and B. K. Chen, "Experimental investigation of quenching effect on mechanical, microstructural and flow characteristics of

reservoir rocks: thermal stimulation method for geothermal energy extraction," *Journal of Petroleum Science and Engineering*, vol. 162, pp. 419–433, 2018.

[9] Z.-x. Liu, M. Lan, S.-y. Xiao, and H.-q. Guo, "Damage failure of cemented backfill and its reasonable match with rock mass," *Transactions of Nonferrous Metals Society of China*, vol. 25, no. 3, pp. 954–959, 2015.

[10] W. Ren, Z. Yang, R. Sharma, C. Zhang, J. Philip, and Withers, "Two-dimensional X-ray CT image based meso-scale fracture modelling of concrete," *Engineering Fracture Mechanics*, vol. 133, pp. 24–39, 2015.

[11] J. Shang, J. Hu, K. Zhou, X. Luo, M. Mohammed, and Aliyu, "Porosity increment and strength degradation of low-porosity sedimentary rocks under different loading conditions," *International Journal of Rock Mechanics and Mining Sciences*, vol. 75, 2015.

[12] J.-H. Hu and D.-J. Yang, "Meso-damage evolution and mechanical characteristics of low-porosity sedimentary rocks under uniaxial compression," *Transactions of Nonferrous Metals Society of China*, vol. 30, no. 4, pp. 1071–1077, 2020.

[13] J. Zhang, J. Yang, T. Liu, R. Cai, and R. Yang, "Study on void structure reconstruction of asphalt mixture by X-ray computed tomography and otsu's method," *Advances in Materials Science and Engineering*, vol. 2020, Article ID 4546731, 13 pages, 2020.

[14] C. Liang, Y. Wang, G. Tan, L. Zhang, Y. Zhang, and Z. Yu, "Analysis of internal structure of cement-stabilized macadam based on industrial CT scanning," *Advances in Materials Science and Engineering*, vol. 2020, Article ID 5265243, 10 pages, 2020.

[15] X. Wang, Z. Yang, P. Andrey, and Jivkov, "Monte Carlo simulations of mesoscale fracture of concrete with random aggregates and pores: a size effect study," *Construction and Building Materials*, vol. 80, 2015.

[16] X. Wang, M. Zhang, P. Andrey, and Jivkov, "Computational technology for analysis of 3D meso-structure effects on damage and failure of concrete," *International Journal of Solids and Structures*, vol. 80, 2016.

[17] K. Kupwade-Patil, S. D. Palkovic, B. Ali, C. Soriano, and O. Büyüköztürk, "Use of silica fume and natural volcanic ash as a replacement to Portland cement: micro and pore structural investigation using NMR, XRD, FTIR and X-ray microtomography," *Construction and Building Materials*, vol. 158, pp. 574–590, 2018.

[18] W. Sun, K. Hou, Z. Yang, and Y. Wen, "X-ray CT three-dimensional reconstruction and discrete element analysis of the cement paste backfill pore structure under uniaxial compression," *Construction and Building Materials*, vol. 138, pp. 69–78, 2017.

[19] Z.-F. Yang, Z.-H. Luo, X.-X. Lu et al., "The role of external fluid in the Shanggusi dynamic granitic magma system, East Qinling, China: quantitative integration of textural and chemical data," *Lithos*, vol. 208-209, pp. 339–360, 2014.

[20] M. Higgins, S. Voos, and A. J. Vander, "Magmatic processes under Quizapu volcano, Chile, identified from geochemical and textural studies," *Contributions to Mineralogy and Petrology*, vol. 170, no. 5-6, pp. 1–16, 2015.

[21] B. O'Driscoll, P. L. Clay, R. G. Cawthorn et al., "Trevorite: Ni-rich spinel formed by metasomatism and desulfurization processes at Bon Accord, South Africa?" *Mineralogical Magazine*, vol. 78, no. 1, pp. 145–163, 2014.

[22] L. N. Hepworth, B. O'Driscoll, R. Gertisser, J. S. Daly, and C. H. Emeleus, "Incremental construction of the unit 10 peridotite, rum eastern layered intrusion, NW scotland," *Journal of Petrology*, vol. 58, no. 1, pp. 137–166, 2017.

[23] R. W. Bradshaw, A. J. R. Kent, and F. J. Tepley, "Chemical fingerprints and residence times of olivine in the 1959 Kilauea Iki eruption, Hawaii: insights into picrite formation," *American Mineralogist*, vol. 103, no. 11, pp. 1812–1826, 2018.

[24] C. Soulié, G. Libourel, and L. Tissandier, "Olivine dissolution in molten silicates: an experimental study with application to chondrule formation," *Meteoritics & Planetary Science*, vol. 52, no. 2, 2017.

[25] L.-L. Cheng, Y. Wang, J. S. Herrin, Z.-Y. Ren, and Z.-F. Yang, "Origin of K-feldspar megacrysts in rhyolites from the Emeishan large igneous province, southwest China," *Lithos*, vol. 294-295, pp. 397–411, 2017.

[26] M. Chen, H. Jing, X. Ma, H. Su, M. Du, and T. Zhu, "Fracture evolution characteristics of sandstone containing double fissures and a single circular hole under uniaxial compression," *International Journal of Mining Science and Technology*, vol. 27, no. 3, pp. 499–505, 2017.

[27] H. Xu, Y. Qin, G. Wang, C. Fan, M. Wu, and R. Wang, "Discrete element study on mesomechanical behavior of crack propagation in coal samples with two prefabricated fissures under biaxial compression," *Powder Technology*, vol. 375, pp. 42–59, 2020.

[28] B. Shen, T. Siren, and M. Rinne, "Modelling fracture propagation in anisotropic rock mass," *Rock Mechanics and Rock Engineering*, vol. 48, no. 3, 2015.

[29] W. Sun, A. Wu, K. Hou, Y. Yang, L. Liu, and Y. Wen, "Real-time observation of meso-fracture process in backfill body during mine subsidence using X-ray CT under uniaxial compressive conditions," *Construction and Building Materials*, vol. 113, pp. 153–162, 2016.

[30] J. Jin, P. Cao, Y. Chen, C. Pu, D. Mao, and X. Fan, "Influence of single flaw on the failure process and energy mechanics of rock-like material," *Computers and Geotechnics*, vol. 86, 2017.

[31] Y.-H. Huang, S.-Q. Yang, M. R. Hall, W.-L. Tian, and P.-F. Yin, "Experimental study on uniaxial mechanical properties and crack propagation in sandstone containing a single oval cavity," *Archives of Civil and Mechanical Engineering*, vol. 18, no. 4, 2018.

Research Article

Research on Carbonation Characteristics and Frost Resistance of Iron Tailings Powder Concrete under Low-Cement Clinker System

Ruidong Wu [ID],[1,2] **Juanhong Liu** [ID],[1,2] **Guangtian Zhang,**[1,2,3] **Yueyue Zhang,**[1,2] **and Shuhao An**[1,2]

[1]*College of Civil and Resource Engineering, University of Science and Technology Beijing, Beijing 100083, China*
[2]*Beijing Key Laboratory of Urban Underground Space Engineering, University of Science and Technology Beijing, Beijing 100083, China*
[3]*Hebei Academy of Building Research, Shijiazhuang 050021, China*

Correspondence should be addressed to Ruidong Wu; wrd0105@163.com and Juanhong Liu; liujuanhong66@126.com

The accelerated carbonation, natural carbonation, fast freeze-thaw test, and pore structure analysis of C30 and C50 concrete with different proportions of iron tailings powder and slag powder were tested, respectively. The results show that the accelerated carbonation depth and natural carbonation depth of concrete increase with the increase of iron tailings powder content. The prediction model of carbonation depth of iron tailings powder concrete is established by introducing the iron tailings content coefficient and strength influence coefficient. The error between the calculated value of the model and the test value of 28 d curing concrete natural carbonation depth is small, which proves that the model is completely feasible. When iron tailings powder accounts for 50% of mineral admixture, it is helpful to improve the frost resistance of concrete. According to the pore structure analysis, the introduction of iron tailings powder can optimize the pore structure, improve the porosity of harmless and less harmful pores, and thus improve the frost resistance.

1. Introduction

Tailings are one of the largest solid wastes in the world, which are widely distributed all over the world. Iron tailings are waste residue discharged from iron ore after beneficiation process, but there is still a lot of space for these solid wastes to be utilized [1, 2]. The comprehensive utilization rate of tailings is not high, which is limited by the development of beneficiation technology, the restriction of production equipment, and other scientific and technological factors, so the comprehensive utilization of tailings has become a worldwide problem [3–7]. A large number of tailings are piled up in the tailings pond and cannot be used, resulting in a large number of waste resources. The accumulation of these wastes also seriously affects the ecological environment and is a major source of pollution and danger. The consumption of concrete is increasing year by year with the continuous expansion of infrastructure construction. The large use of high-performance concrete results in the huge consumption of mineral admixture. In particular, the frequently used admixtures

such as fly ash and slag powder have been in short supply in some areas, which leads to the increase of raw material price and the destruction of market balance. For the sake of economy and environmental protection, it is a good strategy to use iron tailings powder as admixture of concrete, which can not only realize the reuse of iron tailings resources, but also alleviate the actual problem of concrete admixture shortage.

Carbonation and freeze-thaw damage of concrete are important reasons for durability deterioration of concrete [8–12]; the research on carbonation and freeze-thaw of iron tailings powder concrete is the necessary premise to ensure its extensive application. At present, domestic and foreign scholars have some research on the use of iron tailing powder as concrete admixture, mainly focusing on the mechanical properties of concrete [13–17]. There are few reports on the long-term carbonation and frost resistance of concrete mixed with iron tailings powder. It is an important premise for the application of iron tailings powder concrete in engineering practice to clarify the influence of iron

tailings powder on the long-term carbonation and freeze-thaw resistance of concrete. In this paper, the influence of the composite admixture of iron tailings powder and slag powder on the long-term carbonation and rapid freeze-thaw is studied. The long-term carbonation law and model of iron tailings powder concrete are established, and the mechanism of iron tailings powder on the concrete freeze-thaw is revealed, which provides a scientific theoretical basis for the extensive application of iron tailings concrete.

2. Experimental Materials and Methods

2.1. Raw Materials. The reference cement is used in this experiment, for eliminating experimental errors caused by uncertain components in ordinary cement. The main properties of reference cement are shown in Table 1.

The specific surface area of iron tailings powder is $450 \, m^2 \cdot kg^{-1}$, and water demand ratio is 90%, which contains some metal elements such as Cu, Fe, Zn, and so on. According to the method of fly ash, the activity index of iron tailings powder is only 64%. Table 2 shows the main chemical components of iron tailings powder.

The slag powder used is S95 grade, the specific surface area is $485 \, m^2 \cdot kg^{-1}$, the water demand ratio is 96.2%, and the density is $2.8 \, g \cdot cm^{-3}$. All indexes meet the national standards. The particle size distribution of iron tailings powder and slag powder is shown in Figure 1. The particle size of iron tailings powder is slightly coarser than that of slag powder.

The coarse aggregate is divided into big stones (particle size is 10–20 mm) and small stones (particle size is 5–10 mm), and the mass ratio of big stones and small stones is 8:2 in order to accumulate tightly. The fine aggregate is river sand meeting the requirements, and the mud content of river sand is 5.2%. The fineness modulus of river sand is 2.7, which belongs to medium sand with good gradation. The additive is polycarboxylic acid water reducer with 20% solid content produced by Sika company.

2.2. Mix Proportion. Two kinds of commonly used concrete (C30 and C50) are prepared in this paper. The proportion of cement in the mix proportion of C30 and C50 concrete is only 30% and 40%, respectively. This experiment is under low-cement clinker system for the consideration of environmental protection and economy. In order to study the influence of iron tailings powder the content on the performance of concrete, the proportion of iron tailings powder and slag powder is designed as 0:10, 3:7, 5:5, 7:3, and 10:0, respectively. After the preliminary concrete mixing, with the increase of the iron tailings powder content, the water binder ratio of concrete decreases accordingly to ensure that the strength can meet the requirements. Table 3 shows the concrete mix proportion.

2.3. Experimental Methods. Carbonation test is divided into accelerated carbonation and natural carbonation. Accelerated carbonation refers to the fact that the concrete blocks are in standard curing (temperature $20 \pm 2^{\circ}C$, relative humidity ≥95%) for 28 days after the concrete formwork is removed. After drying in an oven at $60^{\circ}C$ for 48 hours, the concrete blocks are put into the carbonation box. The CO_2 concentration of the carbonation box is controlled at (20 ± 3)%, temperature $(20 \pm 2)^{\circ}C$, and relative humidity (70 ± 5)%. There are two kinds of curing conditions for natural carbonization: standard curing for 1 day and standard curing for 28 days. The size of the test block is $100 \, mm \times 100 \, mm \times 100 \, mm$ cube. Split the test piece with a press, drop 1% phenolphthalein alcohol solution, and measure the depth of nondiscoloration from the edge, which is the carbonation depth.

After the concrete is cured under the standard curing condition (temperature $20 \pm 2^{\circ}C$, relative humidity ≥95%) for 24 days, soak the concrete in water (temperature $20 \pm 2^{\circ}C$) for 4 days, and put it into the fast freezing and thawing machine at 28 days. The size of concrete quick freezing and thawing test block is $100 \, mm \times 100 \, mm \times 400 \, mm$, and the size of compression strength test block after freezing and thawing is $100 \, mm \times 100 \, mm \times 100 \, mm$. After a certain number of freezing and thawing cycles, the quality, dynamic elastic modulus, and compression strength of the test piece are tested.

3. Results and Discussion

3.1. Compressive Strength of Concrete. According to the design mix proportion, the concrete test blocks are formed, and the slump of each group is between 200 and 230 mm, which has good workability. The compressive strength of C30 and C50 concrete for 3 d, 7 d, and 28 d is tested, respectively, as shown in Table 4.

Table 4 shows that the concrete strength decreases with the increase of iron tailings powder proportion. In C30 concrete, the 28 d compressive strength of A2 group with 70% slag powder in mineral admixtures is the highest and that of A5 group with iron tailings powder is the lowest, only 28.6 MPa, which cannot meet the C30 strength requirement. The strength of A2 and A3 groups is not much different from that of A1 group. Among C50 concrete, the strength of B1 group is the highest at 28 d and that of B5 group with iron tailings powder is the lowest, only 47.3 MPa, which cannot meet the strength requirements of C50. There is little difference between B2, B3, and B1 groups. Iron tailings powder belongs to inert mineral admixture and does not participate in hydration reaction, so a large amount of iron tailings powder is harmful to the concrete strength, but adding iron tailings powder properly can improve the particle grading and produce microaggregate effect to meet the strength requirements. From the strength point of view, the iron tailings powder should not be mixed alone under the low-cement clinker system. In terms of comprehensive economy and environmental protection, the most reasonable mix proportion is that the ratio of iron tailings powder and slag powder is 5:5.

3.2. Carbonation Depth of Concrete

3.2.1. Carbonation Depth of Iron Tailings Powder Concrete. The carbonation depth of C30 and C50 concrete placed in the carbonation box for 28 days is tested, respectively. The results are shown in Figure 2. The content of iron tailings

TABLE 1: Main properties of reference cement.

Setting time (min)		Compressive strength (MPa)		Flexural strength (MPa)		Standard consistency water consumption (%)	Fineness (mm)	Specific surface area (m²·kg⁻¹)	Soundness
Initial	Final	3 d	28 d	3 d	28 d				
155	215	28.3	53.2	5.5	10.3	27.2	0.5	347	Qualified

TABLE 2: Main chemical composition of iron tailings powder.

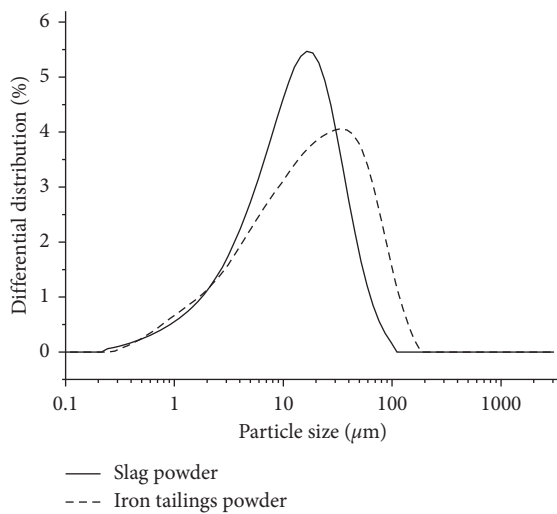| Chemical composition	SiO_2	Fe_2O_3	Al_2O_3	CaO	MgO	CuO	ZnO
Mass fraction (%)	67.59	10.88	4.57	4.02	1.18	0.23	0.11

FIGURE 1: Particle size distribution of iron tailings powder and slag powder.

powder is the mass percentage of iron tailings in the total mineral admixture.

It can be seen from Figure 1 that the accelerated carbonation depth of concrete decreases with the increase of strength, and the carbonation depth of C50 concrete is far less than that of C30 concrete. In the same strength grade, the carbonation depth increases with the increase of the content of iron tailings powder. The carbonation depth of groups A1 and B1 with single slag powder is the smallest, and the difference of carbonation depth between the group with iron tailings powder accounting for less than 50% of mineral admixture and the group with single slag powder is small. The carbonation depth of A5 and B5 groups with single iron tailings powder is the largest, which is 285% and 318% of that of single slag powder group.

There are two curing conditions for the natural carbonation of concrete, the concrete is placed in the natural environment after curing for 1 d and 28 d, and the carbonation depth at different ages is tested, as shown in Table 5.

The effect of curing conditions on the carbonation depth of concrete is very significant. The long-term carbonation depth of concrete placed directly in the natural environment after 1 d curing is far greater than that after 28 d standard curing. The activity of iron tailings is low, and the early hydration products mainly come from the hydration of cement and slag. With the introduction of nonactive admixture, the hydration products are less, and the structure is loose, resulting in a large amount of CO_2 entering into the concrete, causing carbonation. Therefore, the necessary maintenance is very important for the concrete with non-active mineral admixture under the low-cement clinker system. The natural carbonation of concrete also shows the rule that the carbonation depth increases with the increase of the content of iron tailings powder. The results show that the carbonation depth of A1 and B1 group with slag powder is the smallest and that of A5 and B5 group with iron tailings powder is the largest. The natural carbonation depth of 1080 days after 1d curing reaches 190% and 279% of A1 and B1 groups.

Based on the natural carbonation and accelerated carbonation of concrete, the iron tailings powder has a great influence on the carbonation depth. Compared with high-activity slag powder, the hydration products of iron tailings powder concrete are less, and the microcompactness of concrete will decrease with the increase of iron tailings powder content. The hydration products in the concrete are less, which leads to structural looseness, and more carbon dioxide is easy to enter into the concrete, resulting in the increase of carbonation depth. The amount of iron tailings powder should not exceed 70% of the total mineral admixture amount; otherwise, it is very unfavorable to the carbonation resistance of concrete. The adverse effect of iron tailings powder on the carbonation resistance of high strength concrete (C50) is greater than that of low-strength concrete (C30). Therefore, the amount of iron tailings powder in high-strength concrete should be appropriately reduced.

3.2.2. Carbonation Model of Iron Tailings Powder Concrete. From the experimental results, the proportion of iron tailings powder in mineral admixture and concrete strength are two important factors affecting the carbonation depth of iron tailings powder concrete. Referring to the durability evaluation standard of concrete structure [18] and the research of some scholars [19, 20], the coefficient of iron tailings content and strength influence coefficient are introduced, and the carbonation depth model is proposed:

TABLE 3: Concrete mix proportion (kg·m^{-3}).

	Group	Cement	Slag powder	Iron tailings powder	Stone	Sand	Water	W/B	PC
C30	A1	113	264	0	1018	840	151	0.40	3.39
	A2	113	185	79	1018	840	147	0.39	3.39
	A3	113	132	132	1018	840	143	0.38	3.39
	A4	113	79	185	1018	840	140	0.37	3.39
	A5	113	0	264	1018	840	136	0.36	3.39
C50	B1	191	287	0	1071	725	139	0.29	6.69
	B2	191	201	86	1071	725	134	0.28	6.69
	B3	191	143.5	143.5	1071	725	129	0.27	6.69
	B4	191	86	201	1071	725	124	0.26	6.69
	B5	191	0	287	1071	725	119	0.25	6.69

TABLE 4: Compressive strength of C30 and C50 concrete (MPa).

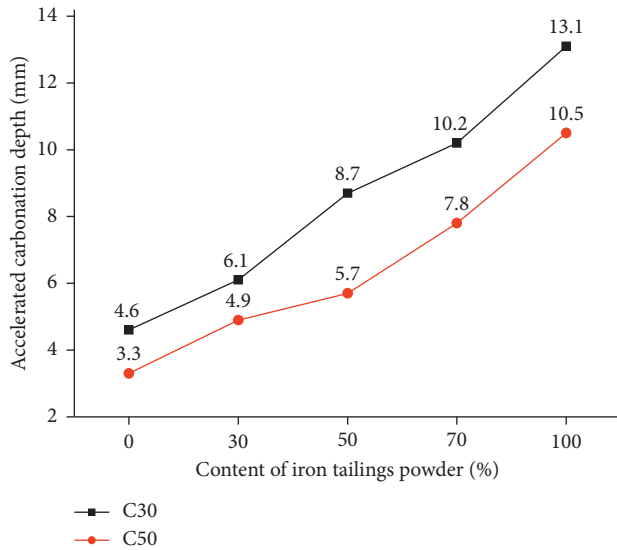|	3 d	7 d	28 d		3 d	7 d	28 d
A1	14.4	28.7	35.5	B1	24.9	50.2	71.4
A2	11.3	26.8	36.3	B2	22.1	48.7	64.4
A3	9.6	23.9	34.8	B3	19.8	44.9	64.1
A4	6.9	19.1	32.9	B4	15.7	34.5	53.8
A5	4.2	17.4	28.6	B5	8.1	29.9	47.3

FIGURE 2: 28 d accelerated carbonization depth of concrete.

$$X(t) = 3K_{CO_2} \cdot K_1 \cdot K_2 \cdot K_3 \cdot K_T \cdot K_E \cdot K_F \sqrt{t},$$

$$K_{CO_2} = \sqrt{\frac{C_0}{0.03}}, \quad (1)$$

$$K_E = T^{1/4} RH^{1.5} (1 - RH),$$

where $X(t)$ represents the carbonation depth of t age, mm. K_{CO_2} represents the influence coefficient of CO_2 concentration. C_0 is CO_2 concentration, %. K_1 is the influence factor of location, taking 1.0. K_2 is the influence coefficient of curing and pouring, taking 1.2. K_3 is the influence coefficient of working stress, taking 1.0. K_E is the influence coefficient of

environment. t is the ambient temperature, °C. RH is the relative humidity, %. K_T and K_F represent the content coefficient and strength influence coefficient of iron tailings, respectively.

K_T and K_F in formula (1) can be fitted according to the test results of 28 d accelerated carbonization. Firstly, based on the carbonation depth of group A1 and B1 with single slag powder, and the ratio of the carbonation depth of concrete with iron tailings powder different amount and that of concrete with single slag powder as the relative carbonation depth, the relationship between the amount of iron tailings powder and the relative carbonation depth is established, so that K_T is determined. Then, K_F is calculated according to the experiment data, and the relationship between K_F and concrete compressive strength is established.

Figure 3 shows the relationship between the content of iron tailings powder and the relative carbonation depth. Through data fitting, the relationship between the iron tailings content influence coefficient K_T on carbonation and the iron tailings proportion α in mineral admixture is as follows:

$$K_T = 0.775\alpha^2 + 1.27\alpha + 0.987. \quad (2)$$

After the iron tailings content coefficient K_T was determined, K_F is calculated according to the experimental value of carbonation depth, and then the relationship between the strength influence coefficient and the average 28 d compressive strength of concrete is established. According to Figure 4, K_F can be calculated by the compressive strength f_{cu}, and the formula is

$$K_F = \frac{7.931}{f_{cu}} + 0.226. \quad (3)$$

Due to the retention of significant figures, the fitting correlation shown in Figure 3 seems to be small, but its correlation coefficient is 0.889, and the true correlation is much larger than that shown in the figure. By substituting formulae (2) and (3) into formula (1), the carbonation model of iron tailings powder concrete is obtained. Combined with the average temperature and average relative humidity of Beijing in three years and the CO_2 concentration under the natural carbonization test conditions, the carbonization depth of different ages is calculated according to the

TABLE 5: Natural carbonization depth of concrete (mm).

Group	Carbonation depth after 1 d curing						Carbonation depth after 28d curing					
	28 d	90 d	180 d	360 d	720 d	1080 d	28 d	90 d	180 d	360 d	720 d	1080 d
A1	2.4	3.1	3.9	6.0	9.8	11.9	0	0.1	0.4	0.8	1.1	1.4
A2	2.5	3.6	5.1	7.4	12.2	13.6	0	0.2	0.8	1.1	1.6	1.9
A3	3.0	4.7	5.4	7.5	12.6	14.8	0.1	0.3	1.0	1.2	1.8	2.4
A4	4.5	6	6.6	9.1	14.8	17.1	0.3	0.5	1.2	1.5	2.5	2.9
A5	6.1	8.6	9.3	11.9	18.6	22.5	0.4	0.8	1.4	2.4	3.6	4.1
B1	1.1	1.9	2.2	3.5	5.6	6.8	0	0	0	0.3	0.8	0.9
B2	1.8	3.0	3.9	5.2	8.8	10.7	0	0	0.3	0.8	1.4	1.6
B3	2.6	3.5	4.2	5.5	10.1	12.6	0	0.1	0.5	0.9	1.6	1.8
B4	2.8	3.8	4.8	7.8	12.7	15.5	0	0.2	1.0	1.5	2.1	2.4
B5	3.3	5.4	6.5	9.4	15.6	18.8	0.2	0.6	1.1	2.1	2.9	3.3
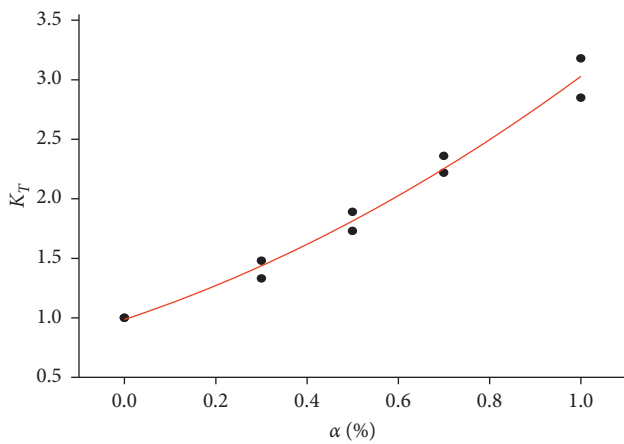
FIGURE 3: K_T-α relationship.
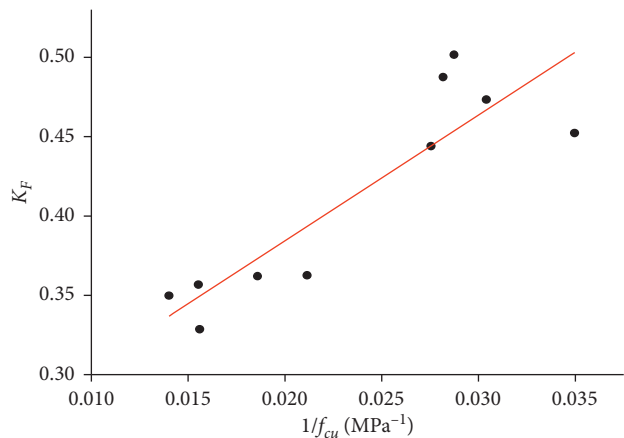
FIGURE 4: K_F-f_{cu} relationship.

carbonization model, and compared with the long-term depth of the natural carbonation experiment after 28 days of standard maintenance. The results are shown in Table 6.

Through the comparison between the calculated value of the model and the measured value of the experiment, the error between them is small. Through the verification of long-term natural carbonation experiment, the established carbonation depth model has high reliability, which can effectively predict the carbonation depth of iron tailings fine powder concrete for a long time. The prediction model is suitable for the prediction of long-term carbonation depth of concrete with iron tailings powder and slag powder as compound admixture in low-cement clinker system.

3.2.3. Natural Carbonation Depth Law of Concrete after 1 d Curing. There are great differences in the curing conditions in the actual project, so it is necessary to study the long-term carbonation law of concrete with poor curing conditions. Figure 5 shows the development of natural carbonation depth of C30 and C50 concrete with age after 1 d standard curing. The content of iron tailing powder has great influence on natural carbonation. The larger the content of iron tailing powder is, the greater the carbonation depth is. The influence of iron tailing powder content on the carbonation depth of C50 concrete is greater than that of C30 concrete. In order to better explore the long-term development law of natural carbonation of iron tailing fine powder concrete, the equation of carbonation depth of each group of concrete with time is fitted with the test data, as shown in Table 7.

From the fitting results, the long-term carbonation depth of concrete meets the equation $X = at^b$. In the equation, the coefficient "a" increases with the increase of the iron tailing powder content, while the coefficient "a" and coefficient "b" of C50 concrete mixed with slag powder and iron tailing powder have little difference. The equation coefficient "a" of single mineral powder or iron tailing powder is quite different, but the coefficient "b" of C50 five groups equations is between 0.54 and 0.59, which has a good correlation. The coefficient "b"of C30 concrete is between 0.42 and 0.57, and the difference of coefficient "a" is large, which shows the law of increasing with the increase of the iron tailings powder content. The "b"value of the equation is higher than that of the normal cement system. The reason may be that in the low-cement clinker system, the cement consumption only accounts for 30% of the cementitious materials, so a large number of inactive admixtures makes the "b"value higher than that of the cement system. The law of long-term concrete natural carbonation after 1 d curing can be explored by using the fitting equation, which lays a theoretical foundation for engineering applications of iron tailing powder in concrete.

TABLE 6: Comparison between calculated value of carbonization model and natural carbonation experiment value (mm).

| Group	360 d carbonization depth		720 d carbonization depth		1080 d carbonization depth	
	Calculated	Experiment	Calculated	Experiment	Calculated	Experiment
A1	0.8	0.69	1.1	0.97	1.4	1.19
A2	1.1	0.99	1.6	1.40	1.9	1.72
A3	1.2	1.28	1.8	1.81	2.4	2.21
A4	1.5	1.63	2.5	2.31	2.9	2.83
A5	2.4	2.37	3.6	3.35	4.1	4.10
B1	0.3	0.52	0.8	0.73	0.9	0.90
B2	0.8	0.78	1.4	1.10	1.6	1.35
B3	0.9	0.98	1.6	1.39	1.8	1.71
B4	1.5	1.31	2.1	1.85	2.4	2.26
B5	2.1	1.85	2.9	2.62	3.3	3.21
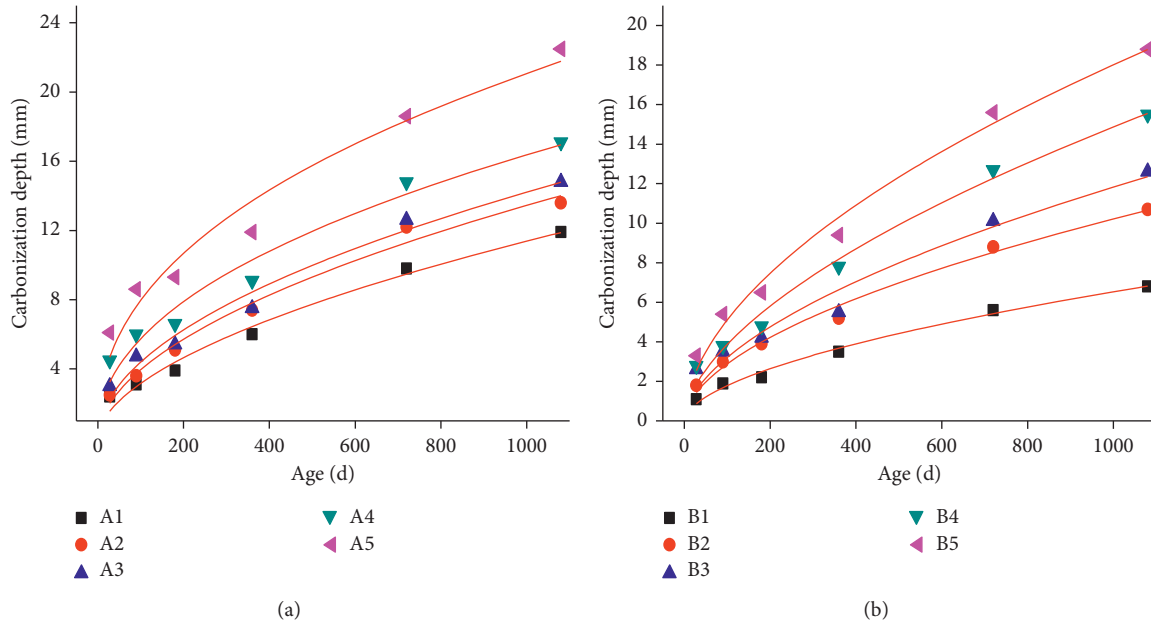
FIGURE 5: Natural carbonation depth of iron tailings powder concrete after 1 d curing. (a) C30. (b) C50.

TABLE 7: Time-carbonation depth fitting equation for iron tailings concrete.

Group	Equation	Group	Equation
A1	$X = 0.243t^{0.556}$	B1	$X = 0.134t^{0.562}$
A2	$X = 0.341t^{0.532}$	B2	$X = 0.231t^{0.548}$
A3	$X = 0.418t^{0.510}$	B3	$X = 0.238t^{0.566}$
A4	$X = 0.712t^{0.453}$	B4	$X = 0.263t^{0.584}$
A5	$X = 1.148t^{0.421}$	B5	$X = 0.412t^{0.547}$

3.3. Frost Resistance of Iron Tailings Powder Concrete

3.3.1. Fast Freeze-Thaw Test of Concrete. When the concrete is damaged by freeze-thaw, its most remarkable feature is that the concrete surface will produce erosion phenomenon, so the quality of concrete will be lost. The mass loss rate of concrete shall be calculated according to the following formula:

$$\Delta W_n = \frac{W_0 - W_n}{W_0} \times 100\%, \tag{4}$$

where W_0 represents the quality of concrete before rapid freeze-thaw, W_n represents the quality of concrete after fast freeze-thaw n cycle, and ΔW_n represents the mass loss rate of concrete after fast freeze-thaw n cycle.

With the increase of freeze-thaw cycles, the cement paste on the concrete surface began to fall off and the aggregate gradually exposed. This phenomenon mainly occurred at the end of the concrete specimen. The surface erosion of concrete groups A5 and B5 mixed with iron tailing powder was the most serious. The quality of each group concrete decreases with the increase of freeze-thaw cycles. The mass loss of C30 and C50 concrete along with the freeze-thaw times is shown in Table 8.

Proper addition of iron tailing powder can reduce the mass loss rate of concrete after rapid freeze-thaw. In C30 and C50 concrete, the mass loss rate of concrete is less than 5% before the cycle of freeze-thaw damage. Group A5 and group B5 with single iron tailings powder have the largest mass loss rate and the worst frost resistance. The reason is that the iron tailing powder is a kind of inactive mineral admixture, which

Table 8: Mass loss rate of iron tailings powder concrete in different freeze-thaw cycles.

Cycle index	50	100	150	200	250	300	350
A1	0.5%	2.1%	**4.4%**				
A2	0.6%	2.2%	**4.1%**				
A3	0.1%	0.7%	1.4%	**1.8%**			
A4	0.4%	1.1%	1.7%	**2.3%**			
A5	1.1%	**4.5%**					
B1	0.3%	1.1%	1.5%	2.8%	**4.5%**		
B2	0.2%	0.8%	1.3%	1.9%	2.7%	**4.1%**	
B3	0.1%	0.4%	0.9%	1.2%	1.9%	3.2%	**3.5%**
B4	0.1%	0.8%	1.1%	1.6%	2.6%	**3.8%**	
B5	1.0%	1.8%	2.5%	**4.2%**			

does not participate in the hydration reaction at the age of 28 days, and there are less cementitious substances in the hydration products of concrete. After the freeze-thaw cycle, a large amount of iron tailing powder will fall off at the edge of the test piece, resulting in a large loss of quality. In C30 concrete, when the ratio of iron tailings powder and slag powder is 5:5, 7:3, the mass loss of concrete is lower than that of single slag powder, and when the ratio of iron tailings powder and slag powder is 3:7, the mass loss of pure slag powder is closer. In C50 concrete, when the ratio of iron tailings powder and slag powder is 3:7, 5:5, and 7:3, the mass loss of the same freeze-thaw cycle times is lower than that of B1 group. For example, after 250 freeze-thaw cycles, the mass loss of group B1 concrete mixed with slag powder is 4.5%. The concrete shows obvious erosion phenomenon, and the aggregate is exposed. The mass loss rate of group B3 concrete with the ratio 5:5 of iron tailings powder and slag powder is only 1.9%, which is far lower than that of group B1. The concrete shows that there is no obvious shedding phenomenon, as shown in Figure 6. The results show that the quality loss of concrete after rapid freeze-thaw can be reduced by adding iron tailing powder properly. When the proportion of iron tailing powder and slag powder is 5:5, the quality loss of concrete is the smallest and the frost resistance is the best.

Another important index of concrete freeze-thaw cycle is the relative dynamic elastic modulus of concrete. The dynamic elastic modulus of concrete with different amounts of iron tailing powder after different freeze-thaw cycles is tested, respectively. Compared with the initial dynamic elastic modulus, the relative dynamic elastic modulus is calculated. When the relative dynamic elastic modulus drops below 60% of the initial modulus, the test is terminated. Table 9 shows the residual dynamic elastic modulus of concrete with different freeze-thaw cycles.

Appropriate addition of iron tailings powder is helpful to improve the residual relative dynamic elasticity modulus of the concrete after rapid freeze-thaw cycles. The influence of freeze-thaw cycles on the relative dynamic elasticity modulus is greater than the mass loss in the iron tailings powder concrete. The residual relative dynamic elasticity modulus of A5 and B5 groups with single iron tailings powder mixed is the smallest, and the ability to resist freeze-thaw damage is the worst. In C30 and C50 concrete, when the ratio of iron

tailings powder and slag powder is 3:7, 5:5, and 7:3, the residual relative dynamic elasticity modulus of concrete is much larger than that of single slag powder group. For example, in C50 concrete, after 250 cycles of rapid freeze-thaw, the residual relative dynamic elasticity modulus of B1 group concrete mixed with slag powder is 53.6%, and the concrete has been damaged by freeze-thaw. The mass loss rate of B3 group is 67.1% when the ratio of iron tailings powder to slag powder is 5:5, which is much higher than that of B1 group. The results show that the residual relative dynamic elasticity modulus of concrete can be increased by adding iron tailings powder properly. When the proportion of iron tailings powder and slag powder is 5:5, the relative dynamic elasticity modulus of concrete decreases the least and the frost resistance is the best.

According to GBT 50082-2009 standard for test method of long-term performance and durability of ordinary concrete, if the mass loss of concrete is more than 5% or the residual dynamic elasticity modulus is less than 60%, it can be regarded as the failure state of concrete during rapid freezing and thawing. The frost resistance of C30 and C50 concrete mixed with single slag powder is F100 and F200, while that of C30 and C50 concrete mixed with single iron tailings powder is the worst, only F50 and F150. When the ratio of tailings powder and slag powder is 5:5, the frost resistance of concrete is the best: C30 concrete reaches F150, and C50 concrete reaches F300; adding iron tailings powder properly is beneficial to improve the frost resistance of concrete.

3.3.2. Compressive Strength of Concrete after Fast Freeze-Thaw. In order to explore the influence of fast freeze-thaw on the compressive strength of concrete, the concrete specimen with the size of $100\,mm \times 100\,mm \times 100\,mm$ was put into the fast freeze-thaw test machine. After a certain number of freeze-thaw cycles, take the test piece out of the freeze-thaw box and test the compressive strength of the concrete, as shown in Table 10.

The compressive strength of concrete decreases with the increase of freeze-thaw cycles. The compressive strength of concrete mixed with slag powder is the highest before freeze-thaw cycles, but the compressive strength of concrete mixed with slag powder decreases rapidly after freeze-thaw cycles. In C30 concrete, the compressive strength of A1 group concrete is lower than that of A2, A3, and A4 group after 50 freeze-thaw cycles. In C50 concrete, the compressive strength of B1 concrete is lower than that of B2 and B3 concrete after 150 freeze-thaw cycles. This shows that the proper addition of iron tailings powder can not only improve the frost resistance of concrete, but also improve the bearing capacity of concrete after freeze-thaw.

Based on the compressive strength before freeze-thaw, the loss rate of compressive strength after the specified freeze-thaw times and before freeze-thaw is calculated, and the influence of iron tailing powder on the loss rate of concrete freeze-thaw strength is studied, as shown in Figure 7.
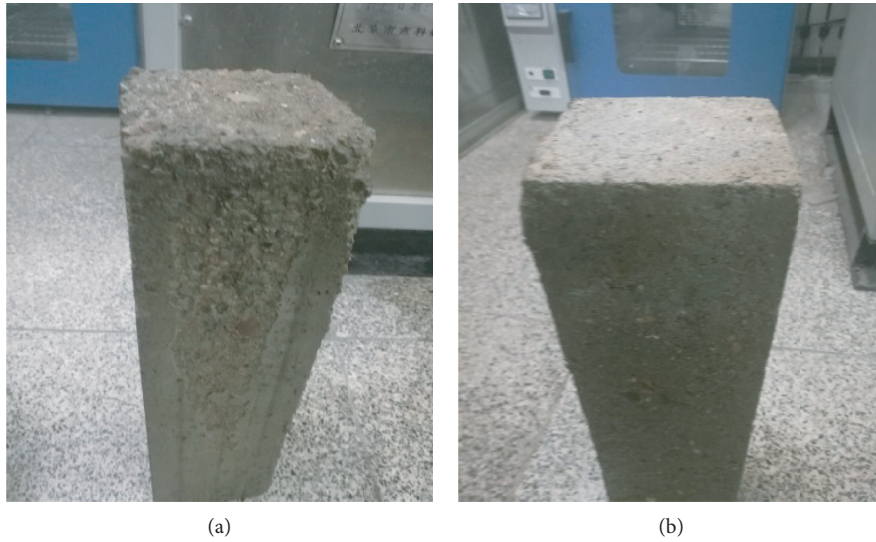
(a)

(b)

FIGURE 6: Appearance of C50 concrete after 250 freeze-thaw cycles. (a) B1. (b) B3.

TABLE 9: Residual dynamic elastic modulus of concrete with different freeze-thaw cycles.

Cycle index	50	100	150	200	250	300	350
A1	85.4%	66.1%	**55.2%**				
A2	86.5%	70.5%	**58.4%**				
A3	88.2%	75.4%	62.2%	**57.7%**			
A4	88%	73.7%	66.1%	**58.9%**			
A5	77.2%	**58.0%**					
B1	93.2%	86.1%	73.2%	64.7%	**53.6%**		
B2	94.3%	87.2%	76.8%	69.1%	63.7%	**55.8%**	
B3	96.8%	90.5%	82.9%	72.2%	67.1%	64.3%	**57.5%**
B4	95.4%	89.1%	79.5%	71.3%	64.5%	**58.1%**	
B5	90.4%	84.5%	70.3%	**59.3%**			

TABLE 10: Compressive strength of concrete after different freeze-thaw cycles.

Group	0	50	100	150	200	250	300	350
A1	35.5	32.3	26.5	24.8				
A2	36.3	34.8	31.1	28.1				
A3	34.8	32.7	31.5	29.6	27.4			
A4	32.9	30.5	29.6	27.5	24.1			
A5	28.6	24.3	20.9					
B1	71.4	68.8	64.1	59.3	54.1	50.8		
B2	64.4	61.5	59.3	57.5	55.9	54.3	51.5	
B3	64.1	63.9	62.5	61.1	59.3	56.5	55.0	51.9
B4	53.8	51.5	49.1	47.6	44.4	42.9	41.2	
B5	47.3	43.4	37.6	33.1	29.5			

From the view of strength loss rate, the loss rate of strength concrete mixed with iron tailings powder is the largest with the increase of freeze-thaw cycles. The compressive strength of concrete mixed with slag powder is higher before freeze-thaw cycle, but the strength loss rate with freeze-thaw failure is also higher. The strength loss rate

of the concrete with 30%, 50%, and 70% iron tailings powder is less than that of concrete with slag powder alone. The strength loss rate of C30 and C50 concrete after freeze-thaw cycle is almost the same. When the concrete is only mixed with slag powder, the strength loss rate is about 30%, while the concrete with slag powder and iron tailings powder ratio of 5:5 is only about 20%. When the ratio of iron tailings powder and slag powder is 5:5, the concrete has the highest freeze-thaw resistance and the lowest strength loss rate.

3.3.3. Pore Structure Analysis of Iron Tailings Powder Concrete before and after Freezing and Thawing. In order to explore the mechanism of iron tailings powder to improve the frost resistance, the pore structure distribution in concrete was tested by NMR, and the total porosity and different pore size distribution were analyzed. The nuclear magnetic resonance was measured by the MesoMR23-060H-type nuclear magnetic resonance tester with the resonance frequency of 23 MHz. Firstly, the concrete samples were saturated with water for more than 24 hours in vacuum; then the samples were taken out, and the porosity and pore size distribution of the concrete samples were measured by ^{1}H NMR analysis. The porosity before freeze-thaw and the porosity after freeze-thaw failure of each group of concrete were tested, respectively; that is, after 150 freeze-thaw cycles for groups A1 and A2, 200 freeze-thaw cycles for groups A3 and A4, 100 freeze-thaw cycles for group A5, 250 freeze-thaw cycles for group B1, 300 freeze-thaw cycles for groups B2 and B4, 350 freeze-thaw cycles for group B3, and 200 freeze-thaw cycles for group B5. There are four types of holes in concrete. The holes with the aperture less than 0.02 μm are harmless holes, the holes with the aperture of 0.02-0.1 μm are less harmful holes, the holes with the aperture of 0.1–0.2 μm are harmful holes, and the holes with the aperture greater than 0.2 μm are multiharmful holes. The porosity of harmless holes, less harmful holes, harmful holes, and more harmful holes in different groups of concrete is calculated by
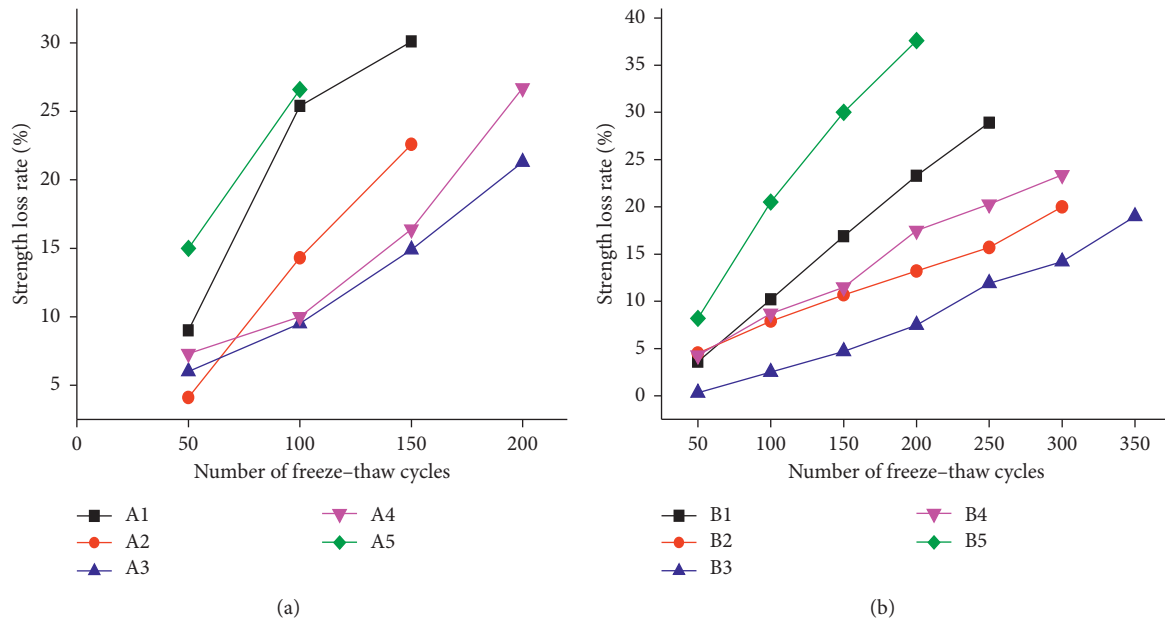
(a)

(b)

FIGURE 7: Strength loss rate of concrete after different freeze-thaw cycles. (a) C30. (b) C50.

using the NMR pore size distribution curve of each group of concrete, as shown in Table 11.

From the analysis of pore size results, after freeze-thaw damage, the proportion of harmless holes and less harmful holes decreased sharply, and the number of harmful holes and more harmful holes increased significantly, resulting in the decline of concrete quality, relative dynamic elastic modulus, and compressive strength. The freeze-thaw damage of concrete is caused by the water in the internal pores forming ice, causing volume expansion and damage. When the water in the pore freezes, the ice pressure and water migration pressure increase continuously. When the pressure exceeds the tensile strength of the concrete, the internal damage of the concrete occurs. With the continuous development of pore volume expansion and the increase of pore diameter, the ratio of harmless pore and less harmful pore space decreases sharply after freeze-thaw damage, and the number of more harmful pores above $0.2\,\mu m$ increases. This kind of damage is from the surface to the inside. The pore water is frozen layer by layer, which causes the surface concrete to peel off and the quality loss. The continuous development of pores causes the internal structure damage of concrete, which affects the dynamic elastic modulus and compressive strength of concrete. The internal expansion stress of concrete is increasing and the internal cracks are expanding continuously, which leads to the decrease of concrete bearing capacity. The macroscopic reaction is that the compressive strength of concrete decreases with the increase of freeze-thaw cycles.

Proper addition of iron tailings powder can increase the harmless pore under $0.02\,\mu m$ in concrete. The frost resistance of concrete is directly related to the porosity of harmless holes and multiple harmful holes before freezing and thawing, that is, the more harmless holes, the less harmful holes, the stronger the frost resistance of concrete.

The freezing point of capillary water is related to the pore size. The smaller the pore size is, the lower the freezing point of water is. The introduction of innocuous holes can play a good buffer role in the freezing expansion of water in the pores, thus reducing the expansion pressure and slowing down the damage of the internal structure of the concrete. With the increase of harmless and less harmful holes in concrete, the expansion stress in freeze-thaw process is significantly reduced, and the crack development speed is slow, which can alleviate the damage rate and degree of concrete quality, dynamic elastic modulus, and compressive strength with freeze-thaw cycle. Although the total porosity of group A3 and B3 is slightly higher than that of groups A1 and B1, the porosity of less harmful holes is significantly increased, which effectively improves the internal pore structure of concrete, thus increasing the frost resistance of concrete. For example, the total porosity of group A1 concrete before freezing and thawing is 15.47%, the porosity of harmless holes less than $0.02\,\mu m$ is 13.68%, and the porosity of multiple harmful holes greater than $0.2\,\mu m$ is 0.57%. However, the total porosity of group A3 is 16.03%, which is slightly higher than that of group A1. The harmless porosity is 15.24%, which is higher than that of group A1, and the multiple harmful porosity is only 0.10%, which was lower than that of group A1. This is also the reason that the frost resistance and strength of group A3 is better than that of group A1. The number of harmless holes and less harmful holes determines the freeze-thaw resistance of concrete. Groups A3 and B3 with the ratio of iron tailings powder to slag powder of 5:5 have the highest porosity of less harmful holes and harmless holes below $0.1\,\mu m$, so their frost resistance is the best.

The frost resistance of concrete with single iron tailing powder is the worst, because the addition of nonactive iron tailing powder increases the porosity of concrete, and the

TABLE 11: Porosity of concrete (%).

	Total porosity		$< 0.02\,\mu m$		0.02–$0.1\,\mu m$		0.1–$0.2\,\mu m$		$> 0.2\,\mu m$	
	Before	After	Before	After	Before	After	Before	After	Before	After
A1	15.47	22.40	13. 68	2.49	1.09	1.40	0.13	3.77	0.57	14.74
A3	16.03	22.98	15.24	4.53	0.43	1.98	0.26	2.42	0.10	14.05
A5	17.83	27.08	15.11	2.85	1.11	2.70	0.39	4.42	1.22	17.11
B1	7.12	13.16	6.64	1.35	0.21	0.29	0.11	1.49	0.16	10.03
B3	7.59	11.09	6.83	1.58	0.58	0.70	0.09	0.31	0.09	8.50
B5	9.61	15.63	7.90	2.11	0.54	0.89	0.26	1.28	0.91	11.35

number of harmful holes and multiple harmful holes is greatly increased compared with other concrete, especially the increase of multiple harmful holes is several times. In the case of small increase of harmless holes, a large number of multiple harmful holes accelerate the freezing failure rate of concrete. After freeze-thaw, the number of large holes larger than $0.2\,\mu m$ determines the compressive strength of concrete after freeze-thaw damage. It is explained that the compressive strength of A3 and B3 has the smallest loss rate with freeze-thaw damage, and A5 and B5 strength loss rate with single iron tailings powder is the largest.

4. Conclusions

(1) The concrete strength decreases with the increase of iron tailings powder content, and the carbonation depth increases with the increase of iron tailings powder content. The strength and carbonation resistance of concrete with single iron tailing powder are poor, so the iron tailings powder should not be used alone.

(2) The prediction model of carbonation of iron tailings concrete is established by using the proportion of iron tailings powder in mineral admixture and 28 d compressive strength. The error between the calculated value and the test value of 360 d, 720 d, and 1080 d concrete carbonation depth is small, and the model is completely feasible, which can predict the long-term carbonation depth.

(3) Adding a certain amount of iron tailings powder can improve the frost resistance. When the ratio of iron tailing powder to slag powder is 5:5, the frost resistance of concrete is the best, C30 concrete reaches F150, C50 concrete reaches F300, and the residual compressive strength of concrete after freeze-thaw cycle is effectively improved.

(4) The mechanism of improving the concrete frost resistance by adding appropriate amount of iron tailings powder is to improve the pore structure characteristics, increase the number of harmless holes and less harmful holes, and reduce the number of more harmful holes and harmful holes, so as to improve the frost resistance of concrete.

Data Availability

The data used to support the findings of this study are included within the article. The data used to support the findings of this study are also available from the corresponding author upon request.

Conflicts of Interest

The authors declare that there are no conflicts of interest regarding the publication of this paper.

Authors' Contributions

Juanhong Liu and Ruidong Wu conceived and designed the experiments; Ruidong Wu, Guangtian Zhang, and Yueyue Zhang performed the experiments; Shuhao An contributed materials; and Ruidong Wu and Juanhong Liu wrote the paper. All authors read and approved the manuscript.

Acknowledgments

References

[1] X. Chen, X. Jin, H. Jiao, Y. Yang, and J. Liu, "Pore connectivity and dewatering mechanism of tailings bed in raking deep-cone thickener process," *Minerals*, vol. 10, no. 4, p. 375, 2020.

[2] R. D. Wu and J. H. Liu, "Experimental study on the concrete with compound admixture of iron tailings and slag powder under low cement clinker system," *Advances in Materials Science and Engineering*, vol. 2018, Article ID 9816923, 7 pages, 2018.

[3] W. Zhao, C. L. Huo, M. Z. Liu, and H. M. Yang, "Research progress on the comprehensive utilization of non-ferrous metal mine tailings," *China Resources Comprehensive Utilization*, vol. 29, pp. 24–28, 2011.

[4] Y. Sun, H. Wang, L. Liu, and X. Wang, "Solid wastes utilization in the iron and steel industry in China: towards sustainability," *Mineral Processing & Extractive Metallurgy*, vol. 126, no. 1-2, pp. 41–46, 2017.

[5] L. Luo, Y. Zhang, S. Bao, and T. Chen, "Utilization of iron ore tailings as raw material for portland cement clinker production," *Advances in Materials Science and Engineering*, vol. 2016, Article ID 1596047, 6 pages, 2016.

[6] Z.-x. Tian, Z.-h. Zhao, C.-q. Dai, and S.-j. Liu, "Experimental study on the properties of concrete mixed with iron ore tailings," *Advances in Materials Science and Engineering*, vol. 2016, Article ID 8606505, 9 pages, 2016.

[7] Z. Zhu, B. Li, and M. Zhou, "The influences of iron ore tailings as fine aggregate on the strength of ultra-high performance concrete," *Advances in Materials Science and Engineering*, vol. 2015, Article ID 412878, 6 pages, 2015.

[8] M. Guiglia and M. Taliano, "Comparison of carbonation depths measured on in-field exposed existing r.c. structures with predictions made using *fib*-model code 2010," *Cement and Concrete Composites*, vol. 38, no. 2, pp. 92–108, 2013.

[9] J. Geng and J. Sun, "Characteristics of the carbonation resistance of recycled fine aggregate concrete," *Construction and Building Materials*, vol. 49, no. 1, pp. 814–820, 2013.

[10] J. Tang, J. Wu, Z. Zou, A. Yue, and A. Mueller, "Influence of axial loading and carbonation age on the carbonation resistance of recycled aggregate concrete," *Construction and Building Materials*, vol. 173, pp. 707–717, 2018.

[11] L. Shen, Q. Li, W. Ge, and S. Xu, "The mechanical property and frost resistance of roller compacted concrete by mixing silica fume and limestone powder: experimental study," *Construction and Building Materials*, vol. 239, p. 117882, 2020.

[12] Y. Yuan, R. Zhao, R. Li et al., "Frost resistance of fiber-reinforced blended slag and class F fly ash-based geopolymer concrete under the coupling effect of freeze-thaw cycling and axial compressive loading," *Construction and Building Materials*, vol. 250, p. 118831, 2020.

[13] X. Y. Ma, A. L. Wang, and X. Yang, "Study on the influence of iron tailings powder compound admixture on concrete performance," *China Concrete*, vol. 7, pp. 90–95, 2013.

[14] B. G. Oladeji and S. C. Aduloju, "Investigation of compressive strength of concrete from cement and iron-ore tailings mixture," *Scholars Journal of Engineering and Technology*, vol. 3, pp. 560–562, 2015.

[15] A. L. Wang, X. Y. Ma, and X. Yang, "Study on activity of iron tailings powder as concrete admixture," *China Concrete*, vol. 8, pp. 66–69, 2013.

[16] X. Y. Zhang, Q. Song, H. Li, and X. D. Fan, "Effect of iron tailings powder on properties of C40 concrete," *Bulletin of the Chinese Ceramic Society*, vol. 32, no. 12, pp. 2559–2563, 2013.

[17] Y. F. Hou and S. R. Zhao, "Effect of iron tailings powder on concrete properties," *Fly Ash Comprehensive Utilization*, vol. 3, pp. 17–24, 2015.

[18] China Engineering Construction Standardization Association, "Standard for durability assessment of concrete structures," China Construction Industry Press, Beijing, China, CECS 220-2007, 2007.

[19] J. C. Wang, J. H. Zhou, X. D. Wang, and C. Z. Mei, "Experimental study of the carbonation depth prediction model for waste fiber recycled concrete," *Industrial Construction*, vol. 48, no. 3, pp. 17–20+5, 2018.

[20] D. T. Niu, C. H. Li, and H. Song, "A model for predicting carbonation depth of concrete with multi-mineral admixtures," *Journal of Xian University of Architecture and Technology*, vol. 42, no. 4, pp. 464–467+472, 2010.

Research Article

Decomposition of Cyanide from Gold Leaching Tailings by Using Sodium Metabisulphite and Hydrogen Peroxide

Dongzhuang Hou [ID],[1] **Lang Liu** [ID],[2] **Qixing Yang,**[2] **Bo Zhang,**[2] **Huafu Qiu,**[2] **Shishan Ruan,**[2,3] **Yue Chen,**[1] **and Hefu Li**[4]

[1]*College of Geology and Environment, Xi'an University of Science and Technology, Xi'an 710054, China*
[2]*Energy School, Xi'an University of Science and Technology, Xi'an 710054, China*
[3]*Xi'an Fill Green-innovation Mining Technology Co. Ltd., Xi'an 710054, China*
[4]*Shanyang Qinding Mining Co. Ltd., Shangluo, 726400, Shanxi, China*

Correspondence should be addressed to Lang Liu; liulang@xust.edu.cn

Cyanidation is widely used by most gold mine worldwide and will remain prevail in years (or decades) to come, while cyanide is hazardous, toxic pollutants whose presence in wastewater and tailings can seriously affect human and its environment; hence, it is necessary to control these contaminants. The purpose of this study was to examine the effects through the investigation of changes in pH, concentration, and contact time, and the optimal conditions were obtained. It has been proven that the decomposition of cyanide in solution and tailings increased as the alkalinity in the presence of $0.5 \, g/L$ $Na_2S_2O_5$. An increase in H_2O_2 (30%) concentration (from 1 to $4 \, mL/L$) increased the decomposition in solution, while the effect on removing cyanide was better when pH was 9 than 8 and 10 in tailings. The cyanide in tailings decreased in the first $4 \, h$ and increased after $4 \, h$. The effective and economic conditions for maximum decomposition of cyanide from leach tailings are first treated in $0.5 \, g/L$ $Na_2S_2O_5$ at pH 10 for 3 hours and then $2 \, mL/L$ H_2O_2 (30%) is added to the tailings at pH 9 for 4 hours through comparative study. The findings provide the basis to optimize the decomposition of cyanide from gold leaching tailings in mining or backfilling by using the synergetic effect of $Na_2S_2O_5$ and H_2O_2.

1. Introduction

Cyanide leaching (cyanidation), which converts the gold into a cyanide complex ($Au(CN)_2^-$) that is soluble in water, is currently the most prevailing and effective process to extract gold from ores [1, 2]. This process requires excess cyanide to improve gold recovery and produces exceptionally large quantities of cyanide-bearing wastes in the form of tailings and waters. Free cyanide, which is the main byproduct that results from metallurgical processes [3], is considered the most toxic cyanide form as it causes harmful effects at relatively low concentration. Other cyanide species are easily dissolved to free cyanide under acid conditions [4]. It will take a longtime for cyanide in the tailings to be reduced to biologically harmless through natural attenuation [5–7], so tailings containing cyanide should be treated before

they are released into the environment to avoid detrimental effects on the receiving environment [8]. The decomposition of cyanide from gold leaching tailings is one of the biggest challenges for the gold mine in the last decades, so the appropriate treatment of the cyanide in the tailings is required to avoid or minimize environmental and health issues.

Several biological, physical, and chemical techniques, electrolytic oxidation, and other methods to decompose or recycle cyanide have been developed for the treatment of cyanide solutions. Currently, as the widely used technologies for industrial production of the decomposition of cyanide are INCO process, alkali-chlorine process, activated carbon process, ozone oxidation process, hydrogen peroxide oxidation process [9], and recovery hydrogen cyanide [10–12]. INCO and alkali-chlorine processes are used to remove high

concentration cyanide, while they cannot completely accomplish the degradation of cyanide species [13, 14]. Activated carbon can absorb cyanide and make it gather, but cannot decompose it [15]. Ozonation and hydrogen peroxide oxidation processes, which are not easy to produce secondary pollution in the treatment of cyanide, are used to treat low concentration cyanide [16, 17], but the cost is higher. Recovery hydrogen cyanide can reduce cyanide content and cost, but it cannot meet the requirements of tailings' backfilling [10–12].

Backfilling technology is the best choice for the mine to break through the bottleneck of resources, environment, and safety [18], but harmful substances such as metal materials and solvent left in the gold leaching tailings should be treated before backfilling in order to prevent them from polluting groundwater. Many organizations and countries around the world have already issued effective cyanide management policies; some countries, include Costa Rica, Argentina, Germany, the Czech Republic, and Turkey, have an outright ban on the use of cyanide in gold extraction throughout the country [19, 20]. In 2018, China issued the technical specification for pollution control of cyanide leaching residue in gold industry (TSPC), in which ozonation and hydrogen peroxide oxidation are selected as a method of deep decyanation. The study on cyanide removal is mainly focused on industrial wastewater [21]; the study on cyanide removal in gold leaching tailings, which contains wastewater and tailings, is still limited. While the mineral composition of gold ore is complex, cyanide, powder of activated carbon, hydrogen peroxide (H_2O_2) and other chemical were also added in the mineral processing flowsheet, which made the composition of tailings more complex. Most of the residual cyanide in tailings are strongly adsorbed on the surface of minerals, only a small amount of free cyanides and hydrolytic complex cyanides are able to enter into the leaching solution [22]. Therefore, it is necessary to explore more efficient methods to remove cyanide. The appropriate decomposition of CN^- is a complex process that requires several approaches are combined to improve the efficiency of the treatment and consider treatment economy, and combination methods were used to try to remove cyanide [23].

Based on the method of cyanide removal in solution, the effects of pH, concentration, and contact time of H_2O_2 for the decomposition of cyanide from leach tailings were analysed after $Na_2S_2O_5$ reaction. The mechanism of cyanide removal was also discussed. The outcome of this study was to find the best conditions for decomposition of cyanide from leach tailings, lead to bulk utilization of tailings in gold metal mine, and alleviate the ground collapse and soil pollution caused by traditional mining.

2. Materials and Methods

2.1. Tailings. The gold leaching tailings used in the experiment comes from Xiajiadian gold mine, Shaanxi province, China, which belongs to orogenic gold deposit, accounting for 52% in China [24]. The concentration of gold leaching tailings, where the diameter of tailings is 100–600 μm, is 35%, pH is 10.78, the initial cyanide concentration in the solution is 30.66 mg/L, and the cyanide leached from the leach tailings is 11.78 mg/L. The total carbon content of tailings is 2.47–6.67%, in which the organic carbon content is 1.47–4.29%. The solution temperature was controlled at $23 \pm 2°C$.

2.2. Reagents. H_2O_2 (30%) and sodium metabisulphite ($Na_2S_2O_5$) were employed as received. Copper employed as the decomposition catalysts [25, 26] was added as the copper sulfate for experiments. Concentrated (98%) H_2SO_4 and NaOH were employed for pH adjustment. All chemicals were of analytical reagent grade. Agitated air was used in this experiment in order to accelerate the decomposition of cyanide, and the inflation rate was 50 mL/min.

2.3. Methods

2.3.1. Experiment of Decomposition of Cyanide from Leach Tailings. 0.5 g/L of $Na_2S_2O_5$ and 0.2 g/L of $CuSO_4$ (as catalyst) were added to 1000 mL gold leaching tailings, and the solutions were air stirred at a constant rate of 50 mL/min to accelerate cyanide oxidation. Individual experiments were carried out at pH values ranging from 8 to 11. After 3 h at each pH, 10 mL sample solutions, which were filtered with a 0.45 μm filter paper and a 100 g solid which was leaching residue, were analysed for residual cyanide. Then, 1, 2, or 4 mL/L of H_2O_2 (30%) was added to 1000 mL gold leaching tailings, which had been treated with $Na_2S_2O_5$ at pH 10 for 3 h. Individual experiments were carried out at pH values ranging from 8 to 10, the solutions were air stirred at a constant rate of 50 mL/min to accelerate cyanide oxidation. After 1 h, 2 h, 4 h, and 8 h at each pH, a 100 g solid which was leaching residue and some 10 mL sample cyanide wastewater were analysed for residual cyanide. NaOH or H_2SO_4 was added to maintain a pH of 8–11 throughout each test.

2.3.2. Experiment of Cyanide Leaching from Leach Tailings. The steps of cyanide leaching of leach tailings follow the technical specification for pollution control of cyanide leaching residue in gold industry issued by China. Contaminated cyanide solution was prepared by mixing the pregnant solution and water (extractant) according to the ratio of 10 L water to 1 kg tailings and oscillated at 30 ± 2 revolutions per min by flip oscillator with $23 \pm 2°C$ for 18 ± 2 hours referring to the technical specification for pollution control of cyanide leaching residue in gold industry.

2.3.3. Analytical Method. Total cyanide (CNT) content was determined by isonicotinic acid-pyrazolone spectrophotometry referring to the water quality-determination of cyanide volumetric and spectrophotometry method. The cyanide reacts with chloramine T to give cyanogen chloride, which reacts with isonicotinic acid to give pentenedialdehyde, and finally condenses with pyrazolone to give blue dye; then, it is measured at 638 nm by UV9100 A ultraviolet-visible spectrophotometer (YQ00302), with a detection limit of 0.004 mg/L.
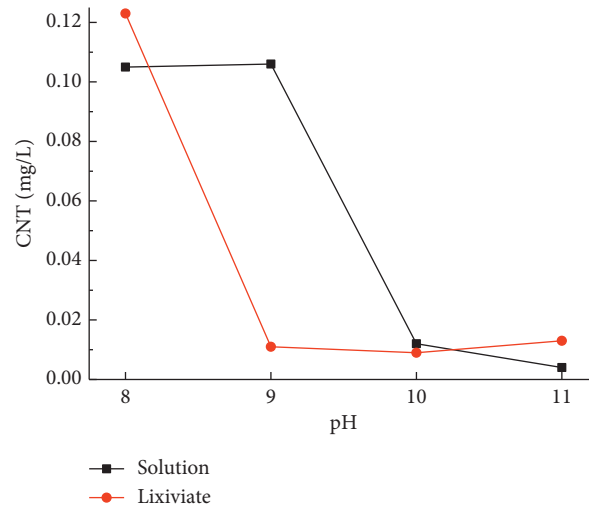
FIGURE 1: Cyanide as a function of pH in the presence of 0.5 g/l $Na_2S_2O_5$ in 3 hours.

3. Results and Discussion

3.1. Effect of pH on the Decomposition of Cyanide by $Na_2S_2O_5$.
Individual experiments were carried out at pH values
ranging from 8 to 11. Figure 1 shows the effect of equi-
librium pH on the cyanide of solution and lixiviant in the
presence of 0.5 g/L $Na_2S_2O_5$ in 3 hours. It is evident that an
increase in pH increased the extent of decomposition of
cyanide in solution and lixiviant of tailings. This result
showed that the decomposition of cyanide increased as the
alkalinity of the solution increased, the cyanide in lixiviant of
tailings was the least when the pH was 10 under the same
conditions, and the effect of cyanide decomposition in
tailings was equivalent to that of pH 9, 10, and 11. Con-
sidering the investment cost, the effect of decomposition of
cyanide from solution and tailing by $Na_2S_2O_5$ is the best
when pH is 10.

3.2. Effect of pH on the Decomposition of Cyanide by H_2O_2.
The pH value had a significant effect on cyanide removal
[21, 27]. The tailings were treated with 0.5 g/L $Na_2S_2O_5$ for 3
hours at pH 10, and then individual experiments were
carried out at pH values ranging from 8 to 11. Figures 2(a)–
2(c) show the effect of equilibrium pH on the cyanide of
lixiviant of tailings after $Na_2S_2O_5$ treatment in the presence
of H_2O_2, and it is evident that the effect on removing cyanide
was better when pH was 9 than 8 and 10 in lixiviant.
Figure 2(d) shows effect of equilibrium pH on the cyanide of
solution added with 2 mL/L H_2O_2 for 2 hour, and it is ev-
ident that an increase in pH increased the extent of de-
composition in solution, which is in agreement with those of
Tu et al. [28] who observed that the decomposition of cy-
anide in mine wastewater added with H_2O_2 increased as the
alkalinity of the solution increased.

Figure 2 shows that the effect of removing cyanide by
H_2O_2 in solution is different from tailing under the same
conditions. The reason for this phenomenon may be that the
cyanide in the solution, which is free cyanide, is easy to be
treated, while the diffusion rate of cyanide in the tailings to

the solution is lower than the removal rate by H_2O_2 of the
solution.

*3.3. Effect of H_2O_2 Concentration on the Decomposition of
Cyanide.* The ability of the decomposition of cyanide will be
affected by the concentration of H_2O_2. Figure 3 shows the
effect of H_2O_2 concentrations ranging from 1 to 4 mL/L on
the decomposition of cyanide. It is evident that an increase
in H_2O_2 concentration increased the extent of decomposi-
tion in tailings; the most cyanide is leached from the tailings
when 2 mL/L H_2O_2 is added to the solution.

In order to remove cyanide in tailings as much as
possible, excessive $Na_2S_2O_5$ was added to the pretreatment,
and the reaction occurs when H_2O_2 reached a certain
concentration, resulting in the low efficiency of cyanide
treatment at 2 mL/L:

$$Na_2S_2O_2 + 5H_2O_2 \longrightarrow Na_2SO_4 + H_2SO_4 \tag{1}$$

$$H_2SO_4 + Na_2SO_3 \longrightarrow Na_2SO_4 + S + SO_2 + H_2O \tag{2}$$

$$SO_2 + H_2O_2 \longrightarrow H_2SO_4 \tag{3}$$

3.4. Effect of Contact Time on the Decomposition of Cyanide.
Contact time is also the influence factor of H_2O_2 for the
decomposition of cyanide [28]. Figure 4 shows the effect of
contact time ranging from 1 to 8 h on the rate of de-
composition of cyanide of lixiviant in tailings. The figure
showed that cyanide decreased in the first 4 h and the
content of cyanide increased after 4 h. In the first four
hours, H_2O_2 reacted with cyanide in the tailings, which
caused the cyanide content in the solution to decrease,
while most of the cyanides adsorbed on pyrite [28, 29]
and chalcopyrite [30], which is widely distributed in gold
ore, are driven by chemisorption of carbon. The
remaining H_2O_2 could not continuously reduce the cy-
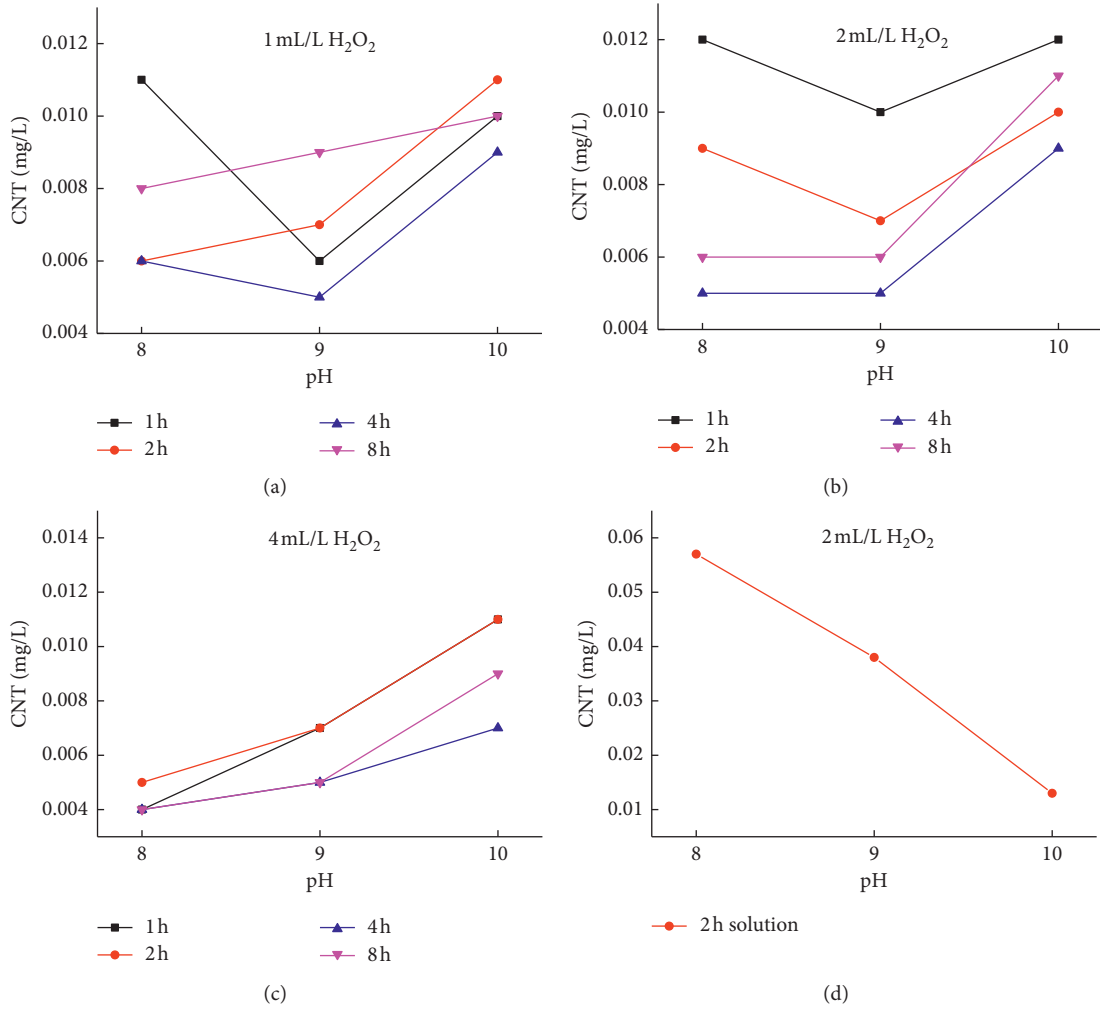anide content in the tailings, and it might be that the

(a)

(b)

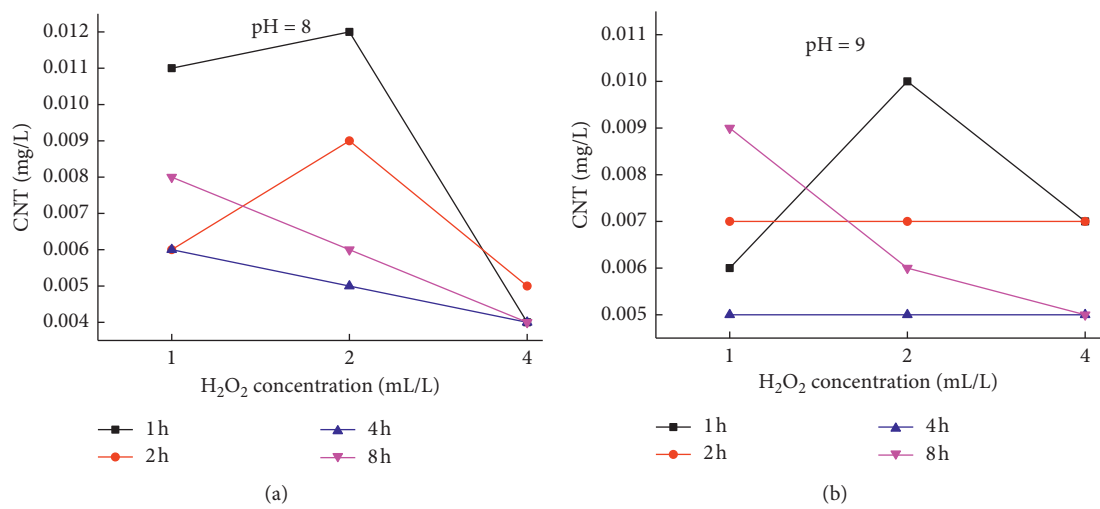(c)

(d)

Figure 2: CNT as a function of pH in the presence of H_2O_2.
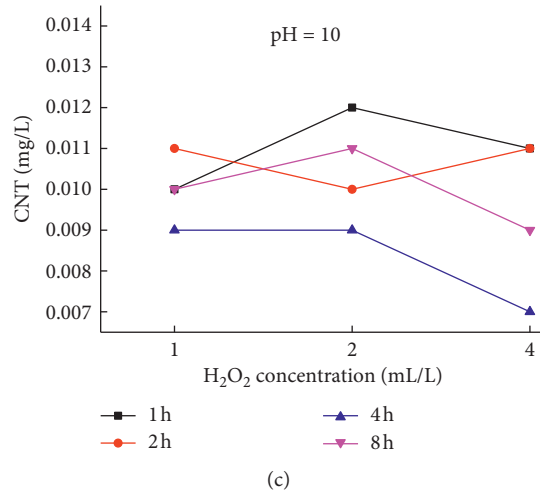

(a)

(b)

Figure 3: Continued.

(c)

FIGURE 3: Cyanide as a function of H_2O_2 concentration.
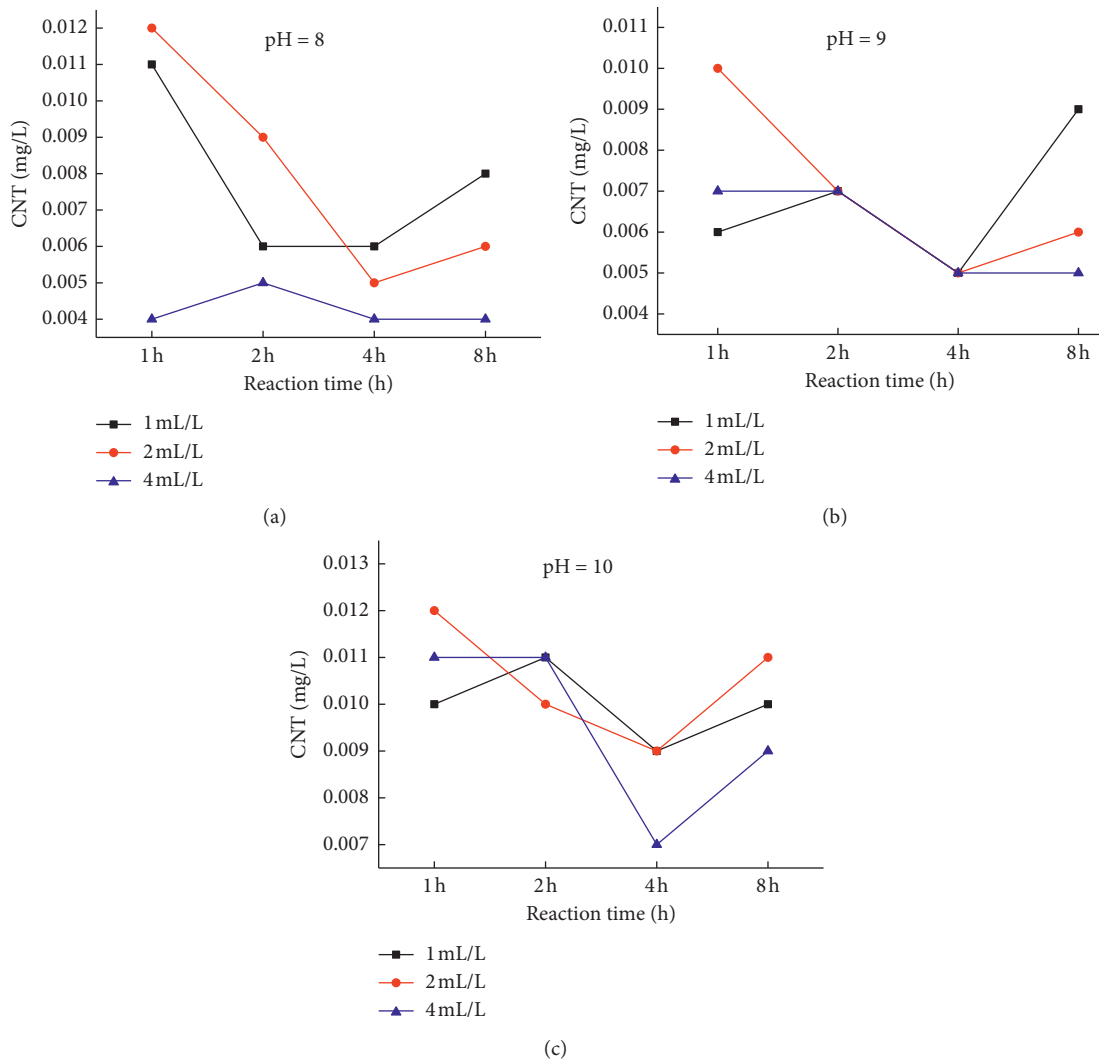

(a)

(b)

(c)

FIGURE 4: Cyanide as a function of contact time.

unreacted cyanide in the tailings adsorbed by activated carbon reentered the tailings with the concentration of H_2O_2 decreased. It is possible that the cyanide adsorbed by pyrite and activated carbon is gradually converted into free cyanide, and the unreacted cyanide in pulp re-enters the tailings with the decrease of H_2O_2 concentration.

As explained above, the best conditions for decomposition of cyanide from leach tailings are first treated in 0.5 g/L $Na_2S_2O_5$ at pH 10 for 3 hours and then 2 mL/L H_2O_2 is added to the tailings at pH 9 for 4 hours.

4. Conclusions

The decomposition of cyanide increased as the alkalinity of the solution and tailings increased in the presence of 0.5 g/L $Na_2S_2O_5$. An increase in pH increased the extent of decomposition in solution in the presence of H_2O_2, while the effect on removing cyanide was best when pH was 9 in lixiviant of tailings. An increase in H_2O_2 concentration increased the extent of decomposition in solution. The cyanide decreased in the first 4 h, and the content of cyanide increased after 4 h by the adsorption effect of active carbon and pyrite.

All the leaching metal of gold leaching tailings treated by $Na_2S_2O_5$ and H_2O_2 can meet the backfilling requirements (0.05 mg/L) of TSPC. Considering fully with effectiveness and practicability, the best conditions for decomposition of cyanide from leach tailings are first treated in 0.5 g/L $Na_2S_2O_5$ at pH 10 for 3 hours and then 2 mL/L H_2O_2 is added to the tailings at pH 9 for 4 hours.

Data Availability

The data used to support the findings of the study are available from the corresponding author upon request.

Additional Points

Highlights. (i) Sodium and hydrogen peroxide for cyanide decomposition are applied. (ii) The factors affecting cyanide removal were explored. (iii) The optimal conditions for cyanide removal were examined. (iv) The lessons are useful for backfilling by gold tailings to develop efficient circularity.

Conflicts of Interest

The authors declared no potential conflicts of interest with respect to the research, authorship, and/or publication of this article.

Acknowledgments

References

[1] M. Botz, *Cyanide Treatment Methods, in Mining Environmental Management*, Mining Journal Books, London, UK, 2001.

[2] D. Adams, *Gold Ore Processing: Project Development and Operations*, Elsevier Science & Technology, New York, NY, USA, 2016.

[3] L. Mekuto, Y. M. Kim, S. O. Ntwampe et al., "Heterotrophic nitrification-aerobic denitrification potential of cyanide and thiocyanate degrading microbial communities under cyanogenic conditions," *Environmental Engineering Research*, vol. 24, pp. 254–262, 2019.

[4] SWA (Safe Work Australia), *Guide for Preventing and Responding to Cyanide Poisoning in the Workplace*, Commonwealth of Australia, Sydney, Australia, 2013.

[5] S. Ebbs, "Biological degradation of cyanide compounds," *Current Opinion in Biotechnology*, vol. 15, no. 3, pp. 231–236, 2004.

[6] N. Kuyucak and A. Akcil, "Cyanide and removal options from effluents in gold mining and metallurgical processes," *Minerals Engineering*, vol. 50-51, pp. 13–29, 2013.

[7] E. Jaszczak, Z. Polkowska, S. Narkowicz, and J. Namieśnik, "Cyanides in the environment analysis problems and challenges," *Environmental Science and Polluion Research*, vol. 24, pp. 15929–15948, 2017.

[8] L. C. Razanamahandry, C. T. Onwordi, W. Saban et al., "Performance of various cyanide degrading bacteria on the biodegradation of free cyanide in water," *Journal of Hazardous Materials*, vol. 380, 6 pages, 2019.

[9] G. Asgari, A. Mohammadi, A. Poormohammadi, and M. Ahmadian, "Removal of cyanide from aqueous solution by adsorption onto bone charcoal," *Fresenius Environmental Bulletin*, vol. 23, no. 3, pp. 720–727, 2014.

[10] E. Yilmaz, F. Ahlatci, E. Y. Yazici, O. Celep, and H. Deveci, "Recovery of cyanide from effluents using carbon dioxide," *Mugla Journal of Science and Technology*, vol. 3, no. 2, pp. 171–177, 2017.

[11] E. Yilmaz, E. Y. Yazici, O. Celep, and H. Deveci, "Recovery of cyanide from effluents: SART process," *Gumushane University Journal of Science and Technology Institute*, vol. 9, no. 3, pp. 600–615, 2019.

[12] E. Yilmaz, E. Y. Yazici, O. Celep, and H. Deveci, "Processes for cyanide recovery from leach effluents," *Scientific Mining Journal*, vol. 58, no. 1, pp. 53–71, 2019.

[13] P. Breuer, C. Sutcliffe, and R. Meakin, "Comparison of industrial cyanide destruction processes," in *Proceedings of International Mineral Processing Congress (IMPC) 2010*, pp. 1483–1493, Brisbane, Australia, September 2010.

[14] D. W. Wei, L. Y. Chai, R. Ichino, and O. Masazumi, "Gold leaching in an alkaline tiourea solution," *Journal of the Electrochemical Society*, vol. 146, no. 2, pp. 559–563, 1999.

[15] A. Jauto, S. Memon, A. Channa, and A. Khoja, "Efficient removal of cyanide from industrial effluent using acid treated modified surface activated carbon," *Energy Sources, Part A: Recovery, Utilization, and Environmental Effects*, vol. 41, pp. 2715–2724, 2019.

[16] N. Pueyo, N. Miguel, J. L. Ovelleiro, and M. P. Ormad, "Limitations of the removal of cyanide from coking wastewater by ozonation and by the hydrogen peroxide-ozone process," *Water Science and Technology*, vol. 74, no. 2, pp. 482–490, 2016.

[17] S. Qiu, Z. G. Chen, P. Z. Guo, and J. Z. Shen, "Engineering application of heap elution process to deal with cyanide pollution soil," *Journal of Environmental Engineering Technology*, vol. 8, no. 1, pp. 104–108, 2018.

[18] C. C. Qi and A. Fourie, "Cemented paste backfill for mineral tailings management: review and future perspectives," *Minerals Engineering*, vol. 144, pp. 1–21, 2019.

[19] G. Laitos, "Cyanide mining and the environment," *Pace Environmental Law Review*, vol. 30, pp. 869–949, 2013.

[20] Q. B. Tran, M. Lohitnavy, and T. Phenrat, "Assessing potential hydrogen cyanide exposure from cyanide-contaminated mine tailing management practices in Thailand's gold mining," *Journal of Environmental Management*, vol. 249, pp. 1–10, 2019.

[21] M. Esparza, C. Cueva, S. Pauker, V. Jentzsch, and M. Bisesti, "Combined treatment using ozone for cyanide from wastwatewater: a comparison," *Revista Internacional De Contaminacion Ambiental*, vol. 35, no. 2, pp. 459–467, 2019.

[22] C. C. Lv, *Applied Fundamental Research of Comprehensive Recovering Valuable Elements from Cyanidation Tailing*, Chinese Academy of Sciences, Beijing, China, 2017, in Chinese.

[23] G. A. Llerena and I. R. López, "Cyanide degradation from mining effluent using two reagents: sodium metabisulphite and the metabisulphite mixture with hydrogen peroxide," *Tecciencia*, vol. 13, no. 25, pp. 1–9, 2018.

[24] S. H. Li, L. M. Zhu, L. L. Ding, X. Xiong, and K. Liu, "Metallogenic age of xiajiadian gold deposit in the zhashuishanyang ore concentration, qinling orogenic belt and its geological significance," *Mineral Deposits*, vol. 38, no. 6, pp. 1278–1296, 2019, in Chinese.

[25] M. Pandit, D. K. Tyagi, and J. C. Kapoor, "Oxidation of cyanide in aqueous solution by chemical and photochemical process," *Journal of Hazardous Materials*, vol. 116, no. 1–2, pp. 49–56, 2004.

[26] M. Zhou, S. Y. Huang, and X. Qu, "Research on treatment of wastewater containing high concentration of cyanide by hydrogen peroxide catalytic oxidation," *Industrial Water & Wastewater*, vol. 44, no. 5, pp. 31–34, 2013, in Chinese.

[27] M. Matsumura and T. Kojima, "Elution and decomposition of cyanide in soil contaminated with various cyanocompounds," *Journal of Hazardous Materials*, vol. 97, no. 1-3, pp. 99–110, 2003.

[28] Y. B. Tu, P. W. Han, L. Q. Wei et al., "Removal of cyanide adsorbed on pyrite by H2O2 oxidation under alkaline conditions," *Journal of Environmental Sciences*, vol. 78, pp. 287–292, 2019.

[29] C. Zhao, D. Huang, J. Chen, Y. Li, Y. Chen, and W. Li, "The interaction of cyanide with pyrite, marcasite and pyrrhotite," *Minerals Enginering*, vol. 95, pp. 131–137, 2016.

[30] A. D. Bas, E. Koc, E. Y. Yazici, and H. Deveci, "Treatment of copper-rich gold ore by cyanide leaching, ammonia pretreatment and ammoniacal cyanide leaching," *Transactions of Nonferrous Metals Society of China*, vol. 25, no. 2, pp. 597–607, 2015.

Research Article

Validating the Use of Slag Binder with 91 Percent Blast Furnace Slag for Mine Backfilling

Xiaobing Yang, Bolin Xiao [iD], and Qian Gao

School of Civil and Resource Engineering, University of Science and Technology, Beijing, China

Correspondence should be addressed to Bolin Xiao; iextia@hotmail.com

The use of ground granulated blast furnace slag (GGBFS) is environmentally sustainable and prevalent in the cement industry, but the original alkali-activated slag binder cannot be used for mine backfilling. Few reports have studied slag binders with high slag proportions (>90%) and low-cost activators (solid waste is used) that have higher performance than cement for backfilling. To increase the utilization of slag in the mining industry, this work presents a new slag binder (SB) comprised of 91% slag powder and 9% activator (3% clinker, 5% desulfurized gypsum, and 1% mirabilite). Its performance was evaluated by testing its strength, yield stress, and viscosity, which are three key properties for backfilling. We also investigated its microstructure using SEM, XRD and thermogravimetric analysis (TG/DTG). The results showed that the SB composites have a slightly lower early-age (<3 d) strength but a higher long-term strength (>28 d). Although the SB backfilling composites had a twofold higher yield stress and nearly the same viscosity as Portland cement, the pressure drop in a pipe was only slightly higher through friction factor modeling. The proposed SB may provide a sustainable binder for the mining industry with better performance and lower cost.

1. Introduction

The metallurgical and mining industries produce large quantities of by-products and solid wastes such as slag, waste rock, and tailings, which are generally disposed of in landfills, which raises environmental issues. Blast furnace slag is generated during iron manufacturing, and 95% of it is comprised of four main oxides: calcium, magnesium, silicon, and aluminum [1]. Blast furnace slag has been used for centuries in many fields. For example, some of the first-known uses of blast furnace slag were as railroad ballast, as a concrete aggregate, in bituminous surfaces, asphalt mixtures, pavement structures, unbound base courses, and embankments [2–6]. Slag is most commonly used in the cement industry due to the similar chemical compositions of the two materials. It is ground to a cement-like grain size known as grounded granulated blast furnace slag (GGBFS) and then used as a cement additive and independent binder [7, 8].

A traditional cement raw material is clinker, whose production is accompanied by large quantities of greenhouse gas emissions, dust air pollution, and excavated clay soil for calcination. The replacement of GGBFS with clinker can address these issues. An academic report found that replacing 45% of ordinary Portland cement with blast furnace slag would result in a 37% reduction in total CO_2 emissions [9]. The use of a higher slag proportion in cement can decrease the total energy required for cement manufacturing [10]. Important applications of alkali-activated slag binder and slag composite binder used in mortar and construction concrete have been reported [11–14]; however, these binders may not be applicable for mine backfilling, which is vastly different from ordinary concrete.

Mine backfill slurries are mixtures of binder, aggregate, and water that are homogeneously mixed in a surface plant and then transported to fill underground voids by gravity or pumping through pipelines [15]. Compared with normal concrete, mine backfill has special characteristics such as follows: (i) low binder content $B_w\%$ (mass percentage of binder/solid mass), which is determined by the geological conditions of the mine and the functionality of the filling body. It usually ranges from 2 to 8% [16], but in most mines

in China, 10–20% is used due to complex geological conditions, such as high in situ stresses and crushed wall rock. In ordinary concrete, B_w% is more than 30%. (ii) High water/cement ratio (W/C). The W/C is < 1.0 for construction concretes, while mine backfill has a larger W/C of 2–10 to improve flow through pipeline transport [17]. (iii) Backfill aggregate can be composed of many different materials, such as tailings, waste rock, solid waste, river sand, and Gobi sand. Aggregate also has a large content of fine particles ($<75\,\mu$m); for example, fine particles may account for more than 80% of tailings [18]. Construction concrete generally has a rigid fine particle content limit of <5%. The strength of concrete significantly decreases upon increasing the fine particle content [19]. (iv) Tap water may be used for mixing mine backfill, but processed water rich with chloride ions, metal ions, sulfate ions, and many other chemicals are generally used. These ions can have complex effects on hydration reactions [20].

With these unique characteristics, the slag binders originally developed for building and civil construction may no longer be suitable for mine backfill. Binders are often specially developed and should be validated for use at mine sites. For example, Olivier used four pozzolanic by-products (waste glass, copper slag, wood bottom ash, and coal fly ash) mixed with Portland cement and GGBFS to create low-cost binders for use in mine cemented paste backfill [21]. The cement replacement level of 35%–45% was validated. Jiang developed an alkali-activated slag with an activator/slag ratio of 0.3 (slag proportion 77%), and the paste backfill workability and early-age compressive strength were confirmed [22].

However, there are few reports of slag binder with large slag proportions (>90%) and low-cost activators (solid waste) with a higher performance than cement for mine backfill. In this study, a new slag binder made of 91% slag and 9% activator is presented and examined for mine backfill. Validation tests were performed on the strength and rheological properties (yield stress and viscosity), which are three key properties for backfill. We also investigated the microstructure using SEM, XRD, and thermogravimetric analysis (TG/DTG) to compare the material with ordinary Portland cement type I (PCI) and PCI-slag blended binder to evaluate its performance.

2. Materials and Methods

2.1. Materials

2.1.1. Binder Materials. Three kinds of binders were used: PCI (CB, which is used industrially), 50/50 PCI-slag blinded binder (BB, which is widely used in many other mines and literature), and the proposed slag binder (SB). The slag was obtained from JISCO in Gansu Province, China, and ground into GGBFS in a local plant. Many studies have reported that the hydration of GGBFS can be activated by alkali [23] and sulfate [24]. Here, a combination activation was applied, in which a small amount of clinker was used to generate an alkali environment, desulfurized gypsum (a solid waste by-product of thermal power plants or iron-steel plants) was

used as a sustainable sulfate activator, and a very small amount of mirabilite was added to improve the early strength. The SB consisted of 91% GGBFS, 3% clinker, 5% desulfurized gypsum, and 1% mirabilite. The main physical and chemical properties of PCI and GGBFS are listed in Table 1. GGBFS is an acidic slag ($M_0 < 1$), and the quality coefficient $K > 1.2$ indicates that it has a good hydration property.

2.1.2. Aggregate. To validate the applicability of the SB for mine backfilling, a practical high-density backfill (HDB) slurry of a nickel mine in northwest China was used. A Gobi sand aggregate was obtained from the mining site, which was excavated from the Gobi, and then sieved and milled in a processing plant to eliminate extra-coarse particles and ensure that the maximum grain size was <5 mm. The final grain size distribution of Gobi sand is shown in Figure 1, which has a fine particle ($<75\,\mu$m) content of 16.5%.

2.1.3. Mixing Water. Tap water was used as the mixing water to simulate an actual engineering situation. Although water chemistry can affect some properties of the backfill slurry [25], this is beyond the scope of this research, which focuses on strength and rheological properties.

2.2. Test Methods

2.2.1. Uniaxial Compression Strength (UCS) Tests. The UCS is an important parameter for mine backfilling, because it determines the functionality of the filling mass body, the backfill slurry configuration, the backfilling cost, and mining profitability; therefore, it was used to evaluate the binders in this research. UCS tests were performed on specimens with three different binders for different curing times (1, 3, 7, and 28 d) in accordance with the ASTM C109 standard. A microprocessor-controlled electronic universal testing machine LGS100 K model was used with a loading capacity of 100 kN and an accuracy of 0.5%. The loading rate was 1 mm/min during the tests. Before the tests, a high-density backfill (HDB) mixture was prepared using the practical mixing proportion of binder content of B_w % = 20% and a solid mass concentration of C_w % = 78%. The binder, aggregate, and water were mixed in a mixing machine for 5 minutes and then poured into a cube triple-module with a side length of 7.07 cm. The module was sealed by a plastic wrap to prevent water evaporation and then placed into a temperature-controlled chamber at 23°C for the designated curing time.

The test for each specimen was repeated at least three times to ensure accuracy and repeatability, and the average value was reported as the strength of the tested sample.

2.2.2. Rheology Tests. Rheology is another important feature for mine backfilling, since the slurry is transported by pipeline, and the slurry flow in a pipe is dominated by its rheological properties. Thus, it is essential to evaluate the rheological properties when applying a backfill material, which is generally characterized by its yield stress and

TABLE 1: Chemical and physical properties of PCI and GGBFS.

Chemical composition	PCI (%)	GGBFS (%)	Physical properties	PCI	GGBFS
CaO	62.82	37.95	Specific gravity	3.1	2.9
Fe_2O_3	2.7	0.63	Specific surface area (m^2/kg)	430	460
SiO_2	18.03	38.34	Fines content (<45 μm) (%)	88	95
Al_2O_3	4.53	12.3	Basicity coefficient, M_o	—	0.90
MgO	2.65	7.82	Quality coefficient, K	—	1.50
MnO	0.41	0.48	D_{10} (μm)	2.85	4.48
K_2O	0.73	0.52	D_{50} (μm)	17.04	12.13
SO_3	3.82	0.2	D_{90} (μm)	43.67	61.68

Note: $Mo = (CaO + MgO)/(Al_2O_3 + SiO_2)$; $K = (CaO + MgO + Al_2O_3)/(SiO_2 + MnO + Ti_2O)$.
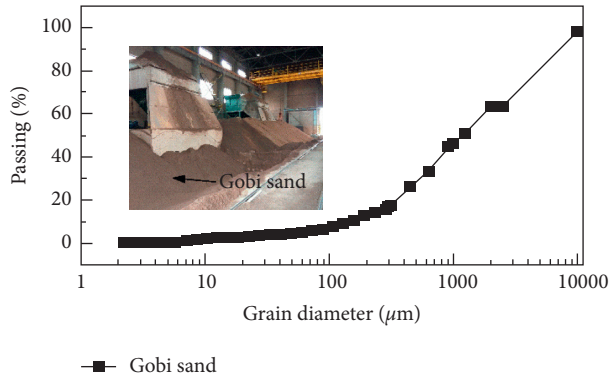

FIGURE 1: Grain size distribution of Gobi sand.

viscosity; therefore, rheology tests were performed using a Brookfield RST Soft Solids Tester (RST-SST) Rheometer and a Rheo3000 software for the HDB with different binders. The tests were conducted at room temperature using a four-blade vane spindle VT-40-20. The rheometer was set to controlled shear rate (CSR) mode, and HDB samples were sheared at a shear rate range of 0–200 s^{-1}. Before the tests, all materials were homogeneously mixed in a mixing machine for 5 min, and then the sample was placed in a 600 mL low-form Griffin beaker for measurement. During the test, samples were first sheared at a maximum rate (200 s^{-1}) for 2 min to simulate the shear that occurs in practice during mixing before slurries are directly dumped into a pipeline system without silencing. Then, the sample was sheared from a rate of 200 s^{-1} declining to 0 s^{-1} over 100 s, with data recorded every 10 s.

2.2.3. Microstructural Analysis. Microstructural analysis, including thermal analyses (thermogravimetry (TG), differential thermogravimetry (DTG)), scanning electron microscope (SEM), and X-ray diffractometry (XRD), were carried out to inspect the HDB properties. TG/DTG and XRD were conducted on the three binder paste samples, which were a mixture of binder and water with a W/C ratio of 1. The SEM samples were made from the cracked cube after UCS tests. To prepare paste samples, the binders and water were mixed using the same procedure and then sealed in a chamber for the desired curing time. Prior to tests, samples were dried in an oven at 40°C until mass stabilization and then ground into powders for measurement.

Thermal analyses were carried out using an SDT-Q600 TGA from TA Instruments, which allowed the simultaneous measurement of weight loss, heat flow, and transition temperature changes. The paste samples (about 10 mg) were heated in an inert nitrogen atmosphere at a rate of 10°C/min up to 800°C during tests.

XRD was conducted to acquire the mineralogical and chemical compositions of the HDB. It was performed using a Bruker D8 advance diffractometer. The scanning was carried out over a 2θ range of 5–70° with a step width of 0.02° and a scanning speed of 1°/min.

SEM observations were performed with a JEOL JSM-6700F, operating in a backscatter electron mode.

3. Results and Discussion

UCS and rheological properties were examined to validate the applicability of sustainable slag binder as mine backfill.

3.1. Strength (UCS) Development of the HDB with Different Binder Agents. The UCS developments of the HDB samples with three binder agents (CB-HDB, BB-HDB, and SB-HDB) are shown in Figure 2.

It can be seen that the BB-HDB has the lowest strength for all times, HDB with a blended binder, and slag binder has nearly the same minimum strength after curing for 1 d and 3 d. Although HDB with PCI binder has the highest early strength (<7 d), the SB-HDB shows the highest strength at 7 d and 28 d. PCI binder has the highest early strength, and partial replacement with slag reduced the UCS. The developed slag binder has a better performance for midterm (7 d) and long-term strength (28 d).

3.1.1. Early-Age Strength (Curing ≤3 d) and Hydration Products. BB-HDB has the lowest strength at 1 d and 3 d of 0.41 MPa and 1.23 MPa. SB-HDB has a slightly higher 3 d strength of 1.33 MPa, while CB-HDB has the highest 1 d and 3 d strength of 0.77 MPa and 1.97 MPa, respectively. The highest strength for CB-HDB was attributed to the rapid hydration rate of its main components (C_3A, C_3S, and C_4AF). The hydration process begins immediately when water is added to produce hydration products, such as hydrated calcium silicate (C-S-H), calcium hydroxide (CH), and ettringite (AFt) [26]. In contrast, slag has a slow hydration rate, and slag particles are only hydrated after an
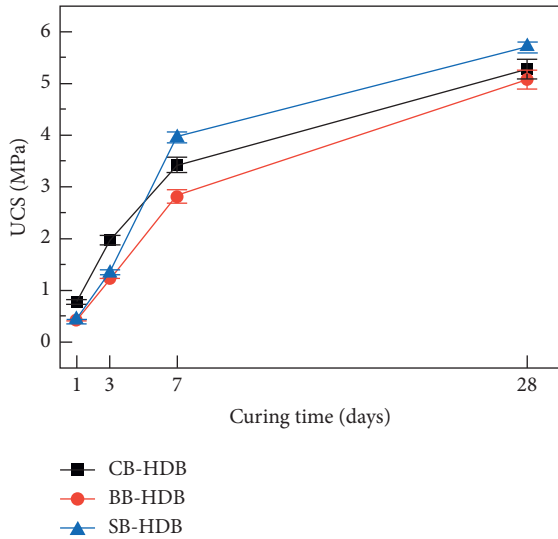
Figure 2: UCS developments for CB-HDB, BB-HDB, and SB-HDB.

alkali activator reacts with water to produce CH [27]. The active ingredients of the slag create a silicic-rich gel, which then reacts with CH to produce C-S-H gel. Furthermore, slag can react with sulfate activator (gypsum) to generate ettringite [28]; however, gypsum has a very low solubility in water, which means this hydration process will last for a long time. SEM images were collected to inspect the microstructures of CB-HDB and SB-HDB, as shown in Figure 3.

As illustrated in Figure 3, the main hydration products, such as C-S-H (clusters) and ettringite (bars), were observed in both samples after curing for 3 d. CB-HDB was more developed with denser and bigger C-S-H and ettringite clusters, while SB-HDB was less developed with many unfilled voids. Consequently, SB-HDB has lower early-age strength due to the presence of more voids and less-developed hydration products. A TG/DTG analysis of binder paste was conducted for validation, as shown in Figure 4.

Figure 4 shows that there are three DTG peaks or weight loss for both binder pastes. The first weight loss occurs around 100°C, which is a result of the dehydration reactions of some hydrates such as C-S-H, carboaluminates, ettringite, and gypsum [29]. The second weight loss occurs near 400°C, which is caused by the dehydroxylation of calcium hydroxide [30]. Finally, a third peak is observed near 700°C, which is attributed to the decomposition of calcite [31]. Overall, the total weight loss for the CB paste (21.5%) is larger than that of SB (14.5%) after curing for 3 days, which demonstrates that the amount of hydration products for CB is larger. Although the third peak of SB is considerably lower, which indicates a lower hydration rate, the first peak for SB is higher, which indicates that SB has a greater amount of C-S-H after curing for 3 days due to the reaction of slag with CH. The extra consumption of CH implies a lower second peak for SB, even though the second peak for both binders is relatively low.

3.1.2. Midterm (7 d) and Long-Term Strength (28 d). The UCS of backfill cured for 28 days is mainly controlled by the binder content B_w %. It is a crucial parameter for mine design, because it determines the mixing proportion and, thus the backfill cost. In this case, the 28 d UCS of the ordinary CB-HDB is 5.27 MPa, which is 1.05 times higher than the design requirement (here, a minimum of 5 MPa is required for ground support at 28 d curing, which is determined in the strength design process due to the extremely high in situ stress load, underhand cut-and-fill mining method requirement, and large portion of coarse Gobi sand used as aggregate). The UCS of BB-HDB is 5.08 MPa which is 96.4% of CB-HDB, but the UCS for SB-HDB reached 5.69 MPa which is 1.14 times higher than the requirement. This result implies that the combination activation SB has a higher performance than SB during long-term curing, which is beneficial for mining in both mechanical properties and cost. The higher long-term performance is attributed to the second hydration process of slag with alkali and sulfate. This produces complex products, such as ettringite (AFt), gypsum, C-S-H, hydrocalumite, and dolomite. The XRD patterns of the three binder pastes after curing for 28 d are presented in Figure 5 to illustrate the difference in hydration products.

It can be seen that SB produces more complex hydration products, but Portlandite (CH) is absent because (i) SB only contains 3 wt% clinker, which generates only a small amount of CH; (ii) the 91 wt% GGBFS in SB can react with CH to generate extra C-S-H gel. Therefore, CH in the SB is completely consumed and absent in Figure 5. Reports have shown that CH does not improve the strength, but it is harmful to the interface transition zone (ITZ), which reduced the strength [32]. In sum, the absence of CH and the extra C-S-H contribute to the higher mechanical performance of the SB. More AFt and dolomite ($CaCO_3$) were detected for the SB due to its complex hydration reaction. Higher mechanical performance is typical of more extrusive paste backfill with ultrafine tailings [33–35]. The cost of SB comprised of 91% GGBFS which can vary geographically, but in China, it is generally 100 CNY/ton cheaper than ordinary Portland cement. Besides, the binder has more environmental benefits, such as lower greenhouse gas emissions, use of natural raw materials during cement production, and iron and steel industry sustainable development.

3.2. Rheological Properties of the HDB. The rheological properties of the HDB with different binder agents were evaluated and compared. Similar to most reported materials, the HDB slurry exhibited Bingham plastic flow, as shown in Figure 6. Although there are some unusual points in Figure 6, which are supposed to be caused by the collision of rotational vane spindle (length 40 mm and diameter 20 mm) and large aggregate particles (maximum diameter 5 mm), the Bingham model fitting shows a reasonable result with an adjusted $R^2 > 0.9$.

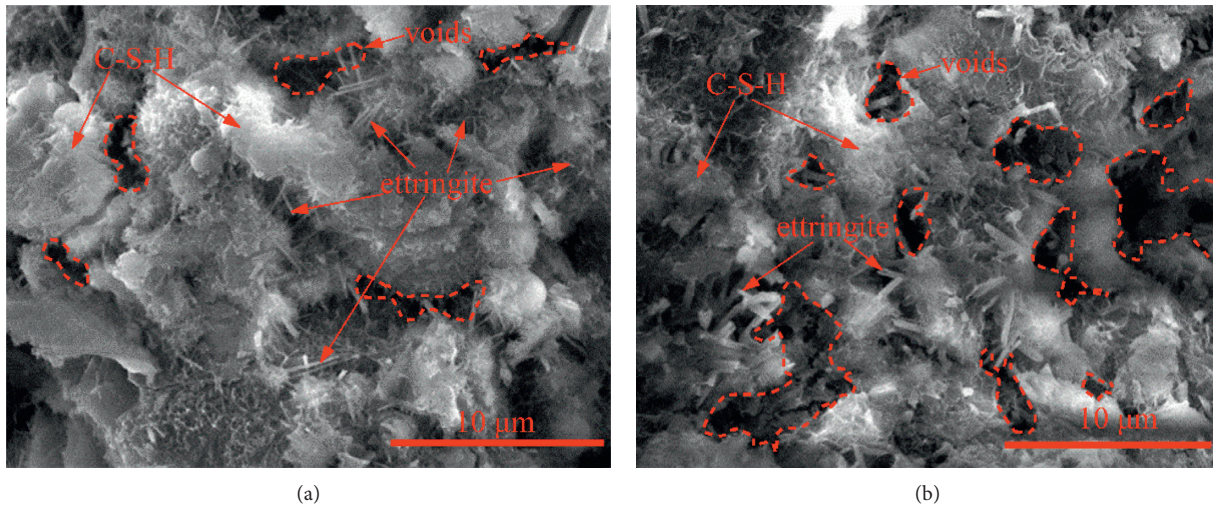(a)   (b)

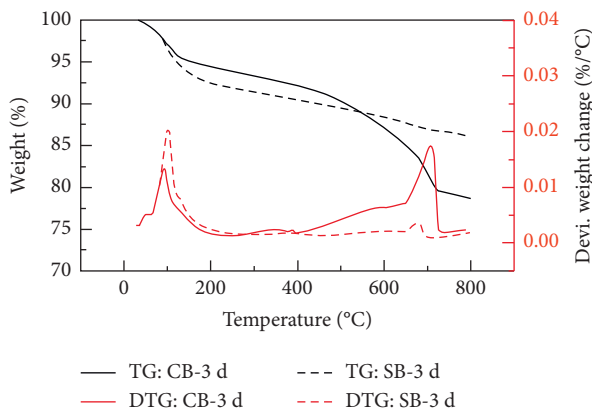FIGURE 3: Microstructures (SEM) of (a) CB-HDB and (b) SB-HDB after curing for 3 days.

FIGURE 4: TG/DTG analysis for CB and SB paste after curing for 3 days.

This finding is consistent with many other studies in the literature. References [36, 37] found that the slag grains with more edges produced high shear stresses, and a higher slag percentage produced higher normal shear stresses.

3.2.2. Viscosity. Figure 6 also shows that the viscosity only slightly changed, regardless of the binder agent. They are 0.431 Pa/s, 0.455 Pa/s, and 0.446 Pa/s for CB-HDB, BB-HDB, and SB-HDB respectively. The apparent viscosities were nearly the same as the three HDB during the test, as shown in Figure 7. It can be observed that the apparent viscosity completely overlapped for the three HDB and remained constant at 0.4 Pa/s when the shear rate exceeds $50 \, s^{-1}$. It can be concluded that the binder type does not affect the viscosity in this case.

3.2.3. Discussion on Rheological Properties. From the above results, the binder agent only slightly changed the yield stress but had nearly no effect on the viscosity for the HDS; however, it is difficult to determine how large of a change of the viscosity will be significant. The magnitude of the rheological property changes is far from practical use when expressed in terms of yield stress and viscosity. Another widely used practical parameter is the pressure drop or friction factor, which evaluates the pressure loss of the backfill slurry when transported via pipeline. The friction factor is closely related to the yield stress, viscosity, and engineering conditions, such as the pipe diameter, flow state (laminar, turbulent, and transition flow), flow rate (velocity), Reynolds number, and slurry bulk density. Many models can be used to predict the friction factor with high accuracy [38, 39]. To better evaluate the practical applicability of the SB, the pressure drop of the three HDBs will be calculated and compared using a friction factor correlation.

Before selecting the model, the flow state of the HDB under practical conditions should be determined, which is evaluated by the Reynolds number Re as shown in equation (1):
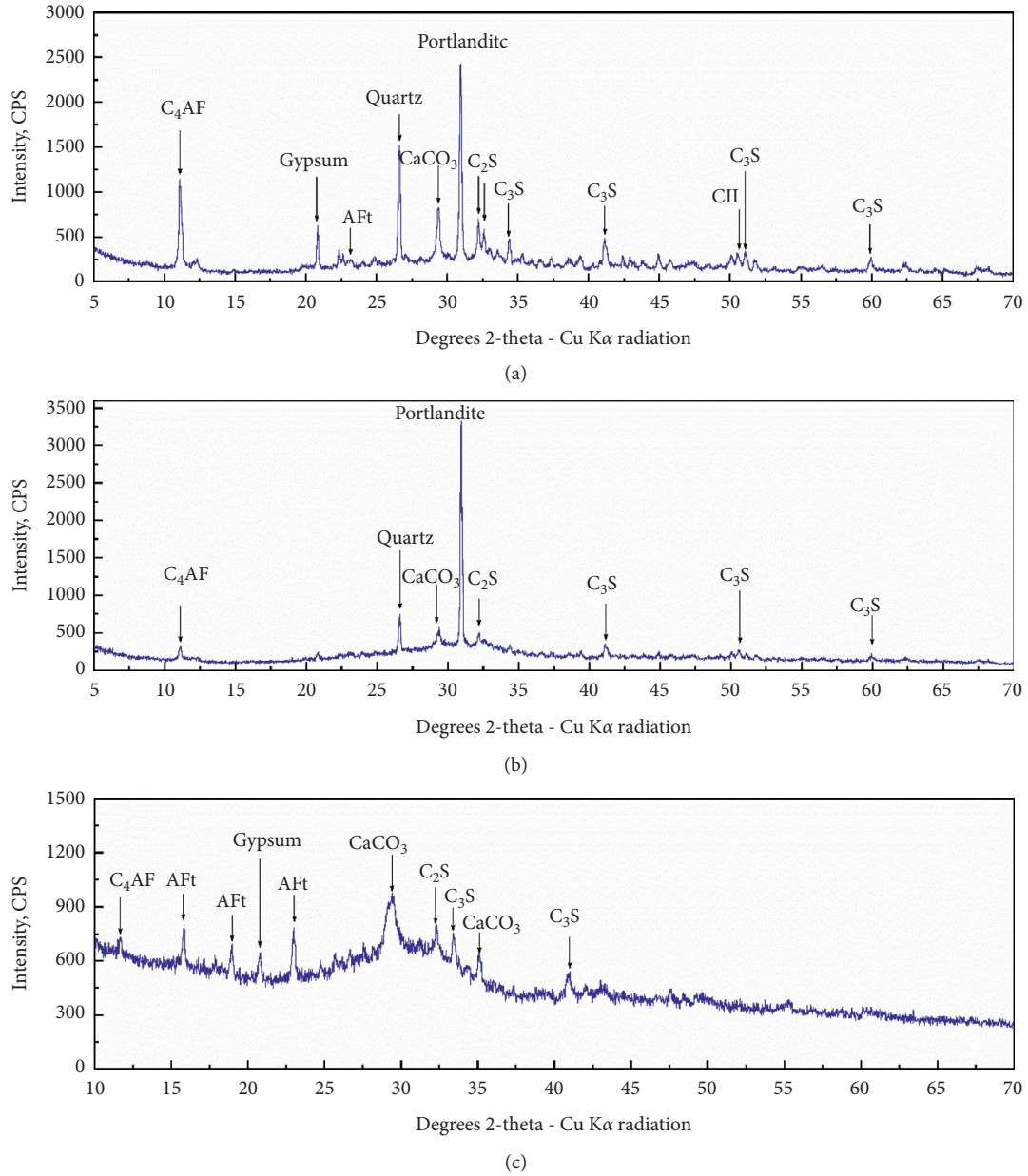
3.2.1. Yield Stress. From Figure 6, the practical use of CB-HDB had the lowest dynamic yield stress of 5.90 Pa, which fully meets the requirement for gravity transport. The yield stress increased to 7.1 Pa when half of PCI was replaced by GGBFS in BB-HDB, and it nearly doubled to 11.50 Pa for SB-HDB when 91% GGBFS was used. This finding indicates that the backfill slurry with GGBFS has a higher yield stress than without GGBFS, which can be explained by the following two mechanisms: (i) GGBFS has a larger specific surface area and fine particle content than PCI; therefore, the formed cementitious gel has a larger surface area when mixed with water, which will, in turn, capture more free water molecules. Thus, the distance between solid particles is reduced, and flocculation and interparticle attractive forces are enhanced, which increases the minimum external force required to break the microstructure (yield stress) and induce flow; (ii) GGBFS can improve the grain size distribution of the mixtures because of its finer particle size ($d_{50} = 12.13 \, \mu$m. This allows the tiny pores between aggregate particles to be filled, which reduces the porosity and produces more compact mixtures with a higher packing density, which increases the yield stress.

(a)

(b)

(c)

FIGURE 5: XRD patterns for (a) CB, (b) BB, and (c) SB pastes after curing for 28 days.

$$Re = \frac{\rho v D}{\mu_p}, \qquad (1)$$

where ρ is the slurry bulk density, kg/m^3; v is the flow velocity, m/s; D is the pipe diameter, m; and μ_p is the plastic viscosity of a Bingham plastic fluid, Pa/s.

In this case, the pipe diameter was 110 mm, the flow velocity in the pipe ranged from 2.0 m/s to 3.0 m/s, the bulk densities of the BB-HDB, CB-HDB, and SB-HDB were 1740.5, 1744.8, and 1736.08 kg/m^3, respectively, and the plastic viscosities are shown in Figure 8. The calculated Re ranged from 840 to 1336, which falls in the laminar flow regime (Re < 2100). Furthermore, HDB behaves as a Bingham plastic fluid as shown earlier; consequently, the

Buckingham–Reiner friction factor correlation [39] was used to calculate the friction factor, as shown in equation (2):

$$f = \frac{64}{Re}\left[1 + \frac{1}{6}\frac{He}{Re} - \frac{64}{Re}\left(\frac{He^4}{f^3 Re^7}\right)\right], \qquad (2)$$

where f is the friction factor; He is the Hedstrom number and He = $((\rho D^2 \tau_B)/\mu_p^2)$; and τ_B is the yield stress of a Bingham plastic fluid.

Once the friction factor is determined, the friction head loss can be determined by the Darcy–Weisbach equation [28] using the following equation:
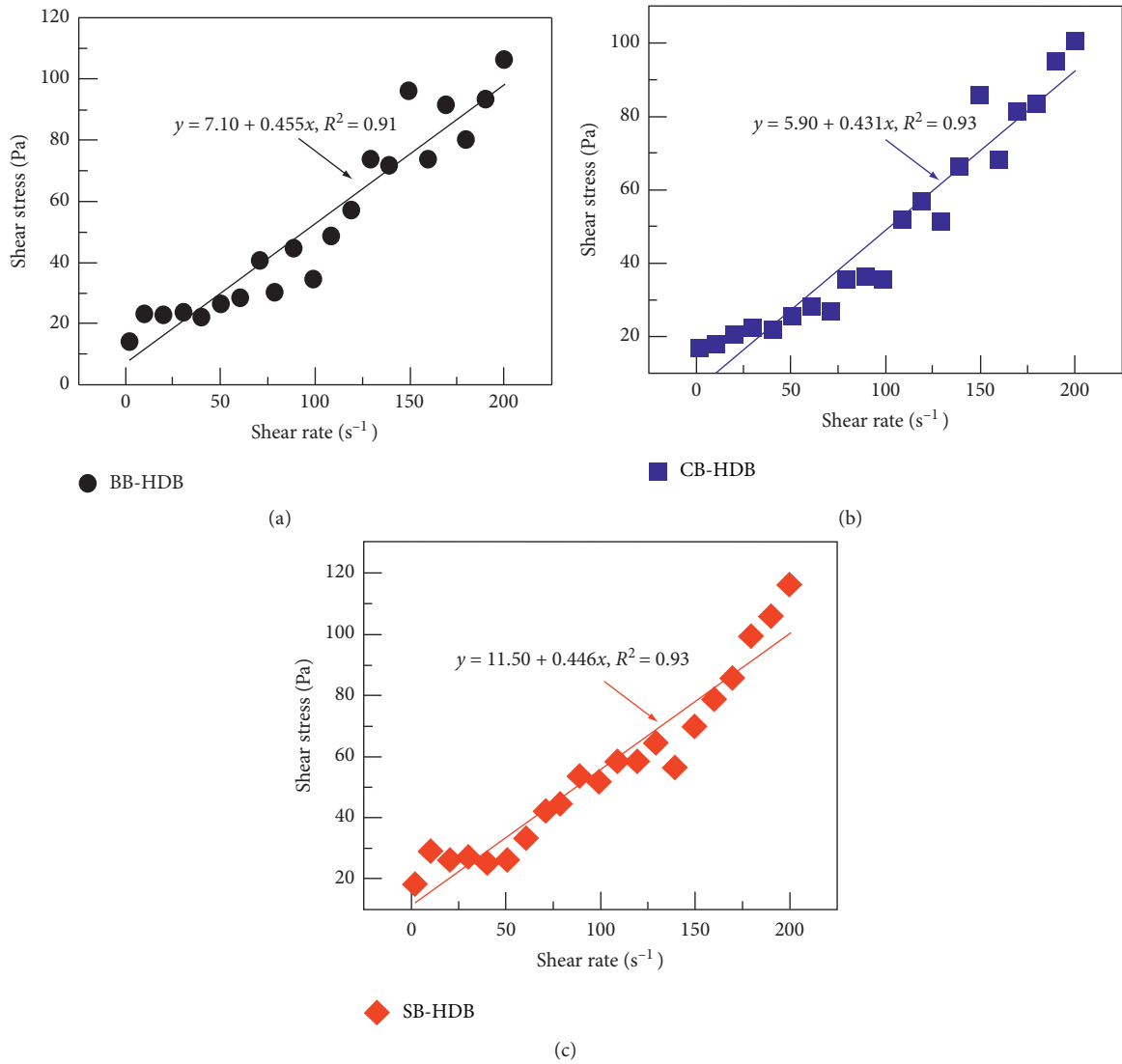
$$f = \frac{2h_f g D}{L v^2}, \qquad (3)$$

FIGURE 6: Rheological properties (shear rate vs. shear stress) of (a) BB-HDB, (b) CB-HDB, and (c) SB-HDB.
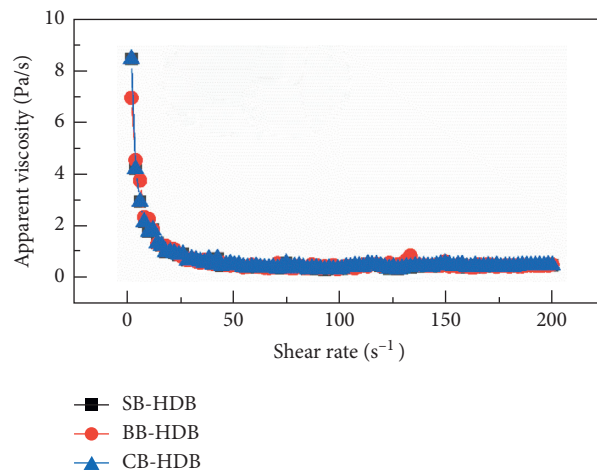

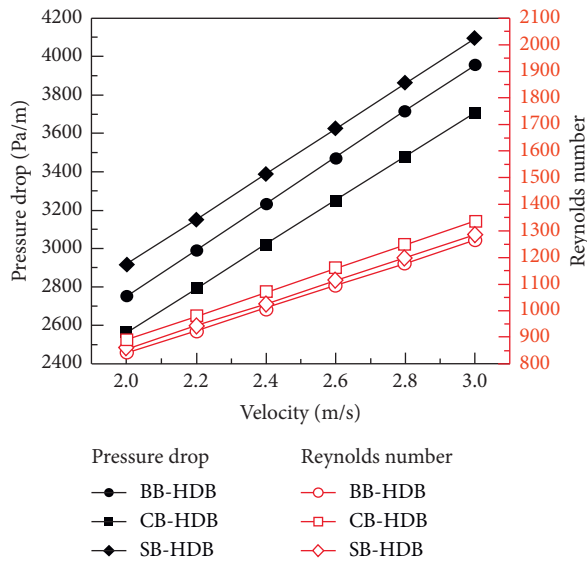FIGURE 7: Apparent viscosity for SB-HDB, BB-HDB, and CB-HDB.

FIGURE 8: Calculated pressure drop and Reynold's number for SB-HDB, BB-HDB, and CB-HDB.

where h_f is the friction head loss, g is the acceleration of gravity (m/s^2), and L is the length of the pipeline (m).

Finally, the friction head loss can be converted to a pressure drop i_m according to the following equation:

$$i_m = \frac{\rho g h_f}{L} = \frac{\rho f v^2}{2 D}. \tag{4}$$

According to the described procedure, the calculated pressure drops for the three HDB are shown in Figure 8. PCI has the lowest pressure drop, while the slag binder with 91% GGBFS has a slightly higher pressure drop than HDB (approximately 350 Pa/m), even with the doubled yield stress and a small increase in viscosity mentioned earlier. In other words, the flowability of the SB-HDB was not much different than that of PCI.

4. Conclusions

This work reported a slag binder for mine backfilling with a large slag proportion (>90%), low-cost activator (solid waste), and higher performance than cement. Strength and rheology tests (yield stress and viscosity) as well as microstructure analysis using SEM, XRD, and TG/DTG were conducted to compare its performance with ordinary Portland cement type I (PCI) and PCI-slag blended binder.

The proposed slag binder consists of 91% GGBFS, 3% clinker, 5% desulfurized gypsum, and 1% mirabilite, and it has a lower cost and is more environmentally friendly than cement. The backfill slurry with PCI binder had a higher early strength due to the fast hydration rate of clinker, while the developed slag binder has better mechanical performance after midterm (7 d) and long-term (28 d) curing, which is beneficial for practical mining applications.

The rheological properties showed that adding slag to HDB produced a higher yield stress, while changing the binder type did not significantly change the viscosity; however, a more

practical parameter—the pressure drop calculated from the Buckingham–Reiner friction factor correlation—showed that SB-HDB was not significantly different than PCI, which indicates that SB is suitable for mine backfilling.

The validation tests showed that the proposed SB can provide a sustainable binder choice for the mining industry with better performance and a lower cost.

Data Availability

The raw and processed data required to reproduce these findings are available to download from [https://doi.org/10.17632/7hrw5bgwj3.3].

Conflicts of Interest

The authors declare that they have no conflicts of interest.

Authors' Contributions

B. X. and X. Y. conceptualized the study; B. X. was involved in the methodology; X. Y. was responsible for the software; B. X. and X. Y. validated the study; B. X. performed the formal analysis, X. Y. investigated the study; X. Y. collected the resources; B. X. curated the data; B. X. wrote, prepared, reviewed, and edited the original draft and visualized the study; Q. G. supervised the study and was involved in the project administration and funding acquisition.

Acknowledgments

References

[1] W. Matthes, A. Vollpracht, Y. Villagrán et al., "Ground granulated blast-furnace slag,""Ground granulated blast-furnace slag," in *RILEM State-of-the-Art Reports*, N. De Belie, M. Soutsos, and E. Gruyaert, Eds., pp. 1–53, Springer International Publishing, Berlin, Germany, 2018.

[2] M. L. Berndt, "Properties of sustainable concrete containing fly ash, slag and recycled concrete aggregate," *Construction and Building Materials*, vol. 23, no. 7, pp. 2606–2613, 2009.

[3] M. K. Dash, S. K. Patro, and A. K. Rath, "Sustainable use of industrial-waste as partial replacement of fine aggregate for preparation of concrete-a review," *International Journal of Sustainable Built Environment*, vol. 5, no. 2, pp. 484–516, 2016.

[4] P. Ahmedzade and B. Sengoz, "Evaluation of steel slag coarse aggregate in hot mix asphalt concrete," *Journal of Hazardous Materials*, vol. 165, no. 1-3, pp. 300–305, 2009.

[5] E. Vejmelková, M. Keppert, S. Grzeszczyk, B. Skaliński, and R. Černý, "Properties of self-compacting concrete mixtures containing metakaolin and blast furnace slag," *Construction and Building Materials*, vol. 25, no. 3, pp. 1325–1331, 2011.

[6] A. Kavak and G. Bilgen, "Reuse of ground granulated blast furnace slag (GGBFS) in lime stabilized embankment

materials," *International Journal of Engineering and Technology*, vol. 8, no. 1, pp. 11–14, 2016.

[7] E. Crossin, "The greenhouse gas implications of using ground granulated blast furnace slag as a cement substitute," *Journal of Cleaner Production*, vol. 95, pp. 101–108, 2015.

[8] C. Li, H. Sun, and L. Li, "A review: the comparison between alkali-activated slag (Si + Ca) and metakaolin (Si + Al) cements," *Cement and Concrete Research*, vol. 40, no. 9, pp. 1341–1349, 2010.

[9] C. Hackländer-Woywadt, "Grinding of granulated blastfurnace slag in Loesche vertical roller mills,""Grinding of granulated blastfurnace slag in Loesche vertical roller mills," in *Proceedings of the 5th European Slag Conference: Proceedings Slag Products—Providing Sustainable Solutions for the Built Environment*, H. Motz and P. Verhaag, Eds., EUROSLAG Publication, Luxembourg, pp. 181–192, September 2007.

[10] A. Ehrenberg, "CO$_2$ emissions and energy consumption of granulated blastfurnace slag,""CO$_2$ emissions and energy consumption of granulated blastfurnace slag," in *Proceedings of the 3rd European Slag Conference: Proceedings Manufacturing and Processing of Iron and Steel Slags*, J. Geiseler and M. Dean, Eds., EUROSLAG Publication, Keyworth, UK, pp. 151–166, October 2002.

[11] S.-D. Wang and K. L. Scrivener, "Hydration products of alkali activated slag cement," *Cement and Concrete Research*, vol. 25, no. 3, pp. 561–571, 1995.

[12] I. Ismail, S. A. Bernal, J. L. Provis, S. Hamdan, and J. S. J. Van Deventer, "Drying-induced changes in the structure of alkali-activated pastes," *Journal of Materials Science*, vol. 48, no. 9, pp. 3566–3577, 2013.

[13] Y. Ding, J.-G. Dai, and C.-J. Shi, "Mechanical properties of alkali-activated concrete: a state-of-the-art review," *Construction and Building Materials*, vol. 127, pp. 68–79, 2016.

[14] P. H. R. Borges, N. Banthia, H. A. Alcamand, W. L. Vasconcelos, and E. H. M. Nunes, "Performance of blended metakaolin/blastfurnace slag alkali-activated mortars," *Cement and Concrete Composites*, vol. 71, pp. 42–52, 2016.

[15] R. Rankine, M. Pacheco, and N. Sivakugan, "Underground mining with backfills," *Soils and Rocks*, vol. 30, pp. 93–101, 2007.

[16] K. Klein and D. Simon, "Effect of specimen composition on the strength development in cemented paste backfill," *Canadian Geotechnical Journal*, vol. 43, no. 3, pp. 310–324, 2006.

[17] A. Gandhe, P. S. Upadhyaya, and C. Lee, "Paste backfill-AIMS towards sustainable underground mining," *Journal of Mines, Metals and Fuels*, vol. 61, pp. 219–224, 2013.

[18] L. Yang, J. Qiu, H. Jiang, S. Hu, H. Li, and S. Li, "Use of cemented super-fine unclassified tailings backfill for control of subsidence," *Minerals*, vol. 7, no. 11, p. 216, 2017.

[19] G. A. Habeeb and M. M. Fayyadh, "Rice husk ash concrete: the effect of RHA average particle size on mechanical properties and drying shrinkage," *Australian Journal of Basic and Applied Sciences*, vol. 3, pp. 1616–1622, 2009.

[20] T. Ikeda, M. Boero, and K. Terakura, "Hydration properties of magnesium and calcium ions from constrained first principles molecular dynamics," *Journal of Chemical Physics*, vol. 127, Article ID 074503, 2007.

[21] O. Peyronnard and M. Benzaazoua, "Alternative by-product based binders for cemented mine backfill: recipes optimisation using Taguchi method," *Minerals Engineering*, vol. 29, pp. 28–38, 2012.

[22] H. Jiang, Z. Qi, E. Yilmaz, J. Han, J. Qiu, and C. Dong, "Effectiveness of alkali-activated slag as alternative binder on workability and early age compressive strength of cemented paste backfills," *Construction and Building Materials*, vol. 218, pp. 689–700, 2019.

[23] F. Puertas, S. Martínez-Ramírez, S. Alonso, and T. Vázquez, "Alkali-activated fly ash/slag cements," *Cement and Concrete Research*, vol. 30, no. 10, pp. 1625–1632, 2000.

[24] M. Michel, J.-F. Georgin, J. Ambroise, and J. Péra, "The influence of gypsum ratio on the mechanical performance of slag cement accelerated by calcium sulfoaluminate cement," *Construction and Building Materials*, vol. 25, no. 3, pp. 1298–1304, 2011.

[25] G. Sarkar and S. Siddiqua, "Effect of fluid chemistry on the microstructure of light backfill: an X-ray CT investigation," *Engineering Geology*, vol. 202, pp. 153–162, 2016.

[26] K. L. Scrivener, P. Juilland, and P. J. M. Monteiro, "Advances in understanding hydration of Portland cement," *Cement and Concrete Research*, vol. 78, pp. 38–56, 2015.

[27] O. R. Ogirigbo and L. Black, "Influence of slag composition and temperature on the hydration and microstructure of slag blended cements," *Construction and Building Materials*, vol. 126, pp. 496–507, 2016.

[28] A. Gruskovnjak, B. Lothenbach, F. Winnefeld et al., "Hydration mechanisms of super sulphated slag cement," *Cement and Concrete Research*, vol. 38, no. 7, pp. 983–992, 2008.

[29] Y. Anderberg, "Spalling phenomena of HPC and OC," in *Proceedings of the International Workshop on Fire Performance of High-Strength Concrete*, NIST, Gaithersburg, MD, USA, pp. 69–73, Feburary 1997.

[30] I. Pane and W. Hansen, "Investigation of blended cement hydration by isothermal calorimetry and thermal analysis," *Cement and Concrete Research*, vol. 35, no. 6, pp. 1155–1164, 2005.

[31] M. Fall and M. Pokharel, "Coupled effects of sulphate and temperature on the strength development of cemented tailings backfills: Portland cement-paste backfill," *Cement and Concrete Composites*, vol. 32, no. 10, pp. 819–828, 2010.

[32] L. Chaurasia, V. Bisht, L. P. Singh, and S. Gupta, "A novel approach of biomineralization for improving micro and macro-properties of concrete," *Construction and Building Materials*, vol. 195, pp. 340–351, 2019.

[33] W. Liu, S. Yan, Y. An, and H. Li, "Research on special cement for the concrete with ultra-fine iron tailings," *Advanced Materials Research*, vol. 476–478, pp. 1974–1978, 2012.

[34] G. Xue, E. Yilmaz, W. Song, and S. Cao, "Compressive strength characteristics of cemented tailings backfill with alkali-activated slag," *Applied Sciences*, vol. 8, no. 9, p. 1537, 2018.

[35] Y. Zhou, H. Deng, and J. Liu, "Rational utilization of fine unclassified tailings and activated blast furnace slag with high calcium," *Minerals*, vol. 7, no. 4, p. 48, 2017.

[36] M. Torres-Carrasco, C. Rodríguez-Puertas, M. d. M. Alonso, and F. Puertas, "Alkali activated slag cements using waste glass as alternative activators. rheological behaviour," *Boletín de la Sociedad Española de Cerámica y Vidrio*, vol. 54, no. 2, pp. 45–57, 2015.

[37] M. Palacios, P. F. G. Banfill, and F. Puertas, "Rheology and setting of alkali-activated slag pastes and mortars: effect if organic admixture," *ACI Materials Journal*, vol. 105, pp. 140–148, 2008.

[38] N. Jia, M. Gourma, and C. P. Thompson, "Non-Newtonian multi-phase flows: on drag reduction, pressure drop and

liquid wall friction factor," *Chemical Engineering Science*, vol. 66, no. 20, pp. 4742–4756, 2011.

[39] B. Bharathan, M. McGuinness, S. Kuhar, M. Kermani, F. P. Hassani, and A. P. Sasmito, "Pressure loss and friction factor in non-Newtonian mine paste backfill: modelling, loop test and mine field data," *Powder Technology*, vol. 344, pp. 443–453, 2019.